University of Nottingham
UK | CHINA | MALAYSIA

PhD Thesis

Continuous Ambulatory Blood Pressure Monitoring Using Optical Fibre Sensors

Itzel Alexia Avila Castro

Supervised by:

Barrie Hayes-Gill

Steve Morgan

Ricardo Goncalves Correia

Serhiy Korposh

David Gomez

Faculty of Engineering

University of Nottingham

April 2025

To my grandma,

who always loved me so much and wanted me to succeed in life –

Te quiero mucho y te quiero ver triunfar.

To my parents,

whose unwavering support and love gave me strength.

To the curious mind that never settles.

Abstract

Abnormal blood pressure (BP) is a key indicator of cardiovascular dysfunction and a leading risk factor for stroke, heart failure, and mortality. Hypertension affects more than a quarter of adults in England, costing the NHS approximately £2.1 billion annually. Despite effective therapies, rates of uncontrolled BP remain high, underscoring the need for earlier detection and continuous monitoring. Beat-to-beat BP measurement offers distinct advantages by capturing rapid cardiovascular dynamics, yet current methods face limitations: invasive catheters are unsuitable for long-term use, oscillometric cuffs lack temporal resolution, and photoplethysmography (PPG) is prone to artefacts, latency, and skin-tone variability.

This thesis presents a **novel, non-invasive cuffless blood pressure (BP) monitoring system** that employs **fibre Bragg grating (FBG) cantilever sensors** to estimate **pulse transit time (PTT)** and integrates **electrocardiography (ECG)** to derive **pulse arrival time (PAT)**. The proposed system offers a light-insensitive and motion-resilient solution capable of high-fidelity pulse detection, making it suitable for real-time monitoring across clinical, home, and telemedicine settings.

A validated pipeline – spanning mechanics, temperature-strain decoupling, phantom haemodynamics, and in-human exercise trials – demonstrates technical feasibility, with a biocompatible FBG cantilever and compact interrogator achieving tens-of-milliseconds timing resolution. In human trials, PAT showed strong inverse correlations with systolic BP and heart rate, supporting its use in cuffless monitoring. Algorithmically, a GAN-based reconstruction stage restored morphology under artefacts, while Bayesian Gaussian Process Regression (GPR) produced calibrated mmHg estimates (SBP $\leq$10 mmHg, DBP $\leq$4 mmHg) and modelled inter- and intra-subject variability.

By combining high-sensitivity optical sensing, probabilistic modelling, and AI-based signal reconstruction, this work establishes a new pathway toward **continuous, personalised BP monitoring**. The findings have direct implications for next-generation medical devices that support early diagnosis, community screening, and digital health strategies aimed at reducing the global burden of hypertension.

Acknowledgements

First, I would like to express my deepest gratitude to my supervisors – each of whom has played a key and significant role in my PhD journey.

To Professor Barrie Hayes-Gill, for opening the door to my PhD and for offering unwavering support, encouragement, and trust from the very beginning. Thank you for all the invaluable knowledge and experience you shared with me; your belief in me and constant guidance have meant more than words can express.

To Professor Steve Morgan, for consistently helping me stay on track throughout this journey. Your invaluable guidance, kindness, broad perspective, steady encouragement and support ensured that I stayed aligned with the end goal. Thank you for believing in me and for keeping me focused when it mattered most.

To Dr Ricardo Correia, for your invaluable technical knowledge, enthusiasm, empathy and constant encouragement. Your support not only helped me navigate challenges with confidence, but also inspired me to explore new skills and perspectives. Your trust in my growth has been key to both my personal and professional development.

To Professor Serhiy Korposh, for always being incredibly supportive, for your critical insights, and for providing constructive feedback throughout this journey. Your guidance has been instrumental in shaping the quality and direction of my research.

To Dr David Gomez, for your remarkably support, for always looking out for me, and for all the skills, insights, constructive feedback and experience you so generously shared. Your mentorship has been crucial to both my research and personal growth.

To my host supervisors during my research internship at INESC TEC: To Dr Tania Pereira, for your invaluable expertise, patience, and guidance during my research stay; and to Dr Helder Oliveira, for your insights and constructive feedback. Both of you made a significant contribution to enriching my research experience. I am

grateful for the opportunity to work alongside you.

To my internal assessor, Dr Rikesh Patel, for your valuable and constructive feedback throughout this journey. Your insights and thoughtful suggestions have played a meaningful role in shaping the quality and direction of my research.

My sincere gratitude to Yi Hsuan Chen and Stuart Murray for their exceptional and valuable contributions to this research.

To my PhD colleagues, James Ell and Nat Limweshasin, for sharing your skills and knowledge, and for the discussions that nurtured and supported my research.

Also, to my PhD colleagues and staff members from the Fibre Optics Group – Agbiki, Ruirong, Delu, Sandor, Chong, Basem,Yasmine, Henry, Brett, Peizhou, Simon, James Bradbury, Nadia Afroze, Nadia Nowshin – thank you for the supportive and collaborative environment throughout this journey.

To CONACYT and the University of Nottingham for the scholarship and financial support that made this PhD possible.

To INESC TEC, for the opportunity to be part of the International Visiting Researcher Programme, which allowed me to expand both my research experience and knowledge.

To my alma mater, the National Autonomous University of Mexico (UNAM), for the solid academic foundation that prepared me for this journey. Specially, to my mentors there – Dr Angel Luis Rodriguez Morales, MSc Francisco Fernandez Escobar, Dr Blanca Millan Chiu, Dr Achim Loske, Dr Rafael Chavez Moreno, and Dr Miguel De Icaza Herrera – thank you for your invaluable inspiration, support and guidance during my undergraduate studies. Your mentorship has been instrumental in shaping my academic path and nurturing my passion for research.

To my PhD sister, Suvvi, for your support, encouragement, and for being a constant source of inspiration. Your friendship has made this journey not only meaningful but truly enjoyable.

To my friends – Oscar, Nilay, Karla, Tammy, Sam, Abril, Marcela, Maritere, Hwaran, Alan, and Irving – for your emotional support and encouragement. Thank you for being there for me through the ups and downs of this journey. Your friendship has been a source of strength and motivation.

To my family – Aracely, Rodolfo, Paulina, and Emeteria – for your cheerful, unconditional support and constant inspiration.

To my parents, Alejandro and Reyna Dolores, for your endless love and support. To my dad, from whom I learned to be passionate about everything I do, and for always looking out for me from afar. To my mum, for your constant encouragement and for always being there. To my brother, Alejandro Isaac, for looking after me and for your joyful spirit. To my grandmother, Francisca, for your love and immense support since the beginning of my studies. Thank you all for believing in me and encouraging me to pursue my dreams.

To my partner, Rodo, for your unconditional love and support. Thank you for always believing in me and looking after me. Your presence has made this journey not only possible, but also incredibly meaningful.

Itzel Alexia Avila Castro

April 2025

Public Outputs

This thesis is based on the following publications and research outputs, which were produced during the course of the research programme.

Conference Papers

- Castro, I. A. A., Chen, Y. H., Hayes-Gill, B. R., Morgan, S. P., Korposh, S., Gomez, D., & Correia, R. (2024, March). *Ambulatory fibre Bragg grating interrogator with applications in blood pressure monitoring.* In *Biophotonics in Exercise Science, Sports Medicine, Health Monitoring Technologies, and Wearables V* (Vol. 12838, pp. 79–91). SPIE. DOI: 10.1117/12.3005056

Journal Articles

- Avila Castro, I. A., Oliveira, H., Goncalves Correia, R., Hayes-Gill, B. R., Morgan, S. P., Korposh, S., Gomez, D., & Pereira, T. (2025). *Generative adversarial networks with fully connected layers to denoise PPG signals. Physiological Measurement.* DOI: 10.1088/1361-6579/ada9c1

- Limweshasin, N., Castro, I. A., Korposh, S., Morgan, S. P., Hayes-Gill, B. R., Faghy, M. A., & Correia, R. (2024). *Respiratory Rate Monitoring via a Fibre Bragg Grating-Embedded Respirator Mask with a Wearable Miniature Interrogator. Sensors (Basel, Switzerland)*, 24(23), 7476. DOI: 10.3390/s24237476

Research Internships

- **INESC TEC International Visiting Researcher Programme**, 2022 Edition at CTM – INESC TEC, Porto, Portugal
  Research Topic: AI-based models to predict HR using PPG signals corrupted by motion artefacts
  Dates: November 2022 – February 2023
  Scientific Hosts: Tania Pereira and Helder Oliveira

Acronyms

ABPM Ambulatory Blood Pressure Monitor.

Aerror Average absolute error.

ANN Artificial Neural Network.

BCG Ballistocardiogram for the signal and Ballistocardiography for the technique.

BP Blood Pressure.

BPV Blood Pressure Variability.

BRDAE Bidirectional Recurrent Denoising Autoencoder.

CCD Charge-Coupled Device.

CI Confidence Interval.

cNIBP Continuous Non-Invasive Blood Pressure.

CV Cardiovascular.

DBP Diastolic Blood Pressure.

DC-GAN Generative Adversarial Network with Deep Convolutional Layers.

DLR Drive Leg Right.

DWT Discrete Wavelet Transform.

ECG Electrocardiogram for the signal and Electrocardiography for the technique.

ED Euclidean Distance.

EMD Empirical Mode Decomposition.

FBG Fiber Bragg Grating.

FC-GAN Generative Adversarial Network with Fully Connected Layers.

GAN Generative Adversarial Network.

GPR Gaussian Process Regression.

GPT Generative Pretrained Transformer.

HR Heart Rate.

HRV Heart Rate Variability.

ICG Impedance Cardiogram for the signal and Impedance Cardiography for the technique.

IMAR Iterative Motion Artifact Reduction.

LASSO Least Absolute Shrinkage and Selection Operator.

MAE Mean Absolute Error.

MBE Mean Bias Error.

MBP Mean Blood Pressure.

MSE Mean Squared Error.

MsumE Mean Summed Error.

NIBP Non-Invasive Blood Pressure.

OFS Optical Fibre Sensors.

PAT Pulse Arrival Time.

PCA-SRGAN Principal Component Analysis - Super-Resolution GAN.

PCG Phonocardiogram for the signal and Phonocardiography for the technique.

PLSR Partial Least Squares Regression.

PPE Peak to Peak Error.

PPG Photoplethysmogram for the signal and Photoplethysmography for the technique.

PSD Power Spectral Density.

PSRR Power Supply Rejection Ratio.

PTT Pulse Transit Time.

PWA Pulse Wave Analysis.

PWV Pulse Wave Velocity.

RFR Random Forest Regression.

RLR Regularized Logistic Regression.

RMSE Root Mean Square Error.

SBP Systolic Blood Pressure.

SCG Seismocardiogram for the signal and Seismocardiography for the technique.

SLA Stereolithography.

SVM Support Vector Machine.

TAG Tonoarteriogram for the signal and Tonoarteriography for the technique.

TROIKA signal decomposiTion for denoising, sparse signal RecOnstruction for hIgh resolution for spectrum estimation, and spectral peaK tracking with verification.

VSD Voltage Spectral Density.

Contents

List of Figures

1. Introduction and Background

1.1 Clinical and Societal Context

Blood pressure (BP) is a fundamental biomarker in the diagnosis, management, and prevention of cardiovascular and systemic diseases. Deviations from normal BP values – either hypertension or hypotension – can reflect underlying organ dysfunction or indicate elevated cardiovascular risk. Hypertension is strongly associated with conditions such as coronary artery disease, stroke, heart failure, chronic kidney disease, vascular dementia, and vision loss. Collectively, these conditions cost the NHS over £2.1 billion annually [1]. While less frequently discussed, chronic hypotension can also present significant risks, contributing to complications such as neurological disorders, adrenal insufficiency, and syncope [2].

Globally, hypertension remains one of the top three leading risk factors for early mortality and disability-adjusted life years (DALYs) according to the Global Burden of Disease study [3]. In the United Kingdom, it is the third-highest risk factor for disease burden [1]. Despite the availability of effective antihypertensive medications, rates of uncontrolled hypertension remain high, particularly in populations with limited access to continuous monitoring or healthcare services [4]. This underscores the need for enhanced diagnostic tools that enable early detection and continuous tracking of BP trends.

Public health authorities have recognised the urgency of addressing this gap. The

NHS Long Term Plan prioritises early detection and personalised management of cardiovascular disease, including through the improved identification and control of hypertension [5]. NICE guidelines (NG136) recommend the use of ambulatory blood pressure monitoring (ABPM) as a standard for diagnosis and control [6]. At the international level, the World Health Organization (WHO) set a global target to reduce the prevalence of raised blood pressure by 25% by the year 2025 as part of its Global Action Plan for the Prevention and Control of Noncommunicable Diseases [7]. However, according to a recent WHO report, this target is unlikely to be met at the global level, despite progress in some countries [8]. This reflects persistent challenges in the detection, treatment, and long-term control of hypertension – particularly in low-resource or ambulatory settings – and reinforces the need for innovative, scalable monitoring technologies.

Moreover, BP is often measured intermittently – whether in clinical, home, or ambulatory settings – which may fail to capture rapid physiological fluctuations that could indicate early signs of cardiovascular instability. Continuous BP monitoring plays a crucial role in perioperative care, especially when patients are under anaesthesia, where sudden haemodynamic changes can be life-threatening [9]. However, existing technologies for continuous monitoring are often invasive, uncomfortable, or poorly suited for long-term use. This reinforces the clinical and economic motivation for developing wearable systems capable of capturing BP in real time and in free-living environments.

1.2 Physiological Basis of Blood Pressure

Blood pressure (BP) is the force exerted by circulating blood on the walls of blood vessels. It is generated primarily when the left ventricle of the heart contracts, ejecting blood into the aorta and subsequently through the arterial system. The pressure peaks during ventricular systole (systolic BP) and reaches its low-

est point during ventricular diastole (diastolic BP). The difference between these values is known as pulse pressure, which reflects the elasticity and compliance of arterial walls. In healthy adults, systolic blood pressure (SBP) is typically below 120 mmHg, while diastolic blood pressure (DBP) should be below 80 mmHg. On average, females tend to have SBP and DBP values approximately 8-10 mmHg lower than males, partly due to differences in vascular compliance and hormonal influences. Blood pressure is highest in the aorta and large systemic arteries, where it reflects the force generated by left ventricular contraction. As blood travels further from the heart, pressure gradually declines. By the time it reaches the systemic capillaries, mean arterial pressure has dropped to approximately 35 mmHg. At the venous end of the capillaries, it further decreases to around 16 mmHg. The pressure continues to fall along the venous circulation and approaches 0 mmHg upon reaching the right atrium. This progressive pressure gradient is essential for maintaining unidirectional blood flow and efficient capillary exchange throughout the circulatory system [10]. Figure 1.1 illustrates a typical arterial blood pressure waveform, highlighting its key morphological features across the cardiac cycle. The waveform begins with the systolic upstroke, a rapid rise in pressure as the left ventricle contracts and ejects blood into the aorta. The curve reaches its highest point at the systolic peak, corresponding to the systolic pressure of approximately 115 mmHg. Following this peak, the pressure declines and a distinct dicrotic notch appears, which marks the closure of the aortic valve and the brief rebound of blood against it. The waveform then continues to fall until reaching the diastolic pressure of around 80 mmHg, representing the lowest arterial pressure during ventricular relaxation [11, 12].

The cardiovascular system functions as a closed-loop circuit in which the heart pumps blood through arteries, veins, and capillaries. The pressure generated must overcome the resistance of the vascular system to ensure adequate tissue perfusion. This resistance is influenced by vessel diameter, blood viscosity, and vascular

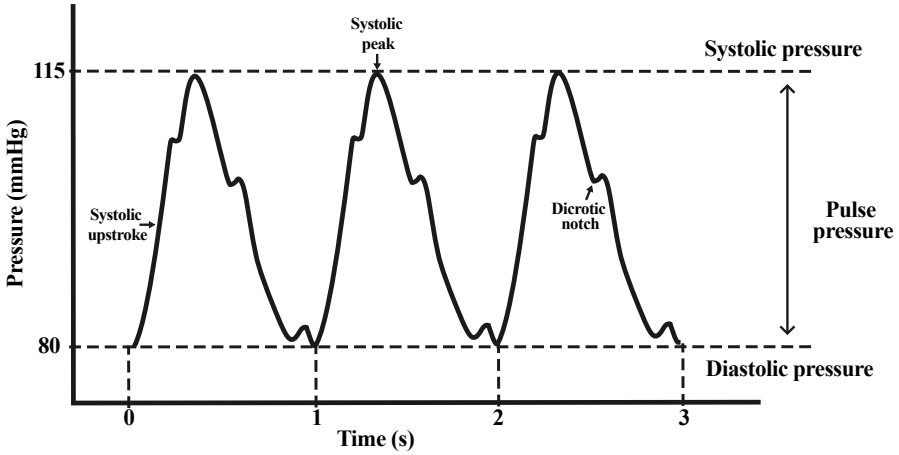

Figure 1.1: *Typical arterial blood pressure waveform diagram with wave features. Blood pressure of 115/80 mmHg and a heart rate of 60 beats per minute (bpm) [11, 12].*

tone. Cardiac output – determined by heart rate and stroke volume – along with systemic vascular resistance (SVR), are the principal determinants of BP. Arterial compliance, or the ability of vessels to expand and contract in response to pressure changes, also plays a critical role. In healthy individuals, elastic arteries accommodate these fluctuations, while arterial stiffening contributes to elevated BP and increased cardiovascular risk.

BP regulation involves a complex interplay of neural, hormonal, and local mechanisms that maintain homeostasis in response to physiological demands. The autonomic nervous system (ANS) governs short-term regulation through the baroreflex, which involves baroreceptors in the carotid sinus and aortic arch. These mechanoreceptors detect changes in arterial wall stretch and relay signals to the nucleus tractus solitarius in the medulla, modulating sympathetic and parasympathetic outputs. Sympathetic activation increases heart rate and vasoconstriction, while parasympathetic activity reduces heart rate. This dynamic balance enables rapid BP adaptation during exercise, posture changes, and emotional stress.

Long-term BP regulation is primarily mediated by hormonal systems, particularly the renin-angiotensin-aldosterone system (RAAS) and vasopressin. These mechanisms influence blood volume, vascular tone, and renal function, stabilising BP

over hours to days [10].

1.3 Importance of Beat-to-Beat Blood Pressure Monitoring

Traditional intermittent BP measurements provide only isolated snapshots and may fail to capture dynamic fluctuations that occur on a beat-to-beat basis. In contrast, beat-to-beat BP monitoring offers high temporal resolution, allowing for the detection of rapid, physiologically relevant changes that may indicate early signs of cardiovascular dysfunction, organ damage or autonomic imbalance.

In patients with autonomic dysfunction or baroreflex impairment, beat-to-beat BP monitoring can reveal abnormal variability patterns that are not evident in routine measurements. The baroreflex, which governs short-term BP regulation, depends on intact neural circuits between arterial baroreceptors and the central nervous system. When these pathways are compromised – as in brainstem stroke, Parkinson's disease, or multiple system atrophy – the body's ability to buffer sudden BP changes is impaired. This manifests as exaggerated fluctuations and loss of BP stability [13, 14].

Another example is early kidney dysfunction. In chronic kidney disease (CKD) and even in its early stages, patients may exhibit elevated nocturnal BP, non-dipping BP profiles, or increased BP variability. These abnormalities often precede over clinical markers such as elevated serum creatinine or diagnosed hypertension. At a beat-to-beat level, the loss of autonomic regulation leads to larger oscillations in BP, resulting in increased shear stress on glomerular capillaries. Over time, this contributes to glomerular injury and the progression of kidney damage [15–17]. Continuous BP monitoring can enable earlier identification of such patterns, supporting timely interventions to slow or prevent further organ deterioration.

1.4 Standard Techniques for Blood Pressure Measurement

A variety of options are available to accurately monitor blood pressure (BP) measurement in both clinical and ambulatory settings. These methods differ in terms of accuracy, invasiveness, temporal resolution, and patient comfort.

1.4.1 Invasive Arterial Blood Pressure (ABP) Monitoring

Invasive intra-arterial blood pressure monitoring involves inserting a catheter into a peripheral artery – commonly the radial, femoral, or axillary artery – which is connected to a continuous column of pressurised saline and a transducer. The saline column transmits pressure fluctuations to the transducer, which converts them into an electrical signal displayed on a monitor. A pressurised saline bag at 300 mmHg acts as a flushing system to prevent clot formation.

This method offers high-fidelity, beat-to-beat measurements and can detect rapid BP fluctuations. It is especially valuable in critical care due to its accuracy in hypotensive states and its suitability for patients with obesity or peripheral oedema. Additionally, the arterial line allows for blood sampling and arterial blood gas analysis. However, the technique has notable drawbacks: it is invasive and expensive, carries a risk of local thrombosis and infection, and may result in catastrophic ischaemia if drugs like thiopentone or antibiotics are inadvertently administered through the line. Brachial artery access is avoided due to the risk of compromising distal perfusion [18].

1.4.2 Auscultatory Methods: Mercury, Aneroid, and Hybrid Sphygmomanometers

The mercury sphygmomanometer, based on the auscultatory Korotkoff method, remains the gold standard for non-invasive BP measurement. A cuff is inflated to occlude the brachial artery, then deflated while a stethoscope detects the Korotkoff sounds corresponding to systolic (SBP) and diastolic (DBP) pressure [10].

While highly accurate, the use of mercury poses environmental and health hazards. Mercury exposure has been linked to neurological, renal, and respiratory damage [19]. Consequently, many hospitals have phased out mercury-based devices in favour of aneroid and hybrid alternatives. Aneroid manometers require frequent calibration, while hybrid devices tend to lose accuracy over time. Furthermore, these methods do not provide beat-to-beat resolution and depend heavily on operator skill and patient cooperation.

1.4.3 Oscillometric Method

Oscillometric monitors, commonly used in ambulatory and home settings, measure BP based on oscillations in the pressure cuff during deflation. The systolic pressure is estimated at the onset of oscillations, the mean pressure corresponds to the peak amplitude, and diastolic pressure is derived from the disappearance of oscillations [20]. Proprietary algorithms are used to estimate SBP and DBP, introducing device-to-device variability.

These monitors are user-friendly and suitable for untrained individuals, but their limitations include poor performance during motion or physical activity, lack of beat-to-beat resolution, and reduced accuracy in patients with arrhythmias or peripheral vascular disease [21].

1.4.4 Volume Clamp Method (Peñáz Method)

The volume clamp method, originally developed by Peñáz, allows for non-invasive continuous BP monitoring using a finger cuff with an integrated photoplethysmography (PPG) sensor, a fast pneumatic servo system, and a dynamic pressure controller [22]. The servo system applies variable pressure to maintain a constant arterial volume, effectively "clamping" the artery to eliminate pulsatile changes. The pressure required to maintain this constant volume approximates the intra-arterial pressure waveform.

While this method offers continuous, beat-to-beat BP waveforms with medical-grade accuracy, its widespread adoption has been hindered by several issues. Prolonged use can cause finger discomfort, numbness, or tingling due to constant pressure. Its accuracy decreases in fingers with stiffer arteries (sick/elderly). Tight or misaligned cuffs can induce temporary ischaemia, skin damage, or even tissue injury [23]. Furthermore, the devices are bulky, costly (Finapres NOVA systems range from £20,000 to £40,000), and require regular calibration and maintenance, making them unsuitable for routine or home-based long-term monitoring.

1.5 Cuffless Blood Pressure Monitoring Technologies

The cuff-based method remains the gold standard for evaluating and managing hypertension in clinical practice. However, as discussed in the previous section, oscillometric cuffs only provide intermittent measurements, while the volume clamp technique is not suitable for extended use. Both approaches fail to capture rapid and dynamic fluctuations in blood pressure in response to the physical and mental demands of daily life [24].

Another approach is pulse tonometry, which employs a pressure transducer to record the pulsatile waveform at superficial arteries. To maintain consistent sen-

sor contact, the artery is partially flattened – a process often supported by an air chamber in modern devices to optimise skin coupling [25]. A key advantage of this method is its ability to generate a peripheral pressure waveform that closely reflects intra-arterial BP. However, tonometry is highly sensitive to sensor placement and typically requires the subject to remain supine, reducing its practicality. Furthermore, accuracy and comfort tend to decline over prolonged use [23]. Although often categorised as cuffless due to the absence of inflatable cuffs, arterial tonometry involves mechanical applanation that partially occludes the artery. Under stricter definitions – such as those outlined in the *Handbook of Cuffless Blood Pressure Monitoring* – it is therefore not classified as a truly cuffless technique [26]. A persistent challenge of such semi-occlusive methods lies in calibrating and interpreting local pressure measurements at peripheral sites.

To understand the broader landscape of BP monitoring technologies, Figure 1.2 categorises the principal methods currently used in both clinical and research settings [26]. The classification begins by distinguishing between invasive and non-invasive techniques. Among the non-invasive approaches, a further division is made based on whether the method involves arterial occlusion.

Fully occlusive methods include intermittent measurements performed using auscultatory or oscillometric techniques – both widely adopted in clinical practice for the management of hypertension. Semi-occlusive methods allow for continuous monitoring by partially compressing the artery, as seen in volume clamp and tonometry techniques.

In contrast, non-occlusive methods – which do not apply any arterial compression – are further divided into two categories. The first includes monitors based on the principle of pulse wave velocity (PWV), which estimate BP by measuring local or regional PWV using at least two pulsatile sensors and/or complementary cardiovascular signals such as ECG. This includes approaches based on Pulse Arrival Time (PAT) and Pulse Transit Time (PTT). The second category includes methods based on pulse wave analysis (PWA), which derive BP estimates from

features of the pressure waveform using a single pulsatile sensor. These latter methods are commonly referred to as cuffless blood pressure monitors. Thus, a cuffless BP monitor has been broadly defined **as a device or technology that estimates blood pressure non-invasively, without applying any form of arterial occlusion** [26].

Recent advances in sensor technologies have enabled the acquisition of high-fidelity pulse waveforms from the skin surface using a variety of non-invasive modalities. These signals – often expressed in arbitrary units depending on the sensing principle – can capture physiological dynamics that correlate with blood pressure [27]. Such technologies are capable of supporting continuous, non-occlusive estimation of blood pressure, aligning with the definition of cuffless monitoring.

As a result, cuffless BP monitoring holds great promise for a wide range of applications, including professional short-term continuous monitoring of hospitalised patients, hypertension diagnosis and long-term follow-up in treated individuals, and simple screening of asymptomatic individuals in primary care. It also offers opportunities to better understand blood pressure profiles in relation to daily habits – while avoiding sleep disturbances caused by cuff inflation. Furthermore, the large-scale deployment of such devices facilitates big data collection for population health research and personalised care, enhances phenotypic classification in epidemiological studies, and supports precision medicine through the integration of genetic, behavioural, and physiological data.

Notably, the importance of blood pressure as a key cardiovascular risk factor was recognised over a century ago, when life insurance companies began recording handwritten annotations of BP values in asymptomatic individuals [28].

The *Handbook of Cuffless Blood Pressure Monitoring* defines the underlying architecture of such devices as comprising three functional layers (Figure 1.3).

The first layer, known as the *transducer layer*, involves the sensing principle used

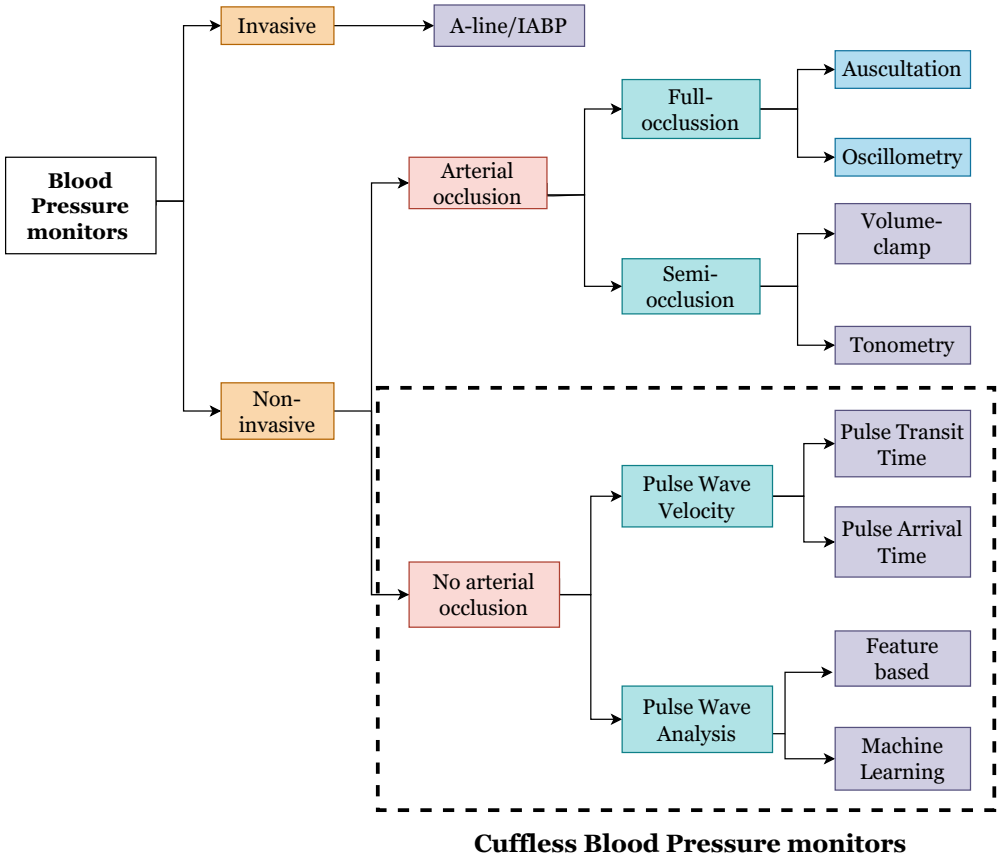

Figure 1.2: *Classification of blood pressure monitoring technologies. Methods are first divided into invasive and non-invasive approaches. Non-invasive techniques are further categorised based on the degree of arterial occlusion: fully occlusive (e.g., oscillometric and auscultatory methods), semi-occlusive (e.g., volume clamp and tonometry), and non-occlusive. Non-occlusive methods are classified into pulse wave velocity (PWV)-based techniques, such as PAT and PTT, and pulse wave analysis (PWA)-based techniques, which rely on a single pulsatile signal. The latter category includes most cuffless BP monitors [26].*

to detect the pulse or pulsatile energy generated at peripheral sites. Several techniques have been developed for pulsatile signal acquisition at the skin surface, including Photoplethysmography (PPG), Impedance Cardiography (ICG), Ballistocardiography (BCG), Seismocardiography (SCG), and Phonocardiography (PCG). Among these, ICG, BCG, SCG, and PCG primarily capture mechanical vibrations associated with cardiac activity [29]. PPG, by contrast, is one of the most widely studied and applied techniques for non-invasive cardiovascular monitoring. It detects blood volume changes in the microvascular bed of tissue by analysing the light transmitted through or reflected from the skin. Standard PPG systems employ light-emitting diodes (LEDs) – typically green, red, or infrared – alongside a photodiode to measure changes in perfusion [30]. Originally developed for pulse oximetry, PPG has emerged as a promising approach for cuffless, beat-to-beat BP estimation due to its non-invasiveness, wearability, and potential for miniaturisation.

The second layer, the *processing layer*, analyses the pulsatile waveform, which contains time-, amplitude-, and frequency-domain features relevant to blood pressure. This waveform may be supplemented with additional cardio-synchronous signals such as Electrocardiography (ECG), ICG, or PCG to improve signal interpretation. These inputs feed into pulsatile-based algorithms, including those based on pulse wave velocity (PWV) and pulse wave analysis (PWA). Recent advances in machine learning have further enabled the use of PPG signals – alone or in combination with ECG – for continuous BP estimation. The integration of ECG and PPG facilitates the derivation of cardiovascular timing parameters such as Pulse Arrival Time (PAT), thereby improving prediction accuracy [31]. Moreover, the availability of large, publicly accessible PPG datasets has supported the development and validation of data-driven models. The output of the processing layer is typically expressed in non-pressure units – such as milliseconds, millivolts, or hertz – that correlate with blood pressure. In some implementations, this output

can be used directly to monitor BP trends or assess blood pressure variability. However, a third layer is required to derive systolic and diastolic pressure values.

The third layer, referred to as the *initialisation layer*, converts the non-pressure values produced by the processing layer into clinically interpretable systolic and diastolic blood pressure values (expressed in mmHg or kPa). This mapping can be achieved using theoretical or empirical parametric models and may involve person-specific calibration parameters, population-based models, or hybrid approaches.

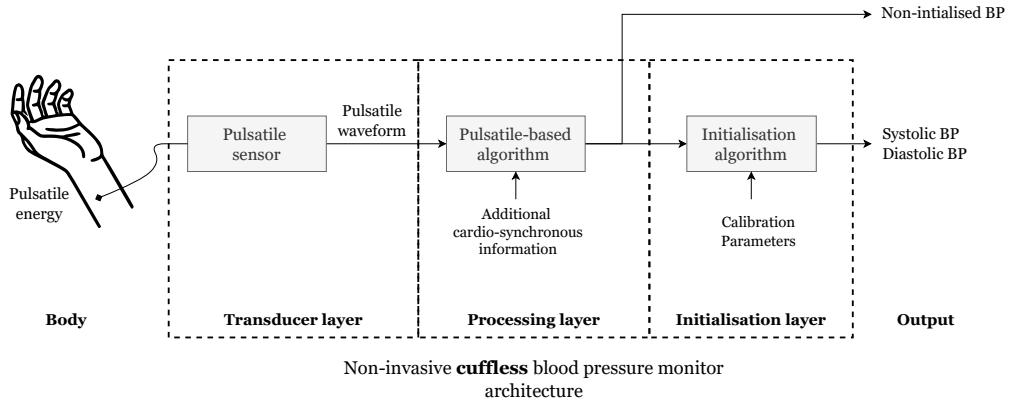

Figure 1.3: *Generic architecture of cuffless blood pressure monitoring systems, comprising three functional layers. The transducer layer acquires pulsatile signals using non-invasive sensing modalities such as PPG, ICG, BCG, SCG, and PCG. The processing layer extracts cardiovascular features and applies algorithms based on pulse wave velocity (PWV) or pulse wave analysis (PWA). The initialisation layer converts the processed signals into clinically interpretable systolic and diastolic BP values through calibration models [26].*

1.5.1 Pulse Wave Velocity Methods

PPG-based signals have been widely used in both Pulse Wave Analysis (PWA) and Pulse Wave Velocity (PWV) estimation – two indirect methods for assessing blood pressure. While PWA focuses on analysing the morphology of the PPG waveform (e.g., systolic peak, dicrotic notch, and reflected wave), this thesis concentrates on PWV-based techniques. The features extracted through PWA are influenced

by arterial compliance, wave reflections, and vascular resistance, offering valuable insight into cardiovascular health [32].

Physiological Basis of PWV Methods. The heart functions as a periodic fluid pump, generating pulsatile blood flow throughout the arterial system. This intermittent flow is influenced by both cardiac performance and the mechanical properties of the arterial tree. The arterial tree serves not only as a conduit for the continuous delivery of oxygen and nutrients but also as a hydraulic cushion that dampens pressure oscillations, thereby ensuring a steady flow at the capillary level. With each heartbeat, a pressure wave is propagated along the arterial walls and can be felt as pulsations in superficial arteries near the skin surface.
The speed at which this pressure wave travels – i.e., the PWV – is directly related to arterial stiffness, which in turn depends on the arterial wall's mechanical properties, particularly its Young's modulus. Importantly, since arterial stiffness increases with distending pressure, PWV serves as a dynamic marker of blood pressure. Therefore, measuring the velocity of the travelling pulse wave provides an indirect estimation of intra-arterial pressure [31].

Time-Domain Parameters. In practice, two timing parameters are commonly derived from physiological signals: Pulse Arrival Time (PAT) and Pulse Transit Time (PTT). PAT is defined as the interval between the R-peak of the ECG and the arrival of the pulse at a distal site (e.g., a finger or wrist PPG), and includes the pre-ejection period (PEP). PTT, on the other hand, excludes PEP and is defined as the time it takes for the pulse wave to travel between two arterial sites. Both parameters are inversely related to blood pressure and form the basis of many model-based approaches for continuous, non-invasive monitoring [29]. Recent advances in machine learning have further enabled the use of PPG – alone or in combination with ECG – for BP estimation. In particular, PAT-based models have benefited from large public datasets and improved algorithmic performance

[31].

Theoretical Models. The Moens-Korteweg equation (Equation 1.1) relates PWV to arterial wall thickness h, radius R, Young's modulus E, and blood density ρ, under the assumption of inviscid flow in a thin-walled elastic vessel:

$$\mathbf{c_0^2} = \frac{\mathbf{L}}{\tau} = \frac{\mathbf{hE}}{\mathbf{2R}\rho} \tag{1.1}$$

Building on this, Hughes et al. [33] demonstrated that Young's modulus increases exponentially with mean distending pressure P, leading to the following relation:

$$\mathbf{c_0^2} = \frac{\mathbf{L}}{\tau} = \frac{\mathbf{hE_0e^{\gamma P}}}{\mathbf{2R}\rho} \tag{1.2}$$

Here, E_0 is the zero-pressure modulus, and γ is a subject-specific constant (typically 0.016-0.018). Combining these equations provides a theoretical basis for estimating blood pressure from PWV measurements, using measured transit time τ over a known arterial path length L.

Based on this physiological and theoretical foundation, cuffless blood pressure estimation using Pulse Arrival Time (PAT) or Pulse Transit Time (PTT) may offer a more direct and physiologically grounded approximation of intra-arterial pressure compared to conventional indirect methods. These include palpatory detection of distal pulses (e.g., in PWA), Korotkoff sounds (auscultatory method), and the analysis of pressure oscillations during cuff deflation (oscillometric method).
One example that illustrates the limitations of direct pressure measurement at the limb skin surface is the case of arterial tonometry. Despite extensive efforts to use tonometry for direct BP assessment, commercial research tools – such as the SphygmoCor (AtCor Medical, Sydney, Australia), Form/VP-2000, and HEM-9000AI (Omron Healthcare Co., Ltd, Kyoto, Japan) – have been primarily used for pulse wave analysis, arterial stiffness assessment, and central BP estimation. This

is largely due to the practical challenges associated with tonometric measurements, including the need for precise sensor positioning, sensitivity to motion artefacts, and frequent calibration requirements.

Discrepancies Between PTT and PAT

Among research groups, there are differences in the definition of PTT, and it is often confused with PAT. The concept of PTT was introduced as early as 1964, using ECG and downstream pulse signals over a known arterial length to measure PWV [34, 35]. In 1981, the introduction of the pre-ejection period (PEP) – defined as the interval between the ECG R-wave and the opening of the aortic valve – led to a clearer distinction between PAT and PTT.

Since then, PAT has been defined as the interval from the ECG R-wave to the arrival of the pulse wave at a peripheral site, encompassing the PEP. Conversely, PTT refers to the time taken for the pulse wave to travel between two arterial locations [36–38]. This thesis adheres to these latter definitions.

Limitations of PPG-Based Methods

Despite the substantial research interest and progress in using PPG-based methods as the transducer for pulsatile detection for Cuffless BP estimation, several fundamental limitations remain that affect signal fidelity, patient-specific variability, and beat-to-beat accuracy.

The primary limitation is the high susceptibility to **motion artefacts**, arising from light scattering, contact pressure variation, and skin movement. These artefacts degrade the beat-to-beat resolution of the PPG waveform and impair feature detection. Additionally, **ambient light interference** can reduce the signal-to-noise ratio if not adequately shielded [30, 39].

Inter-patient variability is another critical factor: **skin tone**, **tissue thickness**, and **measurement site** influence light absorption and scattering, leading to differences in signal strength and waveform morphology. As a result, PPG-based BP

estimation models often require **subject-specific calibration** or large, diverse datasets to generalise effectively [39].

PPG systems also face challenges in **harsh environments** (e.g., MRI), where electronic components may become unstable. Importantly, PPG signal quality is heavily dependent on **peripheral blood perfusion**, which varies with skin temperature and vasoconstriction. These physiological factors affect both the amplitude and the latency of the PPG waveform – the latter typically ranging from 10-50 ms and introducing timing errors in PAT/PTT estimation [40–42].

These latency errors can be as well attributed to the fact that PPG waveforms exhibit markedly lower systolic peak prominence compared to simultaneously recorded invasive arterial blood pressure (ABP) waveforms [43–45]. The diminished upstroke slope and reduced dicrotic notch visibility in PPG complicate the accurate detection of fiducial points, leading to variability in PAT/PTT calculations.

1.6 Optical Fibre Sensors for arterial pulse detection

Optical Fibre sensing systems (OFS) are evolving as an excellent choice compared to opto-electronic components or electrical sensors based on catheters, guidewires and MEMS [46]. For medical applications, specifically arterial pulse detection based on strain sensing, OFS have several strategic advantages over classical measurements technologies.

Footprint and Geometry the diameter range of silica-based optical fibres is around 125 µm such as standard SMF-28, where variants can even reach 80 µm, now commercially available. Advances in tower manufacturing techniques are allowing the fibre fabrication keeping the protective coating, therefore, preserving the fibre mechanical strength. Moreover, the widespread availability of polarizing

independent fibres or bend insensitive fibres, increase the fibre sensor reliability when subjected to narrow curvatures [46, 47].

Multiplexing and Scalability OFS for temperature and strain sensing such as Fibre Bragg Grating sensors enables multiple FBGs with different Bragg wavelengths can be written along a single fibre [48] – enabling multi-site PWV/-PAT measurement. This is based on wavelength division multiplexing (WDM). Distributed sensing systems based on Rayleigh backscattering demodulation can achieve 1 mm of spatial resolution – valuable for detecting subtle mechanical or physiological changes along a body or structure [49].

Long-term stability A key objective in biomedical sensing is to enable long-term physiological monitoring using minimally invasive devices. To meet this requirement, pressure sensors must demonstrate consistent performance over extended periods. OFS exhibit excellent long-term stability, with prototype devices achieving typical drift rates of approximately 1 mmHg/hour [50].

Thermal linearity The performance of pressure sensing technologies is often constrained by their cross-sensitivity to temperature fluctuations. In many conventional sensors – such as electronic or mechanical types – temperature changes introduce non-linear distortions in the output signal, which typically require thermally isolated packaging to reduce their impact. In contrast, OFS exhibit linear responses to both temperature and pressure, enabling effective compensation through appropriate calibration or dual-sensor configurations [49].

EMI immunity OFS are typically manufactured from silica glass – a dielectric material – are inherently immune to electromagnetic interference (EMI). This intrinsic property makes OFS-based systems well-suited for use in clinical environments where EMI is prevalent, such as in magnetic resonance imaging (MRI),

computed tomography (CT), radiofrequency (RF) or microwave ablation, and various other imaging or interventional procedures [51].

Among the various fibre optic sensing technologies with strain and bending sensitivity for arterial pulse detection – such as Fibre Bragg Gratings (FBG), Fabry-Pérot interferometers (FPI), Mach-Zehnder interferometers (MZI), microbending sensors, and hetero-core fibres – FBG sensors appear to offer the most favourable balance between accuracy, wearability, and scalability. [52]. While FPI and MZI systems can achieve extremely high sensitivity, they are not yet practical for wearable or ambulatory applications due to their reliance on complex optical alignment and interrogation setups [53]. Conversely, microbending and hetero-core fibre sensors provide advantages in terms of simplicity, mechanical robustness, and cost-effectiveness; [54, 55], however, they can potentially underperfom as these sensing technologies are based on the intensity of the transmitted light caused by the fibre deformation making them vulnerable to source power fluctuations, connector losses, and any curvature or deformation outside the sensing region.

Table 1.1: Comparison of optical fibre sensing technologies for pulsatile signal detection and cuffless BP monitoring

Feature	**FBG**	**Fabry-Pérot Interferometer**	**Mach-Zehnder Interferometer**	**Microbending Sensor**	**Hetero-Core Fibre**
Sensing principle	Wavelength shift due to strain or pressure	Interference from cavity length change	Interference between two fibre paths	Optical loss due to bending-induced mode coupling	Mode loss at core-cladding mismatch
Signal encoding	Spectral (wavelength)	Interferometric (phase/intensity)	Interferometric (phase shift)	Intensity-based	Intensity-based
Sensitivity	High (picostrain-level)	Very high	Very high	Moderate	Moderate
Temperature compensation	Easy via dual FBGs	Complex (requires reference arm)	Complex (requires stabilisation)	Difficult	Difficult
Multiplexing capability	Excellent (WDM)	Limited	Limited	Limited	Limited
Interrogation complexity	Moderate-High (requires spectrometer or tunable laser)	High (requires interferometric demodulation)	High	Low	Low
Cost	Moderate-High	High	High	Low	Low
Mechanical robustness	High	Moderate (fragile cavity)	Moderate	High	High
Suitability for wearable use	Excellent	Poor-Moderate	Poor-Moderate	Good	Good
BP monitoring potential	Excellent for PAT, PTT, waveform features	Theoretically strong, but impractical for wearables	High theoretical accuracy; low wearability	Basic pulse detection, low BP estimation accuracy	Basic pulse/presence detection; not suitable for full BP estimation

1.7 Fibre Bragg Grating sensing principle

The potential of FBG sensors in physiological measurement based on strain and temperature sensitivity is due to the optical interference generated by the modulation of the refractive index measured in an optical fibre. The modulation of the refractive index is produced by the periodical grating inscription with an ultraviolet laser in the core of a single-mode optical fibre [56] (Figure 1.4). The light travelling along the core of an optical fibre is scattered by each grating plane. The Bragg condition requires the conservation of energy and momentum. Energy conservation (Equation 1.3) occurs when the frequency of the incident radiation ($\hbar\omega_i$) is the same as the frequency of the reflected radiation ($\hbar\omega_f$). The momentum conservation (Equation 1.4) is when the wavevector of the incident wave $\boldsymbol{k}_i$, plus the grating wavevector $\boldsymbol{K}$ are equal to the wavevector of the scattered radiation $\boldsymbol{k}_f$.

$$\hbar\omega_f = \hbar\omega_i \tag{1.3}$$

$$\boldsymbol{k}_i + \boldsymbol{K} = \boldsymbol{k}_f \tag{1.4}$$

The grating wavevector $\boldsymbol{K}$, has its direction normal to the grating planes with a magnitude $2\pi/\Lambda$ (Λ is the spacing between each grating plane.). The diffracted wavevector has the same magnitude but opposite direction, to the incident wavevector $2\pi n_{eff}/\lambda_B$. Therefore, the momentum of conservation condition becomes Equation 1.5, that simplifies to the first order Bragg condition (Equation 1.6).

$$2\frac{2\pi n_{eff}}{\lambda_B} = \frac{2\pi}{\Lambda} \tag{1.5}$$

$$\lambda_B = 2n_{eff}\Lambda \tag{1.6}$$

Where λ_B is the Bragg grating wavelength, the free space centre wavelength of the guided light that will be back reflected from the Bragg grating, and n_{eff} is

the effective refractive index of the fibre core at the free space centre wavelength. When the Bragg condition is satisfied, the contributions of reflected light from each grating plane add constructively in the backward direction that forms a back-reflected peak with a centre wavelength set by the grating parameters. Otherwise, if this condition is not met, the reflected light from each of the planes becomes progressively out of phase, and eventually it cancels out. Furthermore, the light that differs from the Bragg wavelength resonance will have a very weak reflection at each of the grating planes because of the index mismatch, however this reflection accumulates over the length of the grating.

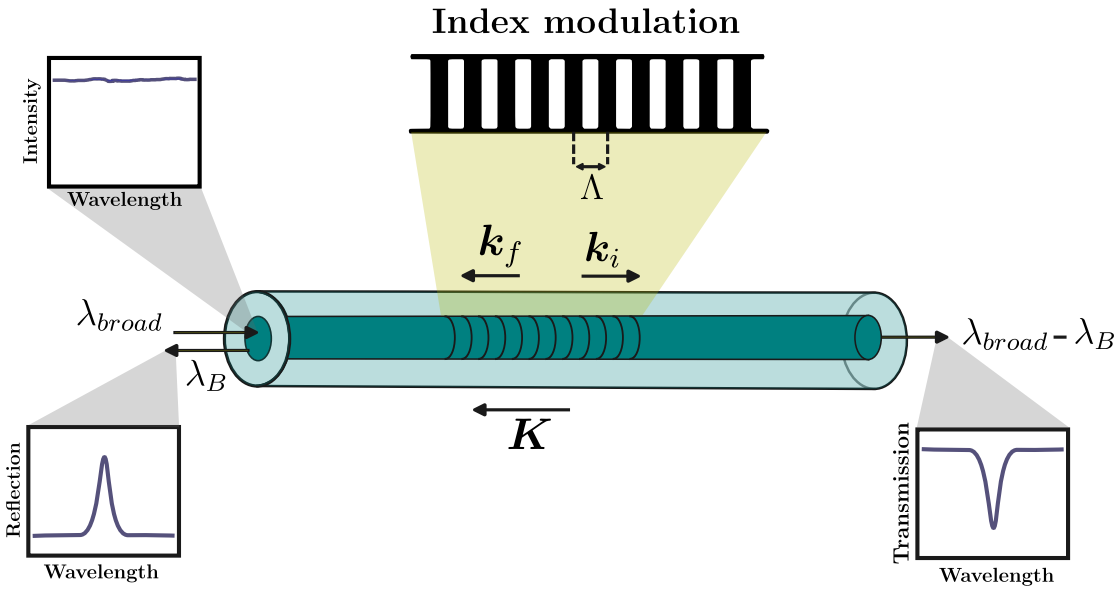

Figure 1.4: *Bragg grating inscribed into the core of an optical fibre. Part of the input light is represented (at the Bragg condition) and rest is transmitted. The bandwidth of the reflected and transmitted light depends on the Bragg grating, its length and modulation.*

1.7.1 Strain and Temperature dependency of Bragg gratings

The centre wavelength of the back-reflected light (Bragg grating resonance) from a Bragg grating, depends on the effective index of refraction of the core and the periodicity of the grating. Where the effective index of refraction and the spacing between the grating planes are affected by changes in strain and temperature [56]. Equation 1.7 describes the shift in the Bragg grating centre wavelength due to

changes in temperature and strain.

$$\Delta\lambda_B = 2[\Lambda\frac{\partial n_{eff}}{\partial l} + n_{eff}\frac{\partial \Lambda}{\partial l}]\Delta l + 2[\Lambda\frac{\partial n_{eff}}{\partial T} + n_{eff}\frac{\partial \Lambda}{\partial T}]\Delta T \tag{1.7}$$

The first term in Equation 1.7 describes the strain effect on an optical fibre, change in the grating spacing and the optical strain induced change in the refractive index.

1.8 Modelling Blood Pressure from PAT and PTT

Numerous studies have reported an inverse, yet non-linear, relationship between pulse arrival time (PAT) or pulse transit time (PTT) and blood pressure (BP). To capture this non-linearity, various modelling strategies have been employed, ranging from empirical calibration curves to advanced machine learning methods such as artificial neural networks. While modern sensors are often sufficiently robust for reliable signal acquisition, translating the measured time delays into accurate BP estimates remains a major challenge. This difficulty stems from the variability in physiological conditions, the frequency and accuracy of calibration procedures, and the site-specific differences in arterial pressure waveforms [57].

To address these challenges, this research proposes the use of Gaussian Process Regression (GPR) to model the non-linear inverse relationship between BP and PAT/PTT features. GPR offers a non-parametric, probabilistic framework capable of capturing complex functional dependencies while also providing uncertainty estimates – a crucial feature for clinical interpretability and risk assessment [58]. This approach also enables the integration of data-driven feature selection mechanisms to mitigate overfitting by eliminating redundant inputs. Such methods are particularly promising in handling the variability and subject-specific characteristics inherent in cuffless BP estimation [59, 60].

1.9 Pulse Waveform Reconstruction Rationale

Physiological, mechanical, and environmental factors contribute to the distortion of the pulsatile waveform measured by any transducer in cuffless blood pressure (BP) monitoring, particularly at distal measurement sites during daily life activities. This research identifies five key sources of waveform distortion: transmural pressure, hydrostatic pressure, physiological variability, variable contact pressure, and motion artefacts.

Transmural pressure – defined as the difference between internal arterial pressure and external tissue pressure – plays a fundamental role in arterial pressure wave propagation due to its intrinsic relationship with the mechanical properties of the arterial wall. This dependency makes pulse wave velocity (PWV)-based methods more physiologically grounded for estimating BP than approaches relying solely on single-point pulse detection (PWA) [31, 57]. However, variations in transmural pressure may also explain differences in waveform morphology along the arterial tree and between individuals, owing to tissue heterogeneity and vasomotor tone.

Another key factor is **hydrostatic pressure**, which varies with the vertical position of the limb relative to the heart. Changes in limb height induce shifts in local pressure, which alter the amplitude (peak prominence) and morphology of the detected waveform [61]. While such variations affect PWV to a lesser extent than pulse wave analysis (PWA), they can still degrade signal quality and reduce the signal-to-noise ratio (SNR), particularly in wearable systems where limb movement is frequent.

Similarly, **variable contact pressure** – arising from body movement or inconsistent sensor attachment – can modulate both the amplitude and baseline of the measured pulse signal [62].

Motion artefacts constitute a particularly complex source of distortion in wearable and ambulatory monitoring systems. These artefacts result from relative movement between the sensor and the skin, tissue deformation during limb mo-

tion, cable tension, or mechanical vibrations transmitted through the body. In the context of FBG sensors, motion artefacts can manifest as low-frequency baseline drift, abrupt transients, or spectral distortion due to unintended strain imposed on the fibre or mounting substrate. Although FBG sensors are inherently more mechanically stable than optical methods such as photoplethysmography (PPG), they remain sensitive to non-cardiac strain – especially under dynamic conditions such as walking, arm swinging, or changes in posture [63].

Unlike optical noise, motion-induced strain overlaps both spectrally and temporally with the cardiac signal, making it difficult to isolate through conventional filtering. Furthermore, since motion artefacts are typically non-stationary and subject-specific, their impact varies depending on sensor placement, attachment method, and individual movement patterns. This complexity necessitates the development of robust reconstruction techniques capable of separating physiological pulsations from artefactual components in real time.

As this research employs a Fibre Bragg Grating (FBG) sensor as the transduction layer, it is also necessary to account for additional sources of signal distortion that are **FBG-dependent**. These include: (i) **spectral FBG crosstalk** [64], arising from overlapping spectra in multiplexed arrays; (ii) **source/interrogator instability**, such as laser wavelength drift or polarisation fluctuations [65]; (iii) **spectral resolution and ADC noise**, due to finite wavelength bin size and digitisation errors [66]; and (iv) **humidity and environmental ingress**[67], which can alter the fibre's refractive index. These factors originate within the optical fibre, grating structure, or interrogation hardware, and are generally addressed through sensor design optimisations such as increased spectral spacing, use of reference gratings, high-resolution interrogators, or hermetic coatings.

In contrast, the **non-FBG-dependent** factors pose greater challenges, typically requiring enhancements in mechanical design, the integration of auxiliary sensors (e.g., inertial measurement units or force sensors), or the application of advanced signal processing. These strategies are often constrained by trade-offs involving

real-time performance, computational complexity, and environmental variability. To overcome these limitations, this work proposes an artificial intelligence-based approach for real-time pulse waveform reconstruction using a Fully Conditional Generative Adversarial Network (FC-GAN) model. The literature review supporting this approach, as well as its implementation, are detailed in Chapters 2 and 6.

1.10 Research Gap and Research Question

Despite enormous efforts to meet the public health demand for non-invasive blood pressure (BP) monitoring – particularly for the early detection of cardiovascular diseases – current standard and emerging technologies including oscillometric cuffs, the volume-clamp method, cuffless PPG wearables, and arterial tonometry remain unsuitable for ambulatory beat-to-beat BP assessment.

Oscillometric cuffs are limited by their intermittent nature lacking a beat-to-beat resolution. The volume clamp method suffers from discomfort and potential health-risks during prolonged use, dependence on finger perfusion, and hardware complexity that hinders miniaturisation and wearability. Arterial tonometry, while capable of high-fidelity waveform capture, often requires precise positioning and external pressure to maintain arterial contact, limiting its practicality in free-living conditions. Cuffless PPG-based methods are highly sensitive to motion artefacts, skin tone, and perfusion variability, leading to signal degradation and reduced accuracy.

Furthermore, PPG waveforms recorded at distal sites often lack the morphological fidelity of invasive arterial pressure waveforms, including reduced systolic peak prominence and poor dicrotic notch visibility, which leads to errors in timing-based BP estimation approaches such as PAT and PTT.

This highlights the need to investigate alternative sensing technologies that can overcome the limitations of PPG-based methods for non-invasive BP estimation.

A solution with sufficient accuracy and robustness that could be adopted as a standard technology for non-invasive, unobtrusive, beat-to-beat BP monitoring.

Among the most promising innovations are fibre Bragg grating (FBG) sensors – optical fibre sensors with remarkable sensitivity to physical parameters such as strain and temperature. Their high strain sensitivity has been widely utilised in structural health monitoring across civil and aerospace engineering, where they detect vibrations and early-stage damage in materials. In biomedical applications, FBG sensors have been explored for monitoring respiratory rate via chest wall movement, heart rate, and body temperature [68].

More recently, early-stage studies have investigated the feasibility of using FBG sensors for BP measurement. These works have demonstrated that FBGs can detect arterial pulse waveforms when mounted using mechanical structures that amplify the minute blood vessel wall displacements. The arterial pulses waveforms detected by FBG sensors can potentially be correlated with arterial pressure waveforms. Such mounting systems are essential to resolve the pulse signal with adequate fidelity. The review of FBG-based methods for BP and arterial pulse methods is discussed in detail in the literature review (Chapter 2).

This research proposes a sensing framework based on an FBG sensor embedded in a millimetre-scale rectangular cantilever, specifically designed to detect distal arterial pulse waveforms. This configuration enables the extraction of PAT and PTT features in conjunction with ECG signals. Building on this physiological and theoretical foundation, cuffless blood pressure estimation using these timing features may provide a more direct and physiologically grounded approximation of intra-arterial pressure compared with conventional indirect methods.

Research Question. *Can a fibre Bragg grating (FBG)-based cantilever sensor capture distal arterial pulse waveforms with sufficient morphological fidelity and timing stability to derive precise PAT and PTT features, thereby enabling accurate beat-to-beat BP estimation in ambulatory conditions?*

1.11 Aims and Objectives

Aim

To develop a continuous, beat-to-beat blood pressure (BP) monitoring system based on a fibre Bragg grating (FBG)-cantilever sensing platform.

Objectives

1. To design and fabricate a wearable FBG-based cantilever sensor capable of detecting distal arterial pulsations.

2. To construct a cardiovascular phantom for controlled validation of the FBG-cantilever sensing system.

3. To evaluate the sensor system's accuracy and reliability through human subject testing.

4. To model the non-linear relationship between BP and timing features (PAT/PTT) using a Gaussian Process Regression (GPR) model.

5. To develop a pulse waveform reconstruction method using generative artificial networks (GAN) to enhance signal quality and improve robustness in ambulatory conditions.

1.12 Methodological Overview

To enhance the sensitivity of distal arterial pulse detection at the skin surface, this research proposes the use of a fibre Bragg grating (FBG) sensor mounted on a rectangular cantilever. To support ambulatory applications, a miniaturised interrogator (FiSpec FBG X100, FiSens, Rolleiwerke GmbH) is integrated to improve system portability and facilitate real-time data acquisition.

The reliability and performance of the FBG-cantilever sensing system are first evaluated in a controlled setting using a custom-built cardiovascular phantom.

This setup enables repeatable pulse waveform generation under known pressure conditions for sensor calibration and validation.

Subsequently, human volunteer experiments are conducted, where blood pressure changes are induced through cycling exercise. During these trials, discrete systolic and diastolic BP values are recorded alongside continuous ECG and FBG data streams.

To derive BP from timing features, a multitask Gaussian Process Regression (GPR) model is employed to capture the non-linear relationships between systolic/diastolic BP and the extracted pulse arrival time (PAT) features.

Finally, to address motion-induced signal degradation in ambulatory settings, generative models are investigated for reconstructing corrupted pulse waveforms and enhancing signal quality.

1.13 Thesis Outline

This thesis is organised in seven chapters (Figure 1.5).

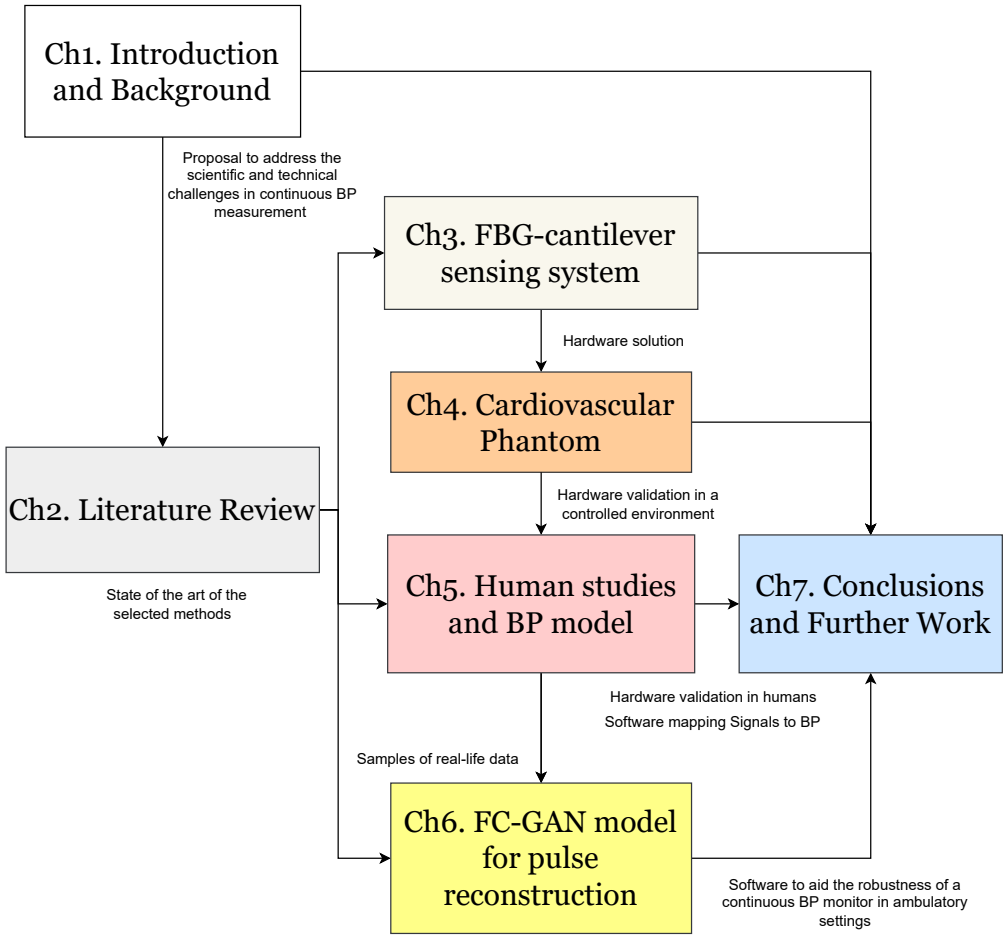

Figure 1.5: *Thesis Outline. Schematic overview of the seven-chapter thesis structure, illustrating the logical progression and interdependencies from the introductory motivation and literature review (Chs. 1-2) through hardware development (Ch. 3), controlled and human validation (Chs. 4-5), AI-based signal reconstruction (Ch. 6), and culminating in the conclusions and proposed future work (Ch. 7).*

- **Chapter 1: Introduction and Background**

  This chapter articulates the motivation for the investigation and situates it within both clinical and societal contexts. It begins with a concise overview of the physiological mechanisms that regulate blood pressure, underscoring the clinical importance of continuous, beat-to-beat monitoring. The discus-

sion then critiques the limitations of standard measurement techniques and surveys recent advances in emerging monitoring technologies. By clarifying the associated scientific and technical challenges, the chapter identifies the central research gap, from which the proposed solution and the guiding research question of this thesis are derived.

- **Chapter 2: Literature Review**

  This chapter presents a comprehensive review of the literature relevant to the proposed methodologies. It examines prior research on the use of Fibre Bragg Grating (FBG) sensors for blood pressure measurement, highlighting key developments and limitations. In addition, it explores software methods for blood pressure derivation, including signal processing and machine learning techniques. The chapter also reviews methods for pulse waveform reconstruction, with a focus on algorithms designed to mitigate signal distortion by motion artefacts. This comprehensive review provides the foundation for selecting and justifying specific methodological approaches within the context of the proposed solution.

- **Chapter 3: FBG-cantilever sensing system**

  This chapter details the development of the FBG-cantilever sensing system. It presents the technical specifications of the rectangular cantilever beam, including its structural and material properties, as well as the characteristics of the integrated FBG sensors. The chapter further outlines the design evolution of the FBG-cantilever assembly, highlighting key iterations and improvements. In addition, it examines the selection, benchmarking, and instrumentation of the FBG interrogator, providing a rationale for the chosen system based on its performance specifications and compatibility with the proposed sensing platform. This chapter outputs the hardware developed for the continuous beat-to-beat BP measurements.

- **Chapter 4: Cardiovascular Phantom**

This chapter describes the development of a customised physical model of the cardiovascular system. The model is designed to facilitate the validation of the FBG-cantilever sensing system under controlled experimental conditions. It enables the acquisition of pulse transit time (PTT) and pulse arrival time (PAT) measurements, providing a reproducible platform for assessing the system's performance and reliability prior to human testing.

- **Chapter 5: Human Studies and BP model**

  This chapter presents the human studies performed to obtain PAT and PTT values using the FBG-cantilever sensing system and ECG. The experimental protocol selected is described as well, the post-processing of the data and the results from 15 participants. This chapter also describes the development of a Gaussian Process Regression model of BP using PAT values, using the data collected from the human studies. The model testing results of this model is also presented in this chapter.

- **Chapter 6: FC-GAN model for pulse reconstruction**

  This chapter presents the development of a generative adversarial network with fully connected layers (FC-GAN) for the reconstruction of arterial pulse waveforms primarily distorted by motion artifacts. It details the creation of an artificially corrupted dataset used to support the training and validation of the model, along with a comprehensive description of the network architecture, training protocol, and implementation strategies. The performance of the proposed model is evaluated using a range of qualitative and quantitative metrics and is benchmarked against existing state-of-the-art approaches reported in the literature. Furthermore, the chapter investigates the application of the FC-GAN to FBG arterial pulse signals obtained from the human subject studies from Chapter 5, and critically examines the implications of deploying such AI-based reconstruction methods in ambulatory medical devices.

- **Chapter 7: Conclusion and Further work** This chapter synthesises the principal contributions and acknowledged limitations of the present investigation. It first summarises the development and experimental validation of the FBG-cantilever sensing system using both cardiovascular phantoms and human cohorts, with particular emphasis on its capacity to acquire PTT and PAT. The discussion then addresses the derivation of systolic and diastolic blood pressure (SBP and DBP) from PAT by means of a Gaussian-process regression model. The chapter also reflects on the development and application of an FC-GAN model for the reconstruction of arterial pulse waveforms. Collectively, these accomplishments are evaluated in terms of their impact on overcoming the scientific and technical barriers inherent in continuous blood-pressure monitoring. The chapter concludes by critiquing the remaining limitations, proposing solutions to mitigate them, and outlining prospective research stages intended to advance this field further.

Figure 1.5 offers a schematic overview of the logical flow and interdependencies among these chapters. At the top left, Chapter 1 ("Introduction and Background") establishes the clinical and societal motivation, reviews relevant physiological fundamentals, and – together with Chapter 2 ("Literature Review") – frames the key research gap, the proposed solution, and the specific methodological approaches. This foundation then drives the hardware development presented in Chapter 3 ("FBG-cantilever sensing system"), whose performance is first validated under controlled conditions in Chapter 4 ("Cardiovascular Phantom"), and subsequently in human subjects in Chapter 5 ("Human studies and BP model"). The human validation also informs the development of the blood-pressure estimation model. Real-world FBG pulse signals collected in Chapter 5 feed into Chapter 6 ("FC-GAN model for pulse reconstruction"), which describes an AI-based approach to reconstruct motion-corrupted waveforms. Finally, Chapter 7 ("Conclusions and Further Work") synthesises the hardware and software contributions, evaluates their collective impact on continuous blood-pressure monitoring, critiques remain-

ing limitations, and outlines proposed next steps.

2. Literature Review

This chapter presents a critical review of the existing literature relevant to the development of the proposed cuffless blood pressure (BP) monitoring system. It is structured around the three key functional layers of the device, as illustrated in Figure 1.3: (i) the **transducer layer**, focusing on the use of Fibre Bragg Grating (FBG) sensors for pulse waveform detection; (ii) the **initialisation layer**, addressing machine learning techniques for BP estimation from physiological signals; and (iii) the **processing layer**, covering signal reconstruction methodologies for pulsatile signals corrupted by motion artefacts, which support the accurate extraction of pulse wave velocity (PWV) features.

The objective of this review is to identify current technological and methodological limitations that the proposed research aims to overcome. The first section explores FBG-based sensing systems, which provide promising capabilities for capturing arterial pulse waveforms at the skin surface but face constraints in terms of repeatability, self-attachment, and portability. The second section evaluates data-driven BP estimation models that rely on features such as Pulse Transit Time (PTT), Pulse Arrival Time (PAT), and morphological descriptors derived from ECG and PPG signals. While these models demonstrate promising accuracy, many depend on high computational resources or frequent calibration protocols. The final section reviews signal reconstruction strategies for recovering distorted pulsatile waveforms, including classical signal processing approaches and generative machine learning methods. These are essential for ensuring reliable PWV feature extraction under real-world motion conditions.

Collectively, this chapter establishes the context and rationale for the methodological framework and system design choices elaborated in the following chapters.

2.1 Fibre Bragg Grating (FBG) Sensors for Pulsatile Detection

As described in Section 1.6, Fibre Bragg Grating (FBG) sensors have demonstrated significant potential for non-invasive pulse wave detection by measuring strain at various skin surface locations. Their ability to capture pulsatile arterial motion offers a compelling alternative to traditional contact-based or optical methods, particularly in wearable and continuous monitoring systems. FBGs offer a miniature footprint, mechanical flexibility, and inherent immunity to electromagnetic interference, making them well-suited for integration into wearable devices and for use in electromagnetically noisy clinical environments such as MRI or CT suites. Unlike intensity-based fibre sensors, which are susceptible to artefacts arising from source power fluctuations or connector losses, FBGs detect strain through shifts in Bragg wavelength, offering improved stability, linearity, and robustness. Furthermore, their capacity for wavelength-division multiplexing enables the integration of multiple sensing sites along a single fibre – crucial for deriving physiological parameters such as pulse wave velocity (PWV) and pulse arrival time (PAT). These features collectively position FBG sensors as ideal transducers for cuffless blood pressure monitoring applications.

Leitão et al. [69] investigated the use of a silica-based FBG sensor embedded in a small housing, featuring a spherical structure designed to transfer carotid artery micro-movements to the fibre (Figure 2.1). As the carotid artery is anatomically close to the aorta, these measurements provide insights into central arterial stiffness. However, the sensor system is not self-attaching, requires operator training for placement, and suffers from limited measurement repeatability.

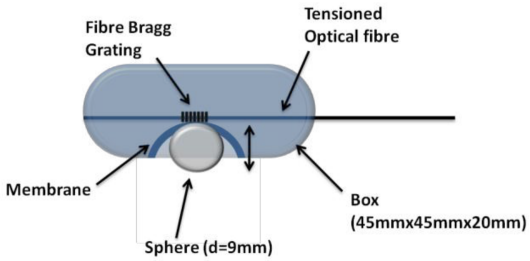

Figure 2.1: *Carotid pulse waveform measured using a silica FBG sensor with a spherical contact mechanism [69], © 2012 SPIE. Reprinted with permission.*

Koyama et al. [70] evaluated a polymer-based FBG sensor for pulsation strain measurements at the fingertip. This plastic optical fibre exhibits a lower Young's modulus than silica, resulting in greater deformation and a larger Bragg wavelength shift under identical pressure, which enhances sensitivity. The sensor was positioned 10 – 15 mm from the distal interphalangeal joint, and measurements were recorded under varying blood flow conditions simulated via upper-arm cuff compression and release. Despite its improved sensitivity, the polymer fibre is more expensive and, like the previous design, lacks self-attachment.

Haseda et al. [71], from the same research group, extended this approach by estimating systolic and diastolic blood pressure (SBP/DBP) from brachial pulse waveforms using Partial Least Squares Regression (PLSR) (Figure 2.2). Their model achieved a moderate correlation (R = 0.54 – 0.72), but the recordings were conducted only at rest and covered a narrow BP range, limiting generalisability.

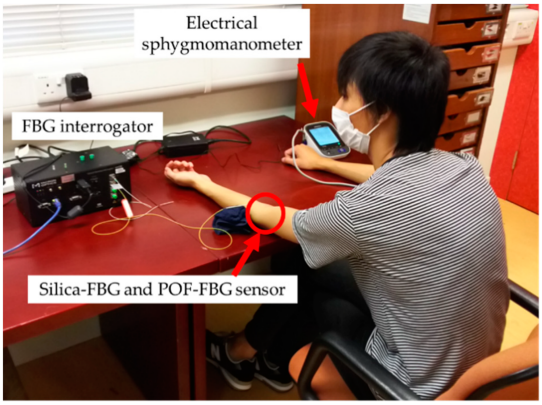

Figure 2.2: *Measurement of arterial pulse using a plastic fibre FBG sensor on the upper arm [71], licensed under CC BY 4.0.*

Jia et al. [72] introduced a radial artery pulse sensing system incorporating a silica FBG sensor and a mechanical lever amplification mechanism (Figure 2.3). The system followed the Traditional Chinese Medicine (TCM) pulse diagnosis protocol for precise pulse localisation. While effective, the bulky design precludes wearable integration.

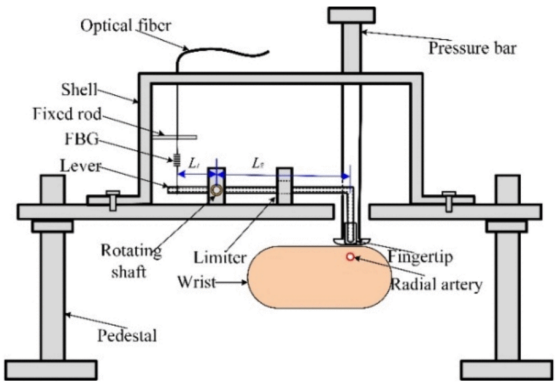

Figure 2.3: *Lever-based amplification mechanism used with a silica FBG sensor to capture radial pulse waveforms [72], © 2018 IEEE. Reprinted with permission.*

Gowda et al. [73] developed a 3D-printed holder integrated with a silica FBG sensor to target radial artery pulse positions based on the TCM "Guan" location (Figure 2.4). The sensor requires manual support for skin contact, making it unsuitable for autonomous or wearable use.

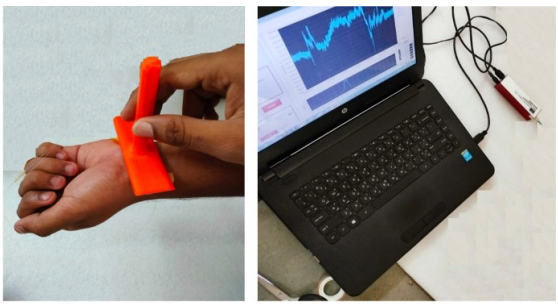

Figure 2.4: *3D-printed FBG device for radial artery pulse monitoring [73], licensed under CC BY 4.0.*

Wang et al. [74] implemented simultaneous bilateral FBG measurements using sensors embedded in PDMS structures (Figure 2.5), placed at the elbows (fossa cubitalis) and wrists. The pulse wave velocity (PWV) was estimated from each arm using these synchronised measurements.

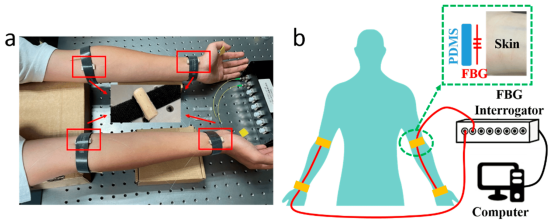

Figure 2.5: *Simultaneous bilateral PWV estimation using FBG sensors embedded in PDMS structures [74], licensed under CC BY 4.0.*

Katsuragawa et al. [75] explored BP estimation using FBG measurements at the radial and brachial arteries (Figure 2.6) with PLSR-based modelling. Their study reported mean differences in SBP/DBP of less than 5 mmHg, although the results were obtained from only three subjects in a supine position and within a limited BP range.

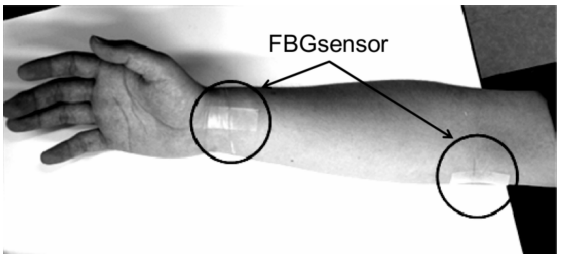

Figure 2.6: *FBG sensor placed along the arterial line (radial and brachial arteries) for BP estimation [75], © 2015 IEEE. Reprinted with permission.*

Table 2.1 summarises key studies that have employed Fibre Bragg Grating (FBG)-based sensors for pulse wave analysis and blood pressure (BP) estimation. The table provides a comparative overview of the sensor types, measurement locations, primary findings, and associated limitations of each approach.

Despite their demonstrated potential in pulse waveform detection, Fibre Bragg Grating (FBG) sensors have seen limited application in blood pressure (BP) monitoring. Several key barriers have impeded their broader adoption, including the lack of access to continuous invasive BP reference data for model development, the limited portability and high cost of commercial FBG interrogators, and the use of mechanically simplistic sensor designs. These limitations contribute to poor signal repeatability, reduced robustness under dynamic conditions, and limited usability – factors that collectively hinder progress toward deployable, beat-to-beat BP

monitoring systems. In response to these challenges, and informed by the current state of the field, this research proposes an enhanced FBG-based sensing system incorporating a rectangular cantilever structure. The cantilever functions both as a stable mounting platform and as a mechanical amplification mechanism, improving strain transfer from arterial pulsations to the embedded FBG sensor and enabling more reliable waveform acquisition for continuous, cuffless BP estimation. To further address cost and portability constraints associated with conventional interrogation systems, this work employs the miniature interrogator FiSpec X100 (FiSens GmbH, Braunschweig, Germany), offering a compact and cost-effective alternative suitable for wearable or semi-portable applications.

Study	**Sensor Type**	**Measurement Location**	**Key Findings**	**Limitations**
Leitão et al. 2012 [69]	Silica FBG	Carotid Artery	Central arterial stiffness Pulse wave profile	Training to apply the sensor Not self-attachment Lack of repeatability
Koyama et al. 2021 [70]	Polymer FBG (Plastic)	Fingertip (10-15 mm from DIP joint)	Lower Young's modulus gives higher sensitivity	More expensive than Silica fibres Not portable not self-attachment
Haseda et al. 2019 [71]	Polymer FBG sampled 1KHz	Brachial Artery	BP through pulse wave analysis-PLSR R = 0.54 - 0.72	Narrow BP reference range only measurements at rest
Jia et al. 2018 [72]	Silica FBG with lever	Radial Artery	Pulse waveform	Bulky lever amplification system
Gowda et al. 2024 [73]	Silica FBG with 3D Printed Device	Radial Artery	Pulse waveform	Not self-attachment
Wang et al. 2024 [74]	2 FBGs attached to PDMS sampled at 1KHz	Fossa cubitalis Wrist	Pulse wave velocities left and right arms self-attachment	Not portable
Katsuragawa et al. 2015 [75]	FBG material not disclosed	radial & brachial arteries	BP through pulse wave analysis-PSLR Average difference: (SBP/DBP) < 5mmHg	Narrow BP reference range only in supine position N subjects = 3 not portable

Table 2.1: FBG-based sensors for pulse wave analysis and blood pressure measurements

2.2 Blood Pressure Machine Learning Models

Machine learning (ML) models are gaining popularity over theoretical approaches for blood pressure (BP) derivation, as they can capture the complex, non-linear, and subject-specific relationships between pulse features – such as Pulse Arrival Time (PAT) and Pulse Transit Time (PTT) – and BP, which theoretical models of-

ten oversimplify due to idealised assumptions about vascular properties. ML models learn directly from data, making them more robust to physiological variability, noise, and signal artefacts commonly encountered in wearable and ambulatory settings. Numerous ML-based methods have been developed to estimate BP from physiological signals such as electrocardiogram (ECG) and photoplethysmogram (PPG), using either transit-time features like PAT/PTT or morphological and spectral descriptors derived from the pulse waveform in both time and frequency domains. These models have consistently demonstrated improved performance in predicting diastolic BP (DBP) over systolic BP (SBP), with further accuracy gains observed under calibration-based conditions.

Yang et al.[76] extracted PAT and signal complexity features from ECG and PPG using least absolute shrinkage and selection operator (LASSO) regression, support vector machines (SVM), and artificial neural networks (ANN). The mean absolute error (MAE) for SBP prediction using SVM was 7.33±9.53mmHg, while DBP prediction using ANN achieved 5.15±6.46 mmHg.

Kauchee et al.[77] applied PWV features to multiple models, including regularised linear regression (RLR), SVM, decision tree regression, adaptive boosting (AdaBoost), and random forest regression (RFR). Calibration-free models yielded an MAE of 11.17±10.09mmHg for SBP and 5.35±6.14 mmHg for DBP, while calibration-based models improved the accuracy to 8.21±5.45 mmHg (SBP) and 4.31±3.52 mmHg (DBP).

Su et al.[78] employed long short-term memory (LSTM) networks on PWV features from ECG and PPG, achieving root mean square errors (RMSE) of 3.73mmHg for SBP and 2.43 mmHg for DBP.

Khalid et al.[79] used PPG-only signals in combination with multiple linear regression, SVM, and decision trees, achieving MAE values of 4.82±4.31mmHg (SBP) and 3.25±4.17 mmHg (DBP).

Wang et al.[80] leveraged morphological and spectral features of PPG segments with ANN, reporting MAEs of 4.02±2.79mmHg for SBP and 2.27±1.82 mmHg

for DBP.

Ertugrul et al.[81] transformed ECG and PPG into spectrograms via short-time Fourier Transform (STFT) and used extreme machine learning (EML), achieving RMSEs of 4.37mmHg (SBP) and 3.95 mmHg (DBP).

Liang et al. [82] applied continuous wavelet transform (CWT) to derive scalogram representations of PPG, then used a pre-trained GoogleNet convolutional neural network (CNN) for hypertension classification.

Baek et al.[83] used time- and frequency-domain features, including derivatives and fast Fourier transform (FFT), from ECG and PPG in a CNN, yielding MAEs of 5.32±5.54mmHg (SBP) and 3.38±3.82 mmHg (DBP) under a calibration-based protocol.

Paviglianiti et al.[84] benchmarked several deep learning techniques using ECG, PPG, and arterial blood pressure (ABP) signals from the MIMIC database. Their ResNet + three-layer LSTM architecture achieved the best results, with MAEs of 4.118mmHg (SBP) and 2.228 mmHg (DBP), satisfying AAMI standards. A secondary LSTM model trained using only PPG and ABP from MIMIC-I aimed to reconstruct BP waveforms. Preliminary outputs showed periodic waveform patterns with amplitude variations but diverged from true ABP morphology.

Ahmed et al. [85] proposed a hybrid machine learning method for estimating systolic and diastolic blood pressure (SBP and DBP) using oscillometric waveform envelopes (OWEs). The authors extract 27 features from the OWEs – including time-domain, chaotic, and frequency-domain components – and use three Gaussian Process Regression (GPR) models (Exponential, Matern 5/2, and Rational Quadratic) to predict BP values. The best performance was achieved with the Exponential GPR model, yielding mean absolute errors of 3.64 mmHg for SBP and 4.27 mmHg for DBP.

Table 2.2 summarises the machine learning approaches reviewed. Long Short-Term Memory (LSTM) models, as demonstrated by Su et al.[78] and Paviglianiti et al.[84], have achieved notable performance by effectively capturing temporal

dependencies in physiological signals. However, their high computational cost presents a challenge for deployment in real-time or resource-constrained embedded systems. In contrast, Bayesian methods such as Gaussian Process Regression (GPR) offer a promising alternative, especially when combined with streamlined feature extraction pipelines. If the complexity of feature engineering is minimised and cuffless signals are utilised, GPR models may represent a practical and energy-efficient solution for real-time blood pressure estimation.

Considering the limitations of existing machine learning approaches, this research proposes the use of a tailored Gaussian Process Regression (GPR) model for blood pressure estimation using pulse wave velocity (PWV) features derived from FBG and ECG signals. GPR offers a principled Bayesian framework capable of capturing the non-linear and subject-specific relationship between pulse arrival time (PAT) and blood pressure without relying on extensive feature engineering. Its probabilistic nature provides both predictive values and associated uncertainty estimates, which are especially valuable in clinical applications where interpretability and reliability are essential. Furthermore, GPR has demonstrated robustness with limited datasets, making it particularly suitable for this study, where sample sizes per participant are constrained. Given these advantages, GPR presents a flexible, interpretable, and data-efficient solution for continuous, cuffless blood pressure monitoring.

Table 2.2: Machine Learning Models for Blood Pressure Prediction

Study	Features	Model	Metric	Results (SBP/DBP) [mmHg]	Notes
Yang et al. 2020 [76]	PAT, Complexity (ECG, PPG)	LASSO, SVM, ANN	MAE	SVM: 7.33±9.53 / ANN: 5.15±6.46	Different models for SBP and DBP
Kauchee et al. 2015 [77]	PWV (ECG, PPG)	RLR, SVM, DT, AdaBoost, RFR	MAE	Cal-Free: 11.17±10.09 / 5.35±6.14 Cal-Based: 8.21±5.45 / 4.31±3.52	Calibration improves accuracy RFR achieves best results
Su et al. 2018 [78]	PWV (ECG, PPG)	LSTM	RMSE	3.73 / 2.43	LSTM achieves lowest RMSE, use temporal dependency, HPC
Khalid et al. 2018 [79]	PPG only	MLR, SVM, DT	MAE	4.82±4.31 / 3.25±4.17	PPG-only approach with good accuracy
Wang et al. 2018 [80]	Morphological, Spectral (PPG)	ANN	MAE	4.02±2.79 / 2.27±1.82	ANN performs well on PPG
Ertugrul et al. 2018 [81]	Spectrogram, STFT (ECG, PPG)	Extreme ML	RMSE	4.37 / 3.95	Exploits signal periodicity for BP estimation
Liang et al. 2018 [82]	Scalogram (PPG, CWT)	CNN (GoogleNet)	-	Hypertension Classification	Focuses on classification, not regression
Baek et al. 2019 [83]	Time, Frequency (ECG, PPG, FFT)	CNN	MAE	5.32±5.54 / 3.38±3.82	Uses FFT for feature extraction
Paviglianiti et al. 2022 [84]	ECG, PPG, ABP (MIMIC) PPG (MIMIC I)	ResNet+LSTM LSTM	MAE -	4.118 / 2.228 Work in Progress	Deep learning hybrid model, Ongoing work on MIMIC dataset exploits temporal dependency HPC
Ahmed et al. 2020 [85]	27 featured from Oscillometric Waveforms	GPR with exponential kernel	MAE	3.64/ 4.27	Efficacy of GPR with engineered features without deep learning complexity Feature extraction complexity

2.3 Machine Learning for Pulsatile Signal Reconstruction

As described in section 1.9, in cuffless BP monitoring, the accuracy of pulsatile waveform detection is compromised by several physiological, mechanical, and environmental factors, including transmural pressure, hydrostatic effects, variable contact pressure, and motion artefacts. Among these, motion artefacts represent the most significant challenge, especially during daily activities, due to their non-stationary and subject-specific nature. Unlike optical noise, motion-induced strain overlaps temporally and spectrally with the cardiac signal, making it difficult to filter using conventional methods. Although Fibre Bragg Grating (FBG) sensors are more mechanically stable than optical methods like PPG, they remain susceptible to motion-induced distortion, as well as FBG-specific limitations such as spectral crosstalk and source instability.

This section reviews techniques for reconstructing pulsatile signals, particularly those corrupted by motion artefacts. FBG waveforms share morphological similarities with PPG signals and are similarly susceptible to motion-induced distortion. As such, PPG denoising literature offers valuable insights for FBG signal recovery. Initial approaches to motion artefact mitigation involved manual segment removal or signal quality assessment using classification [86–88]. More advanced methods combine signal decomposition, adaptive filtering, and deep learning.

Kim and Yoo [89] applied independent component analysis (ICA) and low-pass filtering to separate motion artefacts, reporting mean squared errors (MSE) of 0.4–4. Salehizadeh et al. [90] introduced iterative motion artefact removal using singular spectral analysis, finding no significant differences ($p > 0.05$) between reference and reconstructed heart rate in 7 of 9 subjects.

Mullan et al.[91] used wavelet denoising in combination with acceleration data, achieving MAE = 1.96±2.86 bpm and Pearson's $r = 0.98$ for heart rate estimation. Zhang et al.[92] employed ensemble empirical mode decomposition and

spectrum subtraction, reporting average absolute error (Aerror) = 1.83±1.21 bpm and correlation $r = 0.989$.

Tang et al.[93] used a hybrid of discrete wavelet transform and empirical mode decomposition, with mean sum error (MSumE) ranging from 2.95 to 32.94 bpm depending on signal quality. Lee et al.[94] proposed a bidirectional recurrent denoising autoencoder (BRDAE), achieving an average SNR improvement of 7.9 dB.

Generative models have shown great promise in imaging tasks such as super-resolution, deblurring, and colour normalization. Techniques like PCA-SRGAN and CycleGAN have improved performance and broadened applicability, especially when paired data are unavailable [95]. In biomedical imaging, GAN-based models, including Asymmetric CycleGANs and DC-GANs, have been applied to tasks like smoke removal [96]. Zargari et al.[97] introduced a CycleGAN model for 2D transformation and unpaired signal reconstruction, achieving peak-to-peak error (PPE) of 0.95 bpm and RMSE of 2.18 bpm. Wang et al.[98] proposed a Deep Convolutional GAN (DC-GAN) for PPG denoising, requiring averaging of the reconstructed and raw signals to improve fidelity, with PPE ranging from 0.7 to 1.9 seconds.

Table 2.3 presents a comparative summary of state-of-the-art techniques and their performance metrics in PPG signal reconstruction. Despite advances in deep generative models, accelerometer-assisted methods such as those from Zhang [92] and Mullan [91] still outperform standalone algorithms. However, such hardware dependencies are not always feasible in constrained settings (e.g., oesophageal or tracheal measurements using optical fibre probes [99, 100]).

Thus, there remains a clear need for motion-robust signal reconstruction methods that operate independently of inertial measurements. Approaches capable of real-time sliding window processing without relying on ECG, accelerometers, or gyroscopes would significantly benefit wearable cuffless BP devices.

Paper	**Method**	**Acc. and/or Gyro**	**Outcome**	**Notes**
Kim and Yoo 2006	ICA	No	MSE 0.4 - 4	Sensitive to noise amplitude
Salehizadeh et al. 2014	IMAR	No	HR with $p > 0.05$ in 7 out of 9 subjects	Limited test set
Mullan et al. 2014	Wavelet	Yes	MAE 1.96 ± 2.86 BPM r= 0.98	Relies on acc. input
Zhang et al. 2015	EMD	Yes	Aerror: 1.83 ± 1.21 BPM $\sigma = 3.62$ r=0.989	Relies on acc. inputs
Tang et al. 2016	DWT & EMD	No	MSE 2.95-32.24 BPM	Exploits frequency spectrum
Lee et al. 2019	BRDAE	No	7.9dB SNR improved	Potential in noise reduction, but lack of metrics
Zargari et al. 2021	CycleGAN	No	PPE: 0.95 BPM RMSE: 2.18 BPM	High computational resources
Wang et al. 2022	DC-GAN	No	PPE:.7 - 1.9 s	Needs averaging after reconstruction

Table 2.3: Results comparison of the state-of-the-art techniques for denoising PPG signals with motion artifacts. Different metrics were employed by these authors for performance evaluation, Kim and Yoo evaluated the Mean Square Error between the reference and denoised PPG signal. Salehizadeh evaluated the statistical significance with reference HR values with the HR extracted from reconstructed PPG signals. Mullan assessed the Mean Absolute Error (MAE) by extracting the HR of the reconstructed PPG signals. Zhang used the Average absolute error (Aerror) and Average percentage error, Bland-Atlman, and Correlation analysis with the HR extracted from the reconstructed PPG signals. Tang used the Mean Sum Error, the reference HR and the HR of the reconstructed PPG signal. Zargari calculated the Peak-Peak Error (PPE) and RMSE between the generated and reference signals.

Based on these findings, this research proposes a generative adversarial network with fully connected layers (FC-GAN) tailored for one-dimensional physiological signal reconstruction. The architecture builds upon the GANomaly framework introduced by Akcay et al.(2018) [101] and further refined by Wang et al.(2022) [102], which integrates an autoencoder-based generator, a latent-space feature encoder, and a discriminator implemented as an encoder to enhance reconstruction quality. The key innovation in this study lies in the replacement of convolutional layers with fully connected linear layers.

This design choice is motivated by the observation that linear layers are better suited for processing one-dimensional signals that lack spatial locality or hierarchical structure. Unlike convolutional layers, which are optimised for extracting local features from multi-dimensional data, fully connected layers establish global dependencies by connecting each input element to every neuron in the subsequent layer, thus treating all input points with equal importance [103, 104]. Prior studies have demonstrated that such architectures can effectively capture global patterns in spectral and temporal data, including in applications such as predicting optical properties from diffuse reflectance spectra [105]. Accordingly, the FC-GAN model is expected to offer improved performance in reconstructing pulse-like waveforms with global temporal dependencies, such as those distorted by motion artefacts.

2.4 Proposed Cuffless Blood Pressure Monitoring Architecture

The proposed architecture for cuffless blood pressure (BP) monitoring is depicted in Figure 2.7. This architecture is organised into three functional layers: the transducer layer, the signal processing layer, and the initialisation layer. Each layer has been designed to address and mitigate the key methodological challenges identified in the literature review, including pulsatile detection robustness and repeatability, non-linear relationship between timing features and blood pressure

and waveform distortion, motion artefacts. By adopting this layered approach, the architecture ensures that signal acquisition, reconstruction, and BP derivation are systematically optimised to enhance overall accuracy and reliability.

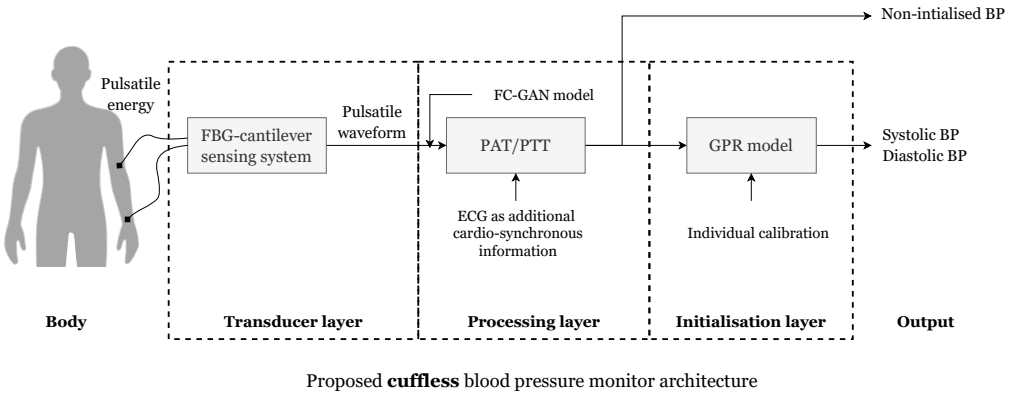

Figure 2.7: *Proposed cuffless BP monitoring architecture. The system is structured into three functional layers: the transducer layer, which employs an FBG-cantilever sensing system to convert pulsatile energy from the body into a measurable strain waveform; the processing layer, using a Generative Adversarial Network with Fully Connected layers (FC-GAN) to reconstruct the waveform and the extraction of PAT and PTT features, with ECG as a cardio-synchronous reference; and the initialisation layer, where a GPR model performs personalised BP estimation using PWV features derived from the pulsatile signals. The system outputs continuous estimations of systolic and diastolic BP.*

Transducer Layer: FBG-Cantilever Sensing Mechanism

At the sensor level, a Fibre Bragg Grating (FBG) embedded in a cantilever structure is employed as the primary transducer. This configuration enables the high-sensitivity detection of pulse-induced skin surface deformations, converting mechanical strain into wavelength shifts. The cantilever mechanism enhances the strain transfer efficiency from the skin to the fibre, allowing the detection of subtle pressure fluctuations associated with the arterial pulse. This layer forms the physical interface with the user and provides the raw data required for downstream feature extraction.

Processing Layer: Feature Extraction and Signal Reconstruction

The signal processing layer extracts timing-based cardiovascular features – specifically PTT from two FBG-derived pulse waveform at the wrist and upper-arm and PAT by synchronising with an ECG signal as a proximal timing reference. Given that real-world signals are often corrupted by noise and motion artefacts, a Generative Adversarial Network with Fully Connected layers (FC-GAN) is integrated into this layer to reconstruct and denoise the distorted pulse waveform.

Initialisation Layer: BP Estimation using Gaussian Process Regression with PWV Features

In the final layer, a Gaussian Process Regression (GPR) model is employed to derive blood pressure values from the reconstructed pulse signals. The model is trained using pulse wave velocity (PWV)-related features, derived from PAT and PTT measurements, as surrogate markers of arterial stiffness and haemodynamic state. GPR is selected for its non-parametric nature and capacity to model the complex, non-linear relationship between timing features and BP. This layer functions as the calibration and inference stage of the system, enabling continuous, cuffless BP estimation with quantified uncertainty.

2.5 Design Specifications and Goals - Proof of Concept

The primary objective of this proof-of-concept (PoC) cuffless blood pressure monitor is to evaluate the technical feasibility of estimating beat-to-beat blood pressure from non-invasive physiological signals, without the use of an inflatable cuff.
At this early stage, the design prioritises signal acquisition fidelity, algorithmic validation, and system integration. Although real-time latency, compact form factor, and wireless connectivity are not strict requirements at this proof-of-concept stage, this research is designed to explore solutions that can be projected toward future implementation in a wearable, real-time blood pressure monitoring system. The system is intended for supervised experimental use and centres on collecting high-quality data from optical (FBG) and electrical (ECG) sensors to investigate the relationship between pulse timing features – such as pulse arrival time (PAT) and pulse transit time (PTT) – and reference blood pressure. Hardware and software configurations support flexible prototyping using benchtop instrumentation, tethered power supply, and post-processing pipelines. Regulatory compliance, safety certifications, and user interface design are not addressed at this stage, as the primary goal is to determine whether the core measurement approach can yield reliable and repeatable results for further development.

Note on clinical relevance. While this PoC study does not aim to meet clinical validation criteria, it is informed by the general design principles outlined in recent international consensus statements on cuffless BP monitoring [24]. In particular, the focus on pulse timing features (e.g., PAT, PTT), the use of reference BP measurements for validation, and the emphasis on reproducibility are aligned with the early stages of developing a system capable of future adherence to such standards. To address the challenge of BP tracking under dynamic conditions, an exercise protocol is proposed to induce measurable changes in cardiovascular state. However, metrics such as long-term drift and calibration stability over extended

periods will be addressed in subsequent studies once feasibility has been confirmed.

The design requirements and feasibility objectives of the proof-of-concept system are summarised in Table 2.4, which outlines key specifications related to accuracy, latency, hardware form factor, and system interface. Detailed hardware considerations, including the use of dual-site FBG sensors and ECG for timing reference, are discussed in the Hardware Specifications section. The algorithmic approach, described in Table 2.5, focuses on exploratory modelling using Gaussian Process Regression (GPR) based on PAT and PTT features, with performance evaluated against cuff-based BP measurements. User safety and operational constraints are summarised in Table 2.6, which clarifies that the system is intended solely for supervised laboratory testing. Finally, the intended validation strategy is outlined in the Testing Goals PoC subsection, which highlights internal phantom testing and controlled human studies as the initial experimental focus.

Table 2.4: Design specifications for proof-of-concept (PoC) cuffless BP monitor

Category	**PoC Goals**
Accuracy	Within ±10 mmHg (exploratory range acceptable)
Latency	Not real-time required – batch or post-processing is acceptable
Form Factor	3D-printed or flexible PCBs may be used
Power	Battery operation not critical – system can be tethered
Connectivity	USB or local storage is sufficient; wireless connectivity is optional
Interface	Developer-facing graphical interface (e.g., Python scripts, MATLAB)

Hardware Specifications

Off-the-shelf development boards (e.g., STM32, ESP32, Raspberry Pi), optical bench setups, or exposed FBG interrogators may be used. The setup includes dual-site FBG sensors for pressure waveform acquisition and a three-lead ECG system to provide timing reference points for PAT estimation.

Algorithm Goals

Table 2.5: Algorithmic goals and performance targets for proof-of-concept (PoC) system

Gaussian Process Regression (GPR) Model	
Feature	**PoC Target**
Algorithm Type	Exploratory: Gaussian Process Regression (GPR)
Input Features	Raw or filtered pulse arrival time (PAT) and pulse transit time (PTT)
Validation	Comparison with reference cuff-based BP measurements; regulatory-grade validation not required at this stage
Performance Metrics	Emphasis on BP trend estimation; target $R^2 > 0.7$, not required to meet AAMI or ISO standards
FC-GAN Model for Signal Reconstruction	
Feature	**PoC Target**
Algorithm Type	Exploratory: FC-GAN model for signal reconstruction
Input Features	MIMIC II database, PPG signals as example of pulsatile signal
Validation	Comparison with ground truth clean PPG signals and HR of ECG signals
Performance Metrics	HR from PPG and ECG signals, SNR and Euclidean Distance

User and Safety Considerations

Table 2.6: User and safety considerations for proof-of-concept (PoC) system

Aspect	**PoC Approach**
Safety	Laboratory-grade electrical isolation is implemented; the system is not intended for clinical or unsupervised use.
User Experience	Designed solely for supervised testing and data collection; not optimised for end-user interaction or deployment.
Materials	Biocompatibility is not a requirement unless human trials are explicitly planned.

Testing Goals PoC

- Internal lab validation with known references (e.g., simulated signals through a cardiovascular phantom).

- Controlled human testing if ethical approval is granted.
- Focused on demonstrating feasibility, not full generalisability.

2.6 Research Scope and Contributions

The preceding review has highlighted key limitations in the current landscape of cuffless blood pressure monitoring technologies. Specifically, three core challenges persist: (i) the limited mechanical robustness and portability of existing FBG-based pulse sensors; (ii) the constrained generalisability and computational demand of machine learning models for blood pressure estimation; and (iii) the susceptibility of pulsatile signals to motion artefacts, which complicates reliable feature extraction in dynamic, real-world conditions.

Informed by these gaps, this research adopts a multi-layered system architecture that integrates novel sensor design, machine learning, and signal reconstruction strategies. The system-level design and specification goals, outlined at the end of this chapter, serve to define the technical scope and performance expectations for the proposed proof-of-concept (PoC) system, particularly in terms of signal fidelity, modelling feasibility, and supervised experimental validation.

The main contributions of this thesis are as follows:

- The design and characterisation of a dual-site FBG-cantilever sensing system optimised for non-invasive pulse waveform acquisition at the wrist and upper arm (Ch 3).
- The development of a cardiovascular phantom that mimics arterial pressure waveforms and enables controlled validation of pulse arrival time (PAT) and pulse transit time (PTT) measurements (Ch 4).
- A preliminary human validation protocol investigating the relationship between FBG-derived timing features and reference blood pressure, under dynamic BP changes (Ch 5).

- A data-driven modelling pipeline for systolic and diastolic BP estimation, based on Gaussian Process Regression (GPR), which addresses the limitations of hand-crafted feature dependence and provides interpretable uncertainty estimates (Ch 5).

- The application of a generative adversarial network with fully connected layers (FC-GAN) for motion artefact mitigation in pulsatile signals, supporting improved signal quality for downstream feature extraction (Ch 6).

3. FBG-cantilever sensing system

This chapter presents the development of the transducer layer for pulsatile signal detection at the skin surface of the proposed architecture of the cuffless BP monitoring system, as illustrated in Figure 2.7. The transducer is based on a novel FBG-cantilever sensing configuration. The originality of this design lies in using an FBG sensor coupled to a rectangular cantilever beam structure for arterial pulse detection. This configuration not only enables targeted measurement of arterial pulse waves but also enhances signal sensitivity through mechanical amplification, guided by the slenderness principles of Euler-Bernoulli beam theory. Additionally, the feasibility of this system for portable applications is investigated with the integration of the miniature FBG interrogator (FiSpecX100, FiSens GmbH, Braunschweig, Germany), allowing real-time signal acquisition in a compact form factor.

By mechanically amplifying subtle deformations at the skin-sensor interface with the proposed 3D printed design, this design addresses key limitations identified in the literature (Table 2.1), including the attenuation of pulse signals due to soft tissue damping and reduced sensitivity in wearable settings, wearability and robustness. The proposed FBG-cantilever system thus contributes to improving the fidelity of distal pulse waveform acquisition under non-invasive and ambulatory conditions.

3.1 Cantilever design and sensor fabrication

As discussed in Chapter 1, Section 1.7, fibre Bragg grating (FBG) sensors are highly sensitive to strain; however, this sensitivity can be compromised by the miniaturisation of the optical interrogation systems. Aiming a portable ambulatory BP monitor, this research explores the integration of the miniature interrogator FiSpecX100, which operates within a spectral bandwidth of 808-880nm. It is believed that this wavelength range yields approximately half the sensitivity compared to conventional interrogators operating within the 1525-1575nm spectral range. Moreover, as highlighted in the literature review (Section 2.1), most previous studies incorporate additional structures to better couple the FBG sensor to the arterial pulse.

To address both sensitivity limitations and targeting of arterial pulsations at the skin surface, the FBG sensor in this study is proposed to be mounted on a rectangular cantilever. This cantilever acts as a mechanical amplifier, magnifying the strain signals induced by arterial wall distension and improving the sensor's ability to detect pulse waveforms.

3.1.1 Strain amplification with rectangular beam

To enable strain amplification in a compact form factor, this work adopts a rectangular cantilever beam design satisfying the slenderness criterion $\frac{h}{L} \leq \frac{1}{10}$, which ensures minimal shear deformation. This assumption allows the use of Euler–Bernoulli beam theory, where the beam is considered to deform primarily through bending moment rather than shear forces [106]. In such bending-dominated deformations, strain varies linearly through the height h of the beam, and the bending moment at the fixed end is proportional to the applied load F and the beam length L, i.e., $M = F \cdot L$, hence the amplification of the physical load detected at the tip of the beam.

Beam dimensions and mechanical properties

The cantilever dimensions were selected to satisfy the slenderness condition while maintaining compatibility with limb-wearable form factors. The rectangular beam dimensions are 10 mm × 4 mm × 1 mm (Figure 3.1). The width $b = 4\,\text{mm}$ was chosen to accommodate the typical external diameters of superficial arteries such as the radial and brachial arteries ($b \geq 3\,\text{mm}$) [107].

Furthermore, the beam – with a height-to-length ratio of 1:10 – behaves as a harmonic oscillator with a natural frequency well above the fundamental frequency range of arterial pulsations (≈ 1-2 Hz). This ensures that the cantilever's response is quasi-static and primarily governed by mechanical coupling with the arterial wall at the skin surface. Wu et al.[108] explored triangular cantilevers to raise resonant frequencies without increasing size; however, the rectangular geometry used here remains suitable for wearable integration and fabrication simplicity.

The structure was fabricated via SLA 3D printing using BioMed White Resin (Formlabs, UK), a certified biocompatible material appropriate for human-contact applications and the human testing goals of this research. According to manufacturer specifications, the post-cured Young's modulus is approximately $E = 2020\,\text{MPa}$ [109]. However, the mechanical properties of this resin may vary with environmental factors such as temperature and humidity. The material density was assumed to be $\rho = 1.14\,\text{g/cm}^3$, consistent with the datasheet values.

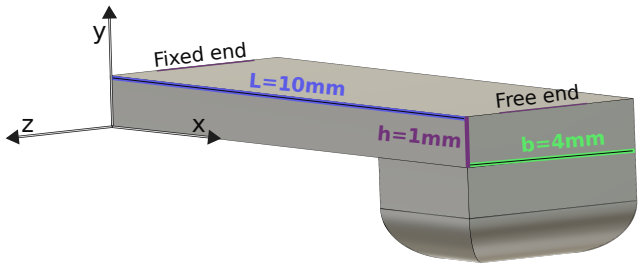

Figure 3.1: *Rectangular cantilever beam with dimensions $L \times b \times h = 10\,\text{mm} \times 4\,\text{mm} \times 1\,\text{mm}$.*

Following Euler-Bernoulli beam theory, the bending moment, shear forces, mo-

ment of inertia, stress distribution, the maximum beam deflection and the beam dynamic behaviour are assessed for the proposed cantilever beam dimensions.

Bending moment and shear forces

The shear force F_{sh} at any point x along the beam's length is constant for a point load applied at the free end $F_{sh} = C$. Whereas the bending moment varies linearly along the length of the cantilever beam L= 10mm.

x (**Position along beam**)	**Shear Force**($F_{sh}(x)$)	**Bending Moment** ($M(x)$)
0 (Fixed end)	C	$C \cdot L$
$L/2$ (Midpoint)	C	$C \cdot (L/2)$
L (Free end)	C	0

Therefore, assuming a unit load of 1 N, the maximum bending moment – located at the fixed end – is $\boxed{M_{\max} = 10, \mathrm{N} \cdot \mathrm{mm}}$. This illustrates the linear relationship between the cantilever length and the maximum bending moment at the fixed end. The proposed beam length satisfies the slenderness requirement for Euler-Bernoulli beam theory, without further increasing the length in order to maintain the smallest possible compact form factor suitable for limb wearability.

Moment of Inertia

The moment of inertia, which represents the beam's resistance to bending, for the designed rectangular cross-section is calculated as:

$$I = \frac{bh^3}{12} = \frac{4\,\mathrm{mm} \times (1\,\mathrm{mm})^3}{12} = \frac{4}{12}\,\mathrm{mm}^4 = \boxed{0.33\,\mathrm{mm}^4} \tag{3.1}$$

This value is essential for understanding the mechanics of motion, force balance, and the dynamic behaviour of the beam.

Normal stress distribution

The stress varies linearly from zero at the neutral axis to a maximum at the top and bottom edges. The maximum normal stress σ_{max} (Figure 3.2) occurs at the outermost layers of the beam (top and bottom surfaces where $y = \pm h/2$), in this case $h/2 = 2\,\text{mm}$, and with the maximum bending moment M_{max}, at the fixed end $x = 0$, constrained by the Moment of Inertia I. Assuming a unit load F of 1 Newton.

$$\sigma_{max} = \frac{M_{max}(h/2)}{I} = \frac{5\,\text{N}\cdot\text{mm}^2}{0.33\,\text{mm}^4} = 15.15\,\text{N/mm}^2 \approx \boxed{15.1\,\text{MPa}} \tag{3.2}$$

This value lies within the elastic regime for typical biocompatible resins. The corresponding surface strain is:

$$\varepsilon_{\max} = \frac{\sigma_{\max}}{E} = \frac{15.1\,\text{MPa}}{2020\,\text{MPa}} \approx 7.5 \times 10^{-3}\,(7.5\,\mu\varepsilon/\text{mN}),$$

ensuring a measurable response for the FBG sensor while maintaining a compact form factor suitable for wearable applications.

Maximum beam deflection

Assuming a unit load F of 1 Newton, the maximum beam deflection δ_{max} would be:

$$\delta_{\max} = \frac{FL^3}{3EI} = \frac{1\cdot 10^3\,\text{N}\cdot\text{mm}^3}{3\cdot 2020.16\,\text{N/mm}^2\cdot 0.33\,\text{mm}^4} \approx \boxed{0.495\,\text{mm}} \tag{3.3}$$

Note: $1\,\text{MPa} = 1\,\text{N/mm}^2$.

The calculated maximum beam deflection of approximately 0.495mm under a unit load indicates a relatively compliant structure, which is advantageous for enhancing strain sensitivity in the context of FBG-based sensing. A higher deflection leads to increased surface strain at the beam's surface, resulting in greater modulation of the Bragg wavelength, which can improve signal resolution. However, this level of deflection must also be assessed in the context of mechanical stability and

repeatability, especially in wearable applications where excessive bending might affect alignment, sensor bonding, or user comfort. The result reflects a good balance between mechanical responsiveness and structural integrity, supporting the use of the proposed cantilever design for dynamic pressure or pulsation monitoring in a compact, wearable format.

Beam dynamic behaviour

The estimated first natural frequency f_1 of the cantilever beam is calculated as:

$$f_1 = \frac{1.875^2}{2\pi L^2}\sqrt{\frac{EI}{\rho A}} = \frac{1.875^2}{2\pi \cdot 100\,\mathrm{mm}^2}\sqrt{\frac{2020.16\,\mathrm{N/mm^2} \cdot 0.33\,\mathrm{mm}^4}{0.08145\,\mathrm{g/mm^3} \cdot 4\,\mathrm{mm}^2}} = \boxed{254.4\,\mathrm{Hz}} \tag{3.4}$$

Note: $1\,\mathrm{N} = 1 \times 10^6\,\mathrm{g \cdot mm/s^2}$.

The calculated first natural frequency of approximately 254.4 Hz indicates that the beam's structural resonance lies well above the typical frequency range of physiological pulsations (1-2 Hz), such as arterial pressure waves. This separation ensures that the beam does not enter resonance during normal operation, thereby avoiding signal distortion or mechanical instability. Furthermore, the relatively high natural frequency reflects the stiffness and compactness of the cantilever design, allowing for fast mechanical response and suitability for real-time, dynamic sensing applications. The result supports the use of Euler-Bernoulli beam theory assumptions, where inertial and damping effects remain negligible at the operating frequencies of interest. Overall, this dynamic profile is ideal for wearable biomedical sensing, as it allows for high-fidelity strain transmission to the embedded FBG sensor without resonance artifacts interfering with signal acquisition.

3.1.2 FBG-cantilever sensor

Figure 3.2 shows arterial pulse measurements at the wrist and upper arm using the developed FBG-cantilever sensors. The strain signals are processed by a miniature optical interrogator. Two cantilever sensors were fabricated to conduct PTT measurements. Figure 3.3 illustrates how distal arterial motion is detected at the skin surface: as the radial artery expands and contracts against the scaphoid bone, the resulting displacement passes through the adipose tissue and skin, allowing the FBG-cantilever sensor to measure the arterial pulse externally. This section describes the fabrication of the FBG-cantilever sensor, using the cantilever described on section 3.1.

Figure 3.2: *Arterial pulse measurement at wrist and upper arm with FBG-cantilever sensors.*

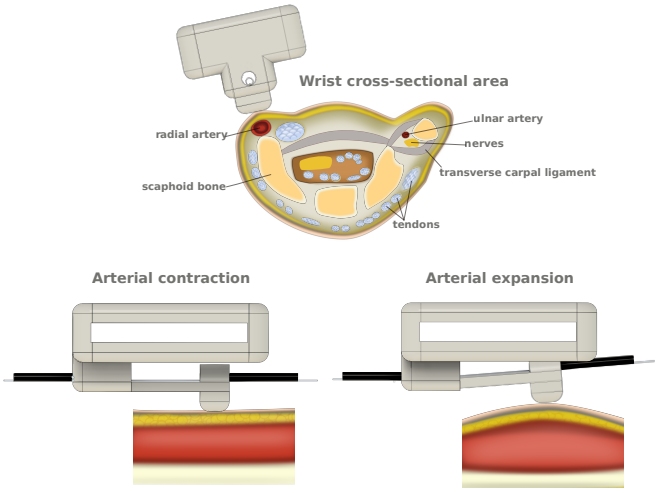

Figure 3.3: *Arterial movement detected on skin surface with the FBG-cantilever sensor.*

FBG sensor attachment to cantilever

Silica optical fibres were chosen based on their accessibility from verified suppliers and cost-effectiveness for prototyping. The FBG sensor consisted in an optical fibre with 2 FBG sections (FBG Sensor Array, FiSens GmbH, Braunschweig, Germany) was used. The specifications of this optical fibre sensor are:

1. An acrylate coated silica fibre of wide spectral range. The fibre core and cladding are made of silica, and it has an acrylate polymer coating. Silica is standard for optical fibres because of its transparency over a broad range of wavelengths. The acrylate coating adds mechanical protection to the fragility of the silica fibre.

2. Hytrel tubing as lead-in protection. Thermoplastic polyester to enhance flexibility and toughness in the "lead-in" portion.

3. Bare fibre sensor capillary. The sensing region is left bare without acrylate coating and, it is housed in a small capillary tube. Thus, the fibre can interact with strain.

4. Two FBG sensors with their corresponding Bragg wavelengths. FBG1 at 850 nm and FBG2 at 860 nm.

This optical fibre sensor was affixed in a 3D printed cantilever with limb support. Several design iterations were performed (Figure 3.4) for the support that holds the cantilever. The contact between the cantilever and the arterial site at the skin surface, as well as the attachment to the limb, was progressively optimised through each design iteration. Iteration #1 corresponds to the cantilever support used for the cardiovascular phantom. Iterations #2 and #3 were developed with the aim of adapting the cantilever for attachment to a human limb. Iteration #4 represents the first mechanical design that successfully enabled the acquisition of a wearable pulsatile signal. Iteration #5 introduced improvements in mechanical stability and pulse detectability. Finally, iteration #6 demonstrated the most effective design, offering optimal contact, signal fidelity and the smallest compact form factor for limb wearability.

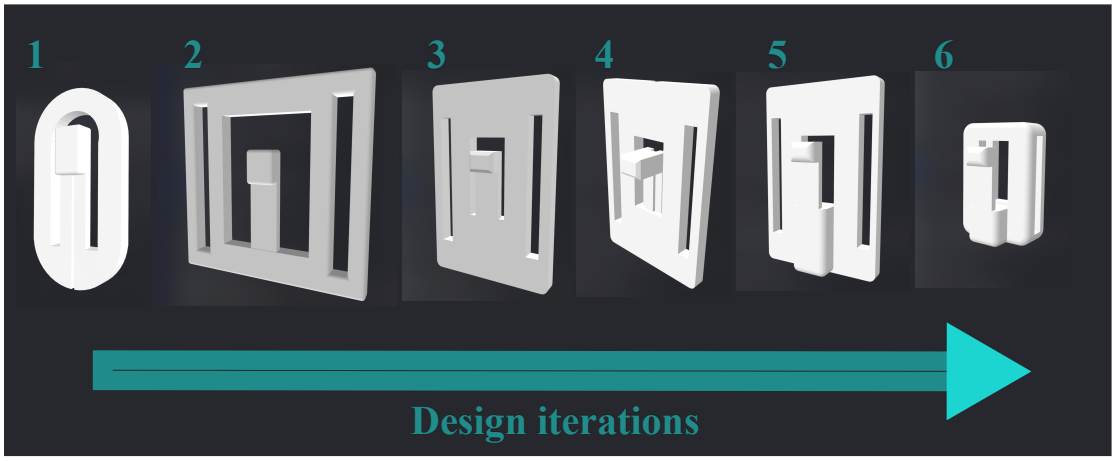

Figure 3.4: *Cantilever support design iterations. The contact of the cantilever beam with skin and limb attachment was optimised through each iteration*

Figure 3.5 illustrates the sensor performance in detecting pulsatile waveforms at the wrist using cantilever support designs from iterations #4 and #6 in the same human subject. Overall, the signal quality improved across iterations; notably, iteration #6 enhanced the visibility of the dicrotic notch as illustrated in Figure 1.1, indicating improved waveform fidelity.

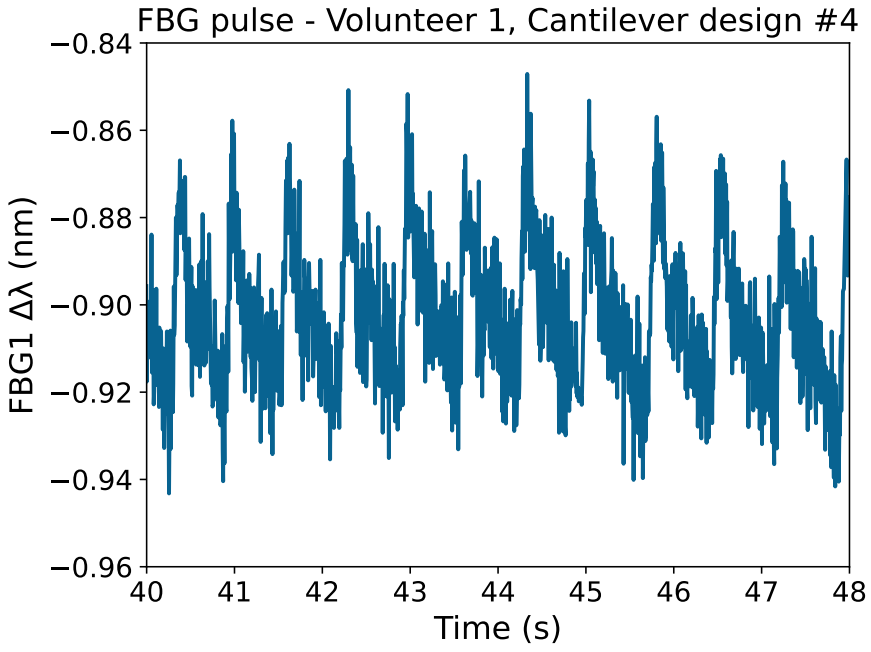

(a)

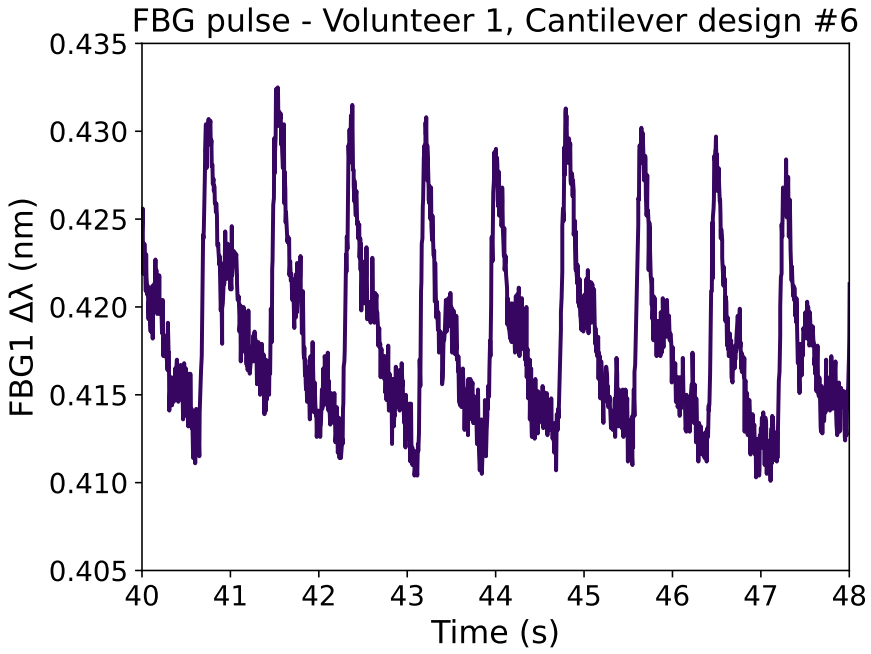

(b)

Figure 3.5: *Comparison of raw FBG pulse waveforms acquired from Volunteer 1 at wrist using two different cantilever designs. (a) Signal obtained using Cantilever design #4, exhibiting higher noise content. (b) Signal obtained using Cantilever design #6, showing improved signal quality and clearer pulsatile features such as the dicrotic notch. These results suggest enhanced strain amplification and mechanical coupling in design #6.*

The final support was attached to the limbs of the body along with an elastic band, Figure 3.6. Specifically, at the skin surface near the radial and brachial

arteries located in the arm at the wrist and upper-arm respectively. Additionally, a ring was designed to secure the band and adjust the fitting of the attachment considering different limb sizes Figure 3.7.

The cantilever with their support were 3D printed and the two FBG sensors of the optical fibre were glued along with their jacket (small capillary tube) with a fast-acting cyanoacrylate (ELFY Super Glue, ELFY Chemical Industries (Pvt) Ltd, Pakistan) covering its whole length near to the fixed-end of each cantilever-beam where the maximum bending moment M_{max} was estimated in Section 3.1.1. Moreover, to enhance the robustness of the FBG-cantilever sensor, a drop of glue was added at the entrance of the optical fibre in the support of the cantilever and at the free-end (placing the FBG sensing area near the entrance). Also, the bare optical fibre was reinforced with hytrel tubing and heat-shrink. This setup is also illustrated in the lateral and top view of Figure 3.6.

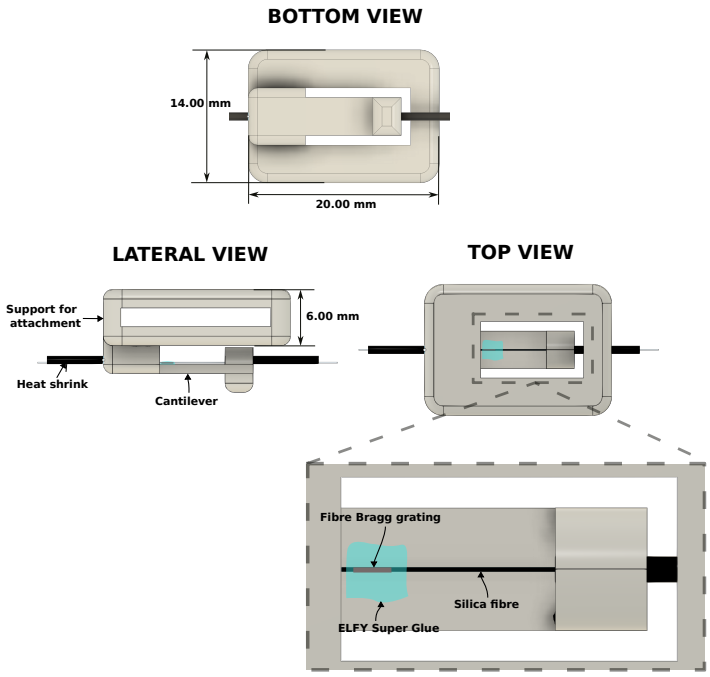

Figure 3.6: *FBG-cantilever sensor. 3D CAD design bottom, lateral and top views. From lateral and top view, the attachment of the FBG sensor to the cantilever is visualised.*

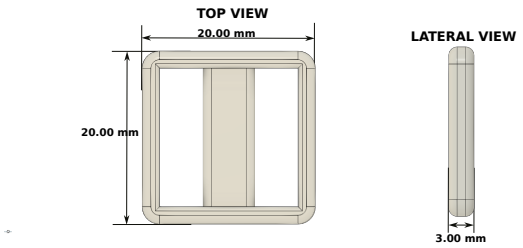

Figure 3.7: *Ring designed to secure and adjust with an elastic band different limb sizes.*

3.1.3 Strain transfer in the FBG–cantilever bonded with cyanoacrylate

This section analyses the strain amplification and strain transfer that occur when bonding the FBG sensor to the cantilever beam using cyanoacrylate adhesive. First, the minimum detectable axial force for a bare, unbonded FBG sensor is calculated based on its intrinsic strain sensitivity. Assuming a fibre Young's modulus $E_f = 72\,\text{GPa}$ and fibre radius $r_f = 62.5\,\mu\text{m}$, the cross-sectional area is

$$A_f = \pi r_f^2 = \pi(62.5 \times 10^{-6})^2 \approx 1.227 \times 10^{-8}\,\text{m}^2 \tag{3.5}$$

Given the interrogator's minimum detectable strain $\varepsilon_{\text{min}} = 1\,\mu\varepsilon = 1 \times 10^{-6}$, the minimum axial force detectable by the bare FBG is:

$$F_{\text{min, axial}} = E_f A_f \varepsilon_{\text{min}} = (72 \times 10^9)(1.227 \times 10^{-8})(1 \times 10^{-6}) \approx \boxed{0.883\,\text{mN}} \tag{3.6}$$

This force represents the threshold at which the bare fibre, without any adhesive or structural interface, will register a detectable strain.

This value is now compared to the minimum force detectable when the same FBG sensor is surface-bonded to a rectangular cantilever beam using cyanoacrylate. In this configuration, strain is induced via bending, and only a fraction k_c of the surface strain is transferred into the fibre due to bonding and shear transfer

limitations. A conservative transfer efficiency of $k_c = 0.9$ is assumed for a thin cyanoacrylate bond [110].

The cantilever beam is fabricated from a biocompatible resin with Young's modulus $E = 2.02\,\text{GPa}$, width $b = 4\,\text{mm}$, thickness $h = 1\,\text{mm}$, and length $L = 10\,\text{mm}$. The second moment of area is calculated in Equation 3.1 as $0.33\,\text{mm}^4$. Then, the surface strain at the fixed end of a tip-loaded cantilever is:

$$\varepsilon_{\text{bending}} = \frac{FLh}{2EI} \tag{3.7}$$

Rearranging to solve for the minimum detectable force with strain amplification and strain transfer included:

$$F_{\text{min, cantilever}} = \frac{2EI\varepsilon_{\text{min}}}{hLk_c} = \frac{2(2.02 \times 10^9)(0.333 \times 10^{-9})(1 \times 10^{-6})}{(1 \times 10^{-3})(10 \times 10^{-3})(0.9)} \approx \boxed{0.149\,\text{mN}} \tag{3.8}$$

This result demonstrates that, due to the cantilever's geometry and the strain amplification from bending, the detectable force threshold is reduced by a factor of nearly 6 compared to direct axial loading. This mechanical advantage makes the FBG-cantilever system suitable for detecting low-magnitude physiological forces such as arterial pulses at the skin surface.

3.1.4 Temperature Effects in FBG Pulsatile Sensing

As noted in Equation 1.7 from Section 1.7.1, the modulation of the effective refractive index within the inscribed gratings of the fibre core – which leads to a shift in the reflected Bragg wavelength – is sensitive to both mechanical strain and temperature. Equation 1.7, the general differential form, can be linearised into Equation 3.9 by assuming several approximations: (i) small perturbations in ϵ and ΔT, where higher-order terms are negligible, (ii) first-order Taylor expansions of n_{eff} and Λ with respect to strain and temperature and (iii) Bragg wavelength shift $\Delta\lambda_B$ expressed as a linear combination of strain and temperature.

$$\Delta\lambda_B = \lambda_B \left[(1 - p_e)\epsilon + (\alpha + \xi)\Delta T\right] \tag{3.9}$$

Where:

λ_B: nominal Bragg wavelength (e.g., 1550,nm or 850,nm)

ϵ: mechanical strain (e.g., from arterial pulse or cantilever bending)

ΔT: temperature change relative to baseline

$\alpha \approx 0.55 \times 10^{-6}$: thermal expansion coefficient (per °C)

$\xi \approx 8.6 \times 10^{-6}$: thermo-optic coefficient (per °C)

$p_e \approx 0.22$: effective photoelastic constant of the optical fibre

These values are widely reported as standard for silica-based FBG sensors [56]. Although both pressure and temperature changes can influence the Bragg wavelength of an FBG sensor, these phenomena in physiological monitoring at the distal skin surface operate on fundamentally different timescales and thus occupy distinct regions of the frequency spectrum. Pressure wave propagation, such as the arterial pulse, is a high-frequency phenomenon typically observed in the 1–2 Hz range (corresponding to heart rates of 60–120 BPM). In contrast, thermal effects at the skin surface, including conductive heat transfer, vasodilation, and evaporative cooling, evolve much more slowly, with dominant frequency components typically below 0.01 Hz [111, 112]. This substantial separation in frequency bandwidths allows for effective differentiation between the two signals using appropriate filtering or decomposition methods, such as high-pass filtering to isolate the pulsatile strain or the use of a reference FBG for temperature compensation. Therefore, despite both affecting the sensor's output, thermal and mechanical signals can be decoupled due to their spectral distinctiveness.

In addition to occupying distinct frequency bands, thermal and mechanical effects differ in their temporal structure. Arterial pressure waves are inherently periodic, driven by the cardiac cycle and typically observed as regular oscillations in the range of 1–2 Hz. In contrast, temperature-induced effects at the skin surface are aperiodic and gradual, evolving over timescales of tens of seconds to several

minutes. These include phenomena such as conductive heat transfer, vasomotor regulation, and sweating, which manifest as slow drifts or non-oscillatory trends in the FBG signal.

To assess the impact of temperature on FBG strain sensing, a simulation was performed modelling the thermal drift experienced by the fibre during physical exercise – one of the daily routines characterised by rapid and sustained increases in body temperature. Reference temperature values were taken from physiological studies on thermal responses to physical activity [113]. Figure 3.8 illustrates the simulation of the temperature changes across different exercise stages (e.g., rest, moderate, intense). The simulated response includes both the strain-induced and temperature-induced wavelength shifts in each stage. Figure 3.9 provides a zoomed-in view that clearly shows how the baseline of the strain waveform is distorted due to temperature variation. These simulated results confirm the physiological nature of temperature signals and their capacity to distort strain-based pulsatile measurements. This highlights how the difference in both frequency bandwidth and periodicity enables decoupling of thermal drift from pressure-induced strain oscillations using filtering techniques or dual-FBG configurations.

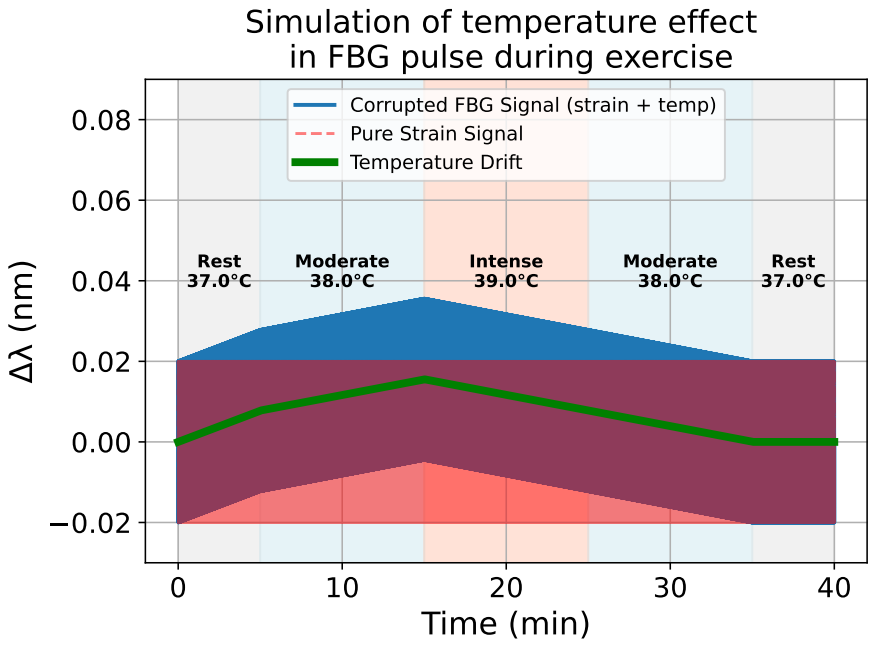

Figure 3.8: *Simulated Bragg wavelength shift of an FBG sine wave corrupted by body temperature drift during a 40-minute exercise routine.*

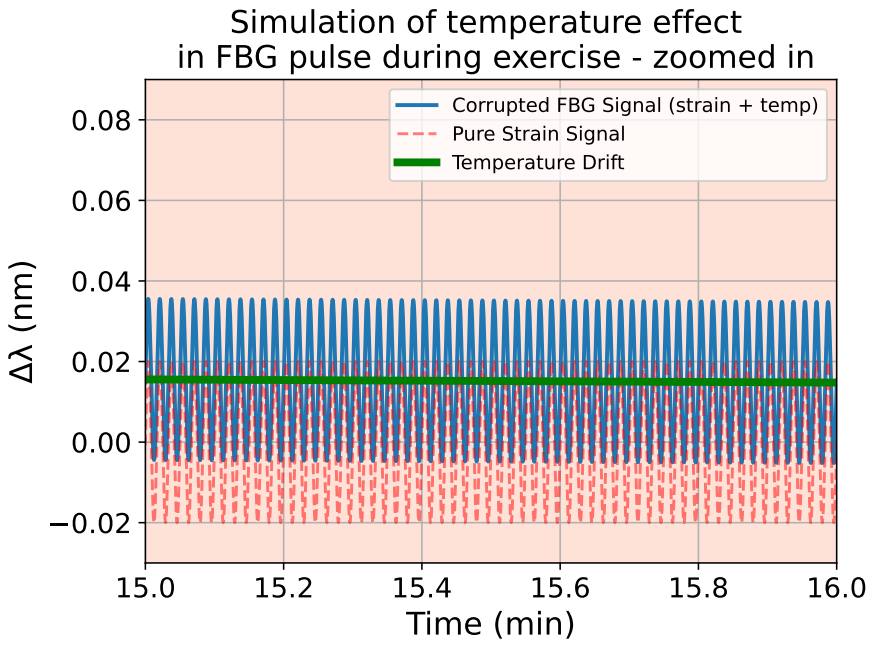

Figure 3.9: *Zoomed-in view of the same simulation, highlighting the baseline shift due to temperature-induced drift.*

3.2 Instrumentation of the miniature interrogator

As illustrated in Figure 3.2, a miniature interrogator device is used to process the strain based on distal arterial movements at skin surfaces (wrist and upper arm). This section details the benchmarking of this portable optical interrogator (FiSpecX100, FiSens GmbH, Braunschweig, Germany) against a benchtop interrogator (DM-8125, SENTEA, Belgium). Furthermore, this section describes the instrumentation FiSpecX100 interrogator with ESP32 and with a Raspberry Pi.

3.2.1 Benchmarking of FiSens Against SENTEA FBG Measurements

Several established schemes exist for detecting Bragg wavelength shifts in fibre Bragg gratings (FBGs). One common approach involves injecting a broadband light source – such as a super-luminescent diode (SLED), edge-emitting LED, or

erbium-doped fibre superfluorescent source-into the fibre and detecting the peak reflected wavelength. Alternatively, the Bragg grating can be interrogated using a laser tuned to the sensor's wavelength, or by embedding the sensor within a laser cavity.

High-resolution Bragg wavelength detection is often performed using optical spectrum analyzers (OSAs), suitable for laboratory environments. For more practical applications, compact and cost-effective alternatives include broadband optical filters, interferometric systems, and fibre laser-based interrogation methods. Among the simplest approaches is passive broadband illumination paired with miniature spectrometers, tuneable filters, or interferometric tracking [56].

In earlier work, Åslund et al. [114] demonstrated that FBGs fabricated using the point-by-point (PbP) technique with femtosecond Ti:sapphire lasers (800 nm) exhibited strong attenuation at shorter wavelengths due to Mie scattering. These scattering effects arise from microstructural irregularities in the gratings. The study showed that diffraction patterns could be observed when HeNe laser light (632.8 nm) was launched into the fibre core, with scattered light projected onto a screen. This property supports the development of compact interrogation systems based on internal diffraction and scattering.

One such compact interrogator is the FiSpecX100 (FiSens GmbH), which is employed in this research. It measures the reflected spectrum of guided SLED light within the fibre by integrating a tilted FBG inscribed via a femtosecond laser. The resulting diffraction and Mie scattering effects couple light out of the fibre, which is then spectrally resolved on a planar surface using a diffraction grating. A CCD sensor captures the spectrum, which is processed by an onboard microprocessor [115]. This design enables high-precision measurements (0.1°C or 1 $\mu\varepsilon$ at 10 Hz) in a highly compact, battery-powered format, ideal for wearable applications.

By contrast, most commercial FBG interrogators – such as those from SENTEA (Belgium), HBM and Polytec (Germany), Smart Fibres (UK), and Micron Optics (USA) – offer high-resolution, multi-channel capabilities suitable for a range

of industrial and medical uses. However, their relatively large size and lack of portability make them less suitable for long-term wearable monitoring.

The FiSens interrogator is approximately seven times smaller than conventional units, making it an attractive option for compact, wearable sensing systems. To assess its suitability for physiological monitoring applications, this study compares the strain sensitivity of the miniature FiSpecX100 (FiSens GmbH, Germany) with that of a reference system, the DM-8125 interrogator from SENTEA (Belgium). The SENTEA operates over a Bragg wavelength range of 1525–1575 nm, while the FiSens operates in the shorter wavelength range of 808–880 nm. Because strain sensitivity in FBGs is proportional to the Bragg wavelength, as shown in Section 3.2.2, the FiSens is expected to have lower sensitivity. This benchmarking therefore aims to quantify the practical performance of the miniature interrogator in terms of resolution and sensitivity under controlled loading conditions.

3.2.2 Strain Sensitivity Prediction at Different Bragg Wavelengths

The strain-induced shift in Bragg wavelength can be estimated by isolating the strain-dependent part of Equation 3.9. Expressing strain as:

$$\frac{\Delta l}{l} = 1\,\mu\epsilon \tag{3.10}$$

and relating the change in effective refractive index n_{eff} to the effective photoelastic constant p_e, the strain sensitivity is given by:

$$\Delta\lambda_B = \lambda_B(1 - p_e)\frac{\Delta l}{l} \tag{3.11}$$

The effective photoelastic constant p_e is defined as:

$$p_e = \frac{n^2}{2}\left[p_{12} - v(p_{11} + p_{12})\right] \tag{3.12}$$

Combining Equations 3.10 and 3.11, the strain sensitivity per microstrain is:

$$\frac{\Delta\lambda_B}{\mu\epsilon} = \lambda_B(1 - p_e) \tag{3.13}$$

Where:

$\mu\epsilon$: micro-strain

n: fibre core refractive index

v: Poisson's ratio

p_{11}, p_{12}: strain-optic coefficients

For a fused silica fibre, $p_e = 0.22$ [116]. Using this value:

At $\lambda_B = 1550$ nm, the predicted strain sensitivity is:

$$\frac{\Delta\lambda_B}{\mu\epsilon} = 1550 \times (1 - 0.22) = \boxed{12.1 \times 10^{-4}\,\mathrm{nm}/\mu\epsilon}$$

At $\lambda_B = 850$ nm, the predicted strain sensitivity is:

$$\frac{\Delta\lambda_B}{\mu\epsilon} = 850 \times (1 - 0.22) = \boxed{6.63 \times 10^{-4}\,\mathrm{nm}/\mu\epsilon}$$

These results predict a strain sensitivity at 850 nm that is approximately half that at 1550 nm. To confirm this theoretical relationship in practice, an experimental comparison was conducted as described below.

3.2.3 Experimental setup to compare FiSens against SENTEA strain sensitivity

To evaluate and benchmark the strain sensitivity of the FiSens FiSpecX100 against the SENTEA DM-8125, a controlled optical bench experiment was designed. The aim was to apply identical, incremental strain steps to two FBG sensors with central wavelengths matched to the operational ranges of each interrogator – 1550 nm for SENTEA and 860 nm for FiSens – while recording the corresponding wavelength shifts. This approach enables a direct comparison of sensitivity and linearity under identical loading.

The experimental setup is shown in Figure 3.10, where both fibres are anchored at identical locations – at the same axis where axial strain is applied – and subjected to precisely controlled displacement using a micrometer stage. The procedure ensures that both sensors experience the same mechanical strain environment, thereby enabling an accurate sensitivity comparison.

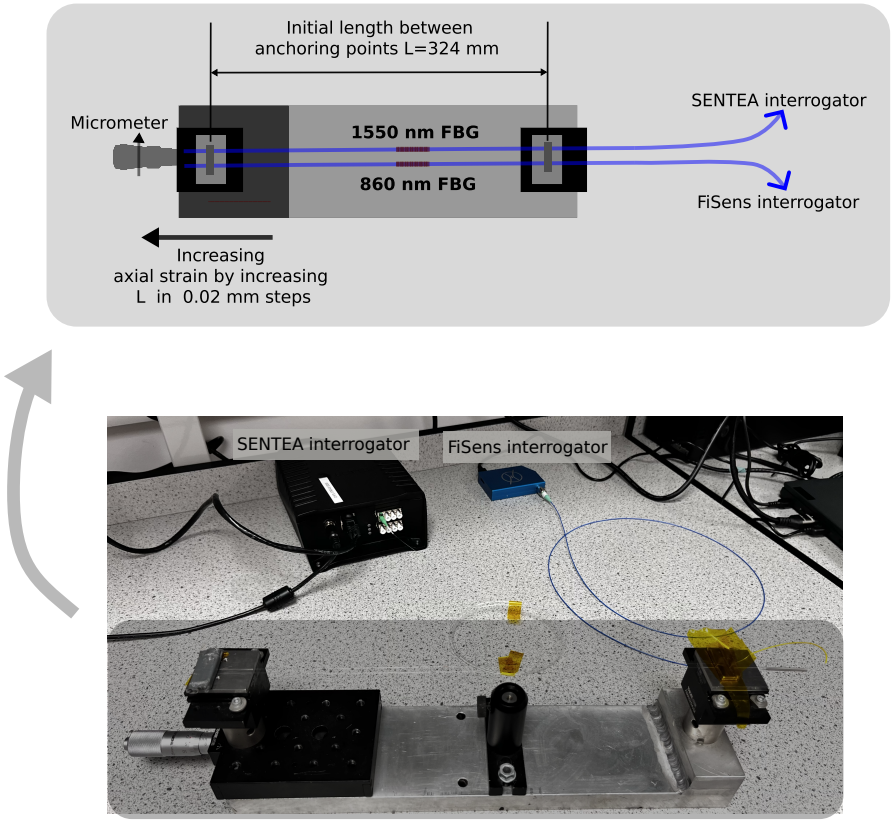

Figure 3.10: *Experimental setup to compare FiSens against SENTEA strain sensitivity.*

Procedure:

1. Connect the interrogators SENTEA and FiSens with their correspondent fibres at wavelengths of 1550 nm and 860 nm respectively.

2. Pre-strain the fibres and set the anchoring points at the same location in both fibres (Figure 3.10).

3. Record the initial length, in this case l=320 mm

4. Apply 8-step increases of strain controlling the micrometer in steps of 0.02 mm

5. Record each step for 30 seconds. Figure 3.11 shows the wavelength response as the strains steps increases.

6. Calculate the average wavelength at each step

7. Calculate the wavelength shift $\Delta\lambda_B$ for each fibre measurement 1550 nm and 860 nm, subtract the measurement from the central wavelength at the initial position.

8. Calculate the microstrain dividing the change in strain by the initial length.

9. Plot wavelength shift against micro-strain measurements for both fibres (Figure 3.12).

Figure 3.12 illustrates the difference in the wavelength shift response to strain between the FiSens and SENTEA interrogators. The slope of the wavelength shift-strain relationship is smaller in the FiSens measurements, indicating lower strain sensitivity. This difference in sensitivity is quantified in Table 3.1, where the strain sensitivity of FiSens is attenuated by a factor of approximately 2. This attenuation is consistent with the theoretical predictions presented in Section 3.2.2. Additionally, a calibration curve was generated to interpolate FiSens strain measurements relative to those obtained with the SENTEA system (Figure 3.13).

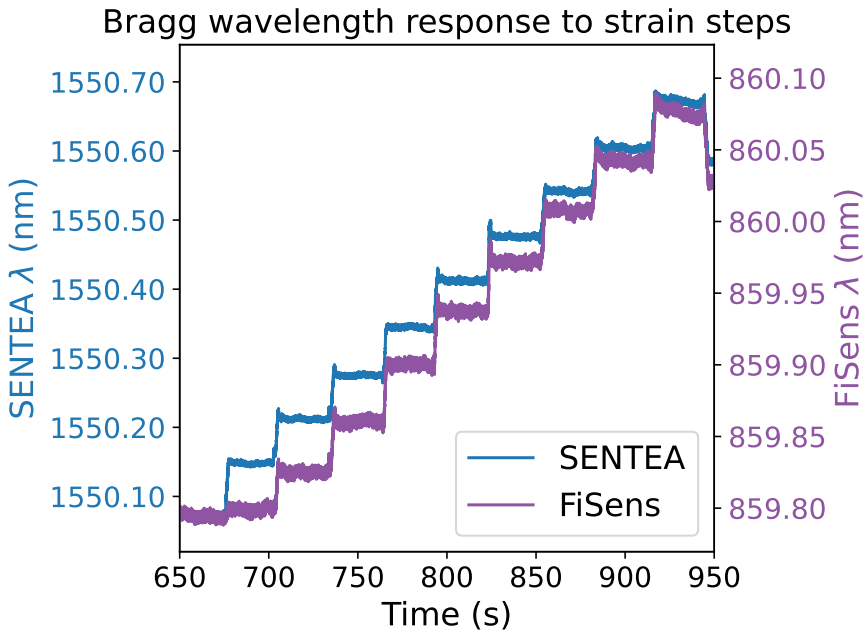

Figure 3.11: *Strain increase in 62με steps in FBG optical fibres. 1550.15 nm is the initial central wavelength measured with the SENTEA interrogator whilst 859.8 nm is the initial central wavelength measured with the FiSens interrogator. This central wavelength is linearly increasing with the strain steps.*

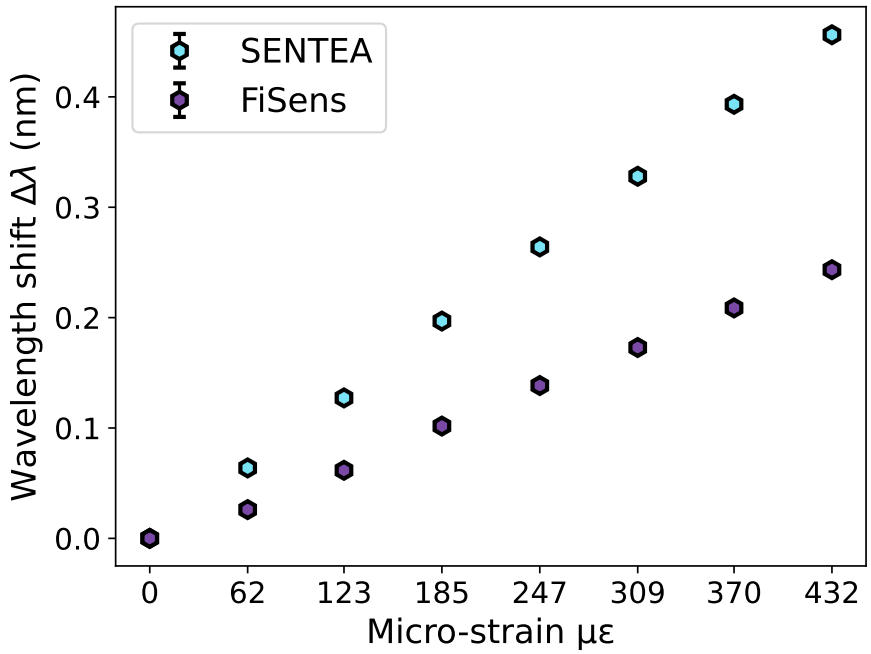

Figure 3.12: *Wavelength shift $\Delta\lambda_B$ against micro strain με using different Bragg wavelengths ranges, SENTEA working with FBG at 1550 nm (blue) and FiSens working with FBG at 860 nm (purple).*

$\mu\epsilon$	**SENTEA $\Delta\lambda_B$ (nm)**	**FiSens $\Delta\lambda_B$ (nm)**	**Ratio $\frac{\Delta\lambda_{1550}}{\Delta\lambda_{860}}$**
62	0.0638± 0.001	0.0260± 0.001	2.45
123	0.1272± 0.001	0.0616± 0.001	2.06
185	0.1968± 0.001	0.1017± 0.001	1.93
247	0.2640± 0.001	0.1384± 0.001	1.90
309	0.3280± 0.001	0.1729± 0.001	1.89
370	0.3932± 0.002	0.2087± 0.002	1.88
432	0.4562± 0.002	0.2434± 0.002	1.87

Table 3.1: Wavelength shift values under different microstrain with different Bragg wavelengths (SENTEA interrogator with 1550 nm and FiSens interrogator with 860 nm, results plotted in Figure 3.12).

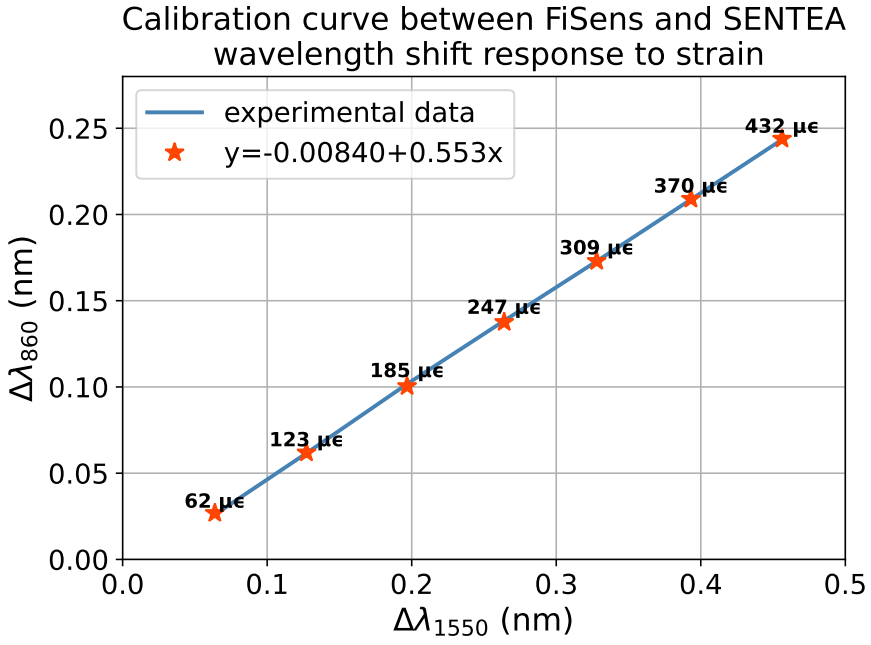

Figure 3.13: *Linear fitting of the wavelength shift from a 1550 nm to 860 nm Bragg Wavelengths using the experimental data from the sensitivity test.*

3.2.4 Instrumentation with ESP32

The ESP32-WROOM-32D module (Espressif Systems, Shanghai, China) was initially selected as the microcontroller platform for interfacing with the FiSpecX100 interrogator via the UART protocol. This module integrates a dual-core Tensilica LX6 processor and multiple hardware UART interfaces, enabling reliable and low-latency serial communication while concurrently supporting tasks such as real-time signal acquisition, data processing, and wireless transmission. Its compact footprint, low power consumption, and integrated Wi-Fi and Bluetooth connectivity make it particularly well suited for wearable and portable biomedical monitoring systems. Furthermore, the availability of extensive open-source development resources and support for real-time operating systems (RTOS) facilitates seamless UART integration, ensuring consistent and robust acquisition of optical data from the FiSpecX100 interrogator in embedded environments.

Two communication protocols were implemented: UART and WebSocket. The UART protocol is used to establish a direct serial connection between the ESP32 microcontroller and the FiSpecX100 interrogator, enabling the acquisition of FBG data. In parallel, the WebSocket protocol enables bidirectional communication between the microcontroller (as a server) and a client-side web application, allowing real-time visualisation of the FBG data. The ESP32 was programmed using MicroPython v1.18 to manage both data acquisition and wireless transmission processes. The overall communication architecture is illustrated in Figure 3.14, and the data acquisition pipeline between the microcontroller and the interrogator is detailed in Figure 3.15.

The integration time of the mini-interrogator was set to 100 ms. This integration time equals a sampling rate of around 10 Hz, which was the maximum allowed by the external UART connection of FiSpecX100, as it is limited to a baud rate of 115,200 bits per second. The follow peak function was enabled with the FiSens interface command “Pv,1>” with a follow peak limit of 50%, and the peak detection mode was set to extreme detection using the 1st derivative. Once the intensity

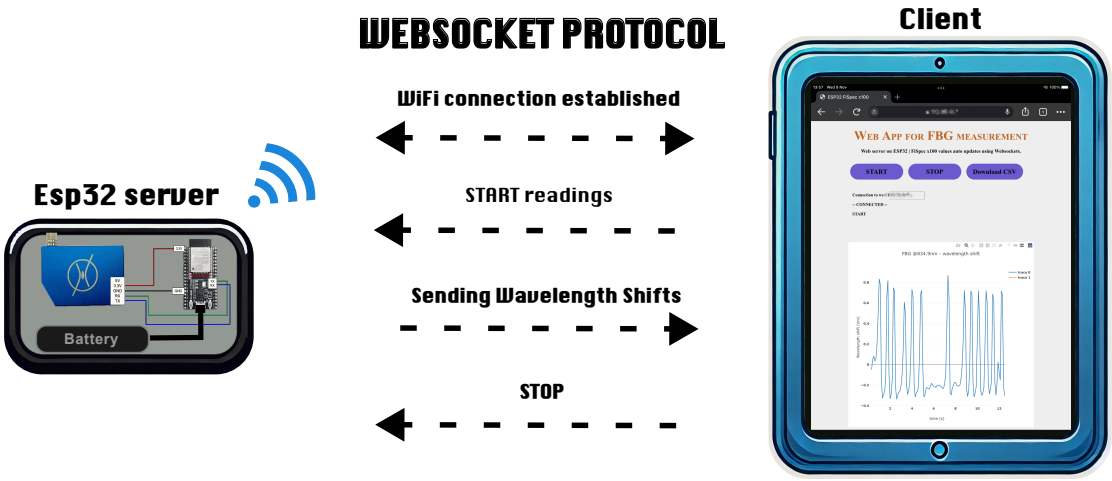

Figure 3.14: *System diagram of the mini-interrogator operation with WebSocket protocol*

and wavelength values were obtained, the Bragg wavelength at rest is measured, which corresponds to the maximum amplitude peak in the reflected spectrum at rest position. When the temperature changes, the Bragg wavelength will shift, and it is recorded relative to the Bragg wavelength at rest.

Following the calculation of the wavelength shift from the FBG sensor, data are sent through the WebSocket and a real time chart of this value was generated until the client stops it.

To start the WebSocket protocol, a Wi-Fi connection was established between the server with an iPhone hotspot, using the credentials of the hotspot. The WebSocket protocol begins when receiving a Handshake from the client (in this case the web app), then the server sends an Acknowledgement, and the full duplex communication is enabled until the connection is closed by the client or the server. The implementation of the WebSocket protocol used an available microWebSrv library in MicroPython [117]. Inside `recvTextCallback` function, the parsing data algorithm was included, and every new wavelength shift value was converted to a JSON array. The JSON array was sent through the function `webSocket.SendText`. The web application was developed in JavaScript, CSS and HTML, furthermore the chart was generated using plotly.js library. Inside the HTML file, JS scripts with different websocket functions were created for different events,`onOpen` , `onClose`,

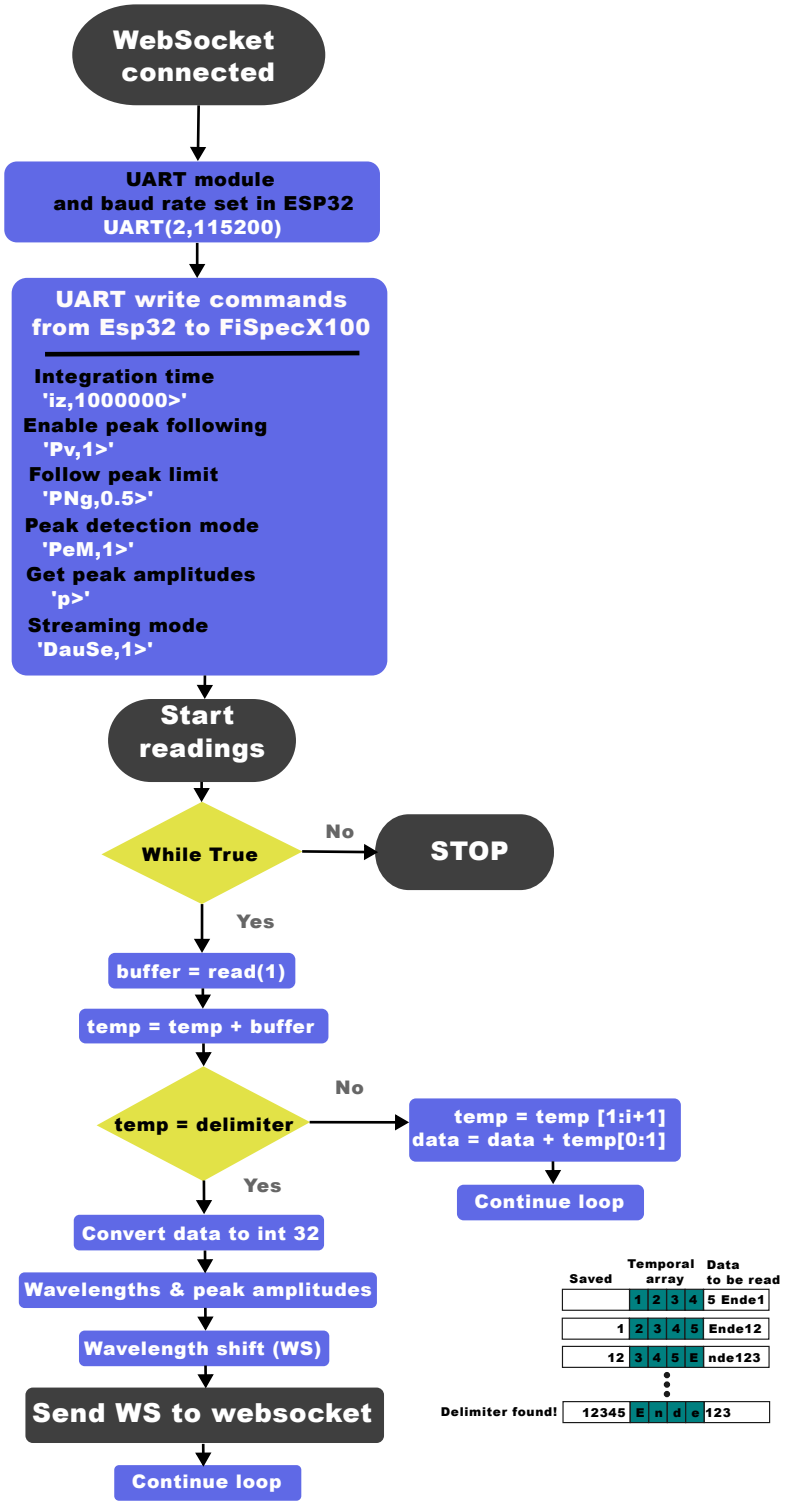

Figure 3.15: *FiSpecX100 instrumentation flow chart, including ESP32, UART protocol, and parsing of FBG data/wavelength shift values.*

`onMessage` and `onError`. Inside the `onMessage` function the JSON data received was parsed and the x, y values were defined from the data parsed and plot. Additionally, the displayed data can be downloaded in a ".csv" file for further processing.

3.2.5 Instrumentation upgrade with Raspberry Pi

When using the ESP32 microcontroller for UART communication with the FiSpecX100 interrogator, it was observed that the external UART interface – accessed via pin header connections – was limited to a baud rate of 115,200 bits per second. In contrast, the internal UART module of the FiSpecX100, accessible through the micro-USB port, supports a significantly higher baud rate of up to 3,000,000 bits per second. This higher rate allows for an increased sampling frequency of the FBG measurements. Additionally, it was found that achieving the maximum sampling rate via the USB-UART interface requires configuring the latency timer of the FTDI USB controller to 1 ms. This adjustment minimizes communication delays and increase the performance capabilities of the FiSpecX100 under the UART protocol.

To use the internal UART, the FiSpecX100 was connected from its micro-USB port to one of the USB ports of a Raspberry Pi 4 Model B. The Raspberry Pi has a Linux customised operating system called Raspbian/Raspberry Pi OS with Python installed. Therefore, the UART protocol and WebSocket protocol were adapted for this case in Python. The UART protocol was adapted using the *pyserial* library. On the other hand, for the WebSocket protocol the *websockets* and *asyncio* libraries were used. Asyncio enables writing asynchronous code, allowing multiple tasks to run concurrently through cooperative multitasking. This is particularly useful in the context of WebSockets, as it facilitates fast, full-duplex communication over a single TCP connection.

Figure 3.16 shows the implementation of the WebSocket communication using Asyncio in Python. The key features of using Asyncio are the event loop that

initialise the asynchronous code and the coroutines that allows the asynchronous tasks execution control from the client messages. The event loop calls the main Asyncio function/coroutine that creates the WebSocket connection, calling the server logic that handles the communication with the client, and specifies the network and port that establishes the connection. The server logic is the coroutine that handles the client messages, which in this case are: start, process, stop and disconnect. If the client message is "start", the Raspberry Pi reads the data parsed (wavelength shifts values) from the FiSpecX100 interrogator and streams the data through the WebSocket. If the client message is "process", the Raspberry Pi checks if there is enough FBG data collected to smooth it and find the peak values to calculate the Pulse Transit Time. Also, the client can stop the data streaming and disconnect from the WebSocket. As the UART transmission in this case was faster (3,000,000 bits per second reaching 100Hz of sampling frequency in the Raspberry Pi), the data was sent to the WebSocket every 10 datapoints to achieve continuous real-time display of the FBG measurements. For the Web application (Figure 3.17) an index.html file in the same folder as the Python file.

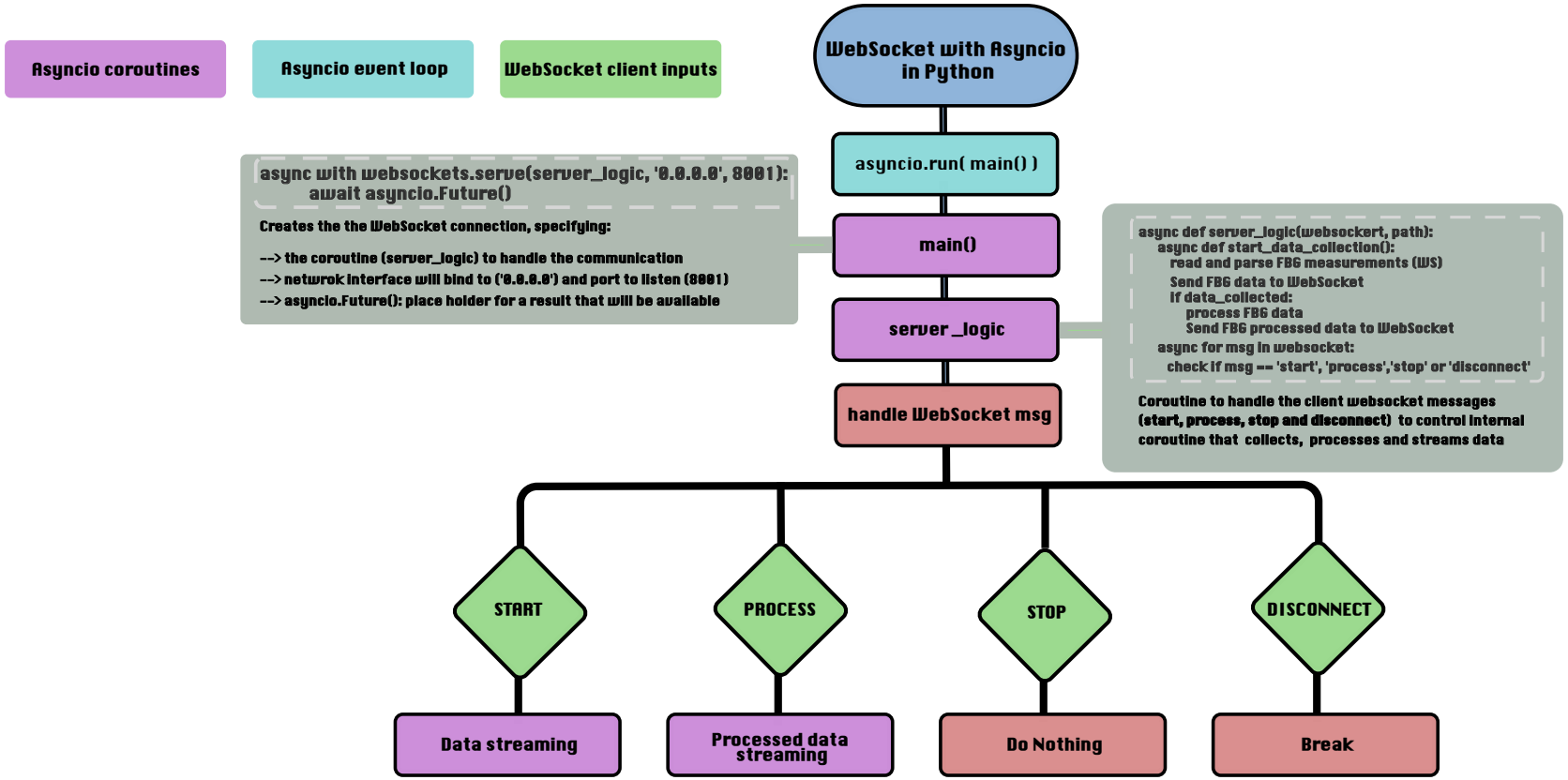

Figure 3.16: *Implementation in Python of WebSocket protocol along with Asyncio.*

Figure 3.17: *Web application for Beat-to-Beat BP measurement using PAT. Left Plot shows ECG and FBG waveforms, and the right plot shows the SBP and DBP derived from PAT using Gaussian Process Regression Model.*

3.3 Summary

This chapter presented the development of the FBG-cantilever sensing system designed to capture arterial pulse signals for BP estimation using PWV methods, in accordance with the cuffless BP monitoring architecture shown in Figure 2.7. The work focused on ensuring high-fidelity signal acquisition and effective system integration, following the design specifications and goals described in Section 2.5, and addressing the first objective of this research: *"To design and fabricate a wearable FBG-based cantilever sensor capable of detecting distal arterial pulsations."*

The feasibility of the proposed design was assessed through calculations of key mechanical properties – including maximum bending moment location, normal stress distribution, beam deflection, and first natural frequency – based on Euler-Bernoulli beam theory for a rectangular beam structure used to mechanically amplify the FBG strain sensitivity, where the beam structure is primarily dominated by bending moment than shear forces, ensuring a linear bending strain transfer along the beam.

The applied sensing element was developed as a compact, 3D-printed component in biocompatible resin – envisioning future human testing – with isotropic mechanical properties for stability, optimising strain transfer from the skin surface to the FBG region in the optical fibre. Strain transfer analysis, assuming the optical fibre was bonded to the beam with cyanoacrylate, was based on a reported transfer efficiency reduction to approximately 90% [110], while still achieving six times the strain response of a bare FBG sensor.

Since FBG sensors are also sensitive to temperature, the influence of temperature variations on pulse measurements was evaluated via simulation of an exercise scenario, introducing body temperature changes reported in the literature into Equation 3.9. The results highlighted that strain and temperature signals differ in frequency content and temporal behaviour – strain being periodic and temperature largely non-periodic – allowing for their separation with signal processing methods.

The miniature interrogator FiSens FiSpecX100, intended for ambulatory use, was

benchmarked against the conventional SENTEA DM-8125 through theoretical and experimental testing with incremental axial strain steps. The FiSens device exhibited approximately half the sensitivity of the SENTEA unit, attributed to differences in the Bragg grating period determining the central Bragg wavelength. For real-time, wireless, and compact integration, the ESP32-WROOM-32D microcontroller was initially used to interface with the FiSpecX100 interrogator. However, using the external UART via pin headers limited the baud rate to 115,200 bps, constraining the sampling frequency. This was improved by employing a Raspberry Pi to access the internal UART via the micro-USB port, achieving baud rates up to 3,000,000 bps and sampling frequencies of up to 100 Hz. This time resolution is critical for resolving PTT measurements on the order of tens of milliseconds. Real-time data visualisation was implemented via a WebSocket protocol and a dedicated web interface.

4. Cardiovascular Phantom

In Chapter 3, the FBG-cantilever sensing system was presented as the hardware platform for the proposed cuffless BP monitor, demonstrating its feasibility for detecting arterial pulsatile signals. Building on this, the present chapter validates the system for pulse arrival time (PAT) and pulse transit time (PTT) measurements using a customised cardiovascular phantom.

The phantom, adapted from Zaki et al. [102], was simplified to focus solely on PTT, without incorporating Windkessel modelling. It was further modified to accommodate FBG-based mechanical pulse acquisition, as well as electrical signal measurement for PAT determination. This customised setup enables the simultaneous acquisition of pressure, mechanical, and electrical pulse data, providing a controlled environment for accurate PTT and PAT estimation.

4.1 Methods

4.1.1 Description of the Cardiovascular Phantom

The proposed cardiovascular phantom (Figure 4.1) is primarily composed of a diaphragm motor pump (RS PRO m400 @10 V), one reservoir, tubes of different internal diameter and wall thickness. The tubing with a smaller wall thickness, regarded as the flexible tube, mimics a blood vessel and is an appropriate location for detecting the pulse pressure wave, as it expands with increasing blood pressure. For different PTT measurements, the largest-diameter pipe was replaced with progressively longer sections to increase the separation distance between sensors.

Within the system, two in-line pressure sensors (PendoTECH, New Jersey, USA) were placed, before the one way valve (PS1) and after reservoir 1 (PS2). Two FBG-cantilever sensors were located over the flexible tubing. The **motor pump** of this system plays an important role, simulating the heart rate, as it is controlled by a pulse wave modulation (PWM) signal every second (1 Hz). This signal is generated from an Arduino MEGA ADK that controls a relay that switches the motor pump on and off. The **pressurised container** is the source of liquid, and it is sealed to maintain the pressure in the system.

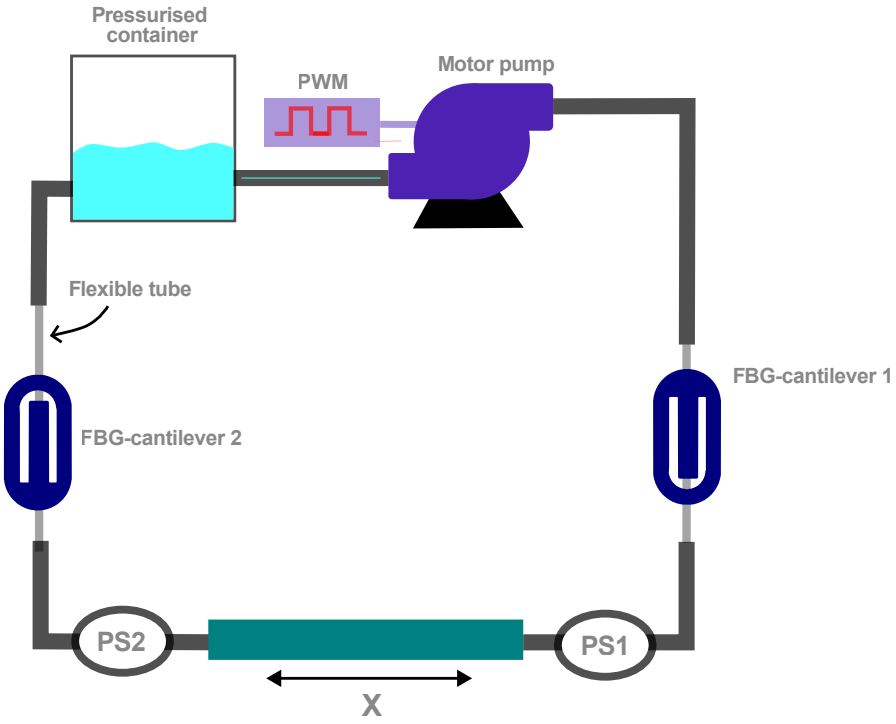

Figure 4.1: *Cardiovascular phantom adapted from Zaki et al. [102], simplified to focus solely on PTT without Windkessel modelling and modified to accommodate FBG-based mechanical pulse acquisition and electrical signal measurement for PAT determination.*

4.1.2 Pressurised container

The pressurised container used by Wan et al. [102] helped to maintain the basal pressure of the system. This container was upgraded with long lasting design and materials. The new design of the pressurised container (Figure 4.2) was created in Free CAD, and it consists of an acrylic container with an aluminium lid. The external dimensions of the reservoir are 100 cm of height and 60 cm of diameter,

on the top of the reservoir, a circular space for the o-rings was left for sealing purposes and drilling holes were added to introduce press inserts for screws that secure the lid with the container. The inner part of the container was considered to remain a considerable wall thickness that make the model less susceptible to fracture, also small rectangular flat surfaces were considered at the sides with holes for the tube connections. Figure 4.3 shows the finished pressurised container which was fabricated at the University of Nottingham.

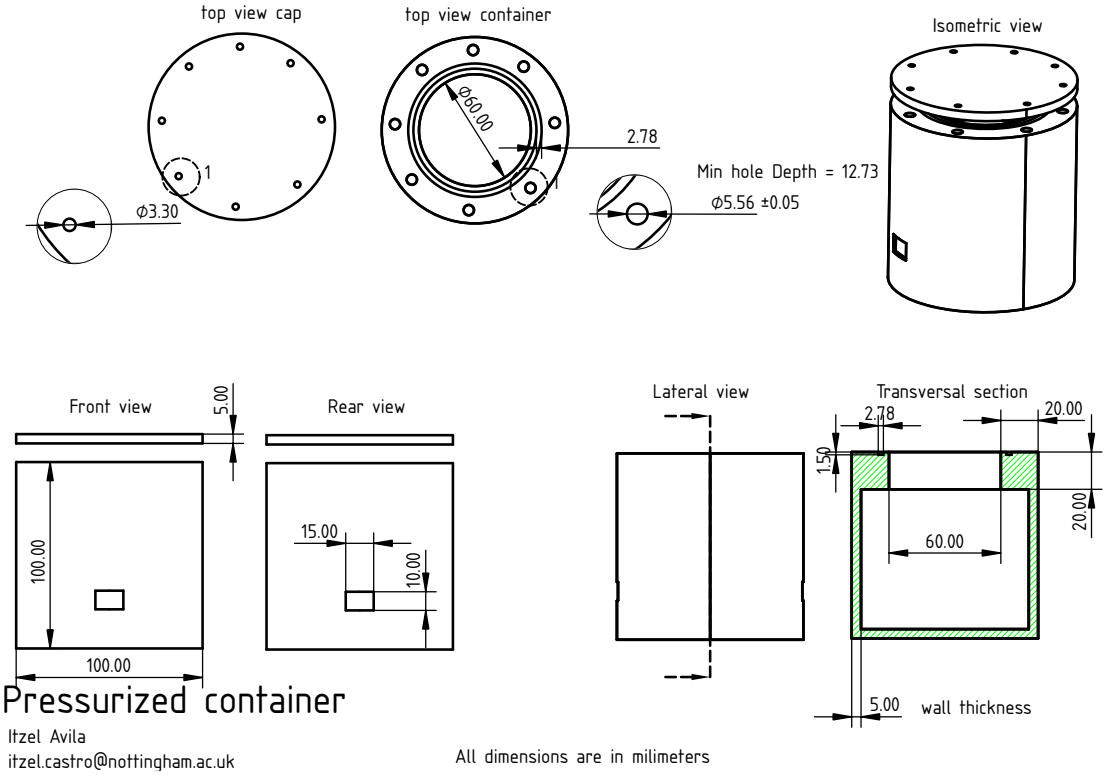

Figure 4.2: *Technical drawing of pressurised container*

4.1.3 PTT measurements

The cardiovascular phantom (Figure 4.1) was tested with the inline pressure sensors (PS1 and PS2) and the FBG-cantilever sensors described in Section 3.1.2 to compare two different PTT measurements. The first measurement involves calculating the time delay between the pulses detected with the two inline pressure sensors as a reference and the second measurement involves the time delay between the pulses detected with the two FBG-cantilever sensors. The pressure

Figure 4.3: *Pressurised container*

measurements from the inline pressure sensors were sampled at 1 KHz using a data acquisition system (DAQ NI USB 6021, National Instruments, Texas, USA). The wavelength shift values detected by the FBG-cantilever measurements were sampled at 250 Hz. The interrogator (SmartScan, Smartfibres, UK) was set at an acquisition rate of 2.5 KHz with a buffer that averages the data every 10 samples, downsampling to 250 Hz. The pressure inside the phantom was decreased by increasing the length of the tube between PS1 and PS2 (See Figure 4.1). This tube has a radius and wall thickness of 3mm. 4 different tube lengths were tested: 30 cm (8.48 mL), 60 cm (16.96 mL), 120 cm (33.93 mL) and 240 cm (67.86 mL). Each recording with the pressure sensors and FBG-cantilever patch sensors took one minute (ensuring 60 pulses), where mean PTT and standard deviation values were obtained.

Furthermore, this experiment was repeated by increasing the volume up to 84.8 mL between the FBG-cantilevers sensors, sampling at 11 different volumes to obtaining higher resolution of the decreasing trend between the sensors. Additionally, to increase the pressure of the tubular phantom, the flow rate of the motor pump

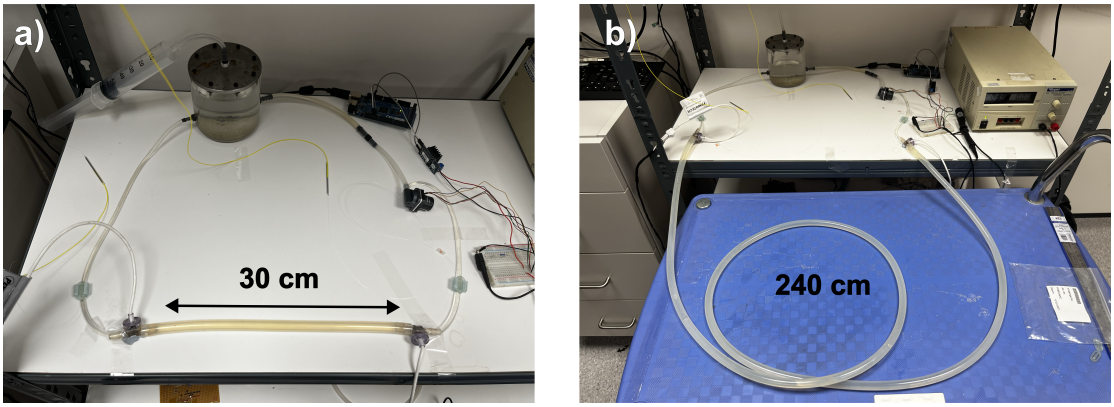

Figure 4.4: *PTT experimental setup for cardiovascular phantom. a) Experimental set up using a tube length of 30 cm. b) Experimental set up using a tube length of 240 cm.*

was increased from 1.5 to 2 L/min by increasing the supply voltage from 6 to 12 V.

4.1.4 Testing FBG-cantilever sensors before human trials

The test of the FBG-cantilevers sensors was performed in a more realistic scenario using the printed support for limb attachment described in Section 3.1.2 and the corresponding FBG array sensor at 850 nm and using the miniature interrogator FiSpecX100 described in Section 3.2. For this case the flexible tubing was placed over an acrylic tube (that mimics a limb size), and covered by a thin layer of Dragon Skin™ 10 VERY FAST (SMOOTH-ON, USA) Figure 4.5.

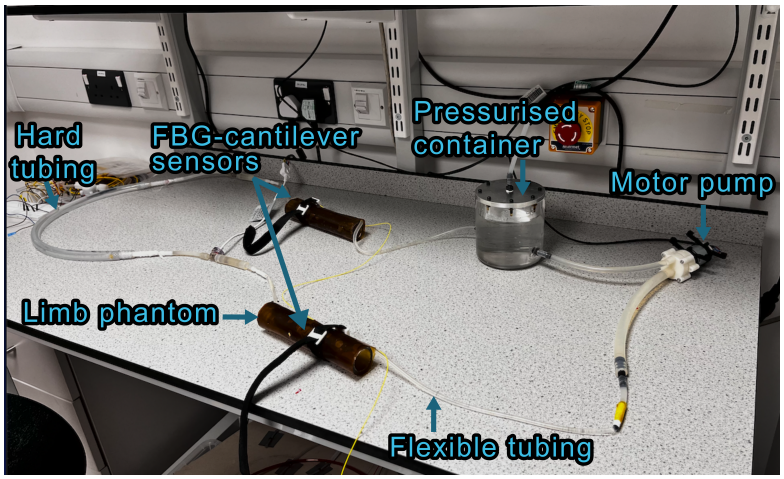

Figure 4.5: *Cardiovascular phantom with the FBG-cantilever sensors attached to the limb phantom(acrylic rod covered by Dragon Skin).*

PAT measurements

The PAT measurements in the tubular phantom consist of detecting the electrical pulse that controls the motor pump (ECG signal) as the start point and the peripheral pulse in the flexible tubing in the limb phantom (arterial pulse at the skin surface) as the end point of PAT.

The tubular phantom was used to calibrate the PAT measurements after using two separate devices, one for the ECG measurements and the second for the FBG measurements, where the processor of both has its own internal clock.

The PAT was obtained in the tubular phantom measuring the electrical pulse that controls the motor pump with the ECG recorder described in Appendix A and by placing the FBG-cantilever sensors over the flexible tube. Moreover, in order to measure the PAT, the pulse of 5 V coming from the Arduino that controls the motor pump had to be attenuated within a range of voltage that the ECG amplifier can operate between 1-200 μV. In this case the 5 V pulse was attenuated to 90 μV, using a potential divider as shown in Figure 4.6. This attenuation was calculated as below:

$$V_{R2} = V_{in} \cdot \left(\frac{R_2}{R1 + R2 + R3}\right) = V_{in} \cdot \left(\frac{33\,\Omega}{920\,\text{k}\Omega + 33\,\Omega + 920\,\text{k}\Omega}\right) = V_{in} \cdot 1.8 \times 10^{-5} \tag{4.1}$$

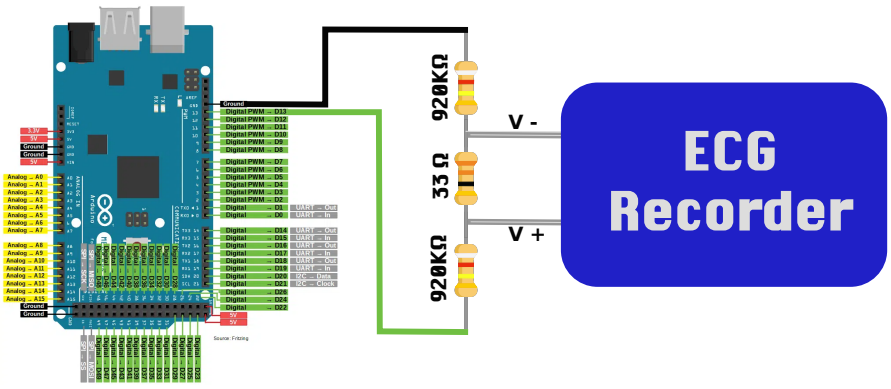

Figure 4.6: *Attenuation from 5 V to 90 μV of the electrical pulse that controls the motor pump in the tubular phantom for its measurement with the ECG recorder.*

4.2 Results

4.2.1 Controlling the pressure of the system by increasing the volume between sensors

The tubular phantom pressure was modified by replacing the hard pipe ($r = 3$ mm) between the inline pressure sensors with tubes of different lengths (30-480 cm). Figures 4.7-4.10 show the resulting pressure waveforms, where increasing tube length visually stretches the wave "strings," reflecting a spatial variation in the axial pressure gradient ($\partial p/\partial z$). This pressure gradient is the driving force that sustains pulsatile flow in the phantom by overcoming the combined inertial, viscous, and elastic wall forces of the tube system. From a haemodynamic perspective, the pressure-flow relationship can be described using the analytical formulations for oscillatory flow in elastic tubes presented by Chandran, Rittgers, and Yoganathan [118], which incorporate viscosity and wall compliance. In this framework, the Moens-Korteweg model defines the baseline wave speed for an inviscid, thin-walled elastic tube; Womersley's analysis accounts for viscous damping and the radial variation of the velocity profile; and the Morgan-Kiely extension couples fluid and wall stresses to describe wave attenuation in compliant vessels. These models predict a phase shift between pressure and velocity due to inertial effects, and that increased compliant volume between sensors will reduce the instantaneous pressure drop for a given flow waveform. Experimentally, this effect was confirmed by measuring the peak amplitude pressure difference between the inline sensors for volumes from 8.5 mL (30 cm tube) to 135.7 mL (480 cm tube), as shown in Figure 4.11; shorter tubes yielded higher pressure gradients.

Although these models provide reasonable solutions for blood velocity profiles, Chandran et al. [118] highlight several assumptions that can limit their direct applicability to physiological conditions. They include: (*i*) laminar flow, which is generally valid except during peak systole or in pathological regions; (*ii*) Newtonian fluid behaviour, an approximation that breaks down at low shear rates or

in the microcirculation where shear-thinning occurs; (*iii*) uniform cylindrical geometry, despite natural vessel tapering and branching; (*iv*) fully developed flow, neglecting entrance effects and curvature; (*v*) absence of reflected waves from geometric discontinuities; (*vi*) thin-walled tube approximation, which may not hold for vessels with $h/R > 0.1$; and (*vii*) homogeneous, isotropic, Hookean wall material, whereas real arterial walls are anisotropic and non-linear. In the context of the phantom experiments, these limitations imply that while the analytical predictions capture the main trends in how pressure gradients respond to changes in volume between sensors, additional factors – such as wall thickness ratio, material non-linearity, and wave reflections – could further influence the measured response.

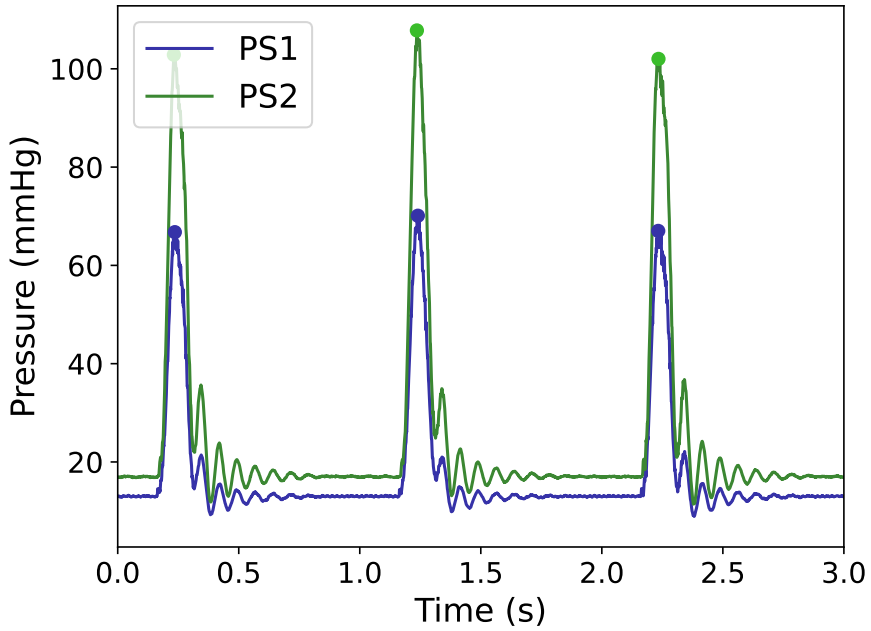

Figure 4.7: *Pressure waves detected with inline pressure sensors at a separation of 30 cm, with tube radius $r = 3$ mm.*

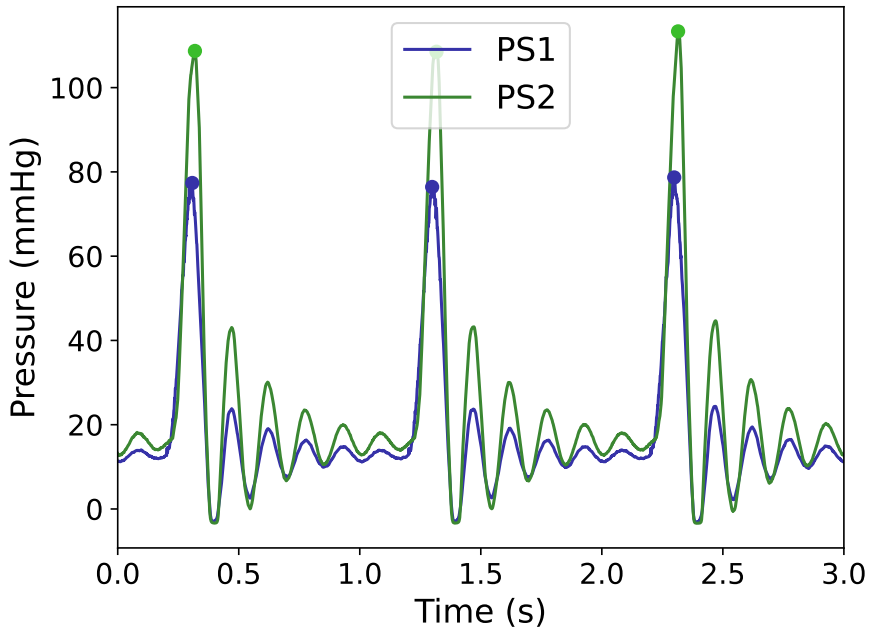

Figure 4.8: *Pressure waves detected with inline pressure sensors at a separation of 120 cm, with tube radius $r = 3$ mm.*

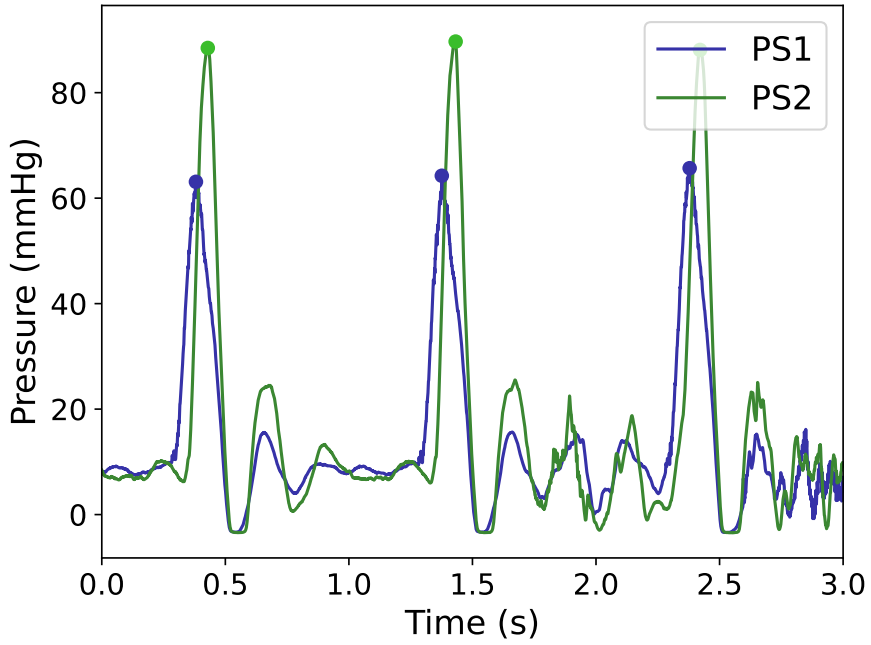

Figure 4.9: *Pressure waves detected with inline pressure sensors at a separation of 240 cm, with tube radius $r = 3$ mm.*

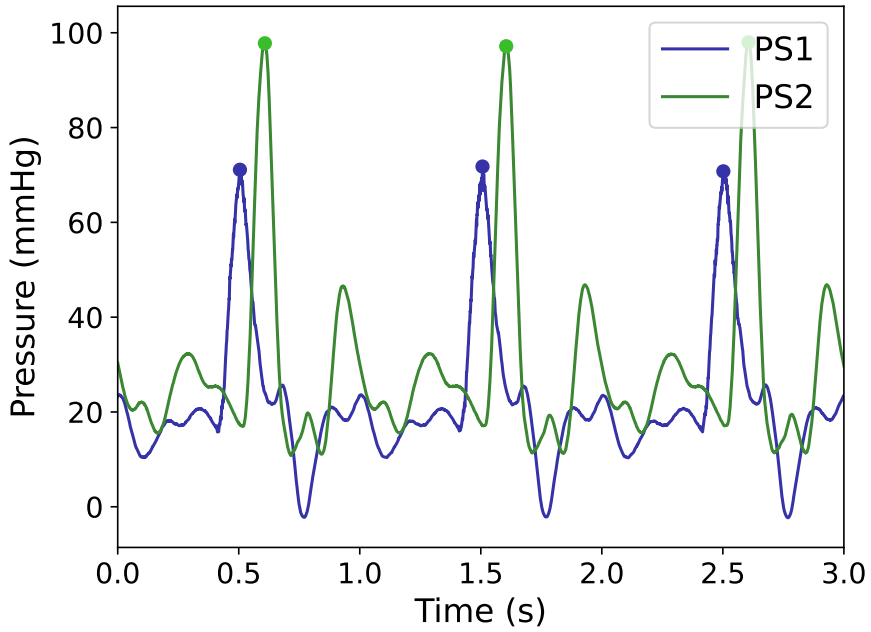

Figure 4.10: *Pressure waves detected with inline pressure sensors at a separation of 480 cm, with tube radius $r = 3$ mm.*

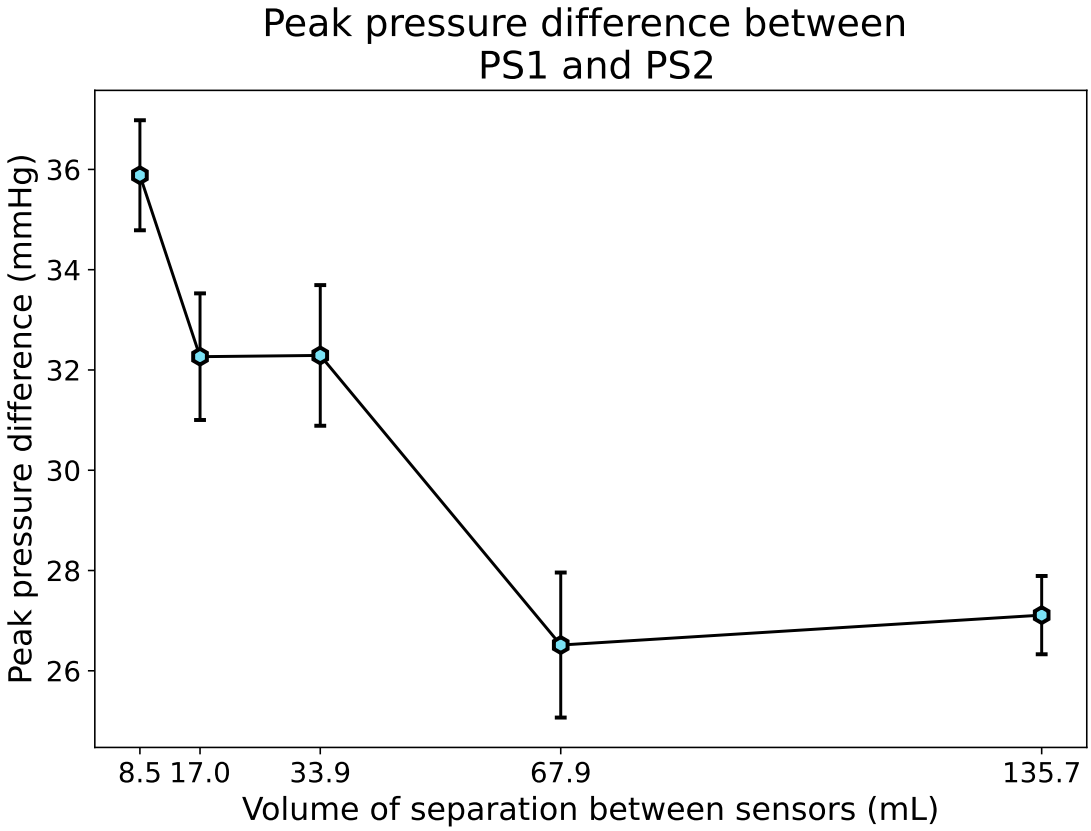

Figure 4.11: *Pressure gradient measured at different tube lengths/volumes of separation between the 2 inline pressure sensors. Increasing the tube length between inline pressure sensors in the phantom (30-480 cm, 8.5-135.7 mL) decreased the measured peak pressure difference, consistent with analytical predictions for oscillatory flow in elastic tubes [118]. Shorter tubes exhibited higher axial pressure gradients due to reduced viscous and elastic storage effects, while longer, more compliant segments lowered the instantaneous pressure drop. This behaviour aligns with Moens-Korteweg, Womersley, and Morgan-Kiely models, which link wave speed, viscosity, and wall elasticity, and predict a phase shift between pressure and velocity. Model assumptions include laminar Newtonian flow, uniform cylindrical geometry, fully developed flow, absence of reflections, thin-walled tubes, and homogeneous Hookean walls.*

4.2.2 PTT measurements

The Pulse Transit Time at different separations (30 cm, 60 cm, 120 cm and 240 cm) between each two pairs of sensors (inline pressure sensors and FBG-cantilever patch sensors) was measured. The PTT between the inline pressure sensors serves as a reference to the PTT measured with the FBG-cantilever patch sensors. Figures 4.9 shows a window of 3 seconds of the pressure waves detected in the cardiovascular phantom with inline pressure sensors, while Figure 4.12 shows a window of 3 seconds of the pressure waves detected in the cardiovascular phantom with the FBG-cantilever sensors, both using the tubing length of 240 cm to separate both pairs of sensors.

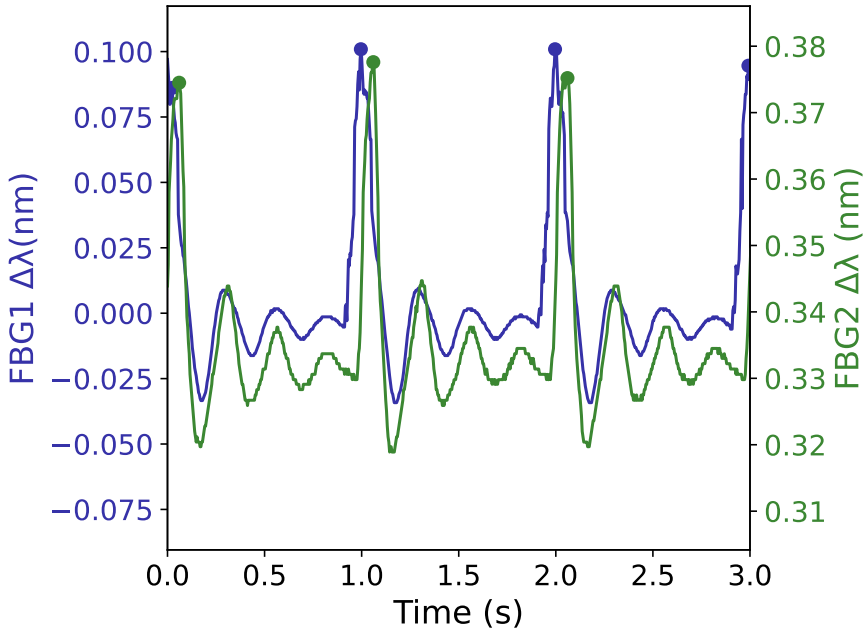

Figure 4.12: *Pressure waves detected in the cardiovascular phantom with a volume of 68 mL between each set of sensors, recorded by both FBG-cantilever sensors (FBG1 and FBG2).*

Figure 4.13 shows the different PTT values obtained by changing the distance between inline pressure sensors (Figure 4.13a) and between FBG-cantilever patch sensors (Figure 4.13b). Both plots show an increasing trend when the separation distance is increased, which reflects the decrease in phantom pressure as the compliant volume between sensors increases. Moreover, a linear relationship begins

to emerge when the separation exceeds 60 cm (hard pipe $r = 3$ mm). The measurements with the inline pressure sensors appear more consistent, as indicated by their smaller error bars compared to the larger variability observed with the FBG-cantilever sensors.

PTT measurements as a function of separation length were further explored by increasing the number of data points in the cardiovascular phantom (Figure 4.14a). A clearer trend was captured, showing that PTT values increase as system pressure decreases and gradually stabilise. Additionally, PTT was measured by fixing the separation length and instead increasing the voltage of the electrical pulse driving the pump (Figure 4.14b). In this case, higher driving voltages increased the intraluminal pressure and resulted in shorter PTT values. These observations are consistent with the theoretical framework described in Equation can: according to the Moens-Korteweg and Hughes formulations, increasing pressure raises effective wall stiffness and wave velocity, thereby shortening PTT and demonstrating the expected inverse pressure-PTT relationship.

Physiological PTT measured in vivo are typically on the order of only a few tens of milliseconds when assessed over short arterial segments. For example, Wang et al. [74] reported a mean PTT of approximately 29 $\pm$ 1 ms for the cubital fossa-to-wrist radial artery segment (268 mm separation), corresponding to a local pulse wave velocity of 9.25 $\pm$ 0.33 m/s in healthy young subjects. Across several volunteers, the reported PWV range of 9-15 m/s translated into PTTs of roughly 18-28 ms for a forearm-length arterial path. More generally, assuming peripheral arterial PWVs of 6-12 m/s and path lengths of 25-35 cm, forearm PTTs are expected to lie between 20 and 60 ms. In contrast, the cardiovascular phantom employed in this work yielded PTTs ranging from 10 ms up to 70 ms depending on tube length, injected volume, and driving conditions, which are within the same order of magnitude as physiological values, albeit often prolonged due to the lower stiffness and simplified structure of the phantom tubing. This comparison highlights that the phantom is able to reproduce physiologically relevant temporal

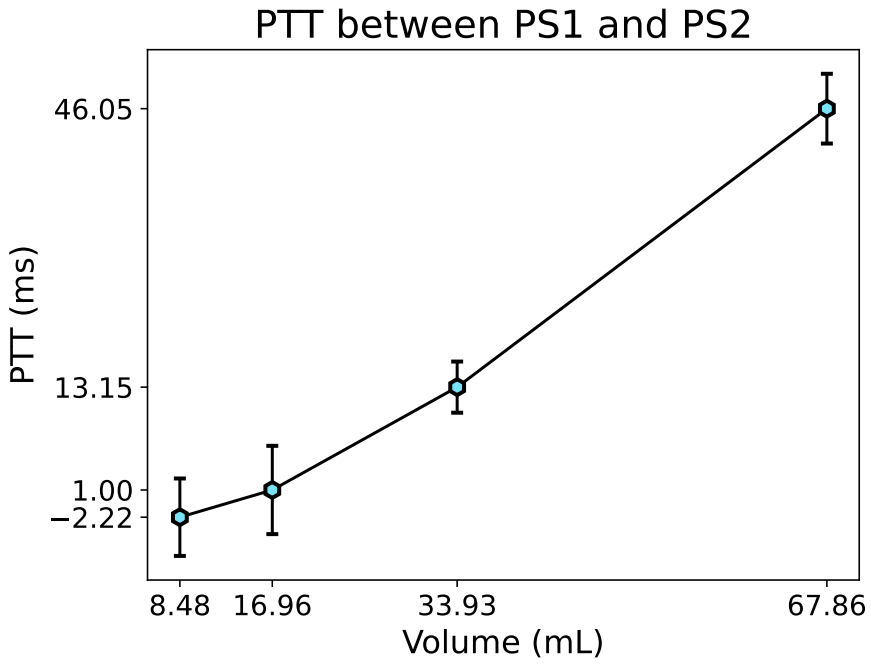

(a)

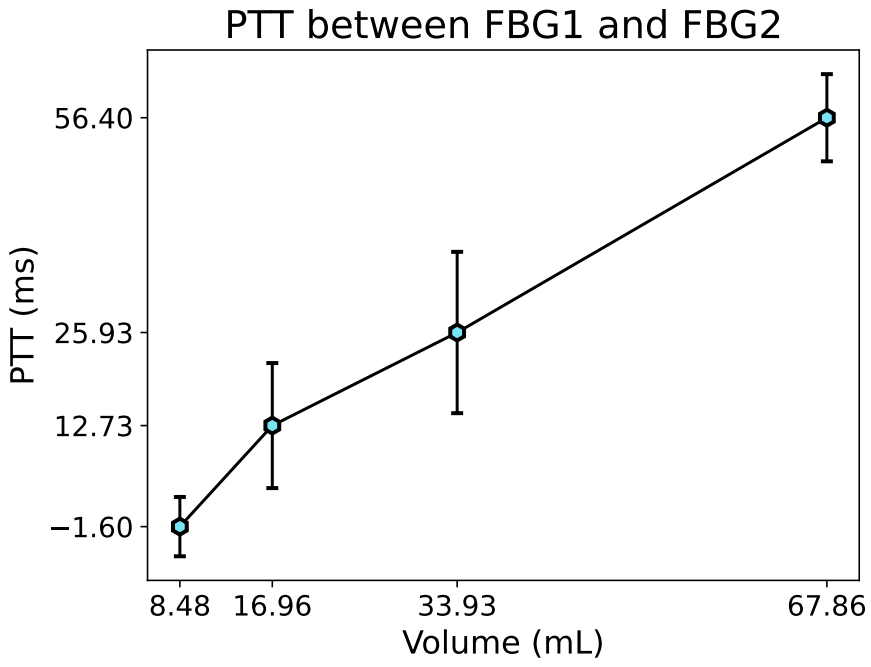

(b)

Figure 4.13: *Pulse Transit Time varying the distance separation between the two inline pressure sensors (a) and the two FBG-cantilever patch sensors (b). Both graphs show an increasing trend when the separation was increased. The volume between each set of sensors was increased from 8.48 - 67.86 mL using different lengths (30 cm, 60 cm, 120 cm and 240 cm) in the tube that separates the sensors.*

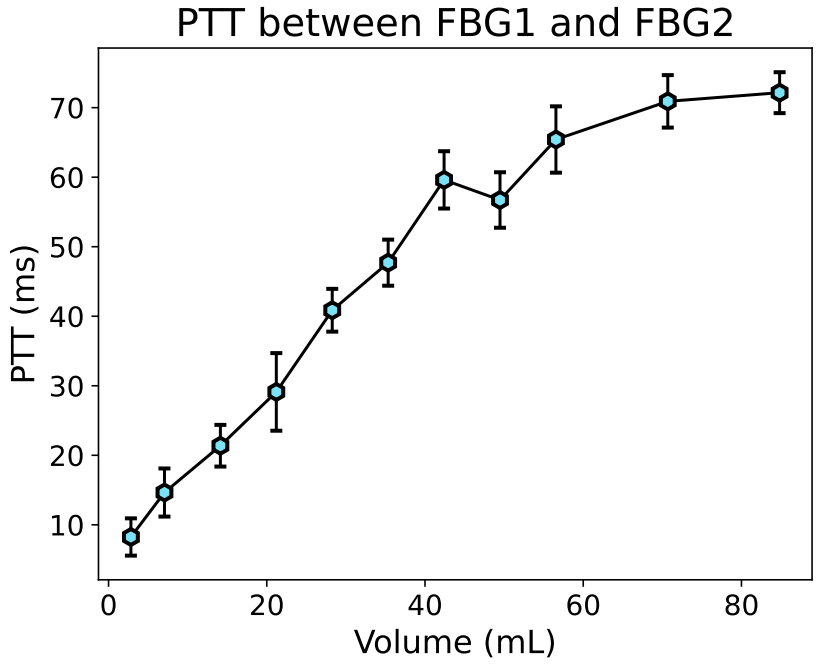

(a)

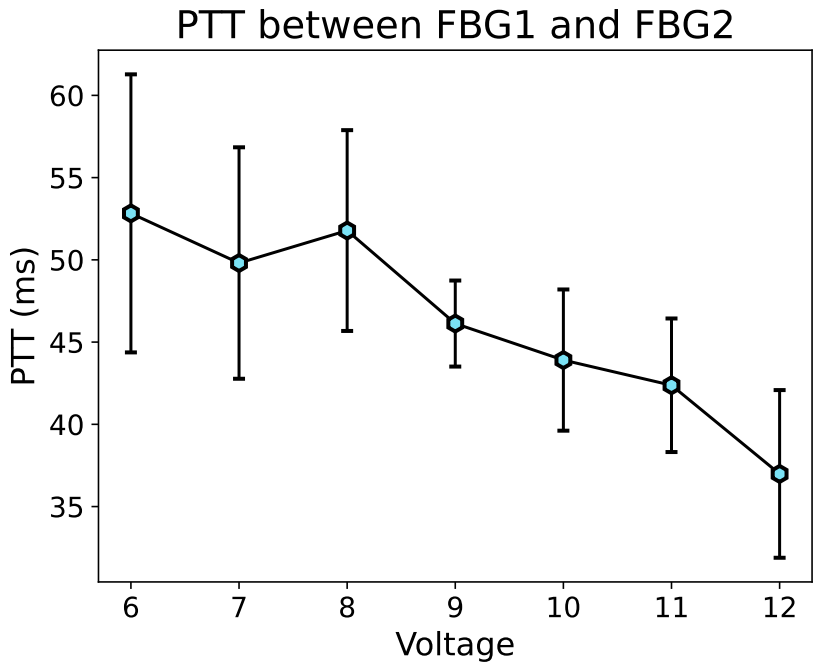

(b)

Figure 4.14: *(a) Pulse Transit Time at 11 different volumes of separation (up to 84.8 mL) between the FBG-cantilever sensors (FBG1 and FBG2). (b) Pulse Transit Time measured with the FBG-cantilever sensors (FBG1 and FBG2) by increasing the voltage across the motorpump from 6-12 V. The FBG-cantilever sensors were fixed 100 cm apart with a tube of radius = 3 mm.*

delays between distal pulse detections, while also offering controlled variability for method validation.

4.2.3 Testing FBG-cantilever sensors before human trials

PTT measurements using miniature interrogator

Figure 4.15 illustrates the PTT measurements obtained with the last iteration of FBG-cantilever sensors (FBG1 and FBG2) placed over the flexible tubing and using the miniature interrogator FiSpecX100. The PTT values were obtained by calculating the time difference between the two peaks of the pressure wave detected by each FBG sensor.

The results demonstrate that the FBG-cantilever sensors using the miniature interrogator FiSpecX100 were able to detect clear pulsatile waveforms in the tubular phantom, enabling the estimation of pulse transit time (PTT). As shown in Figure 4.15a, both sensors captured periodic pressure pulses, although with different amplitudes, reflecting variations in sensitivity and local loading conditions. The derived PTT values in Figure 4.15b predominantly fall within the range of 70-120 ms, which is consistent with physiologically plausible values reported in the literature. Nonetheless, the scatter and presence of outliers highlight experimental variability, likely arising from the weak pulsatile signal detected by FBG2. These findings confirm the feasibility of using FBG-cantilever sensors for PTT measurement in a controlled phantom environment, while also underscoring the challenges of obtaining accurate PTT values when pulse amplitudes are shallow due to damping effects.

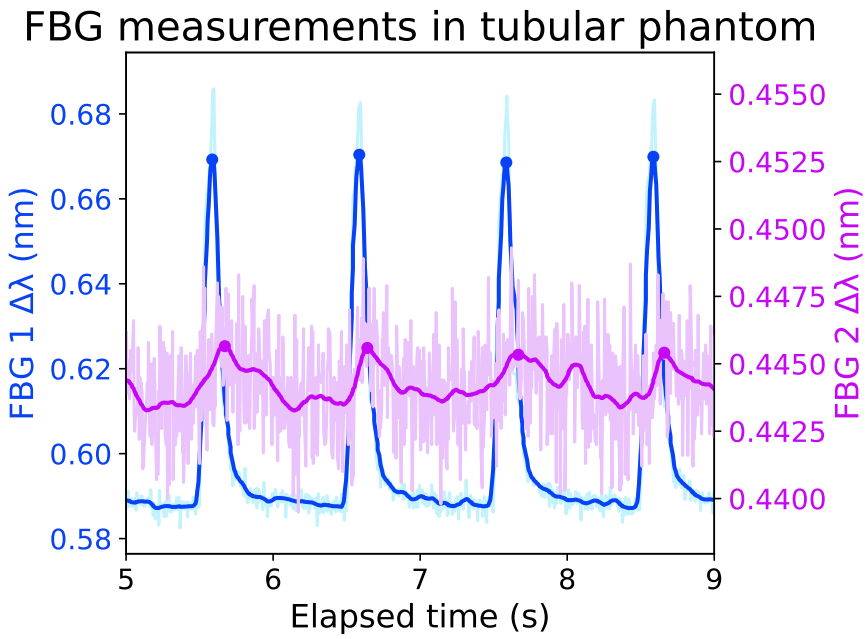

(a)

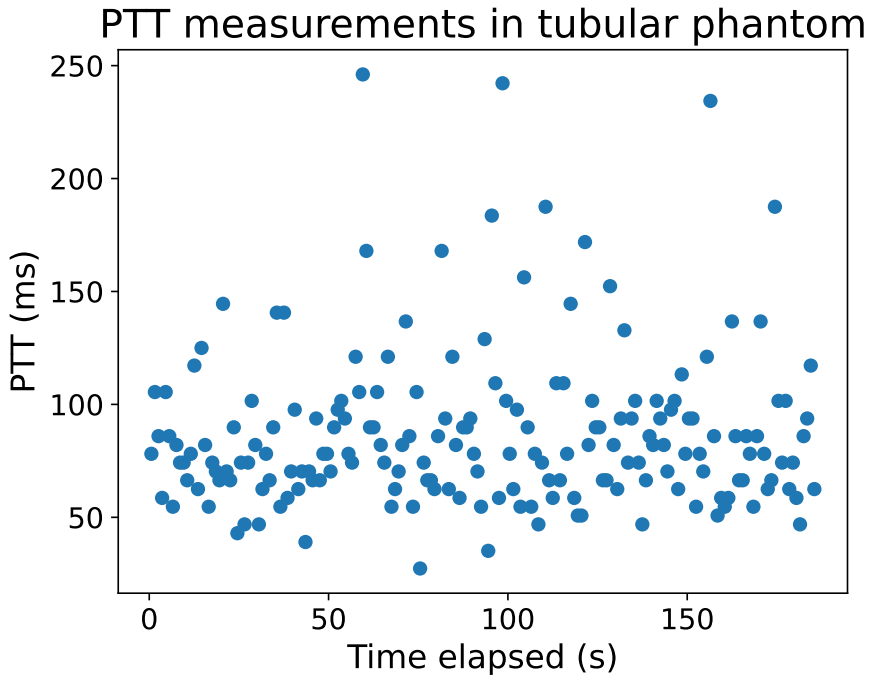

(b)

Figure 4.15: *PTT measurements in the tubular phantom. a) Pressure waves detected by the FBG-cantilever sensors (FBG1 and FBG2). b) PTT values obtained from the pressure waves detected by the FBG-cantilever sensors.*

PAT measurements

Figure 4.16 depicts the electrical signals and FBG-mechanical signals detected from the phantom. The noise perceived in the electrical signal is due to the resistors of the attenuator.

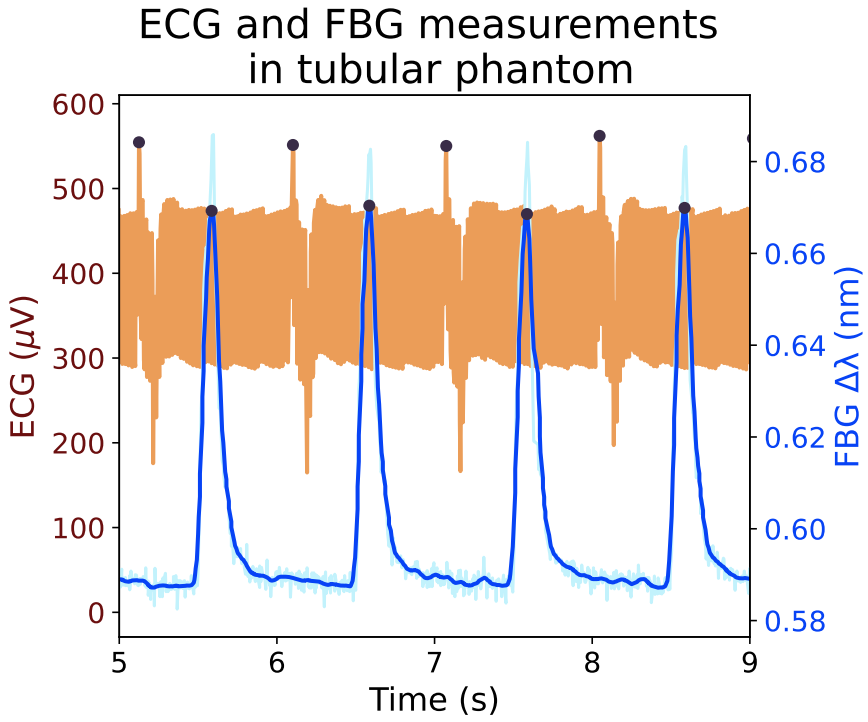

Figure 4.16: *Electrical signal (orange) and FBG-mechanical signal blue (detected in the tubular phantom for PAT measurements.)*

Once these signals were detected, the time difference between them was extracted to obtain PAT. Figure 4.17 shows the PAT obtained. The increasing trend of these PAT measurements in Figure 4.17a are due to a systematic error in the acquisition stage of the electrical device, that causes a drifting between ECG and FBG data acquisition. This was compensated in Figure 4.17b by interpolating a hyperplane – the straight line that models this error – and by subtracting this hyperplane from the raw PAT measurements. $y = 0.026 \times x$. The calibrated PAT values were obtained by subtracting the estimated systematic error from the raw measurements, as given by:

$$\mathrm{PAT}_{\mathrm{calibrated},i} = \mathrm{PAT}_i - (0.026 \times t_{\mathrm{ECG},i}) \,, \tag{4.2}$$

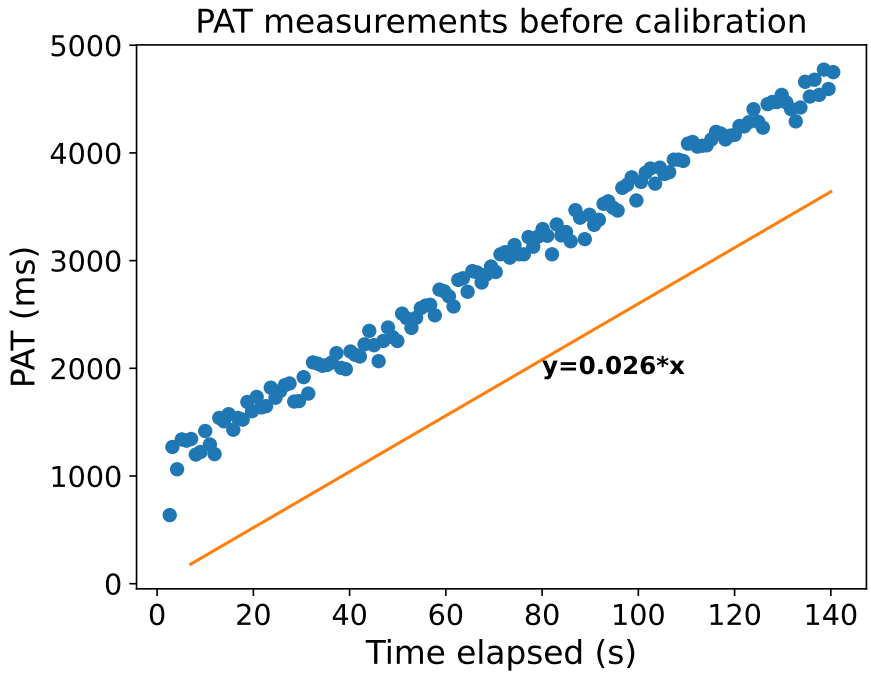

(a)

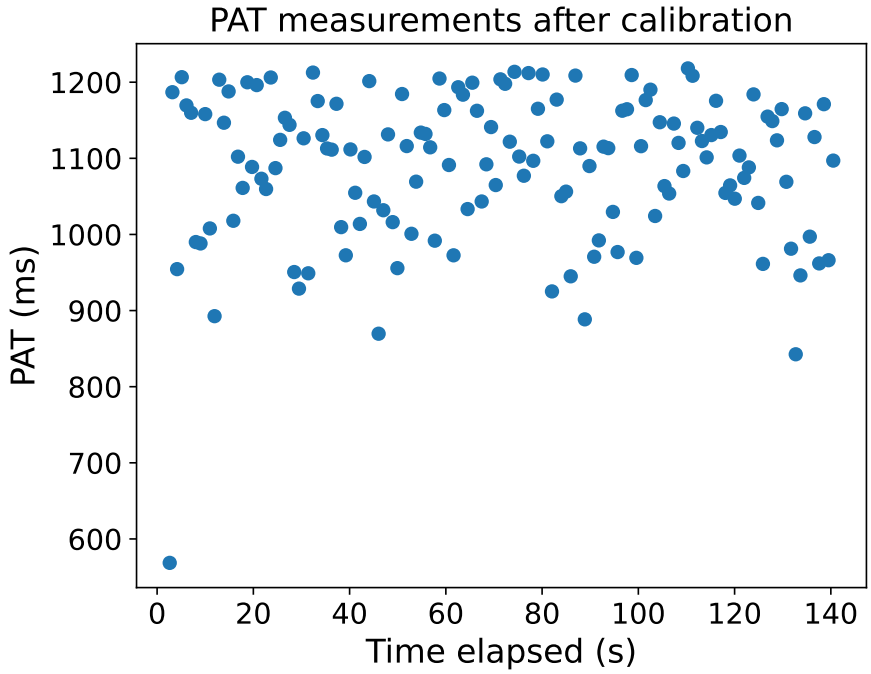

(b)

Figure 4.17: *PAT measurements in tubular phantom. a) PAT measurement with the effect of desynchronisation. b) synchronisation by subtracting the interpolated hyperplane (desynchronisation effect) to the PAT values.*

where PAT_i is the raw pulse arrival time for beat i, $t_{\text{ECG},i}$ is the timestamp (in milliseconds) of the corresponding ECG peak, and $0.026 \times t_{\text{ECG},i}$ represents the systematic error modelled as a straight line (slope = 0.026) fitted to the raw PAT.

These PAT results (Figure 4.15b) highlight the limitations of this model in reproducing the full physiological range. While physiological PAT values are typically on the order of hundreds of milliseconds [119], the phantom provides only an approximate representation of such dynamics. Nevertheless, the ECG and FBG signals exhibited sharp and well-defined peaks (Figure 4.16), indicating good measurement accuracy at the sensor level. Importantly, these results serve as a first step in identifying systematic errors inherent to the time synchronisation of the acquisition systems and emphasize the necessity of appropriate post-processing strategies to ensure reliable PAT assessment in human studies.

4.3 Summary

The cardiovascular phantom experiments provided a controlled framework to validate the FBG-cantilever sensing system, fulfilling the PoC testing goal described in Section 2.5, namely, the construction of a phantom for systematic validation prior to human studies. By varying tube lengths, obtaining a separating volume higher than 8.5 mL, the phantom demonstrated the expected haemodynamic behaviour: increasing tube length stretched the pressure waveforms and reduced the instantaneous pressure gradient, in agreement with analytical formulations of oscillatory flow in elastic tubes [118]. These models predict phase shifts between pressure and flow due to inertial effects, and a reduction in pressure drop with greater compliant volume – both trends experimentally confirmed in the phantom. Furthermore, the PTT trends observed here were consistent with the theoretical predictions from Equation 1.2: both the Moens-Korteweg formulation and the Hughes equation indicate that rising intraluminal pressure stiffens the vessel wall, increases wave velocity, and consequently shortens PTT. Together, these findings demonstrate that the phantom reproduces the key physical mechanisms underlying pressure-flow interactions, while also serving as a controlled platform to experimentally

verify fundamental haemodynamic models.

Within this framework, the phantom enabled simultaneous PAT and PTT assessments. For PTT, the extracted values (10 - 70 ms) were consistent with physiologically plausible ranges, validating the ability of the sensing system to track controlled changes in pressure transmission. In contrast, PAT values were not fully representative of in vivo conditions, since the phantom cannot reproduce the full temporal complexity of cardiovascular dynamics. Nevertheless, the sharp peaks observed in both ECG and FBG signals demonstrated accurate temporal resolution of PAT values. These PAT experiment also provided insight into systematic measurement errors and the post-processing strategies needed for reliable PAT extraction in humans.

The FBG-cantilever sensing system proposed in Chapter 3, integrated with the miniature interrogator, was experimentally tested in this cardiovascular phantom. This setup allowed the combined evaluation of the sensor design and interrogation approach under controlled haemodynamic conditions, providing a practical demonstration of the system's functionality prior to in vivo studies.

Therefore, the work presented in this chapter achieves the second stated thesis objective, *"To construct a cardiovascular phantom for controlled validation of the FBG-cantilever sensing system"*, by providing a physically controlled validation platform prior to human testing.

5. Human Volunteers studies and Blood Pressure regression model

This chapter builds on the cardiovascular phantom validation presented previously, extending the investigation to human volunteers. Having established the feasibility of FBG-cantilever sensors for PTT and PAT estimation in a controlled environment, the next step is to evaluate their performance under physiological conditions. Specifically, this chapter reports blood pressure measurements in human participants, focusing on (i) extracting PTT using two FBG-cantilever sensors and (ii) estimating PAT using an FBG-cantilever sensor combined with ECG recordings.

The study was approved by the Ethics Committee of the University of Nottingham (see Appendix E). BP was modulated through exercise on a cycle ergometer, in line with the ESH consensus recommendations to track BP changes [120]. This physiological response also induced an increase in heart rate (HR) and is discussed in Section 1.2. Briefly, muscular activity during exercise is detected by proprioceptors, which signal the cardiovascular center to activate the sympathetic nervous system. The sympathetic response elevates HR by increasing cardiac contractility and causes vasoconstriction, thereby raising BP.

Finally, this chapter introduces the implementation of a Multitask Gaussian Process Regression (GPR) model to SBP and DBP values from PAT measurements.

The novelty of this work lies in the first human validation of the FBG-cantilever sensing system for blood pressure monitoring, demonstrating the feasibility of deriving physiologically relevant PTT and PAT measurements during exercise. Furthermore, the integration of a multitask GPR model for BP estimation marks an important step toward cuffless, non-invasive monitoring.

In doing so, this chapter validates the proposed sensing system's capacity to track physiological blood pressure changes, addressing a critical concern in the development of cuffless BP monitoring technologies [24].

5.1 Methods

5.1.1 Experimental set up

The experimental setup of these measurements consisted of recording of ECG signals at the chest using the custom-made ECG recorder (See Appendix A), and the detection of the mechanical pulses with the FBG-cantilever sensors and the fibre optical interrogator FiSpecX100 (FiSens, Germany) described in Chapter 3 at the left wrist and upper arm in healthy participants. As it is aimed to investigate the correlation between the PTT and PAT measurements derived from ECG and FBG signals with BP values, a non-invasive BP (NIBP) monitor (OMRON X2 Smart+, Omron, Japan) was used to measure SBP, DBP and HR. Figure 5.1 depicts the experimental set up with the human subject sitting on an exercise cycle(Domyos VM740,Decathlon, France) with all the sensors attached.

ECG electrodes (V+ (red), V- (gray) and RLD/GND(black) (Figure 5.1)) were placed on the chest with a minimal separation distance between (< 3 cm) in a triangular configuration to obtain an input amplified signal < 2.5 V, where the voltage ADC range varies from 0 to 2.5 V. The FBG-cantilever sensor (FBG1) was placed at the left wrist aiming to detect the mechanical pulse generated by the radial artery. The second FBG-cantilever sensor (FBG2) was located at the upper arm following the same arterial line along the brachial artery and its bifurcation

to radial and ulnar arteries.

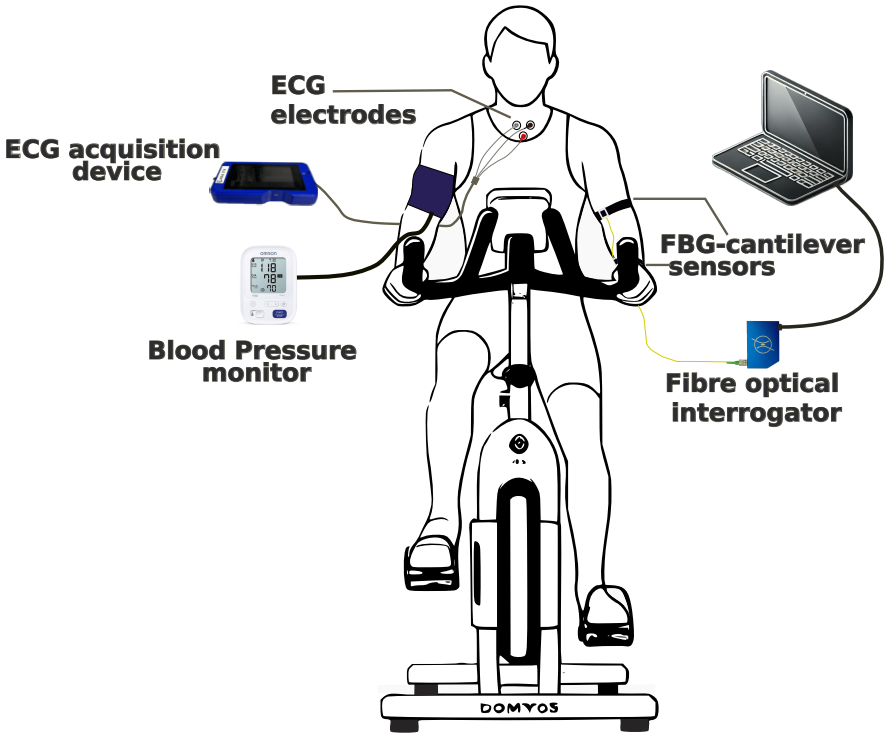

Figure 5.1: *Human volunteer experiment set up. ECG electrodes were placed at the subject's chest and the FBG-cantilever sensors were placed at the wrist (FBG1) and at the upper-arm (FBG2). The BP monitor cuff was placed on the right upper arm.*

5.1.2 Measurement protocol

The protocol for the data acquisition consisted of subjecting the participant to a physical activity that increases the HR and, as a consequence, the BP. At the beginning of the experiment the BP of the participant was monitored to reduce the "white coat effect". For the cycling activity the exercise intensity was fixed to 108 W with 60 turns per minute. The NIBP readings include SBP and DBP along with HR.

Figure 5.2 shows the 3 different consecutive scenarios of the physical activity that the participant undertook and the cases when the data was acquired.

The Scenario 1 of measurements was performed with the participant sitting on a

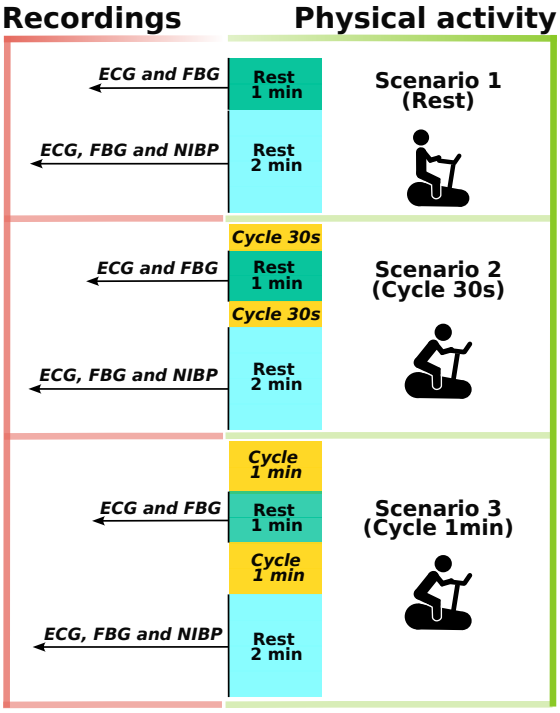

Figure 5.2: *Measurement protocol for Cuffless Blood Pressure measurements on human volunteers. This protocol involved 3 consecutive different scenarios increasing the physical activity of the subject, aiming to increase the HR and in turn the BP with the subject cycling. 2 sets of measurements were obtained in each scenario in the resting states. One set recording only ECG and FBG signals for 1 min and the second set recording ECG, FBG and NIBP for 2 min (2min of NIBP measurements gives 3 discrete readings, each reading with a SBP, DBP and HR value).*

cycle in a resting state (without cycling). Two sets of measurements were recorded in this scenario. The first set of measurement consisted of recording ECG and FBG signals for 1 min, and the second set of measurements consisted of recording for 2 min ECG and FBG signals along with 3 NIBP recordings. For the following Scenario 2, another two sets of measurements were recorded. The first set of measurements recorded ECG and FBG signals with the participant in a resting state for 1 min after the participant cycled for 30 s, and the second set of the measurements recorded ECG and FBG for 2 min along with 3 NIBP readings of the participant in a resting state after cycling again 30 s. Finally, in Scenario 3, two sets of measurements were also recorded. The first set involved recording ECG and FBG participant signals in a resting state for 1 min after the participant cycled for 1 min. The second set consisted of recording ECG and FBG signals for 2 min along with 3 NIBP readings of the participant in a resting state after the subject cycled again another minute.

Notes:

- 2 minutes of measurements at rest allowed at least 3 NIBP readings with the OMRON device.
- The FBG and ECG recordings were sampled at 200 Hz. All measurements were performed only in rest positions.
- The motivation of recording 2 sets of measurements for each scenario was to increase the likelihood of getting high-quality data, where it was assumed that the inflation of the pressure cuff could affect the steadiness of the ECG and FBG signals.

5.1.3 Data processing

The data processing involved several stages to obtain the Pulse Arrival Time (PAT) and Pulse Transit Time (PTT) values. Different stages were included as the signals acquired from human volunteers are more prone to artifacts compared

to those from the cardiovascular phantom shown in Section 4.2. These stages included time synchronisation, filtering, signal quality assessment, and peak detection of the ECG and FBG signals pipeline (Figure 5.3), the PAT values were further calibrated due to the drift in the FBG signals. This drift between ECG and FBG occurred due to a systematic error in the acquisition stage of the electrical device.

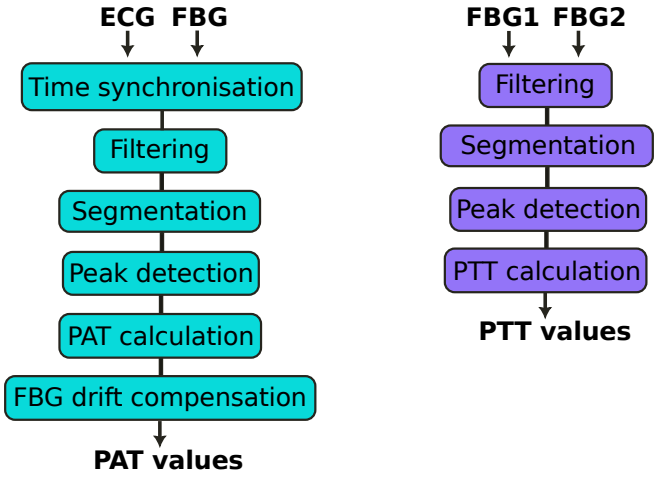

Figure 5.3: *Data processing pipeline for Pulse Arrival Time (PAT) and Pulse Transit Time (PTT).*

Time synchronisation. Since the ECG and FBG signals were sampled using different devices the signals were aligned using the timestamp generated in each raw data file (for ECG and FBG measurements). Following this, two time vector arrays (time elapsed) in milliseconds for each type of signal were calculated since the start of the measurements.

Filtering. ECG and FBG signals were filtered using the BioSPPy libraries for ECG and PPG signals [121]. For the ECG signals, this library a Butterworth bandpass filter with low cutoff: 0.5 Hz and a high cutoff: 45 Hz. The lower range (0.5 Hz of the cutoff frequency) removed the DC amplitude and baseline wander, meanwhile the upper range reduces the power line interference, but preserves

the ECG waveform (P, QRS and T waves). In the case of the FBG signals, the Butterworth bandpass filter uses a low cutoff frequency: 0.5 Hz and high cutoff frequency: 8 Hz with zero-phase filtering (via scipy.signal.filtfilt) – this conditioning compensates the FBG wavelength shift due to temperature described in Section 3.1.4. Additionally, a moving average filter was applied to the FBG signals with a window size of 10 data points. The frequency range for the bandpass filter is chosen since pulsatile signals like PPG, and in this case FBG have most of their relevant information in this bandwidth. Figures 5.4-5.6 illustrates the examples of filtering FBG1 signal at the wrist (a), FBG2 signal at the upper arm (b) and ECG signal at the chest (c).

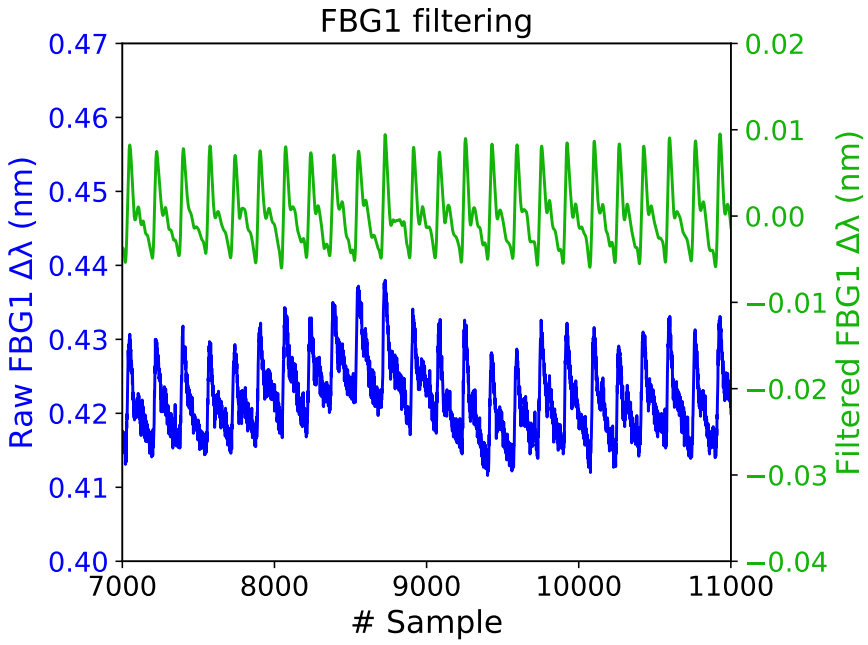

Figure 5.4: *Example of filtering stage of FBG1 signal at the wrist.*

Segmentation. Even though good quality data was recorded in most of the participants, the start and end of the recordings tended to be corrupted in each recording, since the subject moves before and after each recording. Processing a recording together with a corrupted segment (at the beginning or in the middle of the recording) for PTT and PAT can cause an incorrect peak detection, which in turn generates an incorrect pair of peaks of the recording. This affects a range

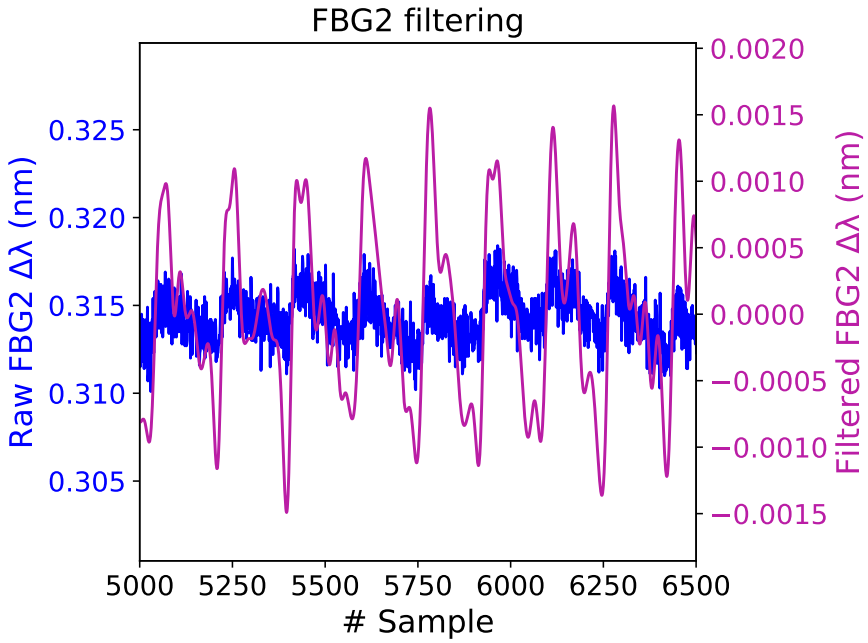

Figure 5.5: *Example of filtering stage of FBG2 signal at the upper arm.*

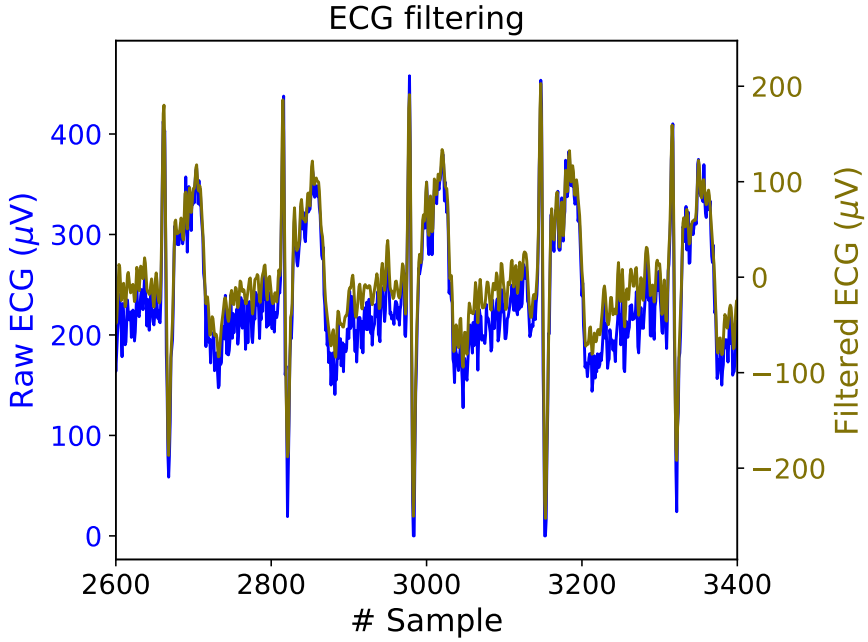

Figure 5.6: *Example of filtering stage of ECG signal at the chest.*

of PTT and PAT values as incorrect peak pairs are identified even though correct peaks are detected. Each recording was segmented for a reliable consecutive PAT and PTT calculation. The start and end of the segment were selected by visual inspection ensuring that high amplitude motion artifacts are not included and a pair of ECG and FBG signals (for PAT) and a pair FBG1 and FBG2 signals (for PTT) were preserved. An example of this visual inspection is depicted in Figure 5.7. This process involves a size reduction of the recording as all the segments after the segmentation will contain at least 40 s of data, with a target of 70 s to 140 s of data preserved.

Peak detection. Two different peak detection algorithms (for ECG and PPG signals) from the BioSPPy library were employed. For the ECG signals, the R-peak detection algorithm consisted of (i) differentiation of the filtered ECG signal, emphasizing rapid changes (steep slopes in the QRS complex), (ii) squaring to make all values positive and enhance the R peaks while suppressing the smaller fluctuations, (iii) moving average filter, (iv) adaptive thresholding to identify the candidate R peaks. Peaks are detected by locating maxima within candidate windows and a refractory period is applied to avoid detecting false or redundant peaks; (v) post-processing of the detected R peaks by verifying the minimum RR interval and signal morphology consistency. For the FBG signals, the PPG peak detection algorithm from BioSPPy was utilised since FBG and PPG signals share a similar waveform. The FBG peak detection algorithm consisted of (i) taking the first derivative to locate the regions of steep slope and local maxima; (ii) apply a threshold to eliminate small peaks caused by noise; (iii) find the true peak by identifying the local maximum. To avoid multiple peaks within a cardiac cycle, a minimum refractory period is enforced with a default value of 250 ms (corresponding to a maximum heart rate of 240 BPM). The detected peaks are post-processed, so they align the physiological features of PPG signals and its peak intervals within the expected heart rate variability. Both ECG peak and PPG peak detection algorithms were employed in the data processing pipeline for

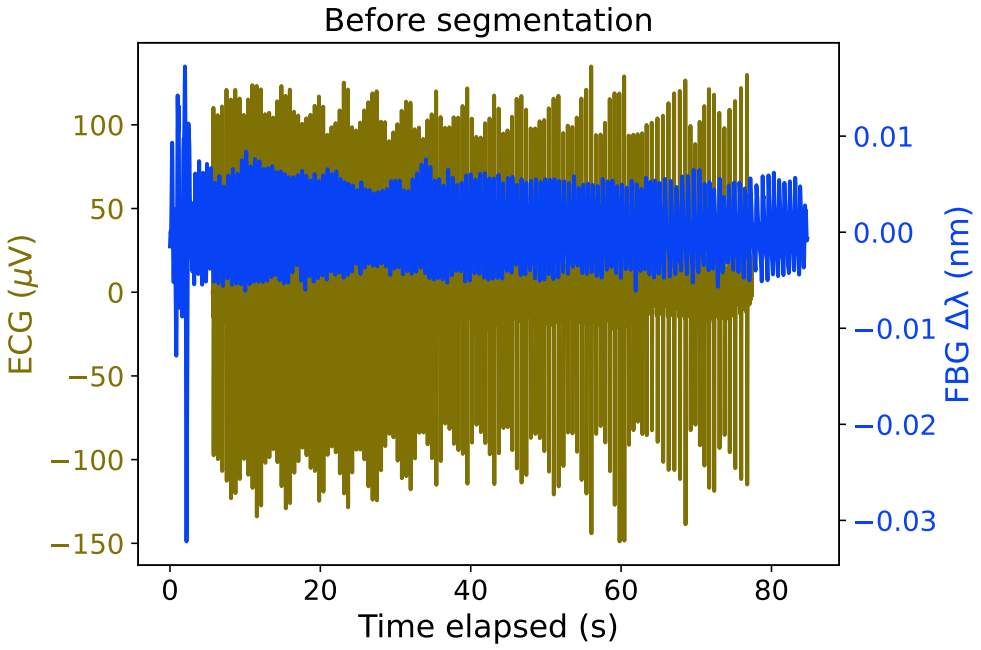

(a)

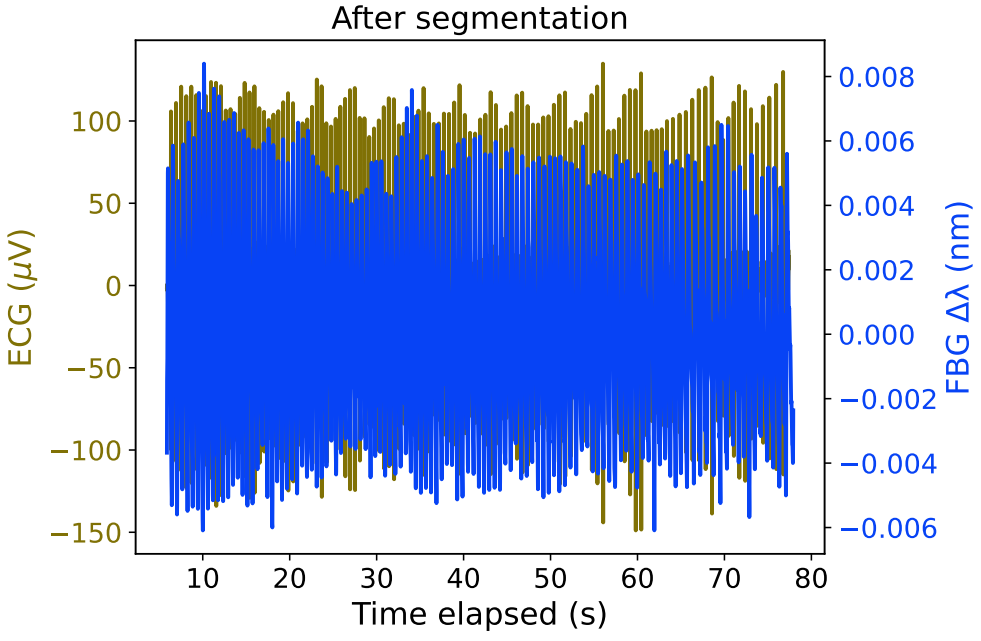

(b)

Figure 5.7: *Example of the segmentation process for PAT, removing the motion artifacts of high amplitude induced by changing to rest position or finishing the recording. (a) shows the FBG trace in blue where the recording lasts longer (220 s) than the ECG trace in brown (140 s). (b) After segmentation the resulting ECG and FBG traces are 130 s long.*

PAT, Figure 5.3. Only the PPG Peak detection algorithm was implemented in the data processing pipeline for PTT, Figure 5.3. Figures 5.8a and 5.8b show an example of the detected peaks for PAT and PTT.

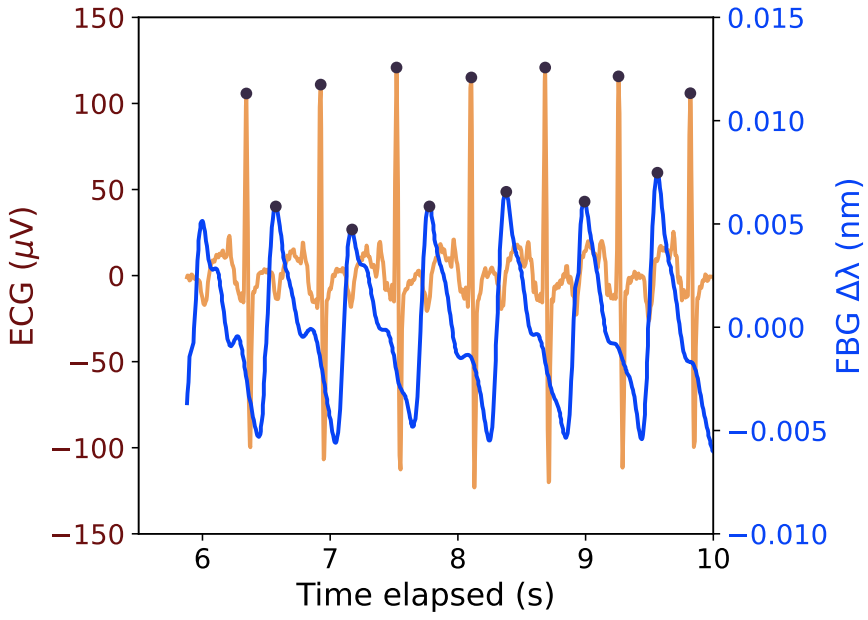

(a)

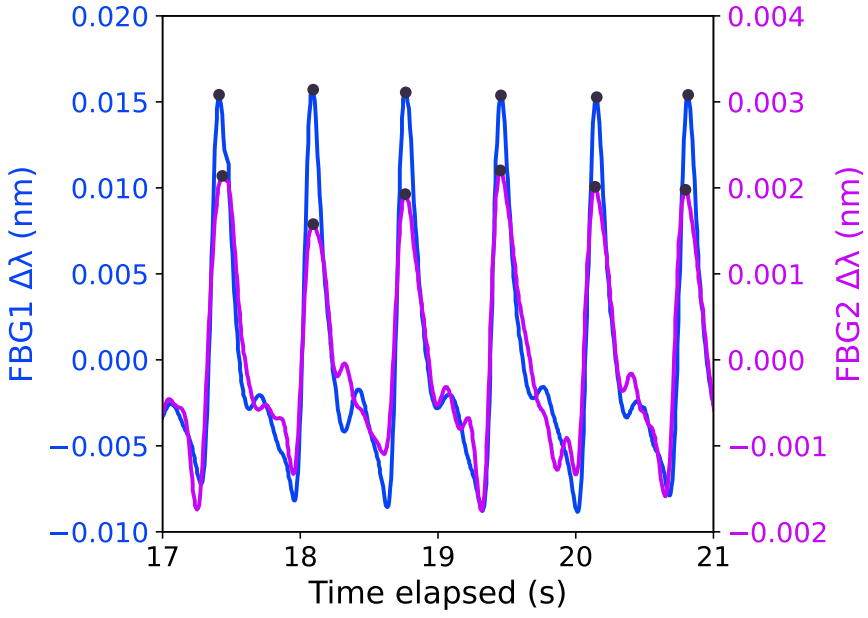

(b)

Figure 5.8: *Example of peak detection for PAT (a) and PTT (b).*

PTT calculation. In the case of the pulse transit time (PTT), from the selected segment with FBG1 (at wrist) and FBG2 (at upper arm) signals, the time t of appearance of the first peaks were assessed, so the PTT is calculated assuming

that the FBG2 peak at the upper arm arrives first.

$$PTT_n = t[\text{FBG1pk}_n] - t[\text{FBG2pk}_n] \tag{5.1}$$

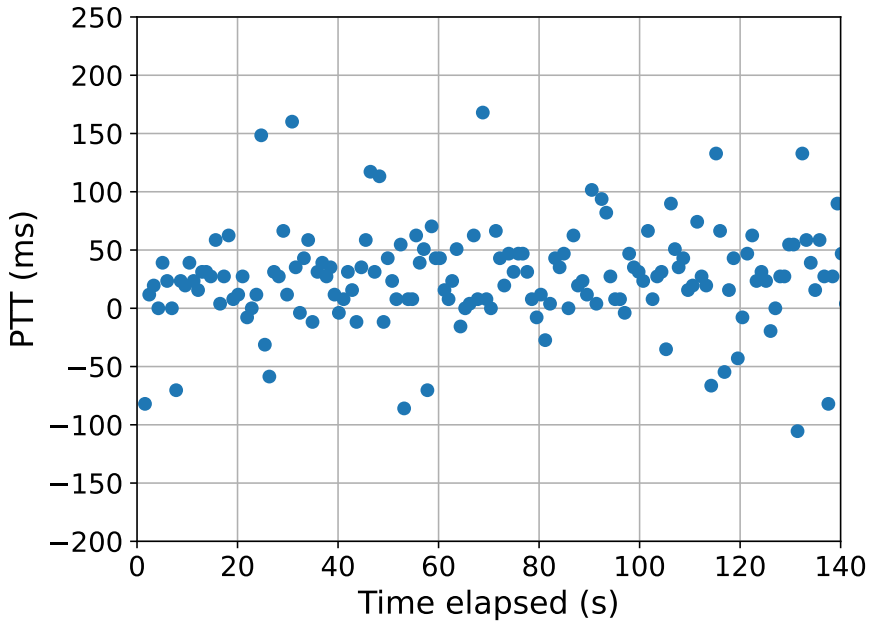

Figure 5.9: *Example of PTT values calculated on* ***volunteer 9*** *at rest (Scenario 1).*

PAT calculation. For the pulse arrival time calculation (PAT), from the selected segment with ECG and FBG signals, the time t of appearance of the first ECG peak and FBG peak were assessed, so the PAT is calculated assuming that the ECG peak comes first. Figure 5.10 explains how the ECG peak and FBG peak pairs should be chosen, assuming that the ECG signal comes first, as a previous FBG pulse can be present, but it does not mean that it belongs to the same cardiac cycle.

$$PAT_n = \begin{cases} t[FBGpk_{n+1}] - t[ECGpk_n], & \text{if } t[ECGpk_0] > t[FBGpk_0] \\ t[FBGpk_n] - t[ECGpk_n], & \text{if } t[ECGpk_0] < t[FBGpk_0] \end{cases} \tag{5.2}$$

FBG drift compensation. The FBG drifting phenomena was observed in the PAT measurements in the tubular phantom in the results Section 4.2. This re-

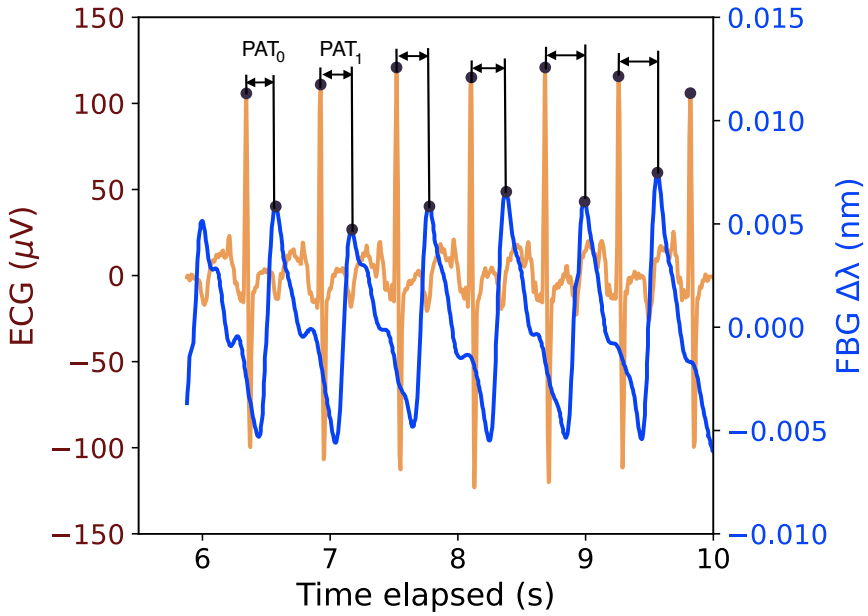

Figure 5.10: *Example of PAT calculation between ECG R peak and FBG peak. In this case an FBG pulse appears before an ECG pulse at the beginning of this segmented recording. Since it is assumed that the electrical pulse occurs before the mechanical pulse, the first FBG pulse detected by the device is not considered for the first PAT value (PAT_0), as it assumed that it belongs to a different cardiac cycle.*

sulted in a systematic error revealed as a linear increase of PAT values. This issue was compensated by interpolating and subtracting a hyperplane $y = 0.026 \times x$ which represents this trend. Figure 5.11a shows an example of this phenomenon, and Figure 5.11b shows the compensation of this systematic error by subtracting the calibrated hyperplane.

PAT and PTT post-processing. PAT and PTT values needed further refinement due to false positive and negative peaks when the FBG signal was corrupted by noise. These events were corrected manually, avoiding incorrect PTT and PAT values. Appendix B describes the examples of the cases of missed peaks and false peaks and how this affected the PAT and PTT values. The PAT and PTT values after this correction is also shown.

Violin plots.

To improve the assessment of the population of the obtained PAT and PTT in

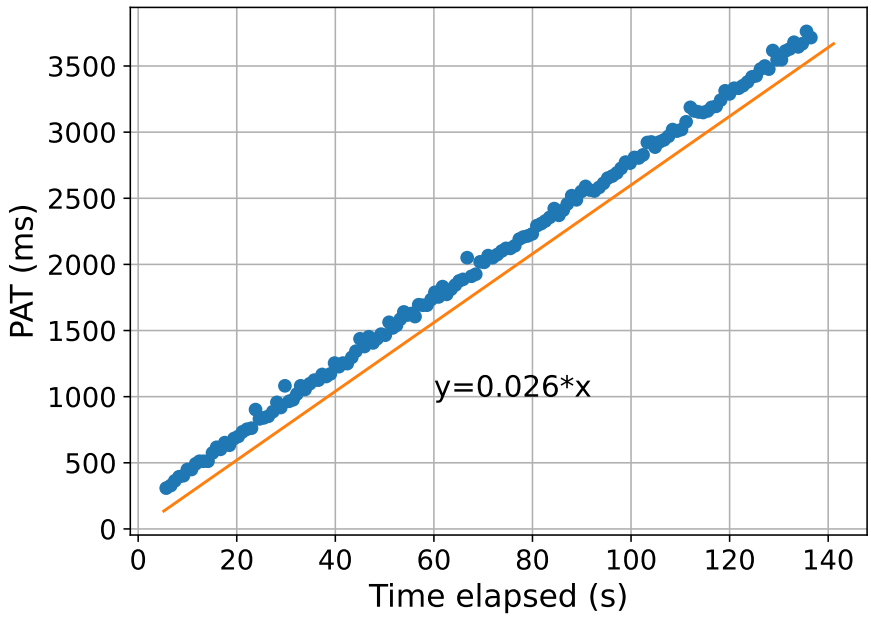

(a)

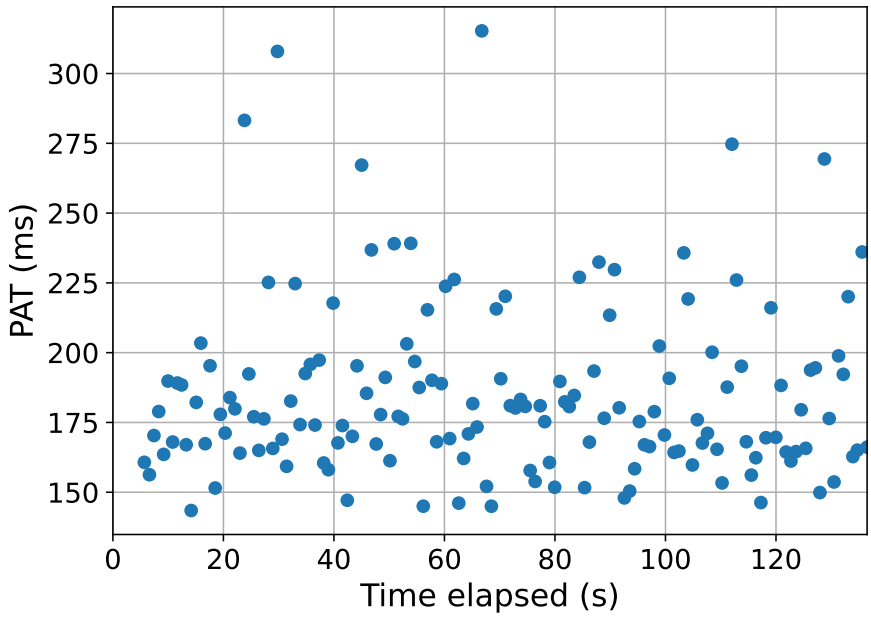

(b)

Figure 5.11: *Example of PAT values calculated on* ***volunteer 9*** *at rest (Scenario 1) (a) without subtracting the hyperplane (in red) generated caused by FBG signal drifting, (b) subtracting the hyperplane to the original PAT values.*

the different scenarios (rest, cycle 30 s and cycle 1 min). Figures 5.12-5.14 shows the example of PAT values at the different scenarios. The implementation of violin plots are proposed (Figure 5.15) to compare the data distribution, median, minimum, maximum values, as well as the outlier identification between scenarios. Figure 5.13 shows a cluster of PAT values below 200 ms that departs from a normal distribution, due to degradation of the signal quality during this interval. The corresponding violin plot in Figure 5.15 (cycle 30 s) confirms this pattern by displaying outliers under 200 ms. In Figure 5.14, two PAT values lie far from the remainder of the distribution; in the corresponding violin plot, these isolated points have negligible weight and are therefore not represented in the density envelope (appearing, at most, as individual outliers).

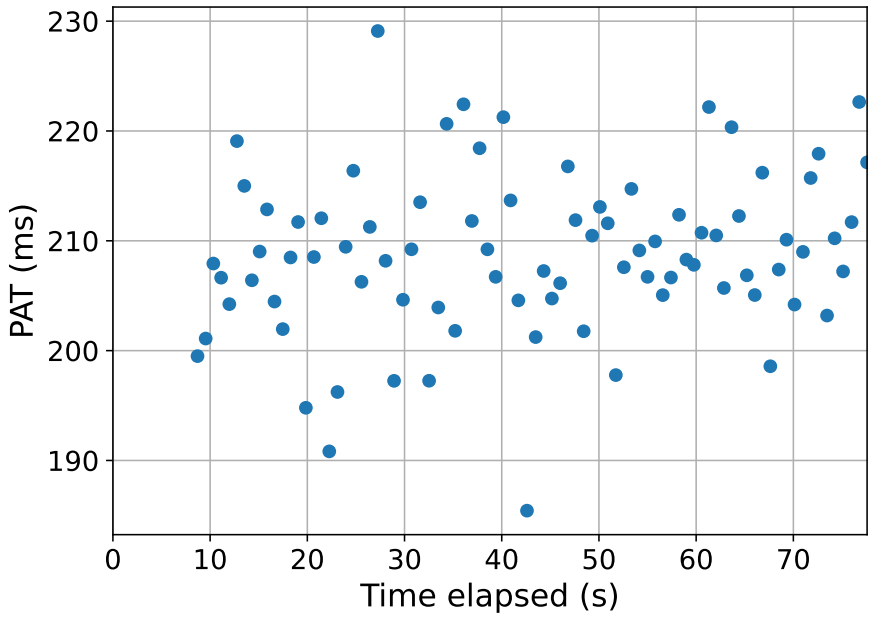

Figure 5.12: *Example of the obtained PAT values from the ECG and FBG recordings for subject 1 at rest.*

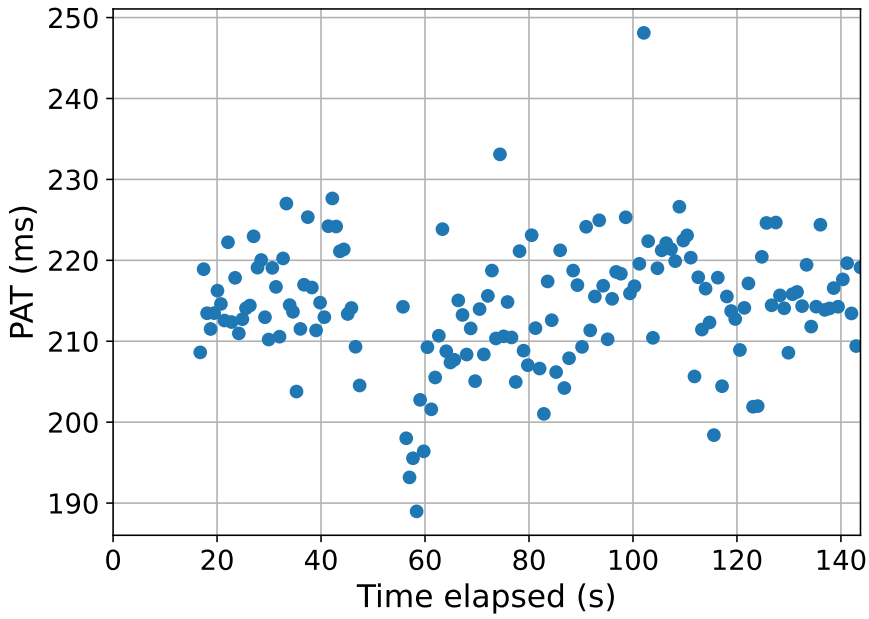

Figure 5.13: *Example of the obtained PAT values from the ECG and FBG recordings for subject 1 during cycling at 30 seconds.*

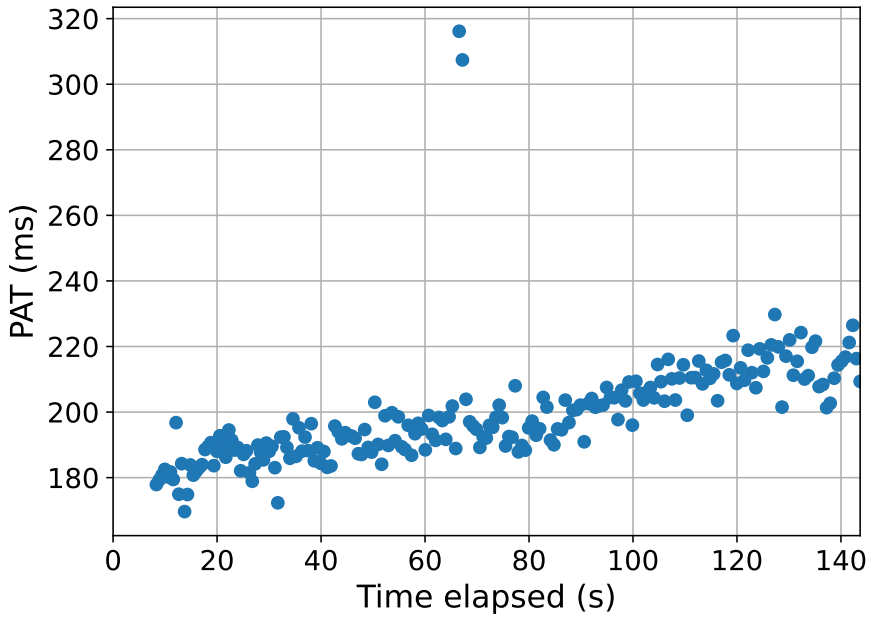

Figure 5.14: *Example of the obtained PAT values from the ECG and FBG recordings for subject 1 during cycling at 1 minute.*

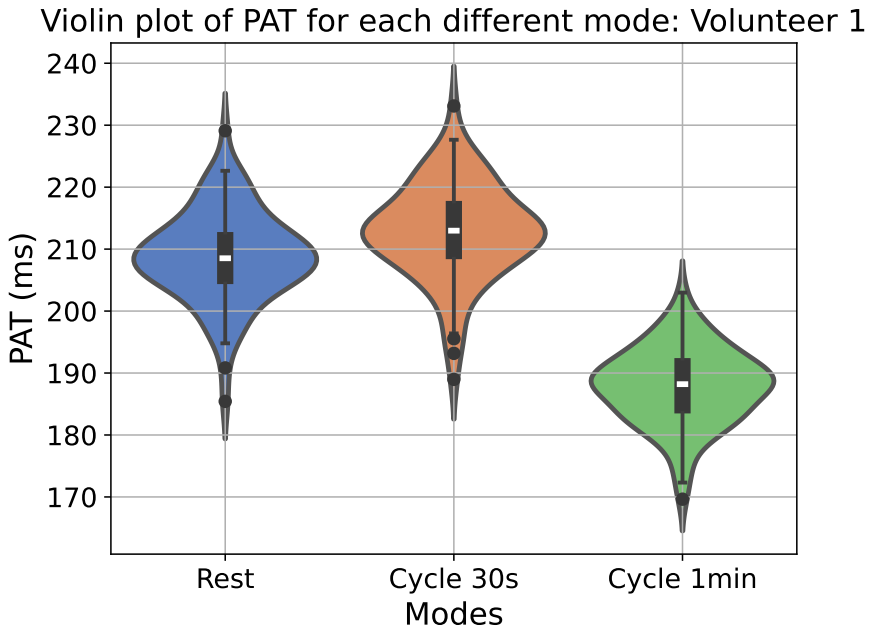

Figure 5.15: *Example of the violin plots obtained from each PAT population at rest, cycle 30 s and cycle 1 min in subject 1.*

5.1.4 Gaussian Process Regression model

To estimate BP values from PAT and PTT measurements, and acknowledging the non-linear relationship between these timing features and BP, this work proposes a Gaussian Process Regression (GPR) model. This model constitutes the initialisation layer of the proposed Cuffless BP monitor (Figure 2.7)

As discussed in Section 1.8 and Section 2.2, the rationale for adopting GPR lies in its suitability for cuffless BP estimation under the constraints of proof-of-concept experimentation. Unlike conventional machine learning approaches that often require extensive feature engineering and large datasets, GPR provides a principled Bayesian framework capable of modelling complex, subject-specific relationships between PAT/PWV features and BP while simultaneously producing predictive uncertainty – an essential aspect for clinical interpretability and risk assessment. Its robustness with limited sample sizes, reduced susceptibility to overfitting, and compatibility with streamlined feature extraction make GPR a practical, data-efficient, and interpretable solution.

The choice of GPR over conventional calibration approaches is motivated by several factors:

- The relationship between BP and PAT is inherently non-linear and varies across individuals; GPR accommodates this variability without requiring explicit feature engineering.
- PAT values approximate a Gaussian distribution, and it is reasonable to assume that beat-to-beat SBP and DBP values follow a similar distribution.
- GPR models have demonstrated robustness with small datasets, making them well-suited for this study where data per volunteer are limited (PAT values ranging from 198-664, with only 7-9 BP reference recordings across rest, cycle 30s, and cycle 1min).
- Unlike many other regression models, GPR provides both predicted values and variance estimates, enabling uncertainty quantification and more

informed decision-making.

PAT was chosen over PTT because the time interval between the ECG R-wave and the FBG pulse peak was easier to identify. In contrast, the time difference between FBG1 and FBG2 signals was often small, with overlapping pulses, and in some cases the FBG2 signal at the upper arm lacked a sufficiently sharp waveform for reliable detection. This resulted in a stronger correlation of PAT with BP compared to PTT.

A Gaussian Process is a collection of random variables, where any finite subset follows a multivariate Gaussian distribution (Equation 5.3). X is a random variable (e.g, blood pressure), μ is the mean (expected value, center of the distribution) and σ^2 is the variance which indicates the spread of the values [122–125].

$$X \sim \mathcal{N}(\mu, \sigma^2) \tag{5.3}$$

The Gaussian process (Equation 5.6) is defined by the mean function (Equation 5.4) and the similarity between inputs using a covariance matrix based on a kernel function (Equation 5.5). Where $m(x)$ is the latent function that is attempted to be modelled, $\mathbb{E}[f(x)]$ is the expected value after evaluating the input in the modelled function.

$$m(x) = \mathbb{E}[f(x)] \tag{5.4}$$

$$k(x, x') = \mathbb{E}[(f(x) - m(x))(f(x') - m(x'))] \tag{5.5}$$

$$f(x) = \mathbb{GP}(m(x), k(x, x')) \tag{5.6}$$

The model makes an initial assumption about the function $f(x)$ before observing any data $p(f(x))$, **prior** distribution, specified by $m(x)$ and $k(x, x')$. After observing the data using Bayes' theorem (Equation 5.7), the GP model updates

its belief about $f(x)$, forming the **posterior** distribution $p(f(x) \mid \text{data})$. The likelihood, how well the function f(x) explains the observed data is described by $p(\text{data} \mid f(x))$.

$$p(f(x) \mid \text{data}) \propto p(\text{data} \mid f(x))p(f(x)) \tag{5.7}$$

For the regression model, given training datapairs (X_{train} and y_{train}), it is aimed to predict y_{test} at test inputs X_{test}. X are the PAT values and y are the SBP and DBP values.

Training data joint distribution:

$$\begin{bmatrix} f(X_{\text{train}}) \\ f(X_{\text{test}}) \end{bmatrix} \sim \mathcal{N}\left(\begin{bmatrix} m(X_{\text{train}}) \\ m(X_{\text{test}}) \end{bmatrix}, \begin{bmatrix} K(X_{\text{train}}, X_{\text{train}}) & K(X_{\text{test}}, X_{\text{train}}) \\ K(X_{\text{train}}, X_{\text{test}}) & K(X_{\text{test}}, X_{\text{test}}) \end{bmatrix} \right)$$

$K(X_{\text{train}}, X_{\text{train}})$: Covariance matrix between training points

$K(X_{\text{test}}, X_{\text{test}})$: Covariance matrix between test points

$K(X_{\text{test}}, X_{\text{train}})$: Covariance matrix between test and training points

Posterior Mean and Covariance:

The predictions for $f(X_{test})$ are:

$\mu_{test} = K(X_{\text{test}}, X_{\text{train}})[K(X_{\text{train}}, X_{\text{train}}) + \sigma^2 I]^{-1} y_{\text{train}}$

$\Sigma_{\text{test}} = K(X_{\text{test}}, X_{\text{test}}) - K(X_{\text{test}}, X_{\text{train}})[K(X_{\text{train}}, X_{\text{train}}) + \sigma^2 I]^{-1} K(X_{\text{train}}, X_{\text{test}})$

Where μ_{test} is the predicted mean and Σ_{test} is predicted variance or uncertainty estimate.

Dataset preparation

Figure 5.16 shows the methodology implemented for the preparation of the dataset to train and test the Multitask GPR model. This pipeline starts with the interpolation of the SBP and DBP to match the measured PAT values. For the interpo-

lation, a PAT value along with the measured BP (SBP and DBP) measured value are required. It is known that each BP recording was measured every 40 seconds, but the exact corresponding PAT value for each recording is difficult to estimate. Therefore, the median of the PAT distribution for every 40s of data is compared with each BP recording. The pairs of BP measured and the corresponding median PAT values are used to build a cubic spline interpolation. Cubic splines are well known for a continuous and smooth interpolation with fewer oscillations compared to a quadratic spline as each spline or connection between the known data points corresponds to a 3rd order polynomial.

After obtaining the interpolated SBP and DBP from the whole population of measured PAT values using the cubic spline interpolation. It was noticed that some interpolated values were outside the realistic physiological BP values (Figure 5.17). To address this issue the BP interpolated value were clipped using the max and min SBP and DBP measured (Figure 5.18). After clipping these interpolated values a saturation in the lower and upper bounds was observed. This saturation was solved (Figure 5.19) by generating a small deviation to the lower and upper bounds. This deviation follows a random normal distribution of $\pm$ 2mmHg for the lower and upper bounds of the interpolated SBP values and a random normal distribution of $\pm$ 1mmHg for the lower and upper bounds of the interpolated DBP values. These deviation ranges were selected as they are the typical error margins of automated BP devices [126–128], the DBP deviation is smaller as this measurement tends to be more stable.

This interpolation pipeline was repeated for the three scenarios (rest, cycle 30 s and cycle 1 min) for each subject. A dataset was created with all the BP and PAT values from each scenario concatenated and shuffled. Finally, the created dataset was split into train and test set following a ratio 80:20.

Table 5.1 shows the size of the train and test sets used for each volunteer assessed. This table also include the number of PAT values extracted from each scenario.

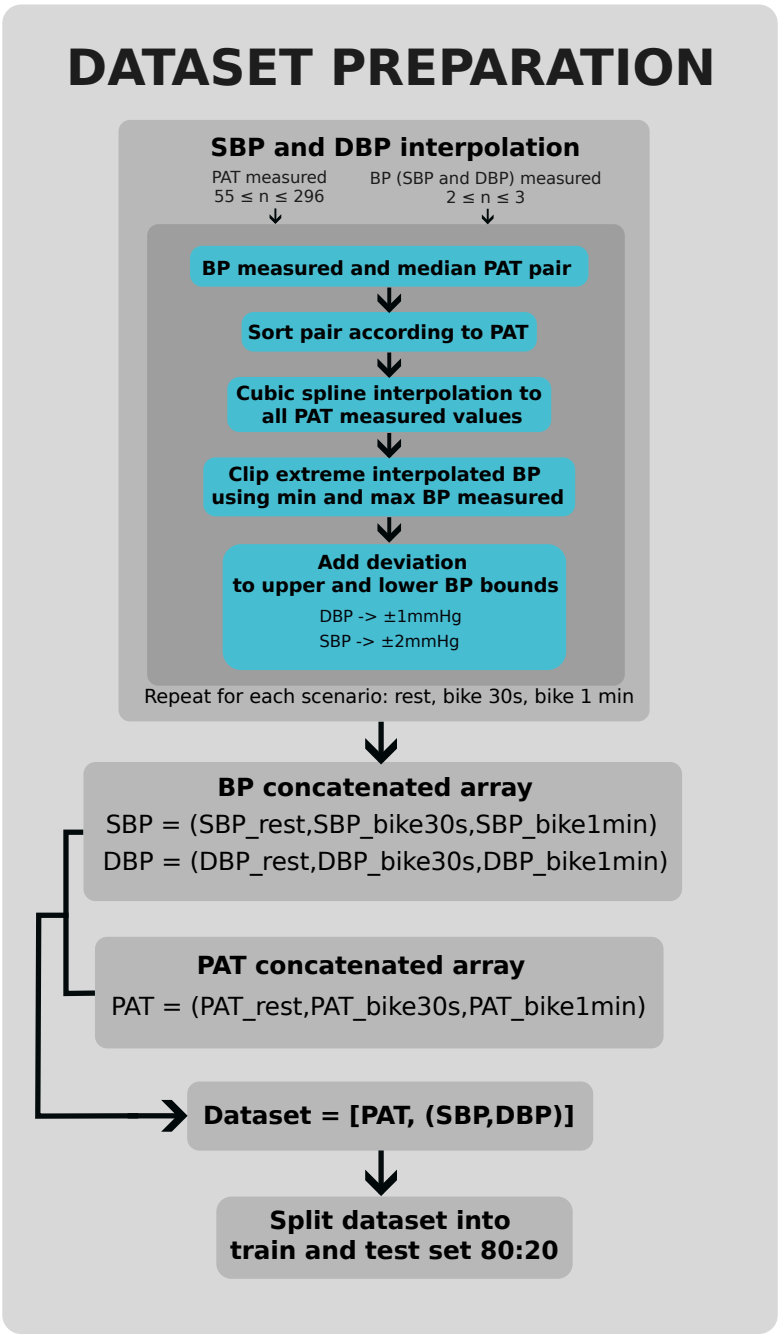

Figure 5.16: *Dataset preparation pipeline for Multitask GPR model. This pipeline consists of the interpolation of SBP and DBP values. For each PAT a tuple of SBP and DBP values was obtained. This interpolation was repeated for the three scenarios (rest, cycle 30 s and cycle 1 min) for each subject. The dataset was created with all the BP and PAT values from each scenario concatenated. The created dataset was shuffled and split into train and test set following a ratio 80:20.*

ID	PATs rest	PATs cycle 30 s	PATs cycle 1 min	Train set	Test set
1	85	130	171	309	77
3	156	142	82	304	76
4	86	93	104	231	57
5	148	115	212	380	95
9	153	215	296	531	133
10	157	175	227	447	112
12	55	60	83	158	40
13	171	183	197	441	110
14	188	196	220	483	121
15	88	115	129	266	66

Table 5.1: Length of train and test datasets and population (N) of PAT values extracted in each scenario.

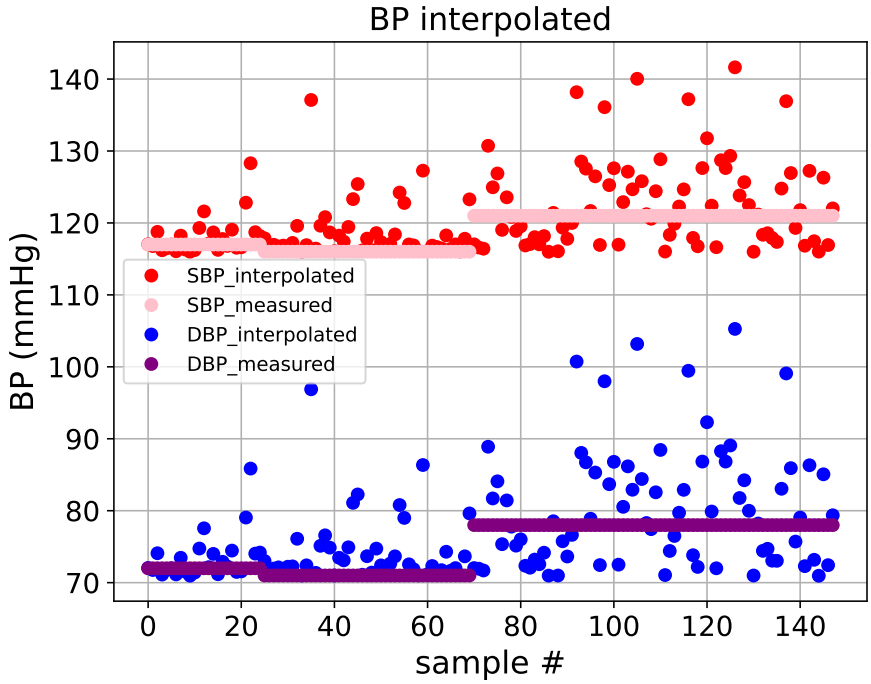

Figure 5.17: *Output of the cubic spline interpolation. SBP (red) and DBP (blue) values are shown along with the measured BP values (SBP in pink and DBP in purple). Non-realistic values appear after interpolation.*

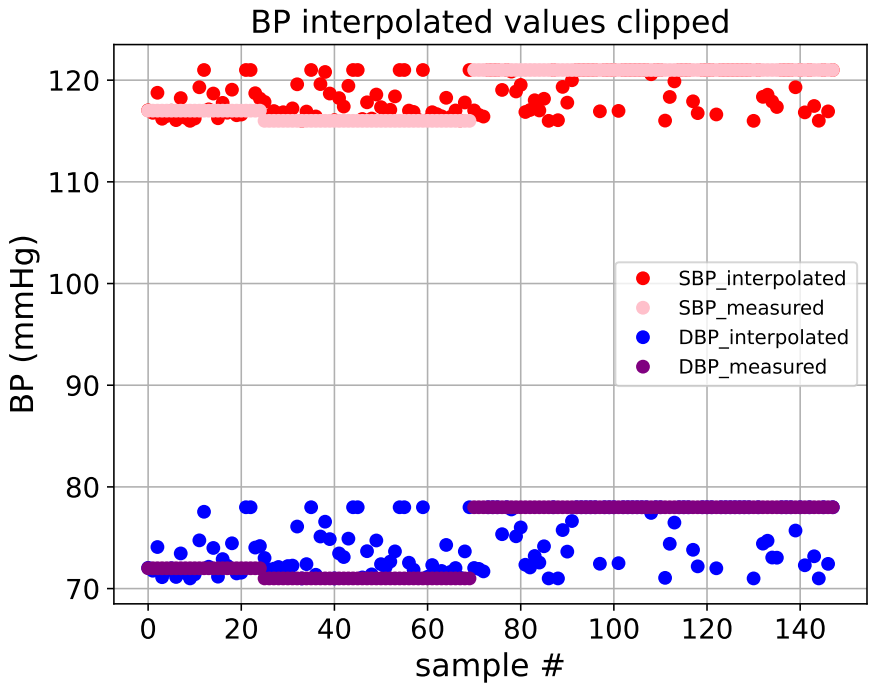

Figure 5.18: *Results after clipping the interpolated SBP (red) and DBP (blue). The lower and upper boundaries correspond to the maximum and minimum measured BP recordings (SBP in pink and DBP in purple).*

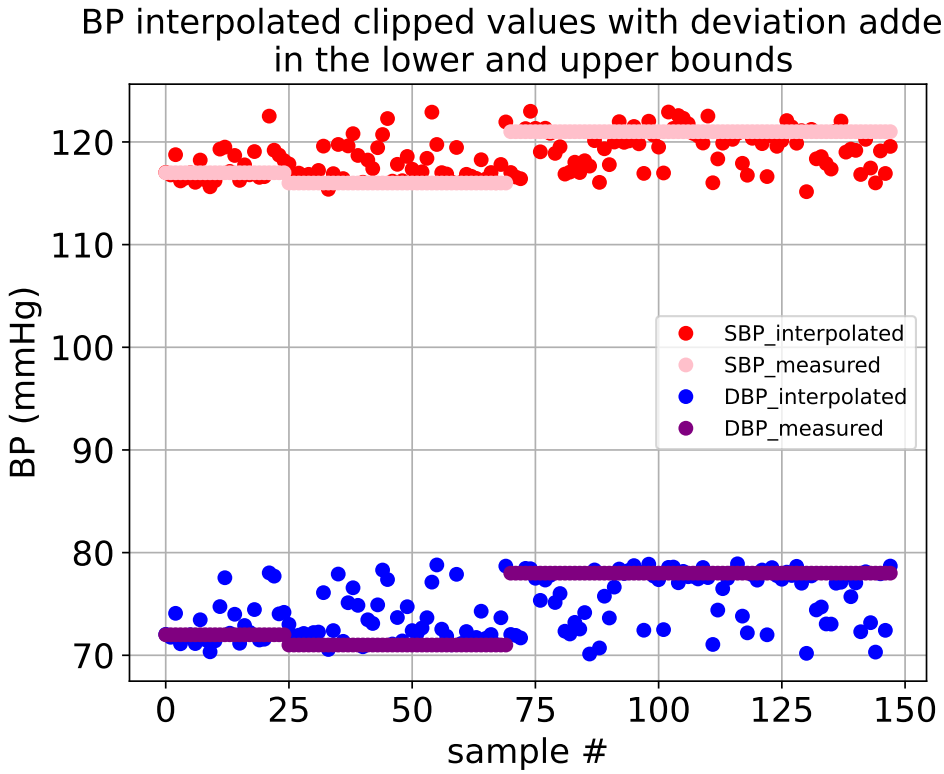

Figure 5.19: *Interpolated SBP and DBP values after adding a deviation to avoid saturation at the lower and upper bounds. Note: the SBP and DBP measured values do not vary after approximately every 40 samples because the same BP reading was repeated. In total, three measured BP readings are shown in each graph.*

Training and Testing

Figure 5.20 illustrates the implementation of the Multitask GPR model, the training and testing stages. During training, the PAT values from the training set are processed using a Multitask GP model based on the Matérn Kernel function, which includes an output scale σ^2(Equation 5.8). The key parameters of the Matérn kernel function include the smoothness $\nu = 2.5$, which provides a moderate balance between smoothness and flexibility to fluctuations; the length scale $\ell = 15.0$, which determines how quickly correlations decay with distance; and the output scale $\sigma^2 = 5.0$, which defines the variance of the GP function. Additionally, the model was configured with two tasks to model the correlation between multiple outputs (SBP and DBP). To improve computational efficiency, the rank of the task covariance matrix was set to 2, reducing the number of free parameters by factorizing it into two latent factors. $K_\nu(\cdot)$ in Equation 5.8 represents the modified Bessel function of the second kind, which governs the shape and correlation between points. The term $\Gamma(\nu)$ is the Gamma function, ensuring proper normalisation of the kernel to maintain scale invariance.

$$K(x, x') = \sigma^2 \frac{2^{1-\nu}}{\Gamma(\nu)} \left(\frac{\sqrt{2\nu}\|x - x'\|}{\ell} \right)^{\nu} K_\nu \left(\frac{\sqrt{2\nu}\|x - x'\|}{\ell} \right) \tag{5.8}$$

During the training stage, the loss that this model tries to optimise is the Exact Marginal Log Likelihood (MLL), Equation 5.9. This likelihood represents the probability of the model best explaining the observed data. In this equation, y represents the observed training outputs (SBP and DBP from the training set) and $m(X)$ represents the mean predicted value, while K is the covariance matrix from the Matérn kernel. The term ϵ represents the likelihood noise variance and I is identity matrix that ensures numerical stability. The kernel hyperparameters, θ, are optimised during training.

The term $-\frac{1}{2}y^T(K + \epsilon I)^{-1}y$ represents the fit term, which measures how well the model fits the data and penalises large residuals to improve prediction accuracy.

The complexity penalty term, $-\frac{1}{2}\log|K+\epsilon I|$, prevents overfitting by discouraging overly complex models. Finally, $-\frac{n}{2}\log 2\pi$ is a normalisation term that ensures the log-likelihood follows a valid probability distribution. In Gaussian Process regression, the likelihood assumes Gaussian noise, where observations are modeled as: $y_i = f(x_i) + \epsilon, \qquad \epsilon \sim \mathcal{N}(0, \sigma^2)$. Here, σ^2 represents the noise variance, which accounts for observation uncertainty. The initial likelihood noise is set to 1 before optimization and a prior is applied to the likelihood noise, constraining it to the range 0.05 - 1 with a standard deviation of 0.1. Backpropagation during training is performed using the Adam optimizer with a learning rate of 0.02.

$$\log p(y|X,\theta) = -\frac{1}{2}(y-m(X))^T(K+\epsilon I)^{-1}(y-m(X)) - \frac{1}{2}\log|K+\epsilon I| - \frac{n}{2}\log 2\pi \tag{5.9}$$

During testing (Figure 5.20), PAT values from the testing set are processed using the trained Multitask GP model, where the likelihood function is applied to obtain the predicted mean values for SBP and DBP, along with their respective lower and upper confidence intervals. Furthermore, a jitter term (1×10^{-2}) is added during Cholesky decomposition to ensure numerical stability of the outputs. This prevents the smallest eigenvalues of the covariance matrix from approaching zero, ensuring numerical robustness.

Implementation details

This model was implemented in Python using the GPytorch library [129]. For Gaussian Process models, the `ExactGP` class was used along with `MultitaskGPModel`, inheriting the GP functionality and adding multitask capability to regress SBP and DBP values. Therefore, the number of tasks was set to 2. The kernel was set using `MultitaskMean(gpytorch.means.LinearMean())`. The base kernel (Matérn) was defined as `gpytorch.kernels.MaternKernel(nu=2.5)`.

The training loop was run for 3000 iterations.

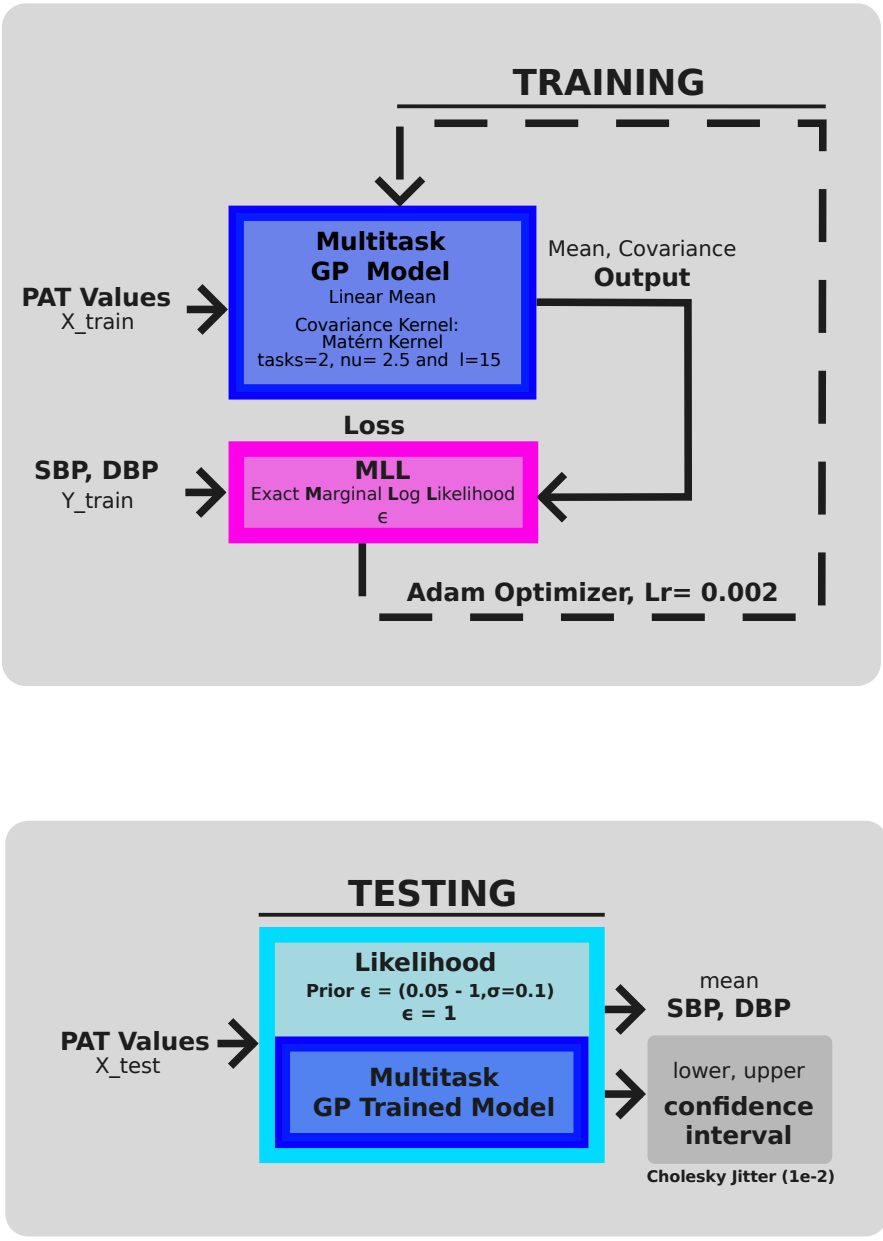

Figure 5.20: *Multitask Gaussian Process regression model. Training and testing stages. The training stage (top gray box) displays the initial hyperparameters values (smoothness ν, length scale ℓ and output scale σ^2) set in the model. This model takes input PAT values from the training set and outputs the mean BP values and covariance matrix results. This output along with the actual BP values are inputs of the loss function to be optimised, the exact marginal log likelihood, this function have an initial assumption of the Gaussian noise in the dataset (ϵ) and back propagates, using the Adam Optimizer, the computed likelihood to maximise its value with a learning rate of 0.002. The bottom box is the testing stage which computes the likelihood to the output of the trained model, to obtain the mean SBP and DBP predictions along with the confidence intervals post-processed with a Cholesky jitter (1e-2).*

5.2 Results

In the human volunteer experiments, 15 participants were recruited (9 male and 6 female). However, a complete dataset across all three scenarios was not obtained (Table 5.2).

For Volunteer 2, the ECG electrodes lost connection in Scenario 3, and the FBG2 pulse at the upper arm was undetectable in all scenarios. Similarly, for Volunteers 6, 7, 8, and 11, insufficient data was available to compare the three scenarios and in some cases, although the FBG1 pulse at the wrist was detected, it was inconsistent across the three scenarios, and in other cases the upper arm pulse was too weak for detection using the FBG2-cantilever sensor. This detection issue at the upper arm also affected the dataset of Volunteers 14 and 15. As a result, a reliable dataset was obtained for 10 volunteers (5 female and 5 male) for PAT values and for 8 volunteers (4 male and 4 female) for PTT values.

Table 5.2: Volunteer's set. Gender of the volunteer (M for male and F for female), metric computed and the reasons for excluding volunteer's set.

ID	Gender	Metric	Reason to not use this dataset
1	M	PTT and PAT	
2	M	None	ECG became disconnected in scenario 3, FBG2 pulse not detected
3	F	PTT and PAT	
4	F	PTT and PAT	
5	M	PTT and PAT	
6	M	None	Not enough data across the three scenarios
7	M	None	Not enough data across the three scenarios
8	F	None	Not enough data across the three scenarios
9	M	PTT and PAT	
10	F	PTT and PAT	
11	M	None	Not enough data across the three scenarios
12	F	PTT and PAT	
13	M	PTT and PAT	
14	M	PAT	FBG2 pulse not detected
15	F	PAT	FBG2 pulse not detected

This section describes the PAT and PTT values measured and its comparison with SBP, DBP and HR values after increasing the physical activity. This section also outlines the results of the Gaussian Process Regression model of SBP and DBP values from PAT values.

5.2.1 Pulse Transit Time (PTT)

According to the Moens-Korteweg and Hughes formulation (Eq. 1.2), pulse wave velocity (PWV) increases with arterial stiffness and pressure. Since PTT is defined as the inverse of PWV scaled by the propagation distance, an increase in blood pressure is expected to shorten the transit time between two arterial sites. In this study, this corresponds to a reduction in the time difference between the pulsatile signal detected at the upper arm with FBG2 and the signal at the wrist with FBG1, as shown in Figure 5.1.

PTT and NIBP data were analysed across eight volunteers. In most cases, SBP and HR increased with physical activity, while DBP showed only modest or inconsistent changes. The violin plots revealed that PTT distributions were generally widest at rest and narrowed with increasing activity, with maximum PTT values typically decreasing by 50-120 ms across exercise stages. This inverse relationship between BP/HR and PTT was evident in some participants (e.g., volunteers 1, 4, 5 and 9), although less consistent in others (e.g., 3, 10, and 12), where reduced signal quality, increased variability, and the limited temporal resolution of the system introduced artefacts such as negative values. The detailed results of all individual analyses are presented in Appendix C.1.

Apart from physiological differences depending on the measurement site – FBG2 pulses at the upper arm are generally less sharp than FBG1 pulses at the wrist – a specific source of variability arises from the limited temporal resolution of the sensing system. The miniature interrogator operated at 200Hz, corresponding to a sampling interval of 5ms, which constrains the accuracy with which the pulse foot can be localised. At short transit times or in noisy recordings, this discretisation introduces jitter in the estimated PTT and occasionally yields apparent negative values. These artefacts do not reflect physiological phenomena but instead highlight the impact of finite time resolution on the robustness of beat-to-beat PTT estimation.

Figure 5.21 presents the results for **volunteer 1**. The scatter plot in Figure 5.21b

shows the NIBP and HR trends. SBP and HR increased with exercise (by 26 mmHg and 17 BPM, respectively), while DBP rose only slightly (+5 mmHg), reflecting the expected cardiovascular response to physical exertion. The violin plot in Figure 5.21a shows that at rest, the PTT distribution was the widest, with large spread and variability. As the exercise intensity increased (cycle 30 s and cycle 1 min), the maximum PTT values decreased from 100 to 50 ms, and the spread narrowed. This decreasing trend indicates that PTT shortens with increased physical activity, consistent with the expected physiological response to elevated BP.

The PTT measurements in this study therefore demonstrated the expected shortening trend with increased blood pressure and heart rate during exercise, although inter-subject variability and negative values were observed. The use of a miniature, low-power interrogator at 200 Hz was intentional, as this form factor and energy budget are compatible with ambulatory BP-monitoring applications. The trade-off is temporal resolution: a 5 ms sampling interval represents up to 20-30% of the physiological PTT range (15-50 ms), thereby explaining the broader distributions and negative values in the dataset.

In contrast, Wang et al. (2024) [74] employed a conventional 1 kHz interrogator (≈1 ms resolution) using soft FBG-PDMS sensor to measure local PWVs simultaneously in both radial arteries under resting conditions. Their system yielded stable PTT estimates (29 ± 1 ms for a 27 cm arterial segment), corresponding to PWVs between 9-15 m/s, with an error margin of only 3.5%. Importantly, Wang et al. did not vary the haemodynamic state of the volunteers, so their results reflect baseline arterial stiffness rather than dynamic changes in vascular tone.

Our study extends beyond this by actively modulating BP and HR through exercise, demonstrating that PTT shortens as cardiovascular load increases. While the lower sampling rate of our interrogator introduced greater uncertainty than in Wang et al., the observed physiological trends align with theoretical expectations and confirm that FBG-based sensing can capture haemodynamically driven PTT changes, even when constrained by the reduced temporal resolution of a miniature

interrogator designed for ambulatory BP monitoring.

5.2.2 Pulse Arrival Time (PAT)

According to the Moens-Korteweg and Hughes formulation (Eq. 1.2), an increase in arterial pressure leads to an increase in pulse wave velocity (PWV) and consequently a shortening of pulse transit time (PTT). Since PAT is defined as the interval between the R-wave of the ECG and the distal pulse arrival at the wrist (FBG1), it incorporates both the pre-ejection period (PEP) and the transit time along the arterial path. Therefore, a rise in blood pressure and heart rate with exercise is expected to shorten PAT values, although with larger variability than PTT due to the additional influence of PEP.

PAT and NIBP data were analysed across ten volunteers. As expected, SBP and HR generally increased with exercise, while DBP showed only modest or inconsistent changes. In most participants, violin plots showed that PAT values decreased with higher exercise intensity, with median reductions ranging between 20-150 ms from rest to cycle 1 min. These trends were in line with the physiological expectation that increased cardiovascular load accelerates pulse wave propagation and shortens PAT. However, the extent of the PAT reduction varied across individuals. In some cases (e.g., volunteers 1, 3, 10, and 12), the distributions preserved their overall shape while shifting toward lower values. In others (e.g., volunteers 5, 13, and 15), the variability between scenarios was higher, suggesting a stronger influence of PEP dynamics and inter-beat variability on the measured PAT. The detailed results of all individual analyses are presented in Appendix C.2.

Figure 5.22 presents the results for **volunteer 9**, where the clearest decreasing trend was observed. The scatter plot in Figure 5.22b shows that SBP, DBP, and HR all increased with exercise (average SBP +27 mmHg, HR +56 BPM, DBP +4 mmHg), reflecting the expected cardiovascular response. The violin plot in Figure 5.22a shows that PAT distributions shifted markedly across scenarios: the median PAT decreased from 170 ms at rest, to 120 ms after 30 s of cycling, and

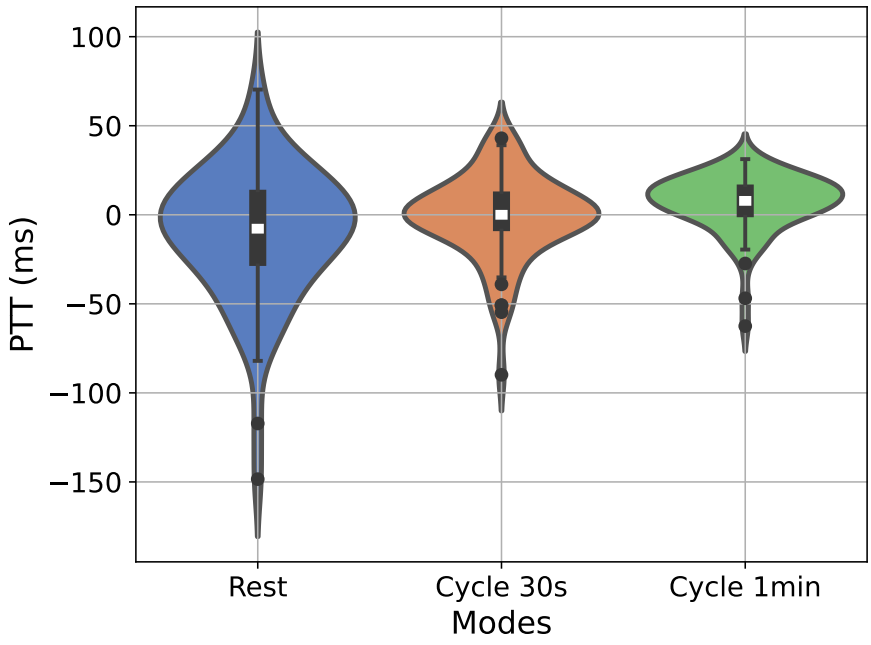

(a)

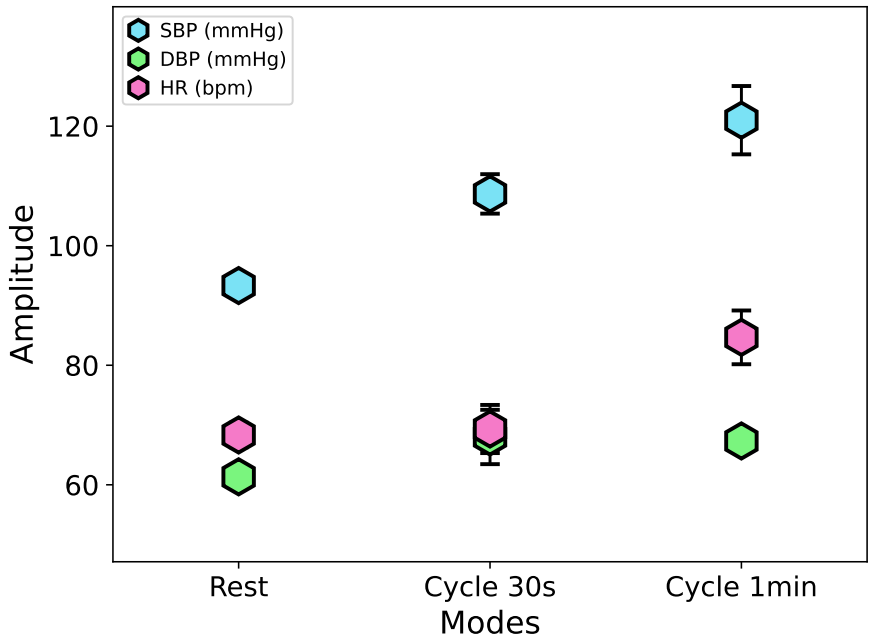

(b)

Figure 5.21: *PTT values condensed in violin plots (a) vs NIBP (SBP and DBP) values and HR (b) of the different modalities (rest, cycle 30 s and cycle 1 min) of the experiment in* ***volunteer 1****. The maximum PTT values and its distribution at each modality follows a decreasing trend meanwhile the SBP and HR follows an increasing trend as the exercise increases.*

further to 25 ms after 1 min of cycling. This inverse relationship between PAT and blood pressure/heart rate demonstrates the strong coupling between haemodynamic load and pulse arrival timing. Notably, this case illustrates that under conditions of large increases in SBP and HR, PAT reduction can be substantial, emphasising its sensitivity to exercise-induced haemodynamic changes.

A comparison with the findings of Finnegan et al. (2021) [36] provides valuable context. In a phenylephrine infusion study involving 30 healthy volunteers, Finnegan et al. found that PTT decreased by 16.8 ms ($\pm$ 7.5 ms), significantly larger than the PEP increase (5.5 ms $\pm$ 4.5 ms); thus, PEP contributed minimally to PAT variation in their protocol. They reported RMSEs of 5.5 mmHg for systolic BP estimation using PAT, slightly higher than those using PTT (4.5 mmHg), and noted large inter-individual variability in the PAT-SBP slope. It is important to note that the accuracy of the PTT measurements in their study relied on impedance cardiography from a central artery in the neck, together with PPG signals acquired at a sampling rate of 512 Hz, providing greater temporal precision than is typically available in peripheral, lower-frequency measurements. Whereas Finnegan's study achieved highly accurate estimates under tightly controlled, pharmacologically induced changes in blood pressure, our work demonstrates that the same inverse trends between PAT/PTT and BP can also be observed under exercise-induced haemodynamic modulation. However, in our case, greater variability was expected due to fluctuations in the pre-ejection period (PEP) and the presence of real-world signal noise.

Together, these data underscore that PAT reliably responds to acute BP and HR changes, whether induced pharmacologically or via exercise. However, for ambulatory or uncontrolled settings, it's essential to consider PEP's contribution and inter-individual variability – highlighting the potential benefit of combined or segmented approaches (e.g., separating PEP and vascular transit time) for improving robustness in PAT-based BP estimation.

The weaker correlations observed between PAT/PTT and DBP in this study are

best explained by the physiological response of DBP during dynamic exercise. Unlike SBP, which rises consistently due to increases in heart rate and stroke volume, DBP is largely determined by systemic vascular resistance (SVR). During cycling exercise, vasodilation in the active skeletal muscles reduces SVR, counterbalancing sympathetic vasoconstriction in non-active vascular beds. As a result, DBP changes are modest (often within 0-5 mmHg) during aerobic exercise [130], limiting the variability available for regression analysis. This suggests that the reduced sensitivity of PAT-derived features to track DBP in this study reflects a limitation of the chosen physiological protocol rather than of the sensing approach itself. Alternative perturbation methods, such as pharmacological modulation or postural changes, may therefore be more suitable for capturing meaningful DBP dynamics. However, pharmacological interventions raise ethical challenges and are more commonly adopted in clinical rather than laboratory research settings [120]. Table 5.3 summarises the PAT and PTT results and its comparison with SBP, DBP and HR measurements for the volunteers data analysed. Across the ten volunteers, the results showed consistent increases in SBP and HR with exercise, while DBP remained largely steady or showed only modest changes. PAT demonstrated a clearer response than PTT, with most participants exhibiting a decreasing trend as exercise intensity increased, in line with the expected physiological relationship between higher BP/HR and shorter pulse timing. PTT results were more variable: while some volunteers (e.g., 1, 5, 9) displayed the anticipated inverse relationship with SBP, others showed inconsistent or even increasing trends, likely reflecting signal quality issues or limited temporal resolution. Overall, the summary indicates that PAT was a more robust marker of exercise-induced haemodynamic changes than PTT across the studied cohort.

Given that PAT showed stronger and more consistent correlations with BP than PTT, it was selected as the primary feature for exploratory modelling. To assess its predictive utility, a Gaussian Process Regression (GPR) framework was applied, providing both BP estimates and associated uncertainty measures.

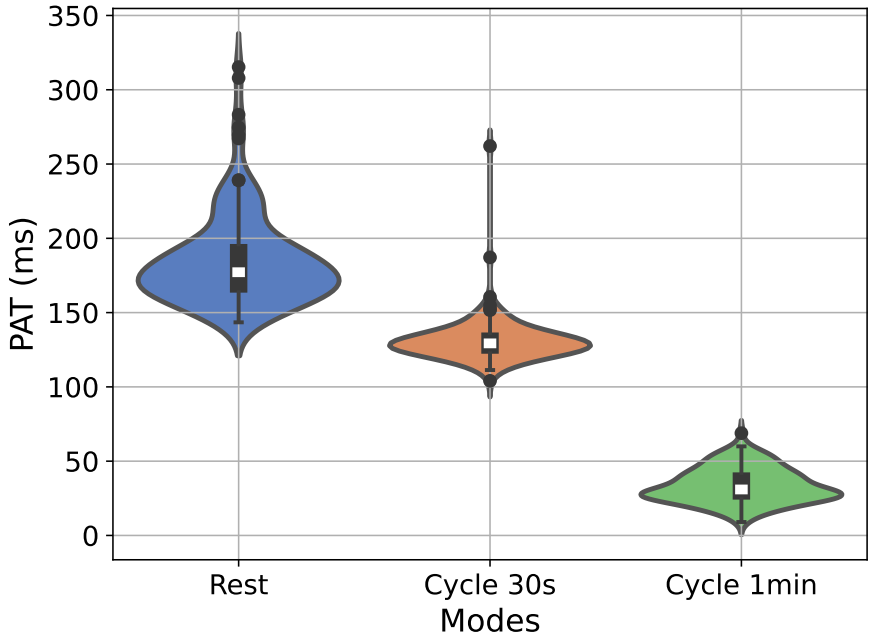

(a)

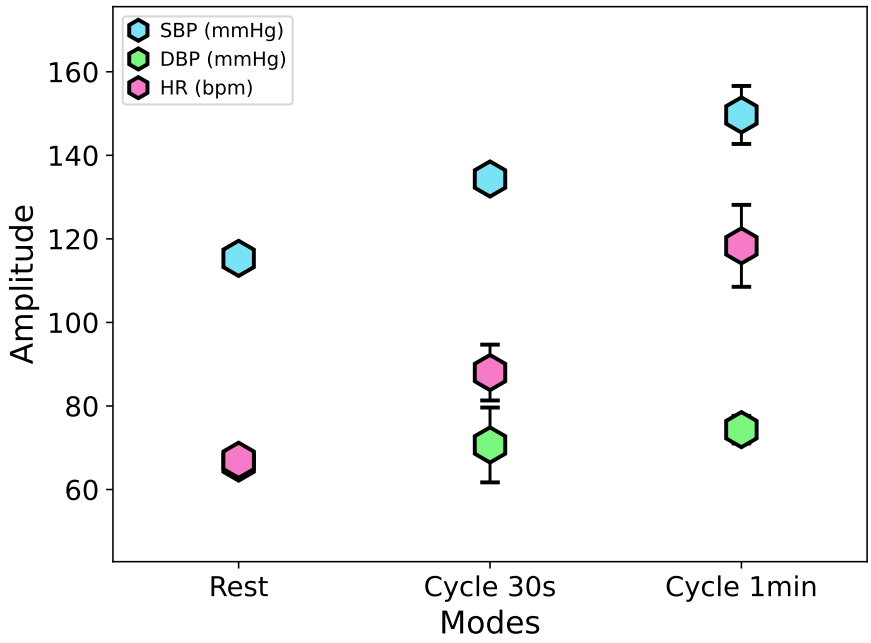

(b)

Figure 5.22: *PAT values condensed in violin plots (a) vs NIBP (SBP and DBP) values and HR (b) of the different modalities (rest, cycle 30 s and cycle 1 min) of the experiment in* ***volunteer 9****. It is clear the decrease in PAT values as the exercise increases and SBP, HR and DBP increase, however the DBP at cycle 30 s shows a large error.*

Table 5.3: PAT and PTT results summary. NIBP (SBP and DBP), HR, PTT and PAT trends with the increase of physical activity across the different modalities: rest, cycle 30 s and cycle 1 min, described in Figure 5.2.

ID	**NIBP and HR trends with increase in exercise**	**PTT trend with increase in exercise**	**PAT trend with increase in exercise**
1	Increase of HR and SBP. Steady DBP.	Decreasing trend in maximum PTT.	Overall decreasing trend in PAT.
3	SBP and HR increase. Slight decrease DBP.	A decreasing PTT trend only from cycle 30 s to 1 min.	Decreasing trend of PAT.
4	SBP and HR increase. Steady DBP.	Not clear PTT trend.	Overall decreasing PAT at cycle 30 s is slightly lower compared to cycle 1 min.
5	Overall increase of SBP and HR. Decreasing trend of DBP. SBP is the lowest at cycle 30 s.	The maximum PTT is observed at cycle 30 s. Inverse trend compared with SBP.	Inverse trend compared with SBP. Highest PAT at cycle 30 s.
9	Increase of SBP, DBP and HR.	Clear decreasing trend of max PTT. Expected inverse relationship with SBP.	Decreasing trend of PAT.
10	Increase of SBP, DBP and HR.	Not clear PTT decreasing trend, only from rest to cycle 30 s.	Decreasing trend of PAT.
12	Increase of SBP and HR, but steady DBP.	Increasing trend of PTT.	Decreasing trend of PAT.
13	Overall increase of SBP and HR, but steady DBP. SBP was higher at cycle 30 s.	The max PTT values follow an inverse relationship with DBP and a direct relationship with SBP.	Inverse PAT trend compared with DBP.
14	SBP and HR increase. Steady DBP.	N/A	Decreasing trend of PAT.
15	SBP and HR increase. Overall steady DBP increased at cycle 30 s.	N/A	Overall decreasing trend in PAT. Lowest PAT distribution at cycle 30 s.

5.2.3 Gaussian Process Regression model

These results illustrate the performance of Gaussian Process Regression (GPR) in predicting SBP and DBP values from PAT across the different volunteer datasets. The GPR model outputs both the predicted mean BP values and associated confidence intervals, enabling assessment of accuracy and uncertainty. Each prediction figure consists of two subplots: the upper panel shows SBP predictions and the lower panel shows DBP predictions. In the SBP subplot, the dotted blue line represents the predicted values, the red dots correspond to interpolated reference SBP values, and the shaded light-blue region indicates the 95% confidence interval (CI). Similarly, in the DBP subplot, the green dotted line shows predicted DBP values, the orange dots represent interpolated reference DBP values, and the light-green shaded region corresponds to the 95% CI.

To further evaluate performance, scatter plots and Bland-Altman plots were generated. In the scatter plots, the x-axis represents the actual interpolated BP values and the y-axis the GPR predictions. The diagonal line denotes the ideal 1:1 relationship, with points clustering around this line indicating high prediction accuracy, while deviations signify under- or over-estimation. Bland-Altman plots complement this analysis: the x-axis shows the mean of actual and predicted values, and the y-axis the difference between them. The dashed line indicates the mean bias, while the solid blue lines ($\pm$1.96 SD) represent the limits of agreement (LoA). Predictions are considered reliable when most points fall within the LoA and are randomly distributed; systematic trends or excessive outliers suggest bias or reduced reliability in certain BP ranges.

In this section, results are presented for Volunteer 5, whose test set showed the best overall performance. Corresponding scatter and Bland-Altman analyses are also provided, while the results for the remaining volunteers are detailed in Appendix D.

Finally, quantitative metrics were computed to complement the graphical analyses (Tables 5.4 and 5.5). These include mean absolute error (MAE), root mean

squared error (RMSE), coefficient of determination (R^2), and mean bias error (MBE). MAE indicates average prediction accuracy, with lower values representing better performance. RMSE, which penalises larger errors, reflects overall deviation from reference values. R^2 quantifies how well the model explains variance in BP, with values approaching 1 indicating stronger predictive power. MBE captures systematic bias, where positive values indicate overestimation and negative values underestimation.

ID	MAE (mmHg)	RMSE (mmHg)	R^2	MBE (mmHg)
1	6.66	8.06	0.5052	-1.00
3	5.45	6.84	0.4708	1.25
4	2.56	3.26	0.6433	0.35
5	0.82	1.28	0.8152	-0.13
9	1.27	2.53	0.9687	-0.09
10	5.22	7.55	0.5654	-0.41
12	11.67	16.56	-1.2145	-2.18
13	6.74	10.03	0.2910	-1.05
14	10.26	12.79	0.2032	-0.75
15	6.67	11.06	0.7572	-2.94

Table 5.4: SBP Prediction Metrics for Different Volunteers

ID	MAE (mmHg)	RMSE (mmHg)	R^2	MBE (mmHg)
1	2.68	3.41	0.1596	-0.16
3	3.98	5.38	-0.0623	0.21
4	1.25	1.85	0.4340	-0.28
5	0.40	0.79	0.9664	-0.00
9	0.42	0.66	0.9888	0.00
10	2.02	3.23	0.5398	-0.13
12	3.53	4.74	-0.7032	-0.98
13	1.17	1.90	0.6489	0.17
14	0.95	1.25	0.2946	0.06
15	1.05	2.37	0.7970	-0.23

Table 5.5: DBP Prediction Metrics for Different Volunteers

The prediction results for systolic and diastolic blood pressure (Tables 5.4 and

5.5) demonstrate that the model achieved variable accuracy across participants, with mean absolute errors (MAE) ranging from 0.82 to 11.67 mmHg for SBP and 0.40 to 3.98 mmHg for DBP. Volunteers 5 and 9 consistently yielded the best performance, with MAE values below 2 mmHg and strong coefficients of determination ($R^2 > 0.8$), confirming robust and reliable agreement with reference measurements. Volunteer 15 also showed strong performance, particularly for DBP, while volunteer 4 achieved balanced and accurate predictions with slightly higher errors. By contrast, volunteers 12 and 14 exhibited the weakest performance, characterised by larger errors and, in the case of volunteer 12, negative R^2 values for both SBP and DBP. The remaining volunteers (1, 3, 10, and 13) demonstrated intermediate outcomes, with moderate SBP tracking but larger deviations at certain pressure ranges and reduced explanatory power for DBP.

Overall, these findings highlight that the model can achieve robust accuracy in favourable cases (volunteers 5, 9, 15, and 4), particularly for DBP where most participants showed low errors and minimal bias. However, the variability in SBP estimation across individuals underscores inter-subject differences that may reflect physiological diversity or signal quality limitations, pointing to the need for strategies that improve model generalisability across a wider population.

Figure 5.23 illustrates the results of the GPR model prediction with confidence intervals using the PAT values of **volunteer 5** dataset. The SBP predictions (blue dotted line) from the model significantly follow the trend of the actual SBP values (red dots). Only 2% of the SBP actual values are outside the confidence intervals. The DBP predictions (green dotted line) also significantly follow the trend formed by the actual DBP values (orange dots), with no DBP actual values outside the CI. The confidence intervals for the SBP predictions (shaded light blue region) vary in width across the samples indicating the difference in uncertainty between predictions, with wider regions, the maximum with of these confidence intervals is 5 mmHg. The confidence intervals are smaller for DBP predictions (shaded light green region) with a maximum 2.5 mmHg width across the samples.

From Figure 5.24a, the points cluttered tightly around the diagonal indicate a strong correlation between the predicted value and the actual SBP values. The scattering is relatively small, suggesting low errors in most of the cases (RMSE = 1.28 mmHg). Overall, the alignment remains significant, but there is a slight spread from 115 to 123 mmHg. From Figure 5.24b, the DBP predictions follow closely the ideal fit (RMSE = 0.79 mmHg) over all the range of actual DBP values (73-79 mmHg).

From Figure 5.25a, it is observed that mean SBP difference is near zero, indicating a minimal systematic bias. Points are spread ± 3 mmHg suggesting small prediction errors. Few points are above 3 mmHg and below -2 mmHg, however, these are not extreme outliers. From Figure 5.25b it is observed that the mean DBP difference is slightly positive, indicating that the suggesting the model neither systematically overestimates nor underestimates DBP predictions. There are very few errors overall as most of the points are spread ± 1.5 mmHg

From Table 5.4, the SBP MAE is 0.85 mmHg, the SBP R^2 is equal to 0.8152 showing the good performance of the model. From Table 5.5, the DBP MAE is 0.40 mmHg, the DBP R^2 is equal to 0.9664, showing a robust model performance.

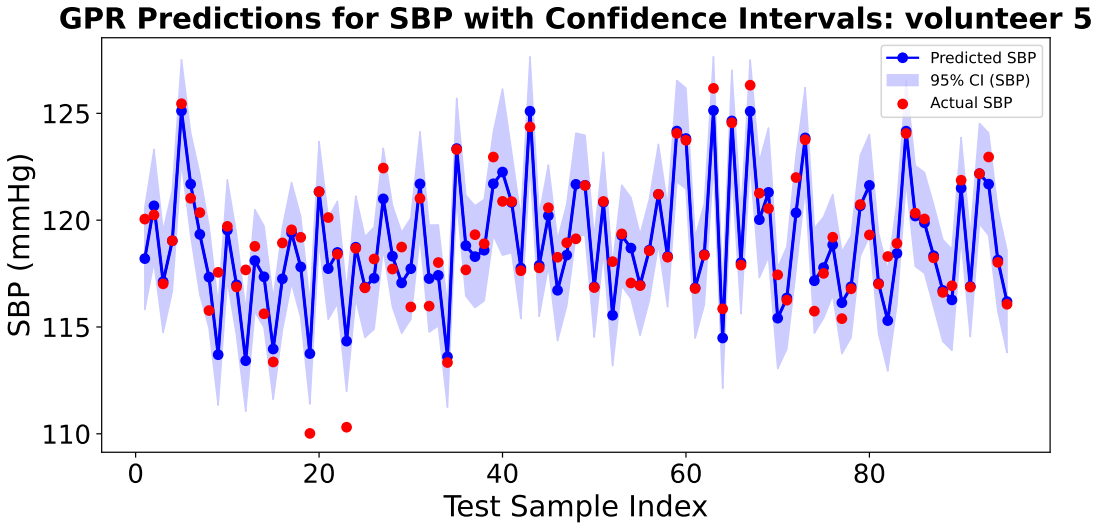

(a)

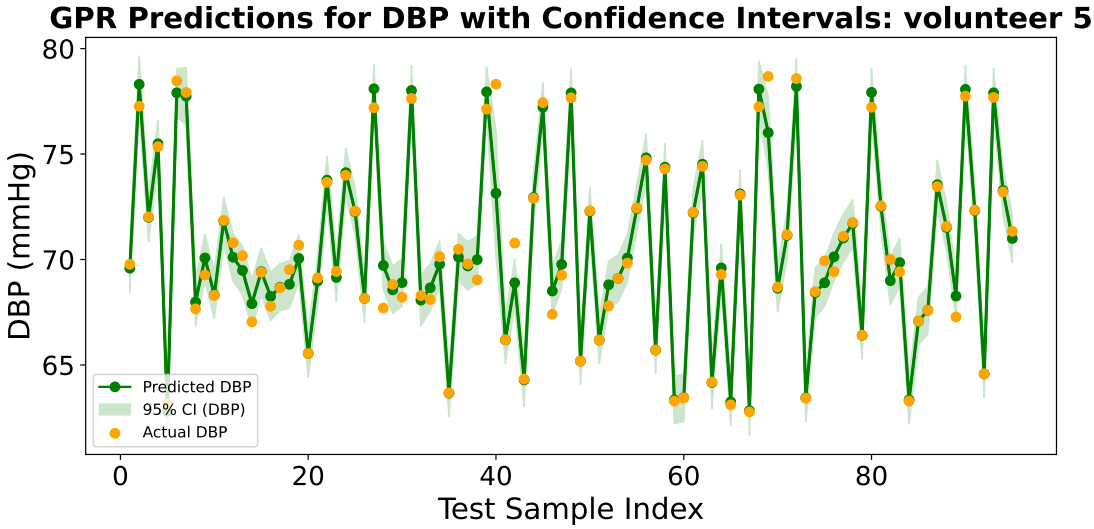

(b)

Figure 5.23: *GPR model BP prediction plots for the* ***volunteer 5*** *test set. (a) SBP predictions: actual SBP values (red dots) vs mean SBP predicted values (blue dotted line) with 95% confidence intervals (light blue shaded region). (b) DBP predictions: actual DBP values (orange dots) vs mean DBP predicted values (green dotted line) with 95% confidence intervals (light green shaded region). Only 2% of the actual SBP values lie outside the CI, while no DBP values are outside. The SBP CI shows larger uncertainty (width* $\leq$ *5 mmHg) compared to the DBP CI (width* $\leq$ *2.5 mmHg).*

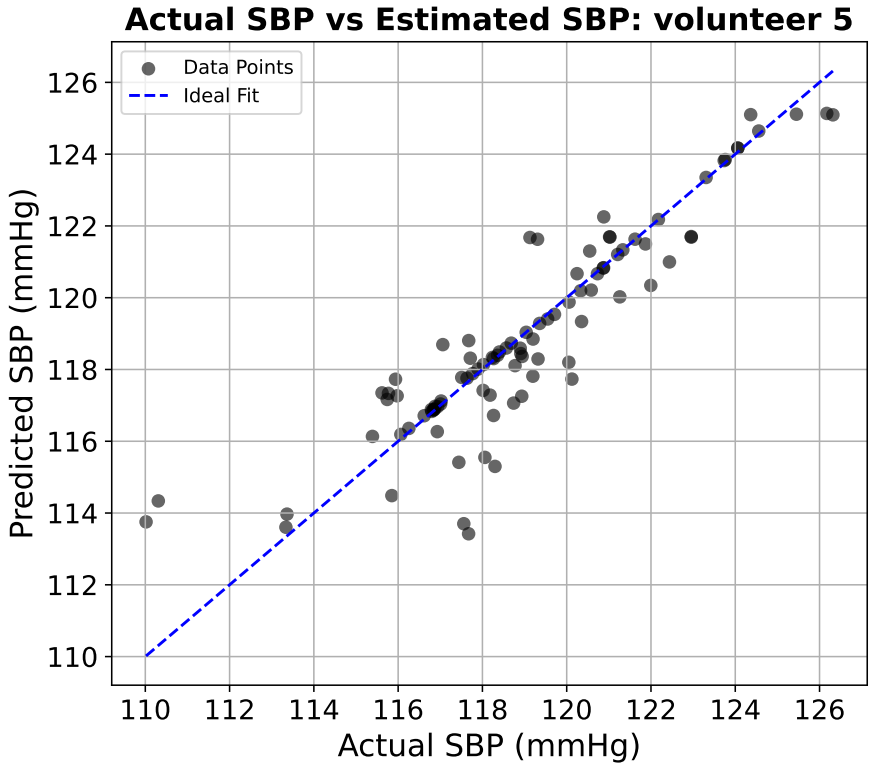

(a)

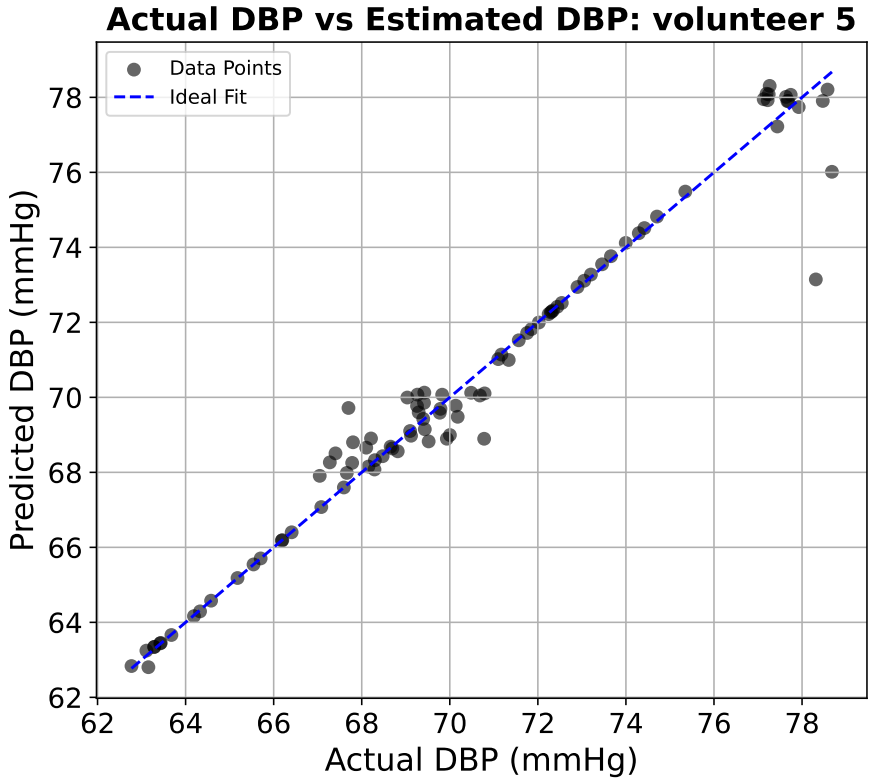

(b)

Figure 5.24: *Correlation analysis for the **volunteer 5** test set. (a) Predicted vs actual SBP. (b) Predicted vs actual DBP. Both plots show strong correlation, with tighter agreement observed in DBP.*

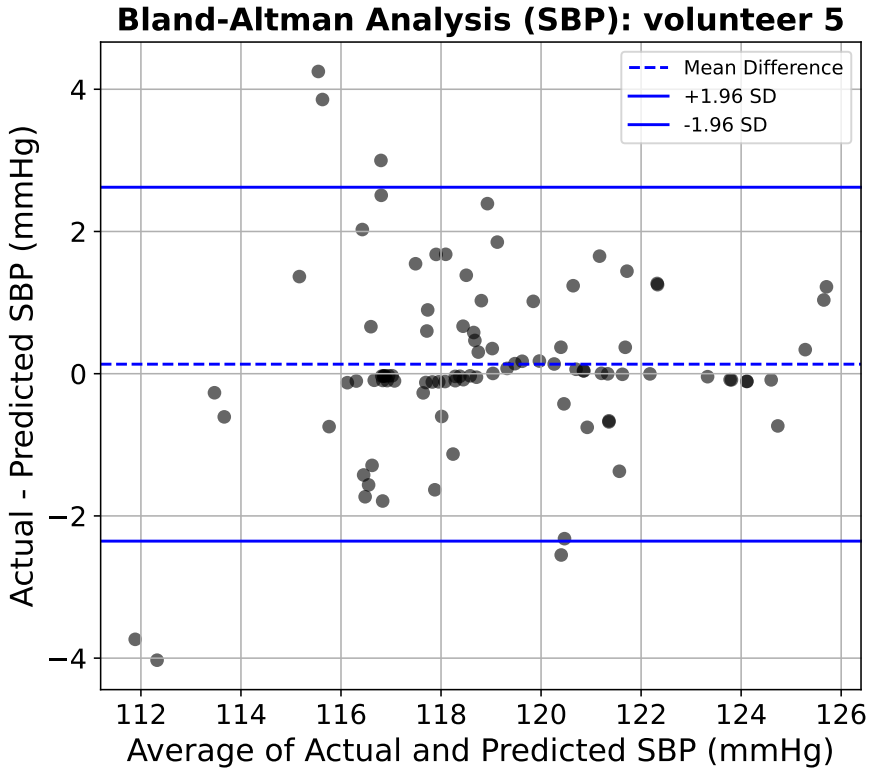

(a)

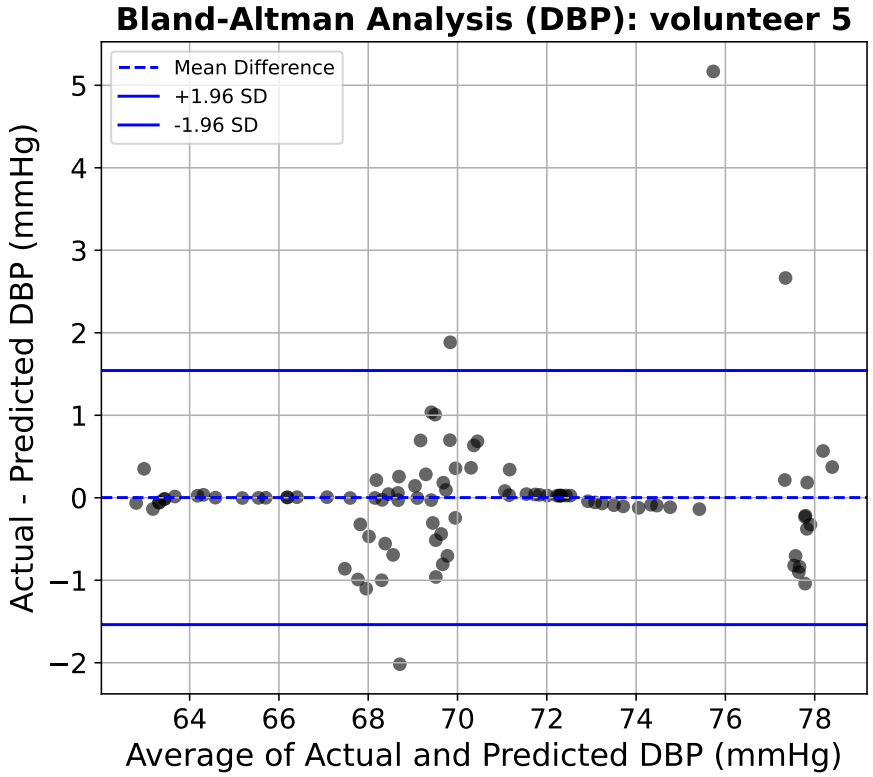

(b)

Figure 5.25: *Bland-Altman analysis for the* ***volunteer 5*** *test set. (a) SBP shows minimal systematic bias with narrow limits of agreement. (b) DBP shows no evident over- or underestimation, with tighter dispersion.*

The normality of the BP data was assessed for each volunteer, and the subsequent paired comparisons were selected accordingly (paired t-test when normality was not rejected; Wilcoxon signed-rank otherwise). Using a two-tailed $\alpha = 0.05$, no statistically significant differences were found between estimated and reference BP values for any volunteer in either SBP or DBP (all $p > 0.05$; Table 5.6). In most cases normality was violated, motivating the non-parametric test; where normality held (e.g., SBP in Volunteer 3 and both outcomes in Volunteer 12), paired t-tests were used and likewise yielded non-significant results. Overall, these analyses indicate that, within-subject, the estimator shows no systematic bias relative to the reference across volunteers.

ID	**BP**	**Normality (p)**	**Test Used**	**p-value**
1	SBP	0.0000	Wilcoxon	0.0955
	DBP	0.0003	Wilcoxon	0.2069
3	SBP	0.0883	t-test	0.1129
	DBP	0.0000	Wilcoxon	0.0676
4	SBP	0.0025	Wilcoxon	0.1223
	DBP	0.0000	Wilcoxon	0.1859
5	SBP	0.0000	Wilcoxon	0.5853
	DBP	0.0000	Wilcoxon	0.3290
9	SBP	0.0000	Wilcoxon	0.3953
	DBP	0.0000	Wilcoxon	0.6985
10	SBP	0.0002	Wilcoxon	0.5812
	DBP	0.0000	Wilcoxon	0.1954
12	SBP	0.0543	t-test	0.4125
	DBP	0.5419	t-test	0.1935
13	SBP	0.0000	Wilcoxon	0.8103
	DBP	0.0000	Wilcoxon	0.3912
14	SBP	0.0089	Wilcoxon	0.8899
	DBP	0.0692	t-test	0.6157
15	SBP	0.0000	Wilcoxon	0.0635
	DBP	0.0000	Wilcoxon	0.7567

Table 5.6: Normality and significance test results for each volunteer. All comparisons were not statistically significant ($p > 0.05$).

Comparison with Previous Work

The findings of this study are consistent with and extend those reported by Zaki [102], who investigated pulse arrival time (PAT), measuring PPG signals using plastic optical fibre (POF) combined with ECG. In their Chapter 5 validation, PAT demonstrated a stronger correlation with SBP than with DBP, particularly when measured at the fingertip, while wrist and underfoot locations yielded weaker and less reliable trends. Their calibration approaches, based on pedal exercise and one-step cuff calibration, achieved moderate agreement with reference SBP (correlation coefficients up to $r = 0.65$, mean absolute error $\approx$ 7–9 mmHg), but remained limited by site dependence and static calibration models. In contrast, the present work demonstrates that FBG-cantilever sensors can reliably capture beat-to-beat PAT during controlled cycling exercise in human volunteers, and further advances the state of the art by integrating a GPR framework for personalised BP estimation.

Despite this, a strong inverse relationship between PAT and SBP, as well as with HR, was confirmed in the majority of participants, whereas PTT trends were less consistent due to sensor temporal resolution constraints. Moving beyond fixed calibration, the proposed GPR model achieved mean absolute errors as low as 3.9 mmHg for DBP and within 10 mmHg for SBP across most participants. This performance is comparable to or better than the best-case calibration reported by Zaki, while additionally providing probabilistic confidence intervals and greater adaptability to inter-subject variability. Together, these findings reinforce PAT as the most reliable parameter for cuffless blood pressure monitoring, with the present work advancing previous approaches by introducing a robust FBG-based sensing modality, a physiologically relevant exercise protocol for BP modulation, and a machine learning framework for personalised BP estimation.

Finnegan et al. [36] investigated PAT as a surrogate for BP under pharmacological modulation in a cohort of thirty healthy volunteers infused with phenylephrine. Both PAT and PTT were strongly and inversely correlated with BP (me-

dian $r < -0.8$), with PTT marginally outperforming PAT in terms of correlation strength. The pre-ejection period (PEP) contributed approximately 30% of PAT but remained nearly constant during vasoconstriction, allowing PAT to track BP reliably in this setting. Importantly, Finnegan et al. reported that individualised *a posteriori* calibration models outperformed population-based ones, achieving root mean squared errors of 5.5 mmHg (SBP) and 3.8 mmHg (DBP). In contrast, the present study validated PAT under physiological modulation through exercise, demonstrating similarly strong SBP correlations but extending the analysis with a machine learning framework. The proposed GPR model matched or exceeded the accuracy of the best-performing *a posteriori* models. These findings reinforce the consensus that PAT can serve as a reliable surrogate for cuffless BP estimation when subject-specific modelling is applied, with the present work demonstrating its applicability in ambulatory conditions.

Finally, in the context of machine learning models for BP estimation as reviewed in Section 2.2, numerous studies have explored both conventional and deep learning approaches, ranging from support vector machines (SVM) and artificial neural networks (ANN) [76, 79, 80] to advanced recurrent and convolutional networks [78, 83, 84]. These methods often achieved mean absolute errors in the range of 3–8 mmHg, particularly for DBP, but typically relied on extensive feature engineering or computationally intensive architectures. Bayesian frameworks such as Gaussian Process Regression (GPR) have been less frequently applied but have shown competitive accuracy with added interpretability and efficiency [85]. The present study contributes to this growing body of literature by implementing a tailored GPR model directly on PAT features derived from FBG and ECG signals, achieving exploratory acceptable errors (3.9 mmHg for DBP, within 10 mmHg for SBP) while offering probabilistic confidence intervals. In doing so, it combines the practical strengths of lightweight Bayesian regression with the novel robustness of optical FBG sensing, demonstrating a viable pathway towards embedded, real-time cuffless BP monitoring.

In contrast to more complex, data-intensive deep learning approaches, the lightweight Bayesian GPR framework met the exploratory accuracy targets defined for this proof-of-concept system, achieving errors within ±10 mmHg for SBP and 4 mmHg for DBP. Crucially, the model incorporates individual calibration and relies primarily on hemodynamic parameters rather than demographic data, contributing a key concern in the development of cuffless BP monitors where population-based models often fail to generalise reliably across individuals.

Table 5.7: Comparison of representative studies on PAT/PTT and BP estimation.

Study	**Protocol**	**Signals / Definition**	**Model & Performance**
Zaki (2019)	Cycling exercise (physiological BP modulation); one-step cuff calibration.	POF + ECG. PAT/PTT at fingertip vs wrist/underfoot.	Linear calibration. r up to 0.65; MAE ≈ 7–9 mmHg (SBP).
Finnegan et al. (2021)	Phenylephrine infusion (pharmacological vasoconstriction).	ECG + PPG + ICG. PAT = ECG→PPG; PEP = ECG→ICG (B-point); PTT = PAT − PEP (central→peripheral).	Population vs *a posteriori* models. Best: RMSE 5.5 mmHg (SBP), 3.8 mmHg (DBP); PAT/PTT median $r < -0.8$.
Best ML (Su 2018; Paviglianiti 2022)	Database-driven (e.g., MIMIC), resting signals.	ECG + PPG; PAT/PTT + morphology/spectral features.	LSTM / ResNet+LSTM. Su: RMSE 3.7/2.4 mmHg (SBP/DBP). Paviglianiti: MAE 4.1/2.2 mmHg.
This Work (2025)	**Cycling exercise (physiological BP modulation).**	**PAT = ECG→FBG-cantilever**	**Gaussian Process Regression, MAE ≤ 10 mmHg (SBP); 3.9 mmHg (DBP). Best RMSE : 1.28 mmHg (SBP), 0.79 mmHg (DBP)**

5.3 Summary

This chapter proposed an exercise protocol to evaluate the ability of the FBG-cantilever sensing system to track physiological blood pressure changes by measuring PTT (upper arm to wrist) and PAT (ECG R-wave to wrist/upper arm). The study was approved by the Ethics Committee of the University of Nottingham.

The results demonstrated that pulse transit time (PTT), derived from FBG-cantilever sensors, shortened with increasing blood pressure and heart rate during exercise, consistent with the Moens-Korteweg and Hughes formulation linking pulse wave velocity to arterial stiffness. Across eight volunteers, SBP and HR increased with physical activity while DBP showed only modest changes, and PTT distributions narrowed with maximum values typically decreasing by 50-120 ms. Although signal variability and the 200 Hz sampling rate of the miniature interrogator introduced artefacts such as jitter and occasional negative values, the physiological trend of PTT shortening with elevated cardiovascular load was evident, particularly in volunteers 1, 4, 5, and 9. Compared with Wang et al. (2024) [74], who reported stable resting PTT values (29 ms) using a higher-resolution (1 kHz) system, this work highlights the trade-off between temporal resolution and wearable form factor, but crucially extends the evidence by showing dynamic haemodynamic modulation. These findings confirm that FBG-based sensing, even under reduced resolution, can capture physiologically driven changes in PTT, supporting its potential for ambulatory BP monitoring.

Similarly, pulse arrival time (PAT), which incorporates both the pre-ejection period (PEP) and arterial transit time, generally shortened with exercise as SBP and HR increased. Across ten volunteers, PAT reductions ranged from 20-150 ms, although inter-individual variability reflected differing PEP contributions and beat-to-beat dynamics. Volunteer 9 showed the clearest trend, with PAT decreasing from 170 ms at rest to 25 ms after 1 min of cycling, alongside a 27 mmHg rise in SBP and a 56 BPM increase in HR, demonstrating the strong coupling

between haemodynamic load and pulse arrival timing. Compared with Finnegan et al. (2021) [36], who reported smaller PEP effects and robust PAT-SBP correlations under pharmacological modulation, our exercise-based protocol revealed similar inverse trends but with greater variability, underscoring the challenge of uncontrolled physiological perturbations. Weaker correlations with DBP were consistent with exercise physiology, where reductions in systemic vascular resistance buffer DBP changes. Overall, these findings confirm that PAT is sensitive to acute haemodynamic changes but emphasize the need to account for PEP and inter-individual variability to improve robustness in BP estimation.

The GPR model further demonstrated promising performance in estimating SBP and DBP from PAT features across the cohort. Prediction plots showed close alignment between predicted and reference values, with narrow confidence intervals and minimal systematic bias. Volunteer 5 achieved the strongest performance, with MAE values below 1 mmHg and R^2 above 0.8 for both SBP and DBP. Across participants, DBP predictions were generally more accurate (MAE 0.4-3.9 mmHg) than SBP (MAE 0.8-11.7 mmHg), though variability persisted in some cases. Importantly, no statistically significant differences ($p > 0.05$) were found between estimated and reference BP values for any volunteer, reinforcing the robustness of the approach.

When compared with prior studies, this work represents a clear advancement in cuffless BP estimation. Zaki's optical fibre approach achieved only moderate correlations with errors of 7-9 mmHg, while Finnegan et al. reported strong inverse PAT-BP relationships under pharmacological modulation (RMSEs: 5.5 mmHg for SBP, 3.8 mmHg for DBP). In contrast, the present study validated FBG-cantilever sensors under exercise-induced haemodynamic changes, demonstrating that GPR can deliver comparable or superior accuracy while also providing probabilistic confidence intervals and adaptability to inter-individual variability. Unlike more complex, data-intensive deep learning approaches, the lightweight Bayesian GPR framework met the exploratory accuracy targets defined for this proof-of-concept

system, achieving errors within ±10 mmHg for SBP and 4 mmHg for DBP. Importantly, the model incorporates individual calibration and relies primarily on hemodynamic rather than demographic parameters, addressing a key concern in cuffless BP monitoring where demographic-based models often fail to generalise reliably across individuals [24].

This chapter therefore accomplished two key objectives of the research: *to evaluate the sensor system's accuracy and reliability through human subject testing*, and *to model the non-linear relationship between BP and timing features (PAT/PTT) using Gaussian Process Regression (GPR)*. The presented work constitutes the processing and initialisation layers of the proposed cuffless BP monitor (Figure 2.7) and contributes to addressing current challenges in cuffless BP monitoring, particularly the reliable tracking of BP under dynamic physiological conditions.

The findings from GPR modelling align directly with the proof-of-concept design specifications and goals: the system successfully demonstrated technical feasibility, signal fidelity, and algorithmic validity, achieving exploratory accuracy targets (≤10 mmHg for SBP, ≈4 mmHg for DBP) while confirming reproducibility through statistical testing. Performance across individuals, however, varied. Robust models with $R^2 > 0.75$ were obtained for three volunteers (IDs 5, 9, and 15), indicating strong predictive capability under favourable signal conditions. Moderate performance was observed in a subset of participants (e.g., IDs 1, 4, and 10), while poor correlations (low or negative R^2) were found in others (e.g., IDs 12, 13, and 14), reflecting the sensitivity of the approach to signal quality and limited data per subject.

These results suggest that while the feasibility of PAT-based GPR modelling has been demonstrated, its reliability can be further strengthened by improving the robustness of the signal acquisition hardware, particularly in enhancing waveform sharpness and temporal resolution, as well as by increasing dataset size to better capture inter- and intra-subject variability. Such improvements are expected to enhance generalisability and reduce the performance gap across individuals,

thereby providing a stronger foundation for future ambulatory, real-time cuffless BP monitoring systems.

From an accuracy perspective, the MAE values are especially encouraging: for several volunteers, errors were below 1 mmHg for DBP and under 3 mmHg for SBP, which is well within the exploratory PoC targets and compares favourably with existing literature. Even in cases with moderate or poor correlations, the MAE remained within a clinically acceptable exploratory range, reinforcing the potential of this approach. This highlights that, despite variability in R^2 across individuals, the GPR model was able to deliver consistently low average errors, suggesting that with improved signal quality and larger datasets, accuracy could reach levels suitable for future clinical translation.

6. FC-GAN model for pulse reconstruction

Chapter 5 showed that the FBG-cantilever sensing system tracks acute haemodynamic changes via PTT/PAT shortening during exercise, but also exposed practical limits for ambulatory use – motion artefacts, sampling constraints, jitter, and dropouts – that impair fiducial detection and destabilise timing features and GPR-based BP estimation. This motivates inserting a signal-level reconstruction stage into the processing layer of the proposed cuffless BP architecture (Figure 2.7) to restore physiologically plausible morphology *prior* to feature extraction.

In this chapter, a GAN with fully connected layers (FC-GAN) is developed and trained on an artificially corrupted dataset derived from the public MIMIC-II PPG database – using PPG as a widely available exemplar of pulsatile signals – and its performance is validated against relevant state-of-the-art models. Cross-domain applicability is then assessed by applying the trained model to FBG arterial pulses from Chapter 5, and the chapter concludes with proposals for further validation and deployment considerations for real-time ambulatory monitoring.

As previously discussed in Section 1.9, cuffless BP monitoring in ambulatory settings is dominated by non-stationary distortions – transmural and hydrostatic pressure shifts, variable contact pressure, and motion artefacts – that alter waveform amplitude, baseline, and morphology; FBG-specific factors (e.g., spectral crosstalk, interrogator drift) further compound the problem [31, 57, 61–67]. As reviewed in Section 2.3, traditional denoising (ICA/SSA/wavelets) and signal-

quality gating can help [89, 90], and accelerometer-assisted pipelines often perform best [91, 92], but they add hardware/energy complexity and are not always feasible (e.g., fibre-probe deployments [99, 100]). Generative models – such as PCA-SRGAN and CycleGAN – have broadened applicability by enabling learning from unpaired data and have been adopted in biomedical imaging; however, unpaired image-to-image approaches typically require 2D embeddings and higher computational cost, while deep autoencoders, though improving SNR, may blur fiducials [94–97].

Novelty and contributions. Building on GANomaly [101], an FC-GAN tailored to *1D* pulsatile reconstruction is introduced that replaces convolutional blocks with fully connected layers, enabling a paired corrupted→clean mapping that preserves physiologically critical fiducials while avoiding costly 2D re-encoding. The contributions are: a lightweight, CPU-only streaming recipe (short, causal windows; overlap-add; confidence gating) that integrates cleanly into the cuffless-BP processing layer; an auxiliary-free design that dispenses with IMU/ECG inputs for broader applicability (e.g., fibre-probe deployments); a cross-domain application from PPG to FBG signals demonstrating modality-agnostic feasibility; and a principled roadmap for robustness (HR-aware augmentation, timing/shift-invariant objectives, variance-preserving HR warping) together with a transparent discussion of limitations (HR-coverage imbalance, synthetic-real gap) and their mitigations.

6.1 Methods

Figure 6.1 illustrate the process pipeline for the development of the FC-GAN model. First (top-panel) PPG segments from the BIDMC dataset undergo feature extraction and an SVM classifier separates them into *clean* and *noisy* sets; the clean subset serves as ground truth. Next (middle-panel), an artificial corruption module distorting the clean segments to create matched clean-corrupted pairs

that form the training/validation/test sets. Finally (bottom-panel), the FC-GAN learns a mapping from corrupted inputs to their clean targets and, at inference, produces morphology-restored signals.

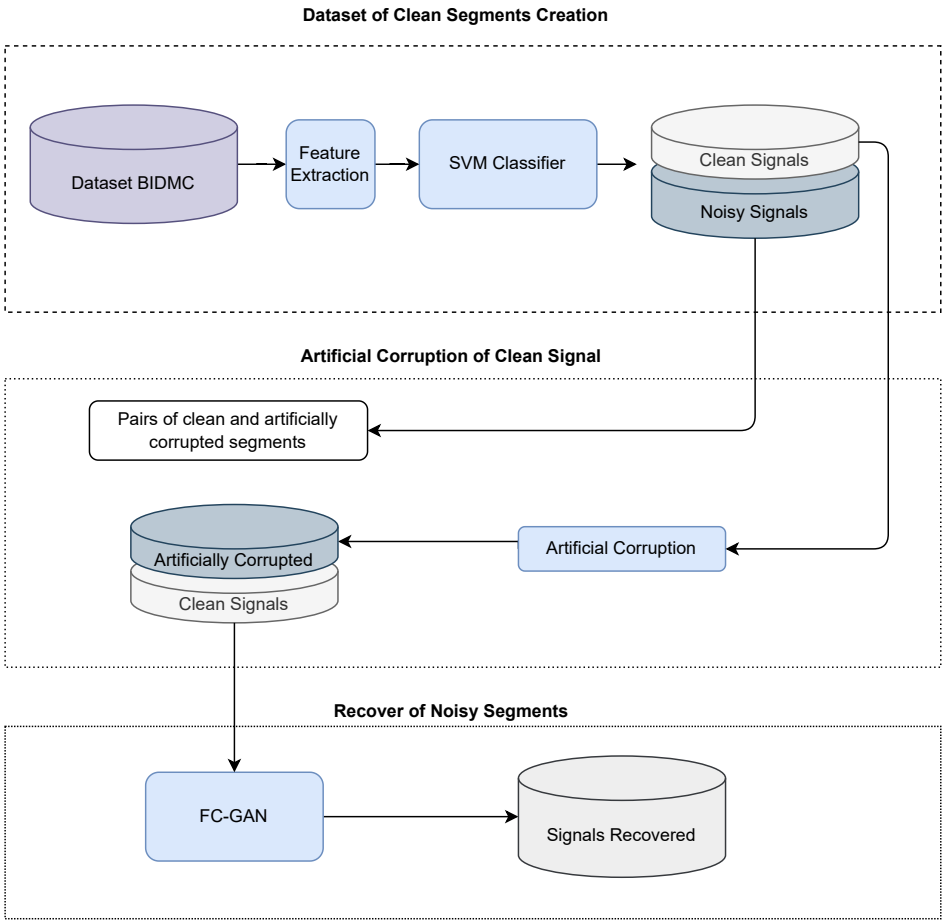

Figure 6.1: *Schematic of the methodology to build and train an FC-GAN for pulsatile signal reconstruction – clean signals are collected, synthetically corrupted to produce clean-corrupted pairs, and used to train the network to restore pulse morphology.*

6.1.1 Artificial Corrupted dataset

The dataset used in this work was the BIDMC Heart Rate Dataset [131], a subset of the MIMIC-II waveform database, comprising 7,949 thirty-two-second time-series segments from 53 patients with PPG (125 Hz) and ECG-derived heart rate (HR). For this study, recordings were partitioned into 8-second segments,

yielding 31,796 samples.

Signal Quality Assessment

A signal-quality assessment was applied to the BIDMC Heart Rate Dataset to isolate clean PPG segments. The goal was to assemble a *dataset* in which noise could be controlled, enabling paired inputs for the proposed network – a corrupted PPG segment (to be reconstructed) and its corresponding clean target. To obtain clean segments, a Support Vector Machine (SVM) classifier was trained using five features extracted from the PPG: cycle-to-cycle variations in kurtosis, skewness, and approximate entropy, plus Shannon entropy and spectral entropy [132]. For training and testing, 300 segments were manually labelled as clean or noisy according to the presence of only small DC amplitude fluctuations (DC amplitude $\leq$ 16% of the segment's overall maximum) and the absence of higher-frequency interference. The SVM used $C = 0.1$ and `random_state`=0, with a 75:25 train-test split.

The trained classifier was then applied to the remaining 31,496 segments. Clean segments were selected by thresholding the SVM decision function at 1.85, yielding 11,718 clean PPG segments. The decision-function value represents the distance of a sample's feature vector from the separating hyperplane; larger distances indicate higher classification confidence. Scores ranged from 0.03 to 2.25, and a cutoff of 1.85 best matched the manual criteria for clean PPG.

Finally, a synthetic corruption procedure was applied to the clean PPG segments identified by the SVM in the BIDMC Heart Rate Dataset to generate paired clean-corrupted data for training, validation and testing of the FC-GAN. For each clean 8 s segment, a sinusoidal disturbance was added to the terminal portion of the record (last 2, 4 or 6 s). The disturbance frequency was drawn from a (truncated) normal distribution over 0.01-10 Hz – frequencies commonly observed in PPG motion artefacts [133–135] – and its amplitude was scaled by one of four weights {1, 0.5, 0.33, 0.25}. At 125 Hz sampling, this corresponds to injecting the

disturbance into the last 250, 500 or 750 samples, yielding three corruption-length conditions. The signal-to-noise ratio (SNR) was computed for every corrupted segment. Note that the 0.01-10 Hz band also spans baseline wander (< 0.1 Hz), respiration-induced variations (0.1-0.5 Hz) and higher-frequency instrumentation noise (> 5 Hz), in addition to motion artefacts [136].

6.1.2 FC-GAN model

The FC-GAN used in this work is based on the GANomaly framework [98, 101, 137], in which an autoencoder acts as the Generator, a Feature Encoder extracts latent descriptors, and an encoder-only Discriminator encourages faithful reconstructions. This research contribution is to replace the convolutional blocks with fully connected (linear) layers throughout (Figure 6.2). It is believed for one-dimensional pulsatile signals without a strong spatial hierarchy, dense linear mappings provide global coupling across the entire waveform – treating all samples uniformly and capturing long-range dependencies – whereas convolutions emphasise local patterns that are especially beneficial in higher-dimensional data [103, 104]. Related evidence shows that simple perceptron-based linear models can effectively exploit global structure in 1D spectra to predict optical properties [105].

The Generator follows an Encoder-Decoder structure where the encoder and decoder comprise both four linear layers where in both cases the first three layers follow a LeakyReLU activation function. The feature encoder has the same structure as the encoder of the Generator. The encoder of the discriminator consists of four linear layers, where the first three include each a LeakyReLU activation function, while the last layer follows a sigmoid function. All the LeakyReLU activation functions were set with a negative slope of 0.5 with the operation in-place.

Loss Functions

Two main loss functions were implemented Generator L_G and Discriminator loss L_D, similar to the GANomaly approach implemented by [101]. The Discriminator

loss was minimised at the first iteration between batches, while the Generator loss was minimised in the remaining iterations in the training period. The Generator loss is a weighted linear combination of an encoder loss L_{enc}, contextual loss L_{con}, and adversarial loss L_{adv}, for a batch of size N.

$$L_G = w_{enc}L_{enc} + w_{con}L_{con} + w_{adv}L_{adv} \tag{6.1}$$

The encoder loss uses the outputs of the feature encoder (x, encoded features of the reconstructed signal and y, encoded features of the target signal) into a Smooth L1 loss function. This function combines the advantages of both L1 loss (mean absolute error) for large errors $|x_n - y_n| \geq \beta$ and L2 loss (mean squared error) for small errors $|x_n - y_n| < \beta$, using β as a regularisation parameter.

$$L_{enc} = \ell(x, y) = \{l_1, ..., l_N\}^T \tag{6.2}$$

$$l_n = \begin{cases} 0.5(x_n - y_n)^2/\beta, & \text{if } |x_n - y_n| < \beta \\ |x_n - y_n| - 0.5 \times \beta, & otherwise \end{cases}$$

The contextual loss takes the output of the reconstructed x and the target signal y to compute the negative value of the Signal to Noise Ratio.

$$L_{con} = -SNR(x, y) = -10log_{10}\left(\frac{P_y}{P_{noise}}\right) \tag{6.3}$$

$$\text{where, } P_{noise} = noise^2, \;\; P_y = y^2, \;\; noise = y - x$$

The adversarial loss used the outputs of the Discriminator and computes a mean squared error loss.

$$L_{adv} = \ell(x, y) = \{l_1, ..., l_N\}^T, \tag{6.4}$$

$$l_n = (x_n - y_n)^2$$

Meanwhile, the Discriminator loss uses the output of the Discriminator layers to compute a binary cross-entropy loss between the target and reconstructed input probabilities.

$$L_D = \ell(x, y) = \{l_1, ..., l_N\}^T, \tag{6.5}$$

$$l_n = -y_n \cdot log x_n + (1 - y_n) \cdot log(1 - x_n)$$

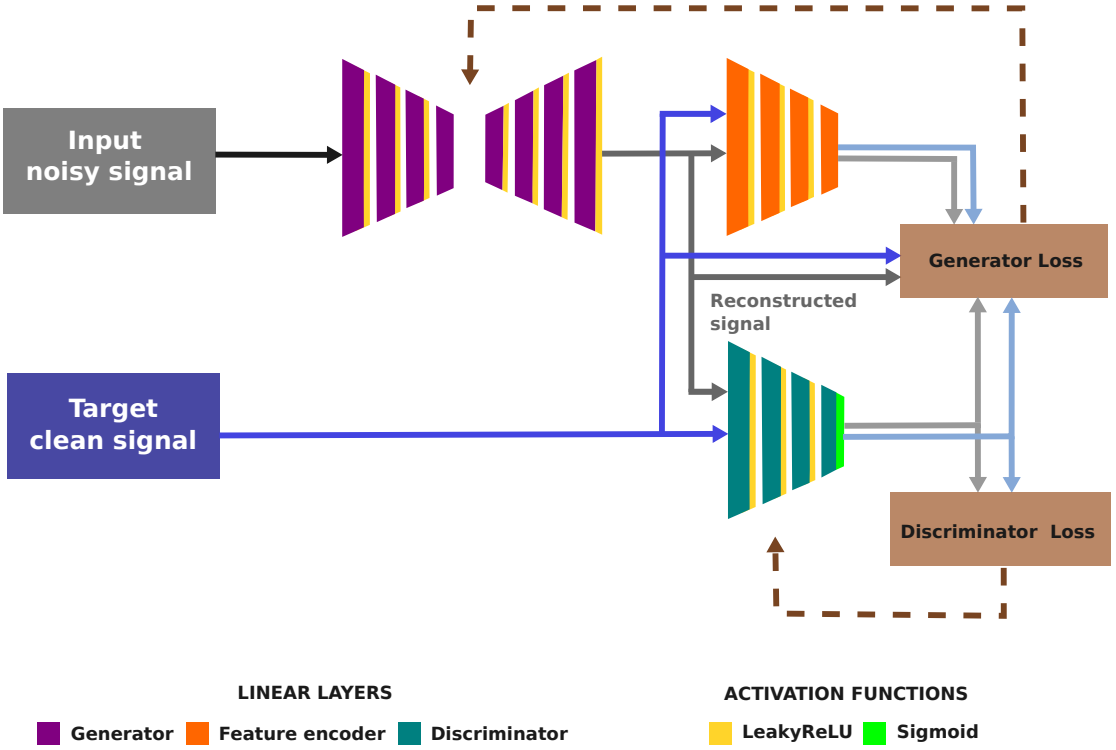

Figure 6.2: *Generative Adversarial Network with Fully Connected layers (FC-GAN). The Generator uses an auto encoder structure (encoder-decoder, each one of four layers, with LeakyReLU activation on the first three layers for both structures), and an additional feature encoder structure is used to compare additional features between the target and reconstructed signal that aids the optimisation of the generator Loss. Then the Discriminator consists of an encoder of four layers with Leaky ReLU layers in the first three layers and a Sigmoid function in the fourth layer that aids the discrimination of the reconstructed signals by comparing the target signal with the generated/reconstructed signal.*

The Smooth L1, mean squared Error and binary cross-entropy losses were implemented using the Pytorch libraries of each function. The β value for Smooth L1 loss function was set by default 1.0.

The Discriminator loss uses as an input the binary output of the Discriminator model which s if the reconstructed segments look like real or fake. Meanwhile, the Generator loss uses as an input the encoded features of the reconstructed segment. During the training stage, the model alternates between training the Discriminator loss (first iteration) and the Generator loss (subsequent iterations). This balances the learning of both optimisations to prevent one from overpowering the other.

6.1.3 Training and Application

To train the FC-GAN model to reconstruct the artificial corrupted segments, the input pairs: artificial corrupted segments, and the correspondent target clean segments were normalized in a range from 0-1 using z-score standardization. The distribution of data among the training, validation, and test sets followed an 80:10:10 ratio. The training set consisted of 9376 inputs. The training process ran 1000 epochs in total with a batch size of 356. The Adam Optimizer from Pytorch library [138] was used as an optimisation algorithm, with the Generator and Discriminator learning rates set at 1e$-$4, $\beta_1 = 0.5$ and $\beta_2 = 0.999$. These parameter values showed the best convergence rates among different combinations tested. The validation process was performed on 1172 input pairs, 10% of the dataset. The trained parameters were saved for the testing process and the remaining 10% of the dataset was tested. For every reconstructed segment after introducing the corrupted segments to the model in the testing phase, the SNR was determined.

6.1.4 FBG signal reconstruction

FBG signals from the human volunteer experiments (Chapter 5) were post-processed to reconstruct motion-degraded segments. Corrupted portions were first identified, and reconstruction was restricted to segments that (i) were preceded by at least 6 s of clean data and (ii) occurred at heart rates within 65-115 BPM. Each eligible corrupted region was then processed with a sliding 2 s window that included the immediately preceding clean context. For each window, the FC-GAN received the

corrupted input (plus clean context) and produced a reconstructed output; the windowed outputs were concatenated to form the recovered FBG segment. The detailed procedure is described below.

Procedure:

1. Check the HR from the signals to be in the range $65 < HR < 115$.
2. Prepare segment for reconstruction, 2 s of the corrupted segment with its previous 6 s. This data must be clean (Figure 6.4a).
3. Rescale the value of the corrupted data relative to the amplitude range of the clean data (Figure 6.4b).
4. Normalise the prepared segment between 0 and 1.
5. Downsample the prepared segment from 200 Hz to 125 Hz.
6. Apply the FC-GAN model recursively n times, n = 10 (Figure 6.3).
7. Slide to the next 2 s of the corrupted segment.
8. Once the corrupted finish the reconstruction, scale it within the range of the original clean signal and upsample back to 200 Hz.

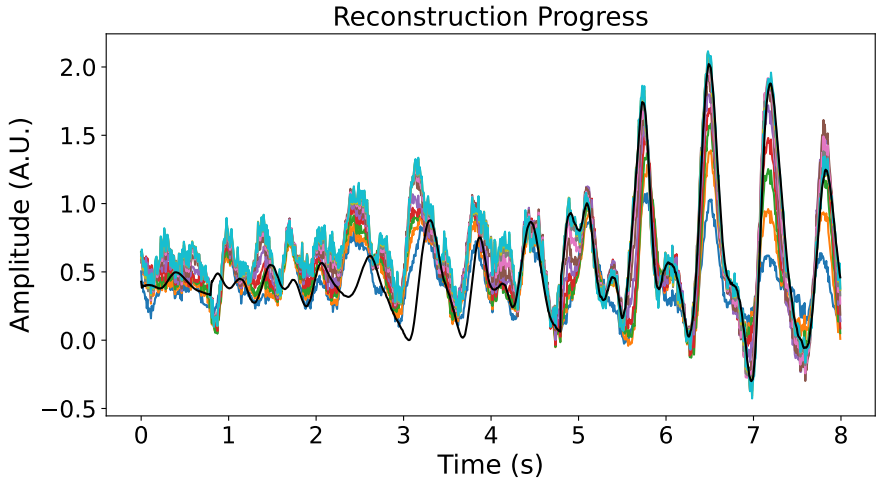

Figure 6.3: *Reconstruction progress after applying the FC-GAN model recursively 10 times, final iteration in black.*

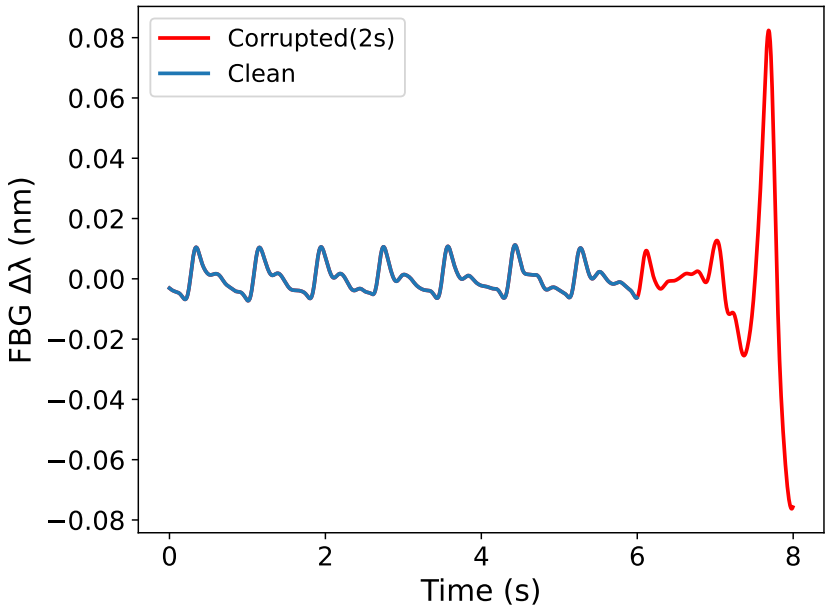

(a)

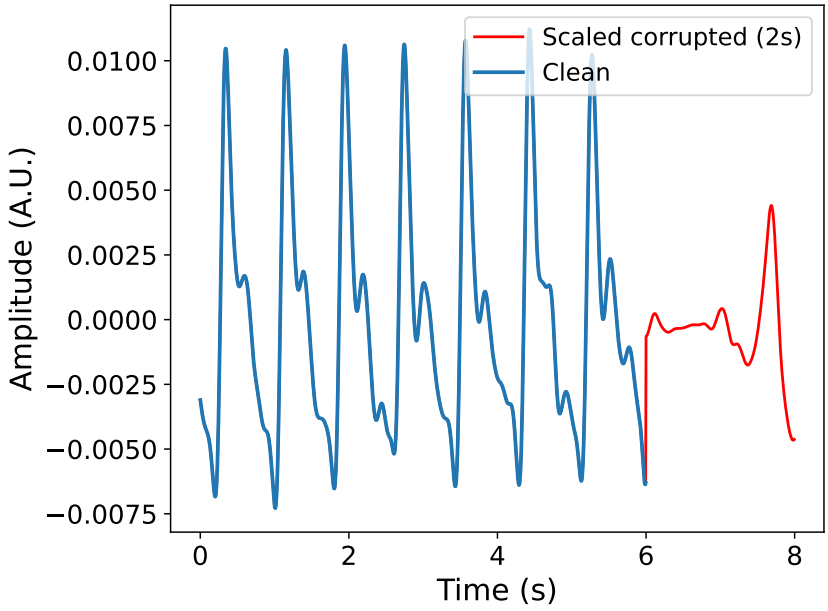

(b)

Figure 6.4: *(a) Prepared segment for reconstruction including 6 s of clean data and 2 s of the corrupted data. (b) Prepared segment, normalising the corrupted part within the range of the clean signal.*

6.2 Results

6.2.1 Model Performance Metrics

The reconstruction performance of the FC-GAN was evaluated on the test set of the artificially corrupted dataset described in Section 6.1.1, using several complementary approaches, including heart-rate (HR) agreement as a proxy for temporal-fiducial fidelity – because HR derives from beat-to-beat intervals, close HR agreement indicates that fundamental pulsatile frequency and fiducial timing (foot/-peak) are recovered even when amplitude scaling or baseline drift persist, and it can be cross-validated against ECG-derived HR in BIDMC.

A visual inspection was conducted first Figures 6.5 and 6.6 show two sets of pulsatile-signal reconstructions. In the first set (Figure 6.5), Figure 6.5a demonstrates successful recovery: the reconstructed waveform preserves beat morphology, fiducial points align with the clean reference, and the derived HR closely matches the target. Figure 6.5b shows modest degradation, plausibly due to low-frequency artefacts overlapping the fundamental HR band. In the second set (Figure 6.6), Figures 6.6a and 6.6b illustrate challenging cases where the reconstruction struggles to align fiducials with the clean signal. These examples correspond to target heart rates of 63.5 and 123 BPM – near the lower and upper extremes of the HR distribution represented during training – which likely contributes to the reduced performance.

Subsequently, two Bland–Altman (BA) analyses were performed to compare HR estimates across modalities. The first BA plot (Figure 6.7a) contrasts HR from the reconstructed PPG with ECG-derived HR from the BIDMC Heart Rate Dataset; the second (Figure 6.7b) compares reconstructed PPG HR with the target (clean) PPG HR. Additionally, the correlation between reconstructed and target PPG HR was computed (Figure 6.8). Agreement is generally strong within the mid-range of HRs (approximately 70–115 BPM); however, outside this range occasional

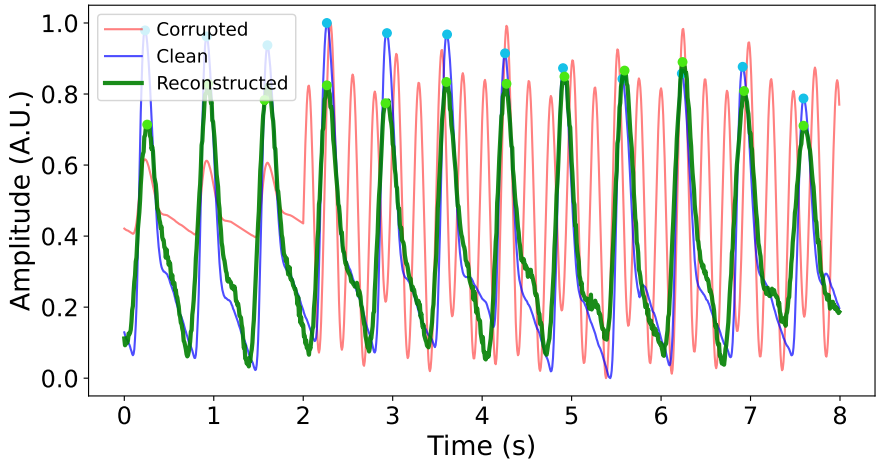

(a)

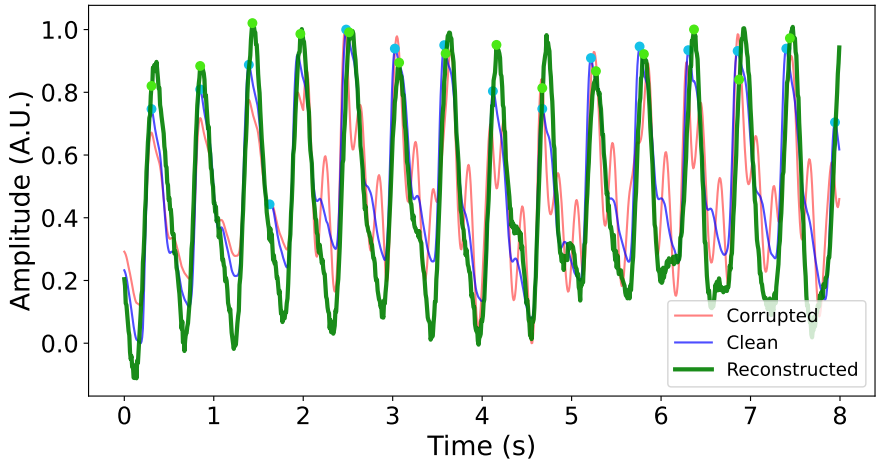

(b)

Figure 6.5: *Best-case reconstruction examples. Clean (blue), corrupted (red), and reconstructed (green) PPG segments. (a) Corruption in the last 6 s; recovered HR = 88.24 BPM for a target = 88.24 BPM; SNR improves from −8.44 to 9.95; noise frequency ≈ 2× the target PPG fundamental. (b) Corruption in the last 4 s; recovered HR = 94.95 BPM for a target = 93.17 BPM; SNR improves from −1.87 to 12.02; noise frequency ≈ 3× the target PPG fundamental.*

large discrepancies are observed, with absolute differences exceeding ±32 BPM, consistent with weaker correlation at the distribution tails in Figure 6.8.

The larger error in Figure 6.7a relative to Figure 6.7b is attributable to a windowing mismatch introduced when constructing the artificially corrupted dataset. The ECG-derived HR is referenced to the original 32 s BIDMC segments (i.e., averaged over the full 32 s window), whereas the reconstructed PPG HR is computed on 8 s subsegments. Consequently, temporal misalignment and differing averaging horizons inflate the ECG-PPG differences, while the PPG-PPG comparison in

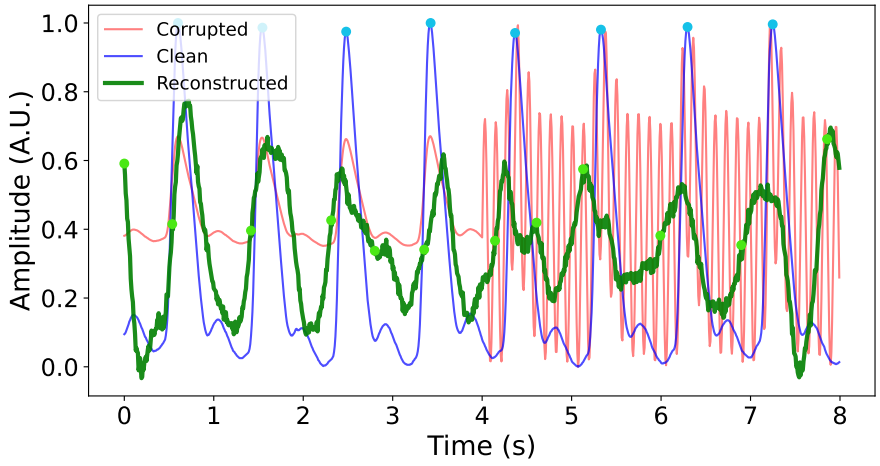

(a)

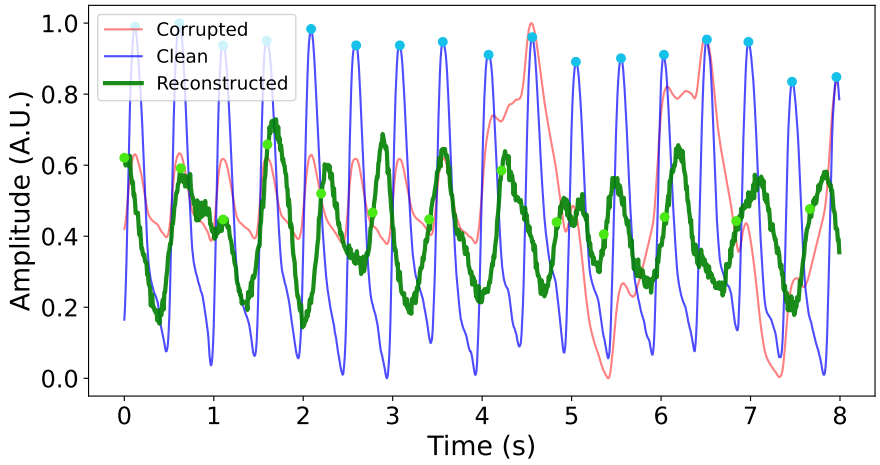

(b)

Figure 6.6: *Challenging (worst-case) reconstruction examples. Clean (blue), corrupted (red), and reconstructed (green) PPG segments. (a) Corruption in the last 4 s; recovered HR = 75.76 BPM for a target = 63.56 BPM; SNR improves from −6.30 to 3.31; noise frequency ≈ 10× the target PPG fundamental. (b) Corruption in the last 4 s; recovered HR = 114.51 BPM for a target = 123 BPM; SNR improves from −9.37 to 5.56; noise frequency roughly matches the target PPG fundamental.*

Figure 6.7b remains better aligned.

Figures 6.9 and 6.10 show the HR distributions for the training and test sets. The ECG-derived HR in the training set differs markedly from the test set – particularly with sparse coverage below 70 BPM and above 115 BPM – indicating a distributional mismatch. This imbalance likely explains the reduced reconstruction performance outside 70-115 BPM, as the model had limited exposure to these regimes during optimisation and therefore generalises poorly at the distribution tails.

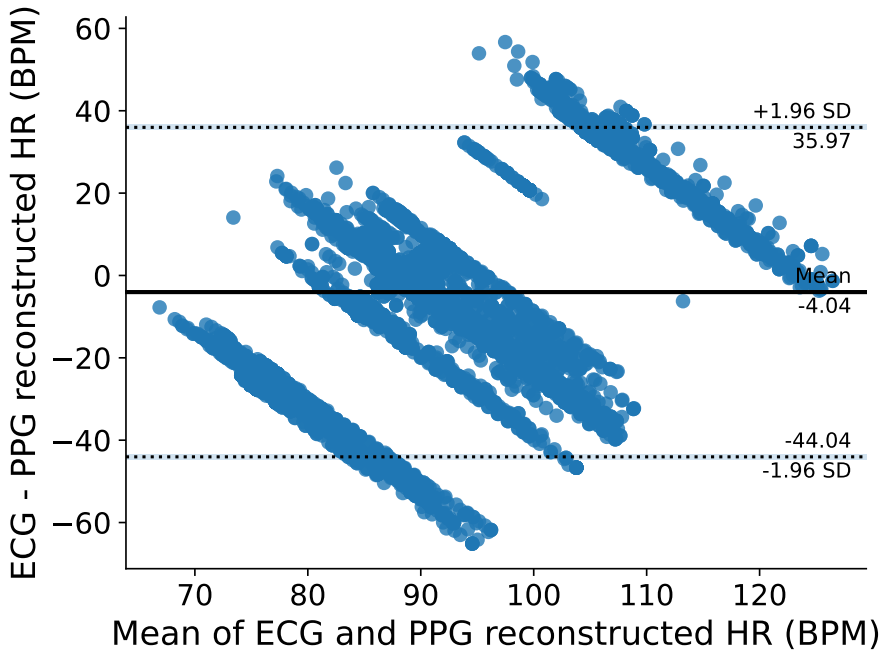

(a)

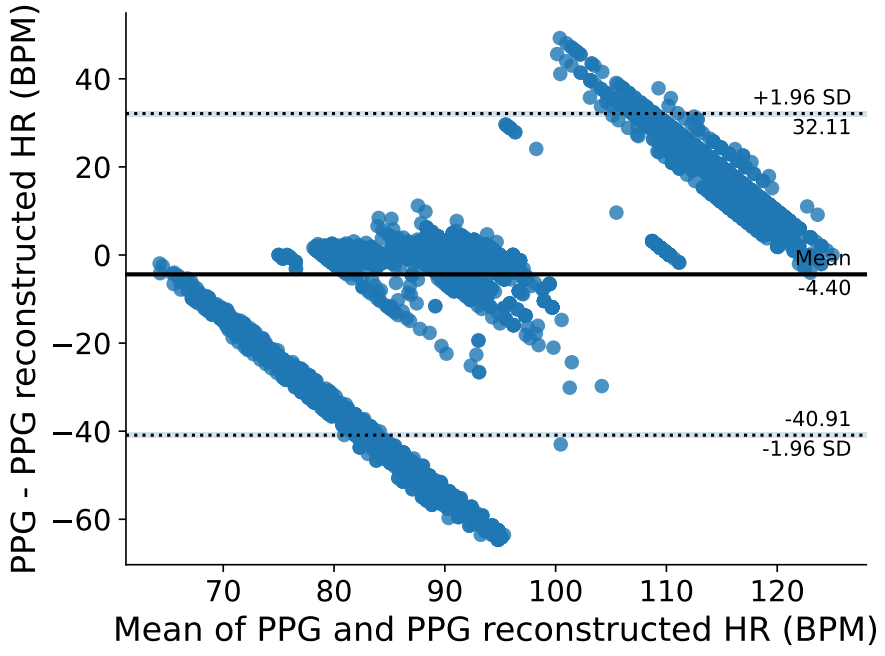

(b)

Figure 6.7: *Comparing HR from PPG and ECG using Bland-Altman analysis. (a) ECG vs. reconstructed PPG HR. (b) Target vs. reconstructed PPG HR. A large proportion of points (69% in (a) and 67% in (b)) fall within the limits of agreement (*±1.96 *SD). Points outside these limits typically correspond to distributions under-represented in training.*

Test-set performance was quantified using (i) the Euclidean distance between reconstructed and target PPG waveforms, (ii) the SNR of the reconstructed signal, and (iii) two mean absolute errors (MAE): one comparing reconstructed PPG HR

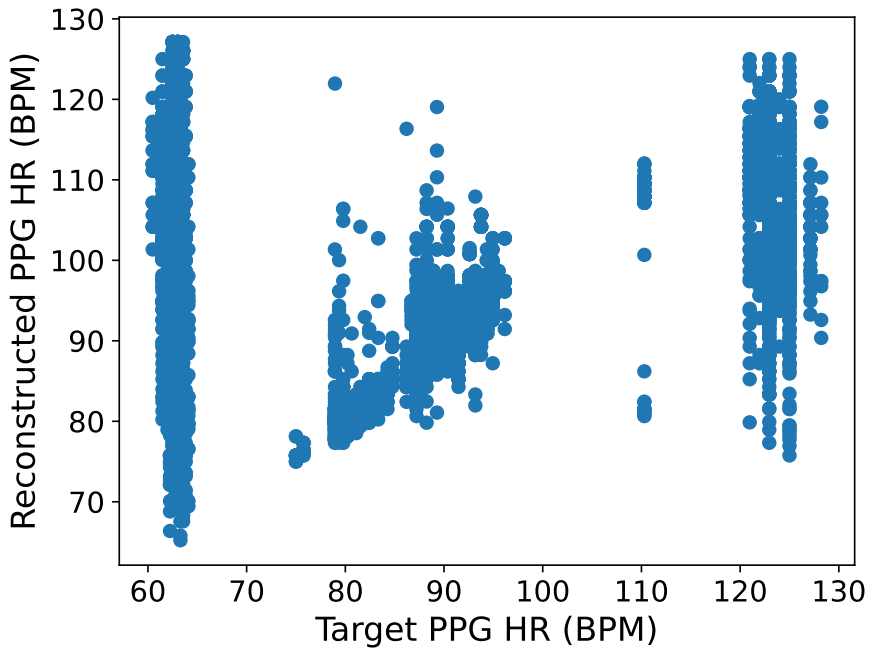

Figure 6.8: *Correlation between target and reconstructed PPG HR for the test set.*

to ECG-derived HR from the BIDMC Heart Rate Dataset, and a second comparing reconstructed PPG HR to target (clean) PPG HR. Based on the observed error patterns, results were stratified into two sets. *Set 1* comprises segments with HR in 70-115 BPM, where the model achieved strong reconstruction (mean Euclidean distance 3.85±1.33; $\text{MAE}_{\text{PPG vs target}} = 1.31$ BPM). *Set 2* contains segments outside 70-115 BPM, where performance degraded (mean Euclidean distance 9.50 ± 0.97; $\text{MAE}_{\text{PPG vs target}} = 29.1$ BPM), consistent with limited training coverage at the distribution tails.

Table 6.1 summarises results across all corruption lengths (2, 4, 6 s) and amplitudes (weights = 1, 0.5, 0.33, 0.25): the mean SNR was 11.8±2.4 for Set 1 and 3.55±0.95 for Set 2; $\text{MAE}_{\text{PPG vs ECG}}$ was 12.8 BPM (Set 1) and 20.8 BPM (Set 2); and the mean Euclidean distances were 3.85 ± 1.33 (Set 1) and 9.50 ± 0.97 (Set 2). Metrics computed per corruption case (length × amplitude) showed no material variation or consistent trend. Table 6.2 provides an example stratified by corruption length (2-6 s) at fixed amplitude (weight = 1).

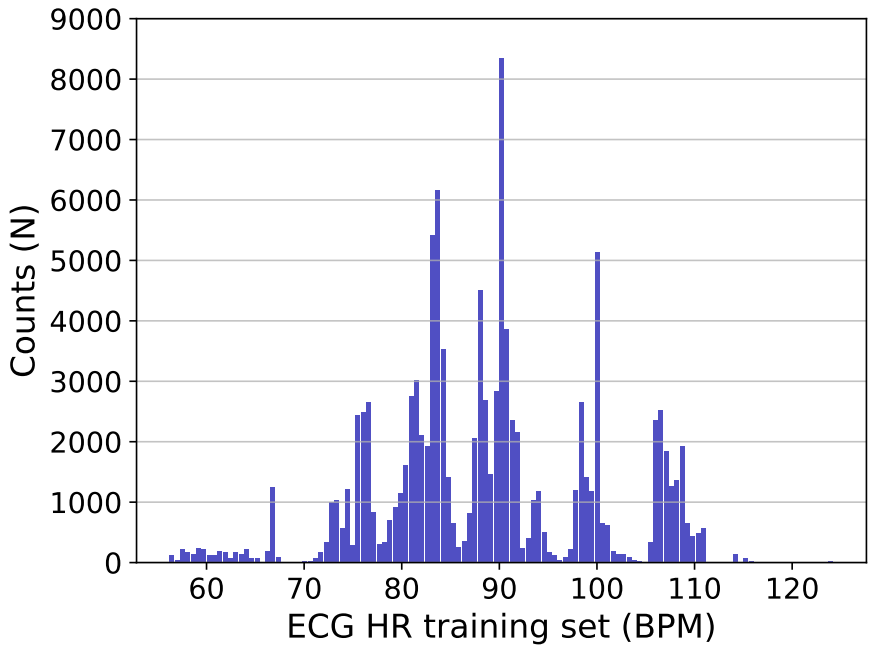

(a)

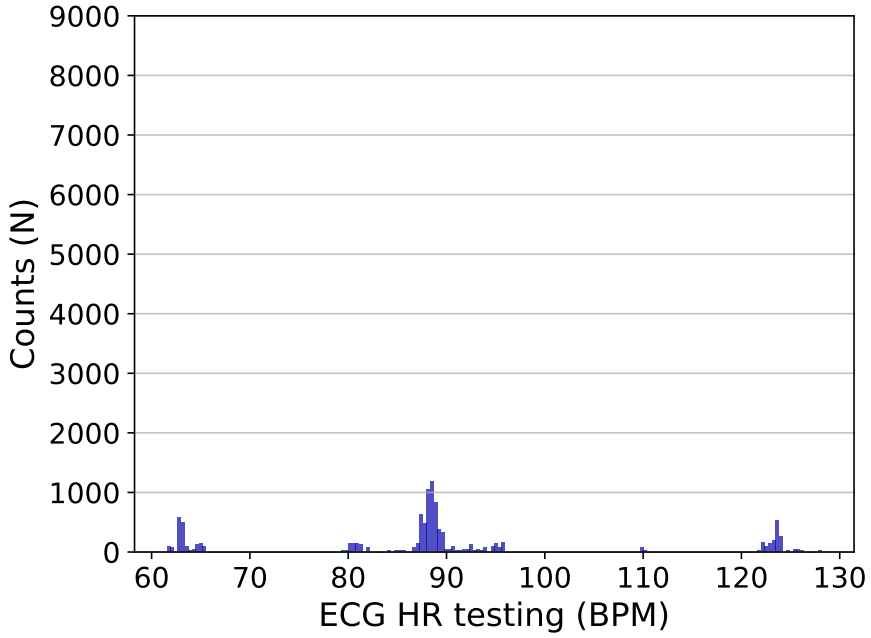

(b)

Figure 6.9: *ECG-derived HR distributions in the BIDMC Heart Rate dataset. (a) Training set. (b) Testing set.*

6.2.2 Comparison with Previous work

In the well-represented HR scenario (*Set 1*), the achieve MAE (1.31 BPM) of this research compares favourably with prior work – specifically Mullan et al. (2014) and Zhang et al. (2015), who reported MAE of 1.96 BPM and absolute error of

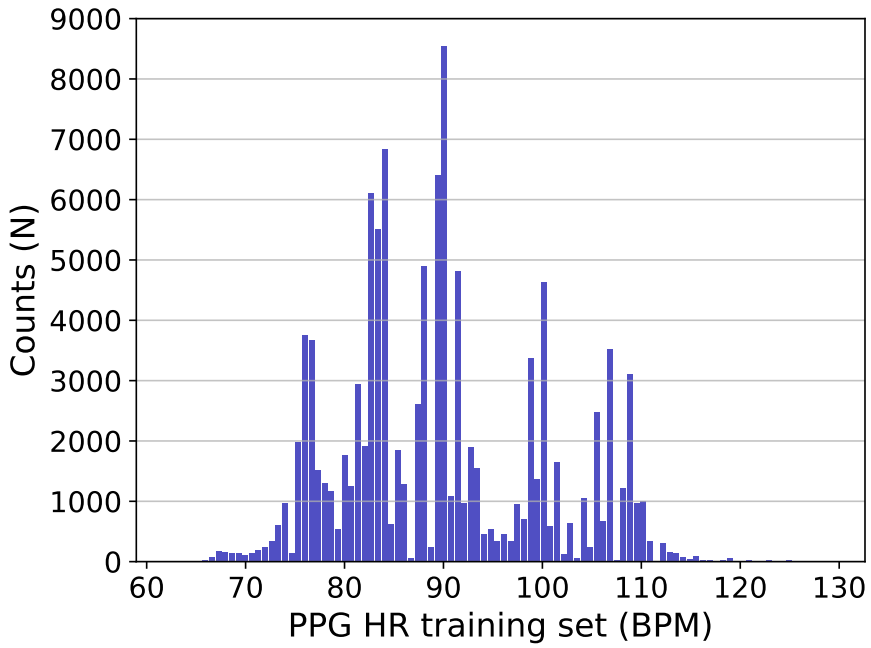

(a)

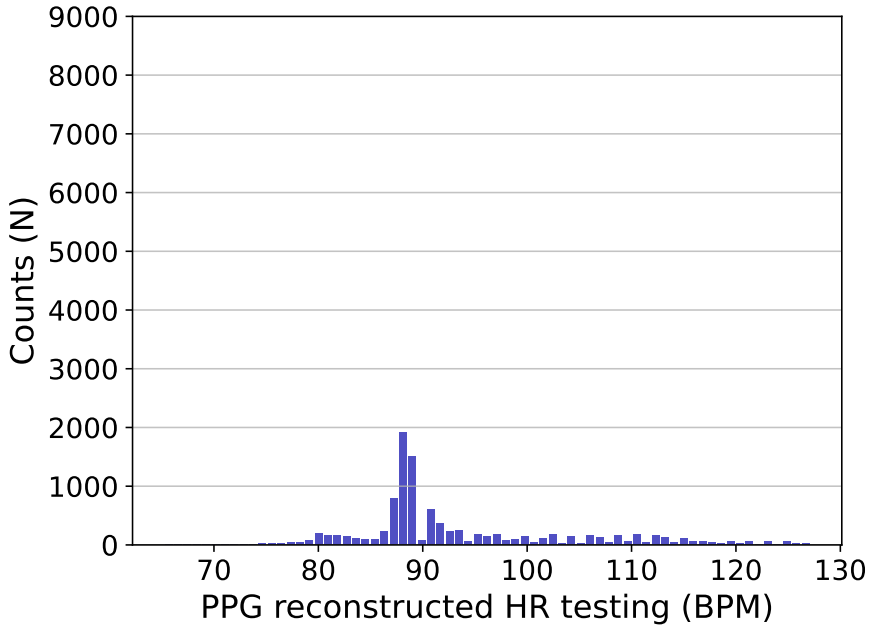

(b)

Figure 6.10: *Reconstructed PPG HR distributions. (a) Training set. (b) Testing set.*

1.83 BPM, respectively (Table 2.3). A key advantage of the proposed approach is that effective reconstruction is achieved *without* auxiliary accelerometer inputs. The main limitation is generalisation: due to the uneven HR distribution in the training data, performance degrades for HRs outside 70-115 BPM.

For a fair comparison, DC-GAN [98] and CycleGAN [97] were also implemented

Table 6.1: Assessment of the quality of the recovery signal based on different metrics. Set 1 corresponds to the population of signals from the testing set within a HR between 70 and 115 BPM and Set 2 corresponds to the population of signals from the testing set with a HR outside the range between 70 and 115 BPM.

Metric	**Set 1**	**Set 2**
Euclidean Distance	3.85 ± 1.33	9.5 ± 0.97
SNR(dB)	11.80 ± 2.4	3.55 ± 0.95
MAE (against ECG HR)	12.8 BPM	20.8 BPM
MAE (against PPG HR)	1.31 BPM	29.1 BPM

Table 6.2: Dataset with the last 2, 4, and 6 seconds corrupted, weight = 1.

	2 s		**4 s**		**6 s**	
Metric	**Set 1**	**Set 2**	**Set 1**	**Set 2**	**Set 1**	**Set 2**
Euclidean Distance	4.22 ± 1.58	9.71 ± 1.08	4.27 ± 1.94	9.64 ± 1.24	3.88 ± 1.17	9.22 ± 0.63
SNR(dB)	11.05 ± 2.67	3.37 ± 1.19	11.08 ± 2.9	3.45 ± 1.25	11.67 ± 2.37	3.88 ± 0.99
MAE against ECG HR (BPM)	12.76	20	12.9	19.68	12.83	20.7
MAE against PPG HR (BPM)	1.43	27.65	1.66	28.86	1.35	25.9

and adapted to the 8 s input-output pairs by resizing the first and last layers accordingly. In the CycleGAN pipeline (signal-to-image transformation), the image width was reduced from 1000 to 128 pixels to lower computational cost. Notably, CycleGAN performed best when trained on a smaller subset (870 segments), whereas DC-GAN and FC-GAN used the full training set (9,376 segments). Qualitative examples are shown in Figures 6.11 and 6.12.

For a fair comparison, DC-GAN [98] and CycleGAN [97] were implemented and adapted to 8 s input-output pairs by resizing the first and last layers to match the segment length. In the CycleGAN pipeline (signal-to-image transformation), the image width was reduced from 1,000 to 128 pixels to lower computational cost. Notably, CycleGAN achieved its best performance when trained on a smaller subset (870 segments), whereas DC-GAN and FC-GAN used the full training set (9,376 segments). Qualitative examples are shown in Figures 6.11 and 6.12.

Table 6.3 reports Euclidean distance, SNR, and MAE (against ECG HR and against target PPG HR) for all models across corruption lengths (2, 4, 6 s) and amplitudes (weights = 1, 0.5, 0.33, 0.25). The proposed FC-GAN achieves the lowest waveform error with a mean Euclidean distance of 3.85 ± 1.33 between reconstructed and target signals, whereas DC-GAN yields the largest error ($13.40 \pm$

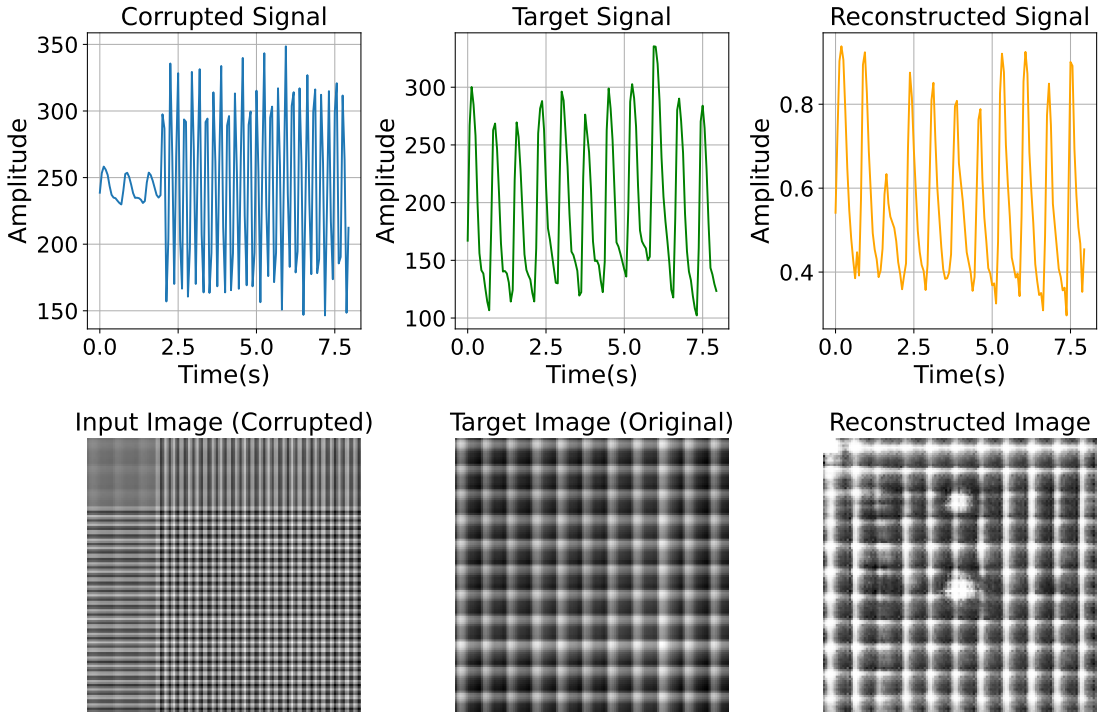

Figure 6.11: *Example of pulstatile reconstruction using Cycle GAN model in the artificially corrupted set.*

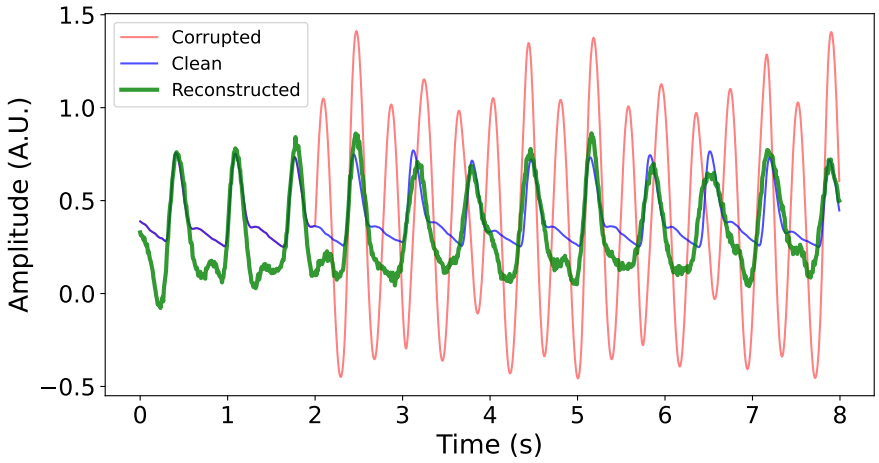

Figure 6.12: *Example of pulsatile reconstruction using DC-GAN model in the artificially corrupted set*

17.08). FC-GAN also attains the highest reconstructed-signal SNR (11.80 ± 2.40); DC-GAN and CycleGAN differ by $\sim$1 dB, with CycleGAN exhibiting lower variance. For HR accuracy, CycleGAN gives the best MAE against ECG-derived HR (9.65 BPM). In contrast, the best MAE against target PPG HR is obtained by DC-GAN (1.13 BPM), narrowly ahead of FC-GAN by $\sim$0.2 BPM, highlighting a trade-off between beat-level HR agreement and waveform-level fidelity.

Table 6.3: Results comparison of the implementation of Cycle GAN [97], DC-GAN [98] and FC-GAN (proposed methodology) models using the same metrics in the artificially corrupted datasets Section 6.1.1, Set 1 with HR between 70 and 115 BPM. Overall the best performance is shown in FC-GAN model considering all the metrics. However, the best MAE against ECG HR is shown by the Cycle GAN model 9.65 BPM and the best MAE against PPG HR is shown by the DC-GAN model 1.13 BPM with a difference 0.20 BPM with this research proposed method FC-GAN with a MAE against PPG HR 1.31 BPM.

Metric	**CycleGAN**	**DC-GAN**	**FC-GAN (proposed model)**
Euclidean Distance	5.45 ± 0.94	13.4 ± 17.08	3.85 ± 1.33
SNR(dB)	9.12 ± 1.29	8.12 ± 3.13	11.80 ± 2.4
MAE (against ECG HR)	9.65 BPM	12.58 BPM	12.8 BPM
MAE (against PPG HR)	2.48 BPM	1.13 BPM	1.31 BPM

Model's runtime

Real-time feasibility was assessed by measuring reconstruction runtime on the test set across corruption lengths (2, 4, 6 s) and amplitudes (weights = 1, 0.5, 0.33, 0.25). Benchmarks were executed on a MacBook Pro with an Apple M2 Pro and 32 GB RAM (CPU-only). The FC-GAN achieved a mean (±SD) processing time of 18.637 ± 0.265 ms to reconstruct an 8 s, 125 Hz segment, i.e., a processing delay $\sim$429$\times$ shorter than the window duration (8 s/0.018637 s $\approx$ 429). For comparison, DC-GAN required 24.486 ± 0.643 ms ($\sim$327$\times$ real-time) and CycleGAN $1{,}845.557 \pm 103.597$ ms ($\sim$4.33$\times$ real-time). Thus, FC-GAN is the fastest of the GAN-based models tested – consistent with its lower architectural complexity (fully connected layers only) – and comfortably satisfies real-time constraints under the evaluated settings.

6.2.3 Reconstruction of FBG signals

Figures 6.13-6.16 illustrate reconstruction results for four volunteers, demonstrating cross-domain applicability of the trained FC-GAN to recover FBG pulsatile signals. Only a very limited number of test segments met the selection criteria described in Section 6.1.4 – namely, at least 8 s of clean data immediately preceding the corrupted portion and heart rates within 65-115 BPM. Figures 6.13-6.15 show

plausible arterial pulse morphology within this HR range, whereas Figure 6.16 presents a challenging case at ≈ 66 BPM, consistent with degraded performance outside the well-represented HR regime in the artificial dataset.

A more quantitative analysis compared the heart rate derived from the preceding clean FBG segment (`HR target`) with that from the reconstructed segment (`HR reconstructed`). Table 6.4 summarises results for four volunteers: the reconstructed HR systematically overestimates the target HR, with MAE ranging from 7.99 to 28.38 BPM and a mean MAE of 15.93 BPM. Reconstructed values cluster narrowly around 91–94 BPM despite targets spanning 65.93–83.52 BPM, indicating an upward bias and variance shrinkage (regression toward $\sim$92 BPM). The smallest error occurs in Volunteer 2 (8.0 BPM), whereas the largest occurs in Volunteer 5 (28.4 BPM). The latter likely reflects a distributional mismatch: Volunteer 5's HR lies near the lower tail of the training HR regime, while the reconstruction pipeline regresses toward the central tendency, yielding inflated estimates at slower rhythms.

Table 6.4: Comparison of target vs. reconstructed HR from FBG segments. MAE reported in BPM. Across four volunteers, the mean MAE is 15.93 BPM.

Volunteer	**HR target (BPM)**	**HR reconstructed (BPM)**	**MAE (BPM)**
1	73.37	91.50	18.13
2	83.52	91.51	7.99
4	81.27	90.50	9.23
5	65.93	94.32	28.38

Although further validation is required in a larger dataset to establish the robustness of the FBG reconstructions, these results provide actionable insights for real-time clinical deployment of cuffless BP monitoring.

Real-time implications. Given the measured runtime ($\approx 18.6 \pm 0.3$ ms per 8 s segment, CPU-only), computational throughput is not the bottleneck; the dominant latency is the sliding window process and the recursive reconstruction for each window. In streaming use, the model should therefore be applied *recursively*

with short, causal windows and overlap (e.g., 2 s windows with 0.5-1 s hop), using the most recent clean/reconstructed context to condition the next inference. In our implementation the model was applied across 10 successive 2 s windows per corrupted region. Assuming near-linear scaling with input length, this corresponds to $\sim$ 4.7 ms per 2 s window ($18.6 \times \frac{2}{8}$ ms) and $\sim$ 47 ms total compute for 10 windows – well below the 2 s window duration and even a 0.5-1 s hop – satisfying real-time constraints. Overlap-add with a smooth cross-fade (e.g., Hann/Tukey taper) limits stitching artefacts [139]; a lightweight confidence gate (e.g., SNR or discriminator/feature distance) decides whether to accept a reconstruction or fall back to the raw segment, and optional per-window gain normalisation plus phase alignment (short-window cross-correlation) mitigates amplitude and timing drift.

Phase alignment. Reconstructed traces occasionally exhibit a small phase (time) shift relative to the target waveform. Online correction can be achieved by estimating the lag Δt via short-window cross-correlation between successive reconstructed windows (or with a clean context) and shifting by $\hat{\Delta} t$ before fiducial extraction. Training-time remedies include shift-invariant/DTW timing losses [140, 141] and constrain foot and peak times with explicit penalties to reduce group-delay artefacts.

HR mismatch: implications. The systematic overestimation of HR in Table 6.4 $\left(\Delta\mathrm{HR} = \widehat{\mathrm{HR}}_{\mathrm{rec}} - \mathrm{HR}_{\mathrm{target}} > 0;\ \text{average MAE} = 15.93\ \mathrm{BPM}\right)$ has several practical consequences for downstream cuffless BP estimation. Erroneous inter-beat intervals propagate to PAT/PTT, biasing BP estimates, degrading regression robustness, and obscuring true BP variability; they also perturb adaptive filter settings and relax acceptance gates, thereby admitting lower-quality beats. In practice, HR mismatch should be treated as a quality control signal: stratify performance by HR bins, flag windows with large $|\Delta\mathrm{HR}|$ for exclusion or fallback to clean context, tune acceptance gates accordingly, and report calibrated HR/BP metrics alongside raw values to communicate residual risk transparently.

Center-shifted, variance-preserving HR warping. To align a reconstructed segment to the preceding clean HR while preserving beat-to-beat variability, decompose the inter-beat intervals (IBIs) as $I_i = \tilde{I}_{\text{rec}}(1 + \epsilon_i)$, where $\tilde{I}_{\text{rec}}$ is a robust center (e.g., median IBI) and ϵ_i are relative deviations. Replace the center with the target $\tilde{I}_{\text{tgt}} = 60/\text{HR}_{\text{target}}$ while keeping ϵ_i unchanged. The cumulative target IBIs define new peak anchors that (set to the window length) induce a monotone time map; cubic-spline resampling then yields a warped signal whose *central* HR matches the context yet retains the original HR-variance pattern.

HR-range limitation. Because the training distribution is sparse outside 65 - 115 BPM, deployment in the volunteer dataset was constrained to scenarios 2 and 3 in Chapter 5 (where HR predominantly falls within this range). Performance degrades near the distribution tails (< 65 or > 115 BPM). Mitigations include rebalancing the training data with additional low/high-HR segments, HR-aware augmentation (tempo scaling and amplitude-frequency coupling), curriculum training that gradually widens the HR range, and auxiliary multitask heads (e.g., HR prediction) to encourage timing robustness across rates.

Synthetic-real gap and PAT/PTT coverage. Because reconstructions are synthetically generated, they should not be given equal weight to real physiological data when extracting timing features. To ensure that reconstruction benefits translate to cuffless BP estimation, quantify the *proportion of feature-bearing data* influenced by reconstruction and its timing impact: (i) *coverage* – the fraction of beats contributing to PAT/PTT that lie within reconstructed windows; (ii) *per-beat timing drift* – ΔPAT and ΔPTT between reconstructed beats and their clean references; (iii) *downstream sensitivity* – the change in GPR SBP/DBP accuracy when reconstructed beats are excluded; and (iv) *confidence stratification* – performance versus a reconstruction-confidence score (e.g., SNR or discriminator/feature distance). As a practical target, require median $|\Delta\text{PAT}|$ and $|\Delta\text{PTT}| <$ 5-10 ms with 95th-percentile errors within clinically tolerable bounds, and include an ab-

lation in which PAT/PTT are computed only from unreconstructed beats.

Amplitude modulation effect. A mild amplitude modulation is visible in reconstructed segments. This has little impact on timing-based features (HR, PAT/PTT), which depend primarily on fiducial timing rather than absolute amplitude; however, it may bias morphology- or amplitude-derived indices (e.g., pulse amplitude, upstroke slope). Mitigations include per-window gain normalisation and adding an amplitude-consistency term to the training loss.

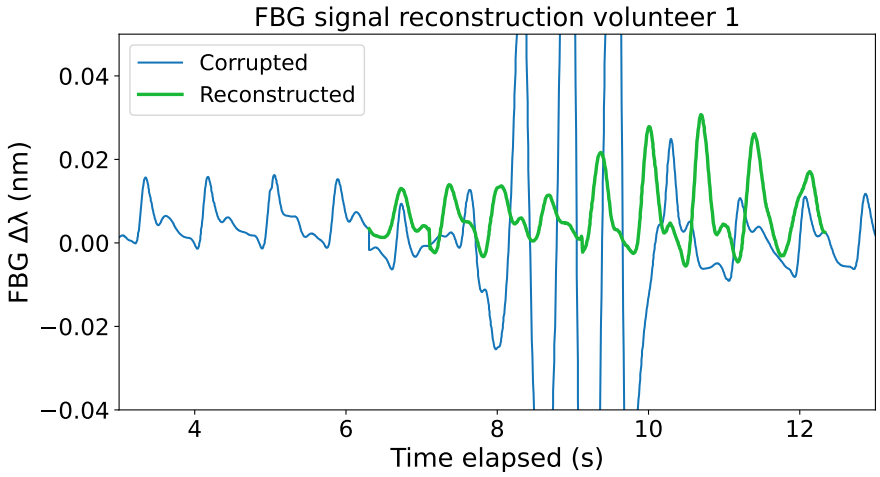

Figure 6.13: *FBG signal reconstruction with FC-GAN model. In blue the pulsatile FBG signal with some corruption of motion artifacts (from 6 to 11 seconds). In green is the reconstruction of this corrupted segment.*

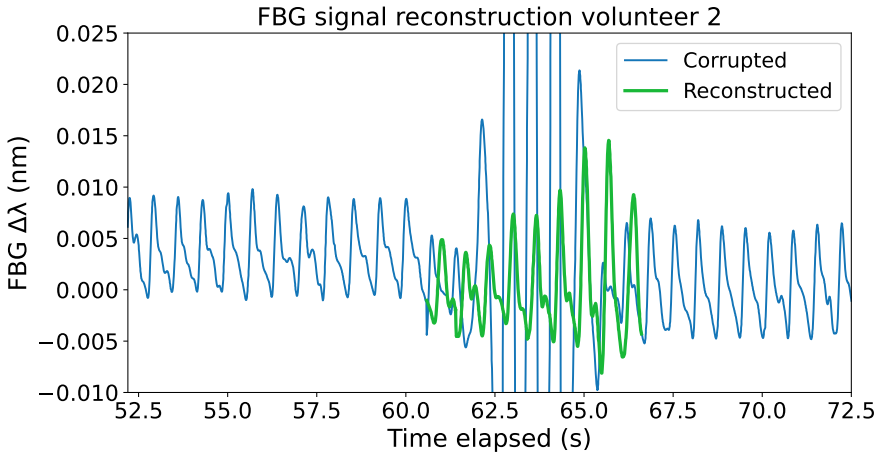

Figure 6.14: *FBG signal reconstruction with FC-GAN model. In blue the pulsatile FBG signal with some corruption of motion artifacts (from 60 to 67 seconds). In green is the reconstruction of this corrupted segment.*

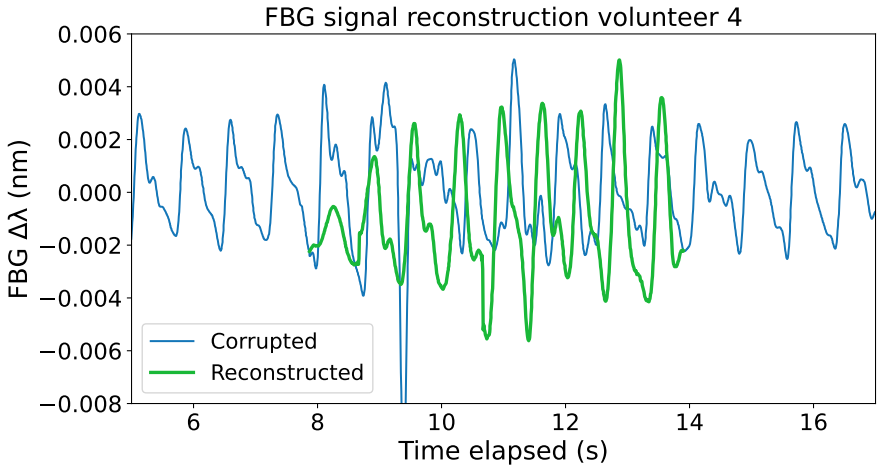

Figure 6.15: *FBG signal reconstruction with FC-GAN model. In blue the pulsatile FBG signal with some corruption of motion artifacts (from 8 to 14 seconds). In green is the reconstruction of this corrupted segment.*

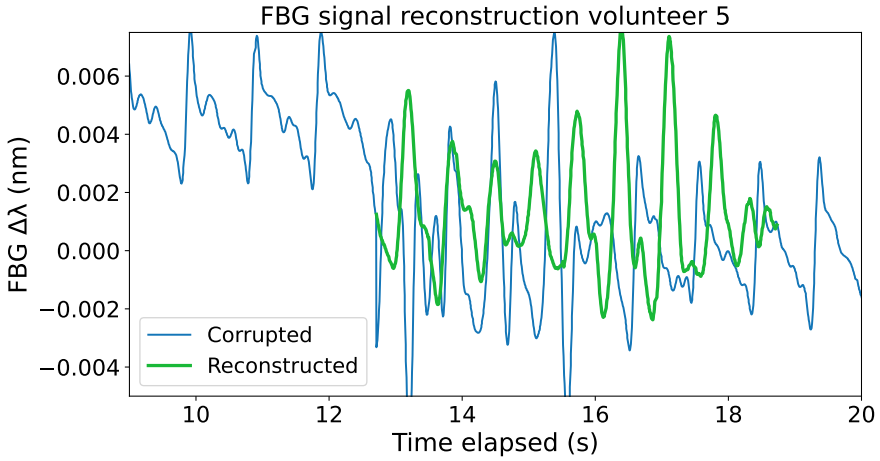

Figure 6.16: *FBG signal reconstruction with FC-GAN model. In blue the pulsatile FBG signal with some corruption of motion artifacts (from 12 to 17 seconds). In green is the reconstruction of this corrupted segment.*

6.3 Summary

This chapter developed a fully connected generative adversarial network (FC-GAN) and trained it on an artificially corrupted dataset derived from the public MIMIC-II PPG database – using PPG as a widely available exemplar of pulsatile signals – and validated its performance against relevant state-of-the-art baselines. Cross-domain applicability was then assessed by applying the trained model to FBG arterial pulses from Chapter 5. The chapter concludes with future insigths and deployment considerations for real-time ambulatory monitoring.

The results from testing the FC-GAN in the testing set of the artificially corrupted dataset demonstrates reliable reconstructions within the mid-range of heart rates ($\approx$ 70-115 BPM), where beat morphology and fiducials were preserved (Figure 6.5) and Bland-Altman agreement was strong; performance degraded near the distribution tails (e.g., 63.5 and 123 BPM in Figure 6.6), consistent with the training-test HR imbalance evident in Figures 6.9-6.10. The larger error in the ECG comparison (Figure 6.7a) relative to the PPG-PPG comparison (Figure 6.7b) is attributable to a windowing mismatch (ECG HR averaged over 32 s vs. reconstructed PPG HR over 8 s), and occasional large discrepancies ($|\Delta\text{HR}| > 32\,BPM$) occur mainly outside the well-represented HR band, as reflected by weaker tail correlations (Figure 6.8). Quantitatively, *Set 1* (70-115 BPM) achieved a mean Euclidean distance of 3.85 ± 1.33, SNR 11.8 ± 2.4, $\text{MAE}_{\text{PPG vs target}} = 1.31\,BPM$, and $\text{MAE}_{\text{PPG vs ECG}} = 12.8\,BPM$; *Set 2* (outside 70-115 BPM) showed a Euclidean distance of 9.50 ± 0.97, SNR 3.55 ± 0.95, $\text{MAE}_{\text{PPG vs target}} = 29.1\,BPM$, and $\text{MAE}_{\text{PPG vs ECG}} = 20.8\,BPM$. Stratifying by corruption length (2-6 s) and amplitude (weights = 1, 0.5, 0.33, 0.25) revealed no material or consistent trends (Tables 6.1-6.2), underscoring that HR distribution coverage – not corruption settings – was the dominant factor governing reconstruction performance.

In the well-represented HR regime (*Set 1*), the proposed FC-GAN achieved MAE = 1.31 BPM, comparing favourably with prior work by Mullan et al. (2014; 1.96 BPM) and Zhang et al. (2015; 1.83 BPM) (Table 2.3), while requiring no auxiliary accelerometer inputs; its main limitation is reduced generalisation outside 70-115 BPM due to the uneven training HR distribution. For a fair benchmark, DC-GAN [98] and CycleGAN [97] were adapted to 8 s input-output pairs (resizing first/last layers; CycleGAN image width $1000 \rightarrow 128$ pixels), with CycleGAN performing best on a smaller subset (870 segments) whereas DC-GAN and FC-GAN used the full set (9,376 segments) (Figures 6.11, 6.12). Across corruption lengths (2, 4, 6 s) and amplitudes (weights = 1, 0.5, 0.33, 0.25), FC-GAN delivered the lowest waveform error (Euclidean distance 3.85 ± 1.33) and highest SNR

(11.80 ± 2.40), while DC-GAN showed the largest error (13.40 ± 17.08); for HR accuracy, CycleGAN yielded the best MAE versus ECG-derived HR ($9.65\,BPM$), whereas DC-GAN achieved the best MAE versus target PPG HR ($1.13\,BPM$), narrowly edging FC-GAN by $\sim 0.2\,BPM$ – highlighting a trade-off between waveform-level fidelity and beat-level HR agreement (Table 6.3).

On CPU-only benchmarks (MacBook Pro, Apple M2 Pro, 32 GB RAM), FC-GAN reconstructed an 8 s, 125 Hz segment in 18.637 ± 0.265 ms – $\sim 429\times$ faster than real time – outperforming DC-GAN (24.486 ± 0.643 ms; $\sim 327\times$) and CycleGAN (1845.557 ± 103.597 ms; $\sim 4.33\times$), thereby comfortably satisfying real-time constraints.

Across real test samples from four volunteers signals acquired in Chapter 5, Figures 6.13-6.16 demonstrate the cross-domain applicability of the trained FC-GAN to reconstruct FBG pulsatile signals, with plausible arterial morphology when segments met the selection criteria ($\geq$6 s clean pre-corruption and HR within 65-115 BPM), and degraded performance near the HR tails (e.g., $\approx 66\,BPM$). Quantitatively (Table 6.4), the reconstructed heart rate systematically overestimated the target: MAE ranged from 7.99 to 28.38 BPM (mean 15.93 BPM), and reconstructed values clustered around 91-94 BPM despite targets spanning 65.93-83.52 BPM, indicating an upward bias with variance shrinkage (regression toward $\sim 92\,BPM$); the smallest error occurred in Volunteer 2 ($\approx 8\,BPM$) and the largest in Volunteer 5 ($\approx 28.4\,BPM$), consistent with a distributional mismatch where lower-HR cases lie near the underrepresented tail of the training regime.

While further validation is needed to establish robustness, the results indicate a practical path to real-time cuffless BP monitoring: CPU-only inference is fast ($\sim$ 18.6 ms per 8 s), so latency is dominated by windowing; applying the model recursively on short, causal, overlapping windows (e.g., 2 s with 0.5-1 s hop), using overlap-add with a smooth taper and a lightweight confidence gate, satisfies real-time constraints, and phase shifts can be corrected online via short-window cross-correlation. The observed HR overestimation (mean MAE $\approx$ 15.9 BPM) can dis-

tort PAT/PTT and downstream BP estimates and should be treated as a quality control signal (flagging large $|\Delta HR|$), while a center-shifted, variance-preserving IBI warping can align central HR to the preceding clean context without erasing beat-to-beat variability. Generalisation remains limited outside 65-115 BPM due to sparse training coverage; mitigations include rebalancing with low/high-HR data, HR-aware augmentation, curriculum expansion of the HR range, and auxiliary multitask HR heads. To bridge the synthetic-real gap, quantify how reconstruction affects PAT/PTT (coverage, timing drift, downstream sensitivity, confidence-stratified performance) and target median $|\Delta PAT|$, $|\Delta PTT| <$ 5-10 ms with 95th-percentile bounds; mild amplitude modulation has minimal impact on timing features but may bias amplitude-based indices, mitigated by per-window gain normalisation and an amplitude-consistency loss.

This chapter addresses the algorithmic goals outlined in Section 2.5 by developing and evaluating an exploratory pulse-waveform reconstruction model that supports the extraction of timing features for blood-pressure (BP) estimation and aligns with the proposed cuffless-BP architecture (Figure 2.7). The results demonstrate the feasibility of this approach under real-world ambulatory conditions, while documenting the practical considerations required for reliable deployment. Furthermore, it fulfils the final objective of this research – *to develop a pulse-waveform reconstruction method based on generative adversarial networks (GANs) that enhances signal quality and improves robustness in ambulatory settings.*

7. Conclusions and Further work

Blood pressure is a pivotal biomarker whose deviations (hypertension or hypotension) signal elevated cardiovascular risk, organ damage, and substantial health-system costs (> £2.1 billion/year to the NHS) [1, 2]. Hypertension remains among the top global risk factors for mortality and DALYs and is the third-highest in the UK, yet rates of uncontrolled BP persist despite effective therapies – particularly where continuous monitoring or access to care is limited [1, 3, 4]. Intermittent measurements miss rapid, clinically relevant fluctuations; while continuous monitoring is vital (e.g., under anaesthesia) [9], existing solutions are often invasive, uncomfortable, or impractical for long-term use – motivating wearable, real-time systems suitable for free-living environments.

This thesis presents a continuous, ambulatory *cuffless* BP monitor based on optical fibre sensors. The architecture (Figure 2.7) comprises: (i) a *Transducer layer* using an FBG-cantilever sensor (Chapter 3) to detect pulsatile energy at the skin surface; (ii) a *Processing layer* that extracts timing features – PAT (with ECG) and PTT using two distal measurements at the wrist and upper arm – and employs a GAN-based reconstruction stage (Chapter 6) to stabilise features under motion; and (iii) an *Initialisation layer* where individualised BP estimation is performed via Gaussian Process Regression (Chapter 5). Feasibility was established on a cardiovascular phantom (Chapter 4) and validated in human volunteers during exercise (Chapter 5).

Evidence chain. Chapter 3 realised a wearable, 3D-printed biocompatible FBG-cantilever in the Euler-Bernoulli regime with near-linear transfer; literature and

bond-line modelling indicate ∼90% transfer efficiency and ∼6× amplification versus a bare FBG. A miniature FiSens FiSpec X100 interrogator enabled an embedded pipeline (ESP32→Raspberry Pi high-speed UART) with ≈100 Hz sampling and real-time streaming; trade-offs include lower spectral resolution and the need for higher sampling at higher BP. Chapter 4 introduced a cardiovascular phantom reproducing key haemodynamics; PTT shortened with rising intraluminal pressure (Moens-Korteweg/Hughes), while PAT timing was informative yet not fully in-vivo representative. Chapter 5 showed physiologically consistent PTT/PAT shortening during exercise, More evident in PAT thanks to the higher timing with less demand of sampling resolution; a subject-specific PAT GPR achieved DBP MAE ≈0.4-3.9 mmHg and SBP MAE ≈0.8-11.7 mmHg (best case MAE <1 mmHg, $R^2>0.8$), with no significant bias ($p>0.05$). Chapter 6 delivered a fast, CPU-only FC-GAN model for pulsatile signal reconstruction that preserved morphology in the 70-115 BPM band and outlined deployment safeguards for timing integrity, while highlighting HR-coverage limits at distribution tails.

7.1 Impact

Clinical relevance. The work advances a wearable, non-occlusive, beat-to-beat approach aligned with NHS/NICE/WHO priorities for earlier detection, longitudinal follow-up, and personalised hypertension control. Robust distal pulsation capture plus timing-based features (PTT/PAT) provide high-temporal-resolution BP trends that complement office, home, and ABPM workflows. Beneficiaries include hypertensive outpatients, perioperative/critical-care settings with rapid haemodynamic shifts, and disorders of autonomic regulation or early renal compromise.

Societal value. Comfortable, free-living monitoring can improve adherence and trigger earlier interventions, with potential to reduce cardiovascular events and costs. EMI-immune optics support technology-dense environments (e.g., MRI),

and multiplexing enables multi-site PWV for population-scale screening and data-driven public health.

Scientific contributions. A traceable validation chain bridges theory to practice: mechanics and temperature-strain decoupling → phantom haemodynamics → in-human exercise dynamics. Algorithmically, a FC-GAN reconstruction stage plus Bayesian GPR: (i) restores morphology before feature extraction, (ii) yields calibrated mmHg estimates meeting exploratory PoC targets in many cases (SBP $\leq$10 mmHg; DBP $\approx$4 mmHg), and (iii) models inter-/intra-subject variability without demographic shortcuts.

Technical impact. A biocompatible, mechanically amplifying FBG-cantilever with miniature interrogation and high-speed UART streaming achieves timing resolution suitable for tens-of-milliseconds PTT features. CPU-only pulsatile reconstruction inference ($\sim$18.6 ms per 8 s window) enables low-latency, overlapping-window operation with quality-control gating to protect fiducials.

7.2 Limitations

Chapter 3 – FBG-Cantilever Transducer. Lower spectral resolution of the FiSens X100 reduces wavelength/strain sensitivity; sampling ceiling ($\sim$100 Hz; $\sim$10 ms) may limit fiducial precision at lower PTT values that correlate to high BP; temperature-strain decoupling is postprocessed with digital filtering; Euler-Bernoulli and $\sim$90% bond-line transfer assumptions need long-wear validation. Another constraint was the FBG2 measurement at the upper-arm: the detected pulse was generally less sharp than at the wrist and, in some cases, absent altogether. While a trained clinician has a better chance of palpating the brachial pulse, when detected by the FBG-cantilever it was consistently weaker than the radial artery signal, limiting its utility for PTT derivation. Finally, although this approach is less obtrusive than conventional BP techniques, the FBG-cantilever

still relies on a degree of applanation at the skin surface to access the arterial pulse. This applanation, proportional to the cantilever-tip height, was incrementally improved across design iterations performed during this research.

Chapter 4 – Cardiovascular Phantom. Limited temporal/physiological complexity means PAT is not fully in-vivo representative; controlled validation does not capture free-living motion; subtle in-vivo factors (autonomic tone, vascular heterogeneity) are absent.

Chapter 5 – Human Studies + GPR. Temporal resolution (200 Hz across sessions), motion artefacts and jitter (occasional negatives) affect particularly PTT; inter-subject variability yields strong models for some, weak/negative R^2 for others; PAT confounded by PEP under exercise; cohort size (PTT: 8; PAT: 10) limits generalisability; subject-specific calibration robustness across sessions remains to be established.

Chapter 6 – Pulsatile Reconstruction. Generalisation drops outside 70-115 BPM due to HR-coverage imbalance; cross-domain FBG application shows upward HR bias and variance shrinkage (regression toward ∼92 BPM), risking PAT/PTT distortion; small real-data sample; timing/amplitude drift requires explicit quality control and quantified impact on fiducials.

7.3 Further Work

A. Transducer & Interrogation Hardware

- Increase sampling to ≥500 Hz (sensor→UART→logger); avoid very low ECG sampling for PAT; aim for ≤2 ms timing granularity.
- Improve miniature-interrogator spectral sensitivity (optics/firmware) or evaluate higher-speed variants (e.g., FiSens X1000).

- Validate on-body temperature compensation (dual FBGs or co-located temperature) and bound residual drift: $|\Delta\text{PAT}|, |\Delta\text{PTT}|$ (95th percentile).
- Stress-test bond-line and linearity across adhesives/interposers, strap tension, and long-wear drift; explore skin-like elastomer amplifiers [142–146].

B. Cardiovascular Phantom & Bench Validation

- Add Windkessel elements, viscoelastic walls, branching, adjustable preload to match in-vivo PTT ranges and phase dynamics.
- Include synchronised pressure/flow ground truth.
- Add temperature ramps and controlled motion artefacts.
- Use phantom data to parameterise Moens-Korteweg/Hughes and pre-calibrate PWV→mmHg mappings.

C. Human Studies & Protocols

- Scale to BIHS-style cohorts ($\geq$85 participants) with multi-session repeats; include short bouts of high-grade continuous BP for benchmarking.
- Derive PTT from carotid artery to wrist to improve detection success rate and timing resolution.
- Incorporate PEP-aware PAT features (e.g., QS2 proxies, aortic valve closure detection) to improve SBP modelling during exercise.

D. Signal Quality, Detection & Reconstruction

- Replace brittle peak heuristics with robust detectors or Reinforcement Learning [147]; report sensitivity/specificity and timing jitter.
- Rebalance HR distributions, expand curriculum to low/high HR; add multitask HR heads to reduce FBG HR bias. Furthermore, Graph Neural Net-

works (GNNs) can be explored to improve model generalisation, enabling extrapolation beyond the training distribution [148].

- Add timing-preservation losses (fiducial penalties, temporal consistency) to bound $|\Delta\text{PAT}|, |\Delta\text{PTT}| <$ 5-10 ms (95th percentile).

- Deploy a front-end noise selector to gate reconstruction, with overlap-add and short cross-correlation for phase alignment; keep CPU latency $\ll$ hop size.

E. Modelling & Calibration

- Extend GPR by incorporating heteroscedastic noise models ($\sigma^2 = \sigma^2(x)$, higher under motion/HR stress), state-aware kernels that adapt smoothness across rest and exercise regimes, and hierarchical priors to share statistical strength across volunteers. Predictive uncertainties are evaluated for calibration by comparing nominal intervals (e.g., 95%) against empirical coverage on held-out data; miscalibration is corrected using post-hoc scaling.

- Define re-/co-calibration triggers (quality control drift, large $|\Delta\text{HR}|$ post-reconstruction) and test session transfer.

- Evaluate PWA features and hybrid PWV+PWA models under matched data.

F. Data Resources & Alternatives

- Bridge synthetic-real with MIMIC ABP+PPG (PPG$\rightarrow$ABP mappings) and domain adaptation FBG$\leftrightarrow$PPG; explore auto-encoders for ABP retrieval from FBG.

- Release anonymised FBG+ECG+reference BP snippets with fiducial/Quality Control annotations to enable external validation.

Milestones & Targets

- Hardware: sampling $\geq$500 Hz, on-body temp compensation with median PAT/PTT drift < 2 ms.
- Reconstruction: 95th-percentile $|\Delta\text{PAT}|, |\Delta\text{PTT}| < 10$ ms; cut FBG HR-MAE by $\geq$50% in low/high HR bands.
- Modelling: cohort DBP MAE $\leq$4 mmHg; SBP MAE $\leq$10 mmHg with calibrated coverage; stable across sessions without full re-calibration.

Concluding remarks. This thesis demonstrates a practical pathway to wearable, non-occlusive, beat-to-beat blood pressure monitoring by uniting a mechanically amplifying FBG-cantilever transducer, a validated phantom-to-human evidence chain, and an algorithmic stack that restores waveform integrity (FC-GAN) and delivers calibrated mmHg estimates (GPR). Across benchtop and exercise studies, timing features (PTT/PAT) tracked haemodynamic load in physiologically consistent ways, meeting exploratory PoC targets in many cases while exposing clear levers for improvement – chiefly higher sampling, on-body temperature compensation, robust peak detection, and broader, multi-session cohorts. The work addresses a recognised clinical gap (NHS/NICE/WHO) where existing continuous methods are invasive or impractical, positioning the proposed system as a complementary tool to office, home, and ABPM workflows. With the outlined milestones (e.g., $\geq$500 Hz sampling, bounded $|\Delta\text{PAT}|, |\Delta\text{PTT}|$, and cohort-scale validation), the approach has a credible route to translation, enabling earlier detection, personalised control, and population-level insight into BP dynamics.

Bibliography

[1] Public Health England, "Health matters: Combating high blood pressure," 2017, accessed: 2025-03-06. [Online]. Available: https://www.gov.uk/government/publications/health-matters-combating-high-blood-pressure/health-matters-combating-high-blood-pressure#scale-of-the-problem

[2] S. Sharma, M. F. Hashmi, and P. T. Bhattacharya, *Hypotension*. StatPearls Publishing, 2023, accessed: 2025-03-06. [Online]. Available: https://www.ncbi.nlm.nih.gov/books/NBK499961/

[3] Institute for Health Metrics and Evaluation, "Risk factors driving global burden of disease," https://www.healthdata.org/research-analysis/library/risk-factors-driving-global-burden-disease, n.d., accessed: 2025-03-06.

[4] A. H. Mokdad *et al.*, "The burden of diseases, injuries, and risk factors by state in the usa, 1990–2021: a systematic analysis for the global burden of disease study 2021," *The Lancet*, vol. 404, no. 10469, pp. 2314–2340, 2024. doi: 10.1016/S0140-6736(24)01446-6 Accessed: 2025-03-06. [Online]. Available: https://www.thelancet.com/action/showPdf?pii=S0140-6736%2824%2901446-6

[5] NHS England, "The nhs long term plan," 2019. [Online]. Available: https://www.longtermplan.nhs.uk/

[6] National Institute for Health and Care Excellence, "Hypertension in adults: diagnosis and management (ng136)," 2019. [Online]. Available: https://www.nice.org.uk/guidance/ng136

[7] World Health Organization, "Global ncd target: reduce high blood pressure," 2016. [Online]. Available: https://www.who.int/publications/i/item/global-ncd-target-reduce-high-blood-pressure

[8] ——, "Prevention and control of noncommunicable diseases: report by the director-general, executive board 156th session," https://apps.who.int/gb/ebwha/pdf_files/EB156/B156_7-en.pdf, 2024, accessed June 2025.

[9] H. J. Baek, K. K. Kim, J. S. Kim, B. Lee, and K. S. Park, "Enhancing the estimation of blood pressure using pulse arrival time and two confounding factors," *Physiological measurement*, vol. 31, no. 2, p. 145, 2009.

[10] G. J. Tortora and B. Derrickson, *Introduction to the Human Body: The Cardiovascular System*, 10th ed. Wiley, 2015.

[11] J. A. Potkay, "Long term, implantable blood pressure monitoring systems," *Biomedical microdevices*, vol. 10, no. 3, pp. 379–392, 2008.

[12] S. A. Esper and M. R. Pinsky, "Arterial waveform analysis," *Best Practice & Research Clinical Anaesthesiology*, vol. 28, no. 4, pp. 363–380, 2014.

[13] T. Kishi, "Baroreflex failure and beat-to-beat blood pressure variation," *Hypertension Research*, vol. 41, no. 8, pp. 547–552, 2018. doi: 10.1038/s41440-018-0056-y

[14] J.-X. Ren, Y. Qu, Y. Gao, and H.-Y. e. a. Ma, "Beat-to-beat blood pressure variability within 24 hours of ischemic stroke onset: A potential predictor of functional prognosis," *Journal of the American Heart Association*, vol. 13, p. e034575, 2024. doi: 10.1161/JAHA.124.034575

[15] G. Parati, J. E. Ochoa, and G. Bilo, "Blood pressure variability: Assessment, predictive value, and potential as a therapeutic target," *Hypertension Research*, vol. 36, no. 9, pp. 836–841, 2013. doi: 10.1038/hr.2013.17

[16] P. Muntner, J. Whittle, A. I. Lynch, L. D. Colantonio, L. M. Simpson, P. T. Einhorn, and et al., "Visit-to-visit variability of blood pressure and coronary heart disease, stroke, heart failure, and mortality: A cohort study," *Annals of Internal Medicine*, vol. 163, no. 5, pp. 329–338, September 2015. doi: 10.7326/M14-2803

[17] Y. Imai, K. Abe, S. Sasaki, N. Minami, M. Munakata, and K. Yoshinaga, "Altered circadian blood pressure rhythm in patients with diabetic nephropathy," *Hypertension*, vol. 19, no. 6, pp. 807–812, 1992. doi: 10.1161/01.HYP.19.6.807

[18] B. Gupta, "Invasive blood pressure monitoring," *Update in Anaesthesia*, vol. 28, no. 1, pp. 37–42, 2012. doi: 10.1016/b978-1-56053-421-1.50122-8

[19] G. Ogedegbe and T. Pickering, "Principles and Techniques of Blood Pressure Measurement," *Cardiology Clinics*, vol. 28, no. 4, pp. 571–586, 2010. doi: 10.1016/j.ccl.2010.07.006

[20] G. W. Mauck, C. R. Smith, L. A. Geddes, and J. D. Bourland, "The meaning of the point of maximum oscillations in cuff pressure in the indirect measurement of blood pressure–part ii." *Journal of biomechanical engineering*, vol. 102, no. 1, pp. 28–33, feb 1980. doi: 10.1115/1.3138195

[21] P. S. Lewis, British, and I. H. Society, "Oscillometric measurement of blood pressure: a simplified explanation. a technical note on behalf of the british and irish hypertension society," *Journal of human hypertension*, vol. 33, no. 5, pp. 349–351, 2019.

[22] J. PENAZ, "Photoelectric measurement of blood pressure, volume and flow in the finger," *Digest of the 10th international conference on medical and biological engineering-Dresden, 1973*, vol. 104, 1973. [Online]. Available: https://cir.nii.ac.jp/crid/1570854176020161024.bib?lang=en

[23] S. Rastegar, H. GholamHosseini, and A. Lowe, "Non-invasive continuous blood pressure monitoring systems: current and proposed technology issues and challenges," *Physical and Engineering Sciences in Medicine*, vol. 43, pp. 11–28, 2020.

[24] G. S. Stergiou, R. Mukkamala, A. Avolio, K. G. Kyriakoulis, S. Mieke, A. Murray, G. Parati, A. E. Schutte, J. E. Sharman, R. Asmar *et al.*, "Cuffless blood pressure measuring devices: review and statement by the european society of hypertension working group on blood pressure monitoring and cardiovascular variability," *Journal of hypertension*, vol. 40, no. 8, pp. 1449–1460, 2022.

[25] G. L. Pressman and P. M. Newgard, "A transducer for the continuous external measurement of arterial blood pressure," *IEEE Transactions on Bio-medical Electronics*, vol. 10, pp. 73–81, 1963. doi: 10.1109/TBMEL.1963.4322794

[26] J. Solà and R. Delgado-Gonzalo, "The handbook of cuffless blood pressure monitoring," *Cham: Springer*, 2019.

[27] J. A. Pandit and D. Batlle, "Snapshot hemodynamics and clinical outcomes in hypertension: precision in the measurements is key," *Hypertension*, vol. 67, no. 2, pp. 270–271, 2016.

[28] J. Fisher, "The diagnostic value of the sphygmomanometer in examinations for life insurance," *Journal of the American Medical Association*, vol. 63, no. 20, pp. 1752–1754, 1914.

[29] X.-R. Ding, J. Liu, W.-X. Dai, P. Carvalho, R. Magjarević, and Y.-T. Zhang, "An attempt to define the pulse transit time," in *International Conference on Biomedical and Health Informatics*, Y.-T. Zhang, P. Carvalho, and R. Magjarevic, Eds. Singapore: Springer Singapore, 2019. ISBN 978-981-10-4505-9 pp. 219–221.

[30] J. Allen, "Photoplethysmography and its application in clinical physiological measurement," *Physiological measurement*, vol. 28, no. 3, p. R1, 2007.

[31] R. Mukkamala, J.-O. Hahn, O. T. Inan, L. K. Mestha, C.-S. Kim, H. Töreyin, and S. Kyal, "Toward ubiquitous blood pressure monitoring via pulse transit time: theory and practice," *IEEE transactions on biomedical engineering*, vol. 62, no. 8, pp. 1879–1901, 2015.

[32] M. Proença, G. Bonnier, D. Ferrario, C. Verjus, and M. Lemay, "Ppg-based blood pressure monitoring by pulse wave analysis: calibration parameters are stable for three months," in *2019 41st Annual International Conference of the IEEE Engineering in Medicine and Biology Society (EMBC)*. IEEE, 2019, pp. 5560–5563.

[33] D. Hughes, C. Babbs, L. Geddes, and J. Bourland, "Measurements of young's modulus of elasticity of the canine aorta with ultrasound," *Ultrasonic Imaging*, vol. 1, no. 4, pp. 356–367, 1979.

doi: https://doi.org/10.1016/0161-7346(79)90028-2. [Online]. Available: https://www.sciencedirect.com/science/article/pii/0161734679900282

[34] G. Weltman, G. Sullivan, and D. Bredon, "The continuous measurement of arterial pulse wave velocity," *Medical electronics and biological engineering*, vol. 2, pp. 145–154, 1964.

[35] A. Steptoe, H. Smulyan, and B. Gribbin, "Pulse wave velocity and blood pressure change: calibration and applications," *Psychophysiology*, vol. 13, no. 5, pp. 488–493, 1976.

[36] E. Finnegan, S. Davidson, M. Harford, J. Jorge, P. Watkinson, D. Young, L. Tarassenko, and M. Villarroel, "Pulse arrival time as a surrogate of blood pressure," *Scientific reports*, vol. 11, no. 1, p. 22767, 2021.

[37] L. Geddes, M. Voelz, C. Babbs, J. Bourland, and W. Tacker, "Pulse transit time as an indicator of arterial blood pressure," *psychophysiology*, vol. 18, no. 1, pp. 71–74, 1981.

[38] M. H. Pollak and P. A. Obrist, "Aortic-radial pulse transit time and ecg q-wave to radial pulse wave interval as indices of beat-by-beat blood pressure change," *Psychophysiology*, vol. 20, no. 1, pp. 21–28, 1983.

[39] R. Spetlík, J. Cech, and J. Matas, "Non-contact reflectance photoplethysmography: Progress, limitations, and myths," in *2018 13th IEEE International Conference on Automatic Face & Gesture Recognition (FG 2018)*. IEEE, 2018, pp. 702–709.

[40] I. C. Jeong, H. Yoon, H. Kang, and H. Yeom, "Effects of skin surface temperature on photoplethysmograph," *Journal of Healthcare Engineering*, vol. 5, no. 4, pp. 429–438, 2014. doi: 10.1260/2040-2295.5.4.429

[41] A. Chandrasekhar, M. Yavarimanesh, K. Natarajan, J. Hahn, and R. Mukkamala, "Ppg sensor contact pressure should be taken into account for cuff-less blood pressure measurement," *IEEE Transactions on Biomedical Engineering*, vol. 67, no. 11, pp. 3134–3140, 2020. doi: 10.1109/TBME.2020.2976989

[42] X. Teng and Y. Zhang, "Theoretical study on the effect of sensor contact force on pulse transit time," *IEEE Transactions on Biomedical Engineering*, vol. 54, no. 8, pp. 1490–1498, 2007. doi: 10.1109/TBME.2007.900815

[43] G. Tusman, A. Scandurra, C. M. Acosta, S. Puca, J. Martinez Arca, M. Madorno, F. Suarez Sipmann, and S. H. Böhm, "Photoplethysmogram's amplitude is well correlated with beat-by-beat changes in arterial blood pressure," *Clinical Medical Reviews and Case Reports*, vol. 8, p. 338, 2021. doi: 10.23937/2378-3656/1410338

[44] G. Martínez, N. Howard, D. Abbott, K. Lim, R. Ward, and M. Elgendi, "Can photoplethysmography replace arterial blood pressure in the assessment of blood pressure?" *Journal of Clinical Medicine*, vol. 7, no. 10, p. 316, 2018. doi: 10.3390/jcm7100316

[45] R. Pal, A. Rudas, S. Kim, J. N. Chiang, A. Braney, and M. Cannesson, "An algorithm to detect dicrotic notch in arterial blood pressure and photoplethysmography waveforms using the iterative envelope mean method," *medRxiv*, 2024. doi: 10.1101/2024.03.05.24303735 Preprint, posted 7 March 2024.

[46] S. Poeggel, D. Tosi, D. Duraibabu, G. Leen, D. McGrath, and E. Lewis, "Optical fibre pressure sensors in medical applications," *Sensors*, vol. 15, no. 7, pp. 17 115–17 148, 2015.

[47] K. O. Hill and G. Meltz, "Fiber bragg grating technology fundamentals and overview," *Journal of lightwave technology*, vol. 15, no. 8, pp. 1263–1276, 2002.

[48] B. Lee, "Review of the present status of optical fiber sensors," *Optical fiber technology*, vol. 9, no. 2, pp. 57–79, 2003.

[49] K. Bremer, G. Leen, E. Lewis, B. J. Moss, S. Lochmann, and I. Mueller, "Pressure sensor with an interferometric sensor and an in-fiber bragg grating reference sensor," Jul. 1 2014, uS Patent 8,764,678.

[50] S. Poeggel, D. Tosi, F. Fusco, J. Ippolito, L. Lupoli, V. Mirone, S. Sannino, G. Leen, and E. Lewis, "Fiber-optic efpi pressure sensors for in vivo urodynamic analysis," *IEEE Sensors Journal*, vol. 14, no. 7, pp. 2335–2340, 2014.

[51] F. Taffoni, D. Formica, P. Saccomandi, G. D. Pino, and E. Schena, "Optical fiber-based mr-compatible sensors for medical applications: An overview," *Sensors*, vol. 13, no. 10, pp. 14 105–14 120, 2013.

[52] S. Majumder, T. Mondal, and M. J. Deen, "Wearable sensors for remote health monitoring," *Sensors*, vol. 17, no. 1, p. 130, 2017.

[53] R. Correia, S. James, S. Lee, S. Morgan, and S. Korposh, "Biomedical application of optical fibre sensors," *Journal of Optics*, vol. 20, no. 7, p. 073003, 2018.

[54] M. Nishiyama, M. Sonobe, and K. Watanabe, "Unconstrained pulse pressure monitoring for health management using hetero-core fiber optic sensor," *Biomedical optics express*, vol. 7, no. 9, pp. 3675–3685, 2016.

[55] X. Yang, Z. Chen, C. S. M. Elvin, L. H. Y. Janice, S. H. Ng, J. T. Teo, and R. Wu, "Textile fiber optic microbend sensor used for heartbeat and respiration monitoring," *IEEE Sensors Journal*, vol. 15, no. 2, pp. 757–761, 2014.

[56] A. Othonos, K. Kalli, D. Pureur, and A. Mugnier, *Fibre Bragg Gratings*, H. Venghaus, Ed. Springer Berlin Heidelberg, 2006. ISBN 978-3-540-31770-8. [Online]. Available: https://doi.org/10.1007/3-540-31770-8_6

[57] A. Avolio, F. Shirbani, I. Tan, and M. Butlin, "Cuffless blood pressure monitoring and the advent of a new era in medicine and society," in *The Handbook of Cuffless Blood Pressure Monitoring*, J. Solà and R. Delgado-Gonzalo, Eds. Cham, Switzerland: Springer Nature Switzerland, 2019, pp. 1–13. [Online]. Available: https://doi.org/10.1007/978-3-030-24701-0_1

[58] S. University, *Gaussian Processes - Stanford CS229*, 2020. [Online]. Available: https://cs229.stanford.edu/summer2020/cs229-notes3.pdf

[59] J. Li, "Pulse wave velocity techniques," in *The Handbook of Cuffless Blood Pressure Monitoring*, J. Solà and R. Delgado-Gonzalo, Eds. Cham: Springer Nature Switzerland, 2019, pp. 61–79. ISBN 978-3-030-24700-3 Global Medical Affairs, Omron Healthcare, Inc. [Online]. Available: https://doi.org/10.1007/978-3-030-24701-0_6

[60] S. G. Khalid, J. Zhang, F. Chen, and D. Zheng, "Blood pressure estimation using photoplethysmography only: comparison between different machine learning approaches," *Journal of healthcare engineering*, vol. 2018, no. 1, p. 1548647, 2018.

[61] D. Buxi, J.-M. Redoute, and M. R. Yuce, "A survey on signals and systems in ambulatory blood pressure monitoring using pulse transit time," *Physiological measurement*, vol. 36, no. 3, p. R1, 2015.

[62] Y.-Z. Yoon, M.-H. Lee, and K.-S. Soh, "Pulse type classification by varying contact pressure," *IEEE Engineering in Medicine and Biology Magazine*, vol. 19, no. 6, pp. 106–110, 2000.

[63] Y. Lee, H. Han, and J. Kim, "Influence of motion artifacts on photoplethysmographic signals for measuring pulse rates," in *2008 International Conference on Control, Automation and Systems*. IEEE, 2008, pp. 962–965.

[64] X. Jia, X. Wen, H. Lv, M. Li, S. Deng, and M.-Y. Li, "Crosstalk suppression in the ofdr system using a dual wavelength wfbg array," *IEEE Sensors Journal*, 2025.

[65] S. K. Ibrahim, J. Van Roosbroeck, J. A. O'Dowd, B. Van Hoe, E. Lindner, J. Vlekken, M. Farnan, D. M. Karabacak, and J. M. Singer, "Interrogation and mitigation of polarization effects for standard and birefringent fbgs," in *Fiber Optic Sensors and Applications XIII*, vol. 9852. SPIE, 2016, pp. 126–137.

[66] D. Tosi, "Review and analysis of peak tracking techniques for fiber bragg grating sensors," *Sensors*, vol. 17, no. 10, p. 2368, 2017.

[67] Y. E. Marin, T. Nannipieri, C. J. Oton, and F. D. Pasquale, "Current status and future trends of photonic-integrated fbg interrogators," *Journal of lightwave technology*, vol. 36, no. 4, pp. 946–953, 2018.

[68] D. Krizan, J. Stipal, J. Nedoma, S. Oliveira, M. Fajkus, J. Cubik, P. Siska, E. Schena, D. Lo Presti, and C. Marques, "Embedding fbg sensors for monitoring vital signs of the human body: Recent progress over the past decade," *APL Photonics*, vol. 9, no. 8, 2024.

[69] C. Leitão, L. Bilro, N. Alberto, P. Antunes, H. Lima, P. André, R. Nogueira, and J. Pinto, "Development of a fbg probe for non-invasive carotid pulse waveform assessment," in *Biophotonics: Photonic Solutions for Better Health Care III*, vol. 8427. SPIE, 2012, pp. 87–92.

[70] S. Koyama, Y. Haseda, H. Ishizawa, F. Okazaki, J. Bonefacino, and H.-Y. Tam, "Measurement of pulsation strain at the fingertip using a plastic fbg sensor," *IEEE Sensors Journal*, vol. 21, no. 19, pp. 21 537–21 545, 2021.

[71] Y. Haseda, J. Bonefacino, H.-Y. Tam, S. Chino, S. Koyama, and H. Ishizawa, "Measurement of pulse wave signals and blood pressure by a plastic optical fiber fbg sensor," *Sensors*, vol. 19, no. 23, p. 5088, 2019.

[72] D. Jia, J. Chao, S. Li, H. Zhang, Y. Yan, T. Liu, and Y. Sun, "A fiber bragg grating sensor for radial artery pulse waveform measurement," *IEEE Transactions on Biomedical Engineering*, vol. 65, no. 4, pp. 839–846, 2018. doi: 10.1109/TBME.2017.2722008

[73] R. B. Gowda, P. Sharan, K. Saara, M. Braim, and A. N. Alodhayb, "An fbg-based optical pressure sensor for the measurement of radial artery pulse pressure," *Journal of Biophotonics*, p. e202400083, 2024.

[74] J. Wang, Z. Wang, Z. Zhang, P. Li, H. Pan, Y. Ren, T. Hou, C. Wang, C.-F. Kwong, B. Zhang *et al.*, "Simultaneous measurement of local pulse wave velocities in radial arteries using a soft sensor based on the fiber bragg grating technique," *Micromachines*, vol. 15, no. 4, p. 507, 2024.

[75] Y. Katsuragawa and H. Ishizawa, "Non-invasive blood pressure measurement by pulse wave analysis using fbg sensor," in *2015 IEEE International Instrumentation and Measurement Technology Conference (I2MTC) Proceedings*, 2015. doi: 10.1109/I2MTC.2015.7151320 pp. 511–515.

[76] S. Yang, W. S. W. Zaki, S. P. Morgan, S. Y. Cho, R. Correia, and Y. Zhang, "Blood pressure estimation with complexity features from electrocardiogram and photoplethysmogram signals," *Optical and Quantum Electronics*, vol. 52, no. 3, pp. 1–16, 2020. doi: 10.1007/s11082-020-2260-7. [Online]. Available: https://doi.org/10.1007/s11082-020-2260-7

[77] M. Kachuee, M. M. Kiani, H. Mohammadzade, and M. Shabany, "Cuff-less high-accuracy calibration-free blood pressure estimation using pulse transit time," *Proceedings - IEEE International Symposium on Circuits and Systems*, vol. 2015-July, no. 2, pp. 1006–1009, 2015. doi: 10.1109/ISCAS.2015.7168806

[78] P. Su, X. R. Ding, Y. T. Zhang, J. Liu, F. Miao, and N. Zhao, "Long-term blood pressure prediction with deep recurrent neural networks," *IEEE EMBS International Conference on Biomedical and Health Informatics*, pp. 323–328, 2018. doi: 10.1109/BHI.2018.8333434

[79] S. G. Khalid, J. Zhang, F. Chen, and D. Zheng, "Blood Pressure Estimation Using Photoplethysmography Only: Comparison between Different Machine

Learning Approaches," *Journal of Healthcare Engineering*, vol. 2018, 2018. doi: 10.1155/2018/1548647

[80] L. Wang, W. Zhou, Y. Xing, and X. Zhou, "A novel neural network model for blood pressure estimation using photoplethesmography without electrocardiogram," *Journal of Healthcare Engineering*, 2018. doi: 10.1155/2018/7804243

[81] Ö. F. Ertuğrul and N. Sezgin, "A noninvasive time-frequency-based approach to estimate cuffless arterial blood pressure," *Turkish Journal of Electrical Engineering and Computer Sciences*, vol. 26, no. 5, pp. 2260–2274, 2018. doi: 10.3906/elk-1712-215

[82] Y. Liang, Z. Chen, R. Ward, and M. Elgendi, "Photoplethysmography and deep learning: Enhancing hypertension risk stratification," *Biosensors*, vol. 8, no. 4, pp. 1–13, 2018. doi: 10.3390/bios8040101

[83] S. Baek, J. Jang, and S. Yoon, "End-to-end blood pressure prediction via fully convolutional networks," *IEEE Access*, vol. 7, pp. 185 458–185 468, 2019. doi: 10.1109/ACCESS.2019.2960844

[84] A. Paviglianiti, V. Randazzo, S. Villata, G. Cirrincione, and E. Pasero, "A comparison of deep learning techniques for arterial blood pressure prediction," *Cognitive Computation*, vol. 14, pp. 1689–1710, 9 2022. doi: 10.1007/s12559-021-09910-0

[85] A. S. Alghamdi, K. Polat, A. Alghoson, A. A. Alshdadi, and A. A. Abd El-Latif, "Gaussian process regression (gpr) based non-invasive continuous blood pressure prediction method from cuff oscillometric signals," *Applied Acoustics*, vol. 164, p. 107256, 2020.

[86] T. Pereira, K. Gadhoumi, M. Ma, X. Liu, R. Xiao, R. A. Colorado, K. J. Keenan, K. Meisel, and X. Hu, "A supervised approach to robust photoplethysmography quality assessment," *IEEE journal of biomedical and health informatics*, vol. 24, no. 3, pp. 649–657, 2019.

[87] S. Asgari, M. Bergsneider, and X. Hu, "A robust approach toward recognizing valid arterial-blood-pressure pulses," *IEEE transactions on information technology in biomedicine*, vol. 14, no. 1, pp. 166–172, 2009.

[88] J. A. Sukor, S. Redmond, and N. Lovell, "Signal quality measures for pulse oximetry through waveform morphology analysis," *Physiological measurement*, vol. 32, no. 3, p. 369, 2011.

[89] B. S. Kim and S. K. Yoo, "Motion artifact reduction in photoplethysmography using independent component analysis," *IEEE Transactions on Biomedical Engineering*, vol. 53, pp. 566–568, 3 2006. doi: 10.1109/TBME.2005.869784

[90] S. M. Salehizadeh, D. K. Dao, J. W. Chong, D. McManus, C. Darling, Y. Mendelson, and K. H. Chon, "Photoplethysmograph signal reconstruction based on a novel motion artifact detection-reduction approach. part

ii: Motion and noise artifact removal," *Annals of Biomedical Engineering*, vol. 42, 11 2014. doi: 10.1007/s10439-014-1030-8

[91] P. Mullan, C. M. Kanzler, B. Lorch, L. Schroeder, L. Winkler, L. Laich, F. Riedel, R. Richer, C. Luckner, H. Leutheuser, B. M. Eskofier, and C. Pasluosta, "Unobtrusive heart rate estimation during physical exercise using photoplethysmographic and acceleration data," 2015. ISBN 9781424492701 pp. 6114–6117.

[92] Y. Zhang, B. Liu, and Z. Zhang, "Combining ensemble empirical mode decomposition with spectrum subtraction technique for heart rate monitoring using wrist-type photoplethysmography," *Biomedical Signal Processing and Control*, vol. 21, pp. 119–125, 7 2015. doi: 10.1016/j.bspc.2015.05.006

[93] S. D. Tang, Y. S. Goh, M. D. Wong, and Y. E. L. Lew, "Ppg signal reconstruction using a combination of discrete wavelet transform and empirical mode decomposition." IEEE, 1 2017. doi: 10.1109/ICIAS.2016.7824118

[94] J. Lee, S. Sun, S. M. Yang, J. J. Sohn, J. Park, S. Lee, and H. C. Kim, "Bidirectional recurrent auto-encoder for photoplethysmogram denoising," *IEEE Journal of Biomedical and Health Informatics*, vol. 23, pp. 2375–2385, 11 2019. doi: 10.1109/JBHI.2018.2885139

[95] H. Dou, C. Chen, X. Hu, Z. Xuan, Z. Hu, and S. Peng, "Pca-srgan: Incremental orthogonal projection discrimination for face super-resolution," in *Proceedings of the 28th ACM international conference on multimedia*, 2020, pp. 1891–1899.

[96] Y. Zhou, Z. Hu, Z. Xuan, Y. Wang, and X. Hu, "Synchronizing detection and removal of smoke in endoscopic images with cyclic consistency adversarial nets," *IEEE/ACM Transactions on Computational Biology and Bioinformatics*, vol. 21, no. 4, pp. 670–680, 2024. doi: 10.1109/TCBB.2022.3204673

[97] A. H. A. Zargari, S. A. H. Aqajari, H. Khodabandeh, A. M. Rahmani, and F. J. Kurdahi, "An accurate non-accelerometer-based PPG motion artifact removal technique using cyclegan," *CoRR*, vol. abs/2106.11512, 2021. [Online]. Available: https://arxiv.org/abs/2106.11512

[98] Y. Wang, I. Azimi, K. Kazemi, A. M. Rahmani, and P. Liljeberg, "Ppg signal reconstruction using deep convolutional generative adversarial network," vol. 2022-July. Institute of Electrical and Electronics Engineers Inc., 2022. doi: 10.1109/EMBC48229.2022.9871678. ISBN 9781728127828. ISSN 1557170X pp. 3387–3391.

[99] R. Correia, B. Gadsby, S. Korposh, A. M. Norris, B. R. Hayes-Gill, R. Sinha, J. G. Hardman, D. S. Gardner, S. Talbot, D. Harvey *et al.*, "Intra-tracheal multiplexed sensing of contact pressure and perfusion," *Biomedical Optics Express*, vol. 13, no. 1, pp. 48–64, 2022.

[100] P. A. Kyriacou, "Pulse oximetry in the oesophagus," *Physiological measurement*, vol. 27, no. 1, p. R1, 2005.

[101] S. Akcay, A. Atapour-Abarghouei, and T. P. Breckon, "Ganomaly: Semi-supervised anomaly detection via adversarial training," 5 2018. [Online]. Available: http://arxiv.org/abs/1805.06725

[102] W. Suhaimizan and W. Zaki, "Monitoring the pulse transit time using optical fibre sensors," Ph.D. dissertation, 7 2019, https://eprints.nottingham.ac.uk/id/eprint/60974.

[103] A. G. Schwing and R. Urtasun, "Fully connected deep structured networks," *arXiv preprint arXiv:1503.02351*, 2015.

[104] D. M. Vo and S.-W. Lee, "Semantic image segmentation using fully convolutional neural networks with multi-scale images and multi-scale dilated convolutions," *Multimedia Tools and Applications*, vol. 77, no. 14, pp. 18 689–18 707, 2018. doi: 10.1007/s11042-018-5653-x. [Online]. Available: https://doi.org/10.1007/s11042-018-5653-x

[105] L. Fernandes, S. Carvalho, I. Carneiro, R. Henrique, V. V. Tuchin, H. P. Oliveira, and L. M. Oliveira, "Diffuse reflectance and machine learning techniques to differentiate colorectal cancer ex vivo," *Chaos: An Interdisciplinary Journal of Nonlinear Science*, vol. 31, no. 5, p. 053118, 05 2021. doi: 10.1063/5.0052088. [Online]. Available: https://doi.org/10.1063/5.0052088

[106] O. A. Bauchau and J. I. Craig, "Euler-bernoulli beam theory," in *Structural analysis*. Springer, 2009, pp. 173–221.

[107] S. Saito, H. Ikei, G. Hosokawa, and et al., "Intravascular ultrasound assessment of the radial artery for transradial coronary procedures," *Catheter Cardiovasc Diagn*, vol. 35, no. 2, pp. 116–121, 1995.

[108] H. Wu, Q. Lin, F. Han, L. Zhao, and Z. Jiang, "Design and analysis of high-frequency fiber bragg grating vibration sensor," *Measurement Science and Technology*, vol. 32, no. 2, p. 025108, 2020.

[109] Formlabs, "Technical data sheet: 2201601-tds-enus-0," https://formlabs-media.formlabs.com/datasheets/2201601-TDS-ENUS-0.pdf, 2025, accessed: 4 March 2025.

[110] P. Motwani, N. Perogamvros, S. Taylor, M. Sonebi, A. Laskar, and A. Murphy, "Experimental investigation of strain sensitivity for surface bonded fibre optic sensors," *Sensors and Actuators A: Physical*, vol. 303, p. 111833, 2020.

[111] E. V. Osilla, J. L. Marsidi, and S. Sharma, "Physiology, temperature regulation," 2018.

[112] H.-N. Ho and L. A. Jones, "Modeling the thermal responses of the skin surface during hand-object interactions," 2008.

[113] M. N. Sawka, C. B. Wenger, A. J. Young, and K. B. Pandolf, "Physiological responses to exercise in the heat," *Nutritional needs in hot environments: applications for military personnel in field operations*, vol. 55, 1993.

[114] M. L. Åslund, N. Jovanovic, N. Groothoff, J. Canning, G. D. Marshall, S. D. Jackson, A. Fuerbach, and M. J. Withford, "Optical loss mechanisms in femtosecond laser-written point-by-point fibre bragg gratings," *Optics express*, vol. 16, no. 18, pp. 14 248–14 254, 2008.

[115] C. Waltermann, P. Guehlke, J. Koch, and W. Schippers, "Shaping spectra within optical fibers: Embedding high-resolution spectrometers into the cores of optical fibers," *PhotonicsViews*, vol. 16, no. 2, pp. 42–45, 2019.

[116] G. Meltz and W. W. Morey, "Bragg grating formation and germanosilicate fiber photosensitivity," in *International workshop on photoinduced self-organization effects in optical fiber*, vol. 1516. SPIE, 1991, pp. 185–199.

[117] J.-C. Bos, "Microwebsrv: A micro http web server supporting websockets and templating for micropython," https://github.com/jczic/MicroWebSrv, n.d., accessed: 2025-08-08.

[118] K. Chandran, S. Rittgers, and A. Yoganathan, *Biofluid Mechanics: The Human Circulation, Second Edition*. Taylor & Francis, 2012. ISBN 9781439845165. [Online]. Available: https://books.google.co.uk/books?id=EYmTM9rXQl4C

[119] M. Nitzan, B. Khanokh, and Y. Slovik, "The difference in pulse transit time to the toe and finger measured by photoplethysmography," *Physiological measurement*, vol. 23, no. 1, p. 85, 2001.

[120] G. S. Stergiou, A. P. Avolio, P. Palatini, K. G. Kyriakoulis, A. E. Schutte, S. Mieke, A. Kollias, G. Parati, R. Asmar, N. Pantazis *et al.*, "European society of hypertension recommendations for the validation of cuffless blood pressure measuring devices: European society of hypertension working group on blood pressure monitoring and cardiovascular variability," *Journal of hypertension*, vol. 41, no. 12, pp. 2074–2087, 2023.

[121] T. B. Contributors, *BioSPPy: Biosignal Processing in Python*, 2025, accessed: 2025-01-25. [Online]. Available: https://biosppy.readthedocs.io/en/stable/index.html

[122] C. E. Rasmussen and C. K. I. Williams, *Gaussian Processes for Machine Learning*. MIT Press, 2006. [Online]. Available: http://gaussianprocess.org/gpml/chapters/

[123] K. P. Murphy, *Probabilistic Machine Learning: Advanced Topics*. MIT Press, 2023. [Online]. Available: https://probml.github.io/pml-book/book2.html

[124] D. Barber, *Bayesian Reasoning and Machine Learning*. Cambridge University Press, 2012. [Online]. Available: https://www.cs.ucl.ac.uk/staff/d.barber/brml/

[125] J. Quinonero-Candela and C. E. Rasmussen, "Sparse gaussian processes using pseudo-inputs," 2005. [Online]. Available: https://proceedings.neurips.cc/paper/2005/file/4491777b1aa8b5b32c2e8666dbe1a495-Paper.pdf

[126] International Organization for Standardization, *ISO 81060-2:2018 - Non-invasive sphygmomanometers – Part 2: Clinical validation of automated measurement type*, Std., 2018. [Online]. Available: https://www.iso.org/standard/73339.html

[127] T. G. Pickering, J. E. Hall, L. J. Appel, B. E. Falkner, J. W. Graves, M. N. Hill, D. W. Jones, T. Kurtz, S. G. Sheps, and E. J. Roccella, "Recommendations for blood pressure measurement in humans and experimental animals," *Circulation*, vol. 111, no. 5, pp. 697–716, 2005. doi: 10.1161/01.CIR.0000154900.76284.F6. [Online]. Available: https://doi.org/10.1161/01.CIR.0000154900.76284.F6

[128] E. O'Brien, B. Waeber, G. Parati, J. Staessen, and M. G. Myers, "Blood pressure measuring devices: recommendations of the European Society of Hypertension," *BMJ (Clinical research ed.)*, vol. 322, no. 7285, pp. 531–536, mar 2001. doi: 10.1136/bmj.322.7285.531. [Online]. Available: https://pubmed.ncbi.nlm.nih.gov/11230071

[129] J. R. Gardner, G. Pleiss, K. Q. Weinberger, D. Bindel, and A. G. Wilson, *GPyTorch: A Gaussian Process Library in PyTorch*, 2023. [Online]. Available: https://gpytorch.ai/

[130] R. H. Fagard, "Exercise is good for your blood pressure: effects of endurance training and resistance training," *Clinical and Experimental Pharmacology and Physiology*, vol. 33, no. 9, pp. 853–856, 2011. doi: 10.1111/j.1440-1681.2006.04453.x

[131] M. A. Pimentel, A. E. Johnson, P. H. Charlton, D. Birrenkott, P. J. Watkinson, L. Tarassenko, and D. A. Clifton, "Toward a robust estimation of respiratory rate from pulse oximeters," *IEEE Transactions on Biomedical Engineering*, vol. 64, pp. 1914–1923, 8 2017. doi: 10.1109/TBME.2016.2613124

[132] A. Mahmoudzadeh, I. Azimi, A. M. Rahmani, and P. Liljeberg, "Lightweight photoplethysmography quality assessment for real-time iot-based health monitoring using unsupervised anomaly detection," vol. 184. Elsevier B.V., 2021. doi: 10.1016/j.procs.2021.03.025. ISSN 18770509 pp. 140–147.

[133] J. Lee, M. Kim, H. K. Park, and I. Y. Kim, "Motion artifact reduction in wearable photoplethysmography based on multi-channel sensors with multiple wavelengths," *Sensors (Switzerland)*, vol. 20, 3 2020. doi: 10.3390/s20051493

[134] J. F. Rojano and C. V. Isaza, "Singular value decomposition of the time-frequency distribution of ppg signals for motion artifact reduction," *International Journal of Signal Processing Systems*, pp. 475–482, 12 2016. doi: 10.18178/ijsps.4.6.475-482. [Online]. Available: http://www.ijsps.com/index.php?m=content&c=index&a=show&catid=52&id=229

[135] S. Bagha and L. Shaw, "A real time analysis of ppg signal for measurement of spo2 and pulse rate," *International journal of computer applications*, vol. 36, no. 11, pp. 45–50, 2011.

[136] A. E. Awodeyi, S. R. Alty, and M. Ghavami, "On the filtering of photoplethysmography signals," in *2014 IEEE International Conference on Bioinformatics and Bioengineering*. IEEE, 2014, pp. 175–178.

[137] Open Edge Platform, "anomalib: Anomaly detection library," https://github.com/open-edge-platform/anomalib, 2025, gitHub repository, version 2.1.0; accessed 29 Aug 2025.

[138] A. Paszke, S. Gross, F. Massa, A. Lerer, J. Bradbury, G. Chanan, T. Killeen, Z. Lin, N. Gimelshein, L. Antiga, A. Desmaison, A. Kopf, E. Yang, Z. DeVito, M. Raison, A. Tejani, S. Chilamkurthy, B. Steiner, L. Fang, J. Bai, and S. Chintala, "Pytorch: An imperative style, high-performance deep learning library," in *Advances in Neural Information Processing Systems 32*. Curran Associates, Inc., 2019, pp. 8024–8035. [Online]. Available: http://papers.neurips.cc/paper/9015-pytorch-an-imperative-style-high-performance-deep-learning-library.pdf

[139] A. K. Datta, DATTA., and Premnath, *Epoch Synchronous Overlap Add (ESOLA)*. Springer, 2018.

[140] L. Wang and P. Koniusz, "Uncertainty-dtw for time series and sequences," in *European Conference on Computer Vision*. Springer, 2022, pp. 176–195.

[141] V. Singla, S. Ge, B. Ronen, and D. Jacobs, "Shift invariance can reduce adversarial robustness," *Advances in Neural Information Processing Systems*, vol. 34, pp. 1858–1871, 2021.

[142] J. Sun, X. Zhao, W. R. K. Illeperuma, O. Chaudhuri, K. H. Oh, D. J. Mooney, J. J. Vlassak, and Z. Suo, "Highly stretchable and tough hydrogels," *Nature*, vol. 489, no. 7414, pp. 133–136, 2012. doi: 10.1038/nature11409

[143] J. T. Muth, D. M. Vogt, R. L. Truby, Y. Mengüç, D. B. Kolesky, R. J. Wood, and J. A. Lewis, "Embedded 3d printing of strain sensors within highly stretchable elastomers," *Advanced Materials*, vol. 26, no. 36, pp. 6307–6312, 2014. doi: 10.1002/adma.201400334

[144] T. Yamada, Y. Hayamizu, Y. Yamamoto, Y. Yomogida, A. Izadi-Najafabadi, D. N. Futaba, and K. Hata, "A stretchable carbon nanotube strain sensor for human-motion detection," *Nature Nanotechnology*, vol. 6, no. 5, pp. 296–301, 2011. doi: 10.1038/nnano.2011.36

[145] Y. Cao, Y. Tan, M. Li, and L. Li, "Stretchable capacitive strain sensors based on conductive double network hydrogels," *Journal of Materials Chemistry C*, vol. 6, no. 19, pp. 5044–5052, 2018. doi: 10.1039/C8TC00580H

[146] B. Yin, Y. Li, B. Wang, S. Wang, P. Shi, J. Ma, and Y. Cui, "A high-performance wearable strain sensor with advanced thermal management for motion monitoring," *Nature Communications*, vol. 12, p. 154, 2021. doi: 10.1038/s41467-020-20456-4

[147] Q. Xiao and C. Wang, "Adaptive wavelet base selection for deep learning-based ecg diagnosis: A reinforcement learning approach," *PLOS ONE*, vol. 20, no. 2, p. e0318070, Feb 2025. doi: 10.1371/journal.pone.0318070

[148] R. R. Nerem, S. Chen, S. Dasgupta, and Y. Wang, "Graph neural networks extrapolate out-of-distribution for shortest paths," *arXiv preprint arXiv:2503.19173*, 2025. [Online]. Available: https://arxiv.org/abs/2503.19173v2

[149] (2025) Ad8221 instrumentation amplifier data sheet. Accessed: 2025-01-03. [Online]. Available: https://www.analog.com/media/en/technical-documentation/data-sheets/AD8221.pdf

A. Appendix

A.1 ECG recorder

This appendix presents the design and testing of an ECG device used in conjunction with an FBG-cantilever sensor to measure the pulse arrival time (PAT) between the electrical signal from the chest and the mechanical signal from the wrist. This appendix includes, the design sent to a subcontractor for the fabrication of the ECG recorder, the fabrication process of the ECG leads is described. Two different protocols were employed to analyse the noise performance of the ECG amplifier: the load resistor test and the sine wave test. Finally, the results of the sine wave test are compared with those of a commercially available ECG amplifier (BIOPAC).

The ECG device (Figure A.1) is composed of an analogue-front end that filters and amplifies the electrical signals detected at the skin surface. This an analogue-front end is mainly composed of the instrumentation amplifier AD8221 [149], a voltage follower to match the skin impedance to the screen impedance, an inverter amplifier for the drive leg right (DLR), an active low pass filter in the feedback reference of AD8221 followed by a band-pass filter to capture the morphology of the ECG complex. Furthermore, an anti-aliasing filter is set to condition the signal for the ADC input. This amplified signal is digitalised with an ADC AD7124 (Analogue Devices Inc. Massachusetts, USA) of 24 bits communicated via SPI protocol to the iMX7ULP microprocessor (NXP Semiconductors, Eindhoven, Netherlands) with a Linux kernel installed. This microprocessor has an embedded MultiMediaCard, eMMC H26M64208EMR (SK hynix, Korea) of 16 GB to store the electrical recorded signals. The design of the ECG recorder was provided to a subcontractor. This subcontractor built the integration of the ECG analogue-front end, ADC, power supply unit PSU and micro-processor.

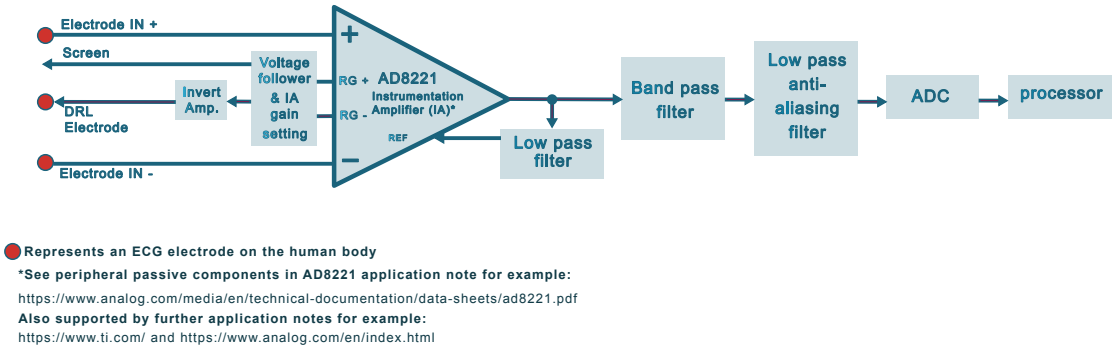

Figure A.1: *Block diagram of the ECG recorder.*

A.1.1 ECG lead.

For the ECG leads (Figure A.3), shielded lead wires (B/R/W, 3pk) with 'snap on' connectors (ADINSTRUMENTS, UK) were soldered to a Hirose male connector ST40X-18S-CVR(30) (Hirose Elecric Co Ltd, Japan) as the pin out diagram in Figure A.2. The DLR corresponds to the black snap on connector lead, the positive electrode input corresponds to the red snap on connector lead and the white electrode input of the Hirose connector corresponds to the common electrode.

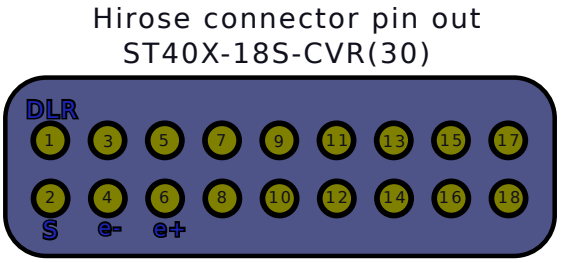

Figure A.2: *Hirose male connector pin configuration for Drive Leg Right (DLR), Screen (S), positive electrode (e+) and common electrode (e-).*

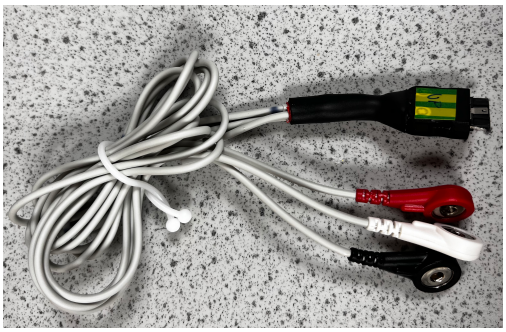

Figure A.3: *ECG leads fabricated with Hirose connector, positive electrode (red), common electrode (white), DLR (black).*

A.1.2 Noise measurements on ECG amplifier.

Two protocols were employed to analyse the noise performance of the ECG amplifier: the load resistor test and the sine wave test. The load resistor test consisted of measuring the output of the ECG analogue front-end (AFE) when placing a resistor across the input and gradually increment this resistor value from 1 kΩ-470 kΩ. The second noise test consisted of putting an attenuated sine wave of 5 µV and analysing its amplification at the output. Finally, these latter results were compared with the BIOPAC ECG Amplifier.

Load resistor test

Determine the input referred peak-to-peak (p-p) noise of the ECG amplifier for different input resistances.

Experimental setup:

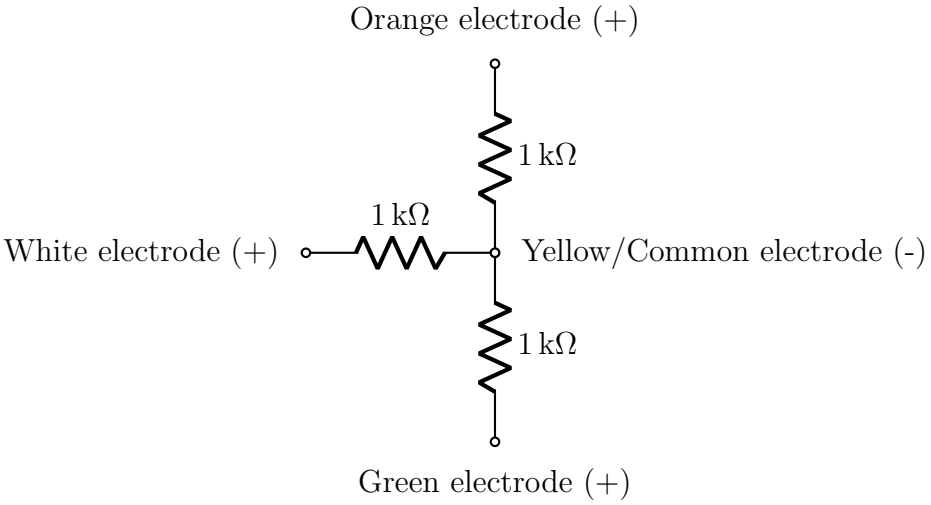

Procedure:

1. Select the input load resistor [1 kΩ, 4.7 kΩ, 10 kΩ 47 kΩ, 100 kΩ and 470 kΩ]
2. Measure output voltage in time domain channel of ECG(AFE) (These measurements were recorded using the oscilloscope PicoScope with a sampling rate of 20 kHz.)
3. Determine output voltage spectral density plot $V/\sqrt{Hz}$.
4. Divide step 3 by gain (3000) frequency response to create input referred voltage spectral density plot $V/\sqrt{Hz}$.
5. Determine the average voltage value $V/\sqrt{Hz}$.
6. Convert frequency to time domain by multiplying step 5 by $\sqrt{40Hz}$ - this is the RMS noise at the input over 40 Hz.

7. Multiply step 6 by 6.6 or $(3.3 * \sigma)$ to get p-p amplitude at the input over 40 Hz.

8. Repeat for different load resistors and plot graph load vs step 7 values

9. Calculate the theoretical thermal noise for the different resistors
   $Vth = \sqrt{4kTBR}$, where :
   Boltzmann Constant k = 1.38e-23
   Temperature T= $25°C+$ 273K
   Bandwidth B=1
   R = [1 kΩ, 4.7 kΩ, 10 kΩ 47 kΩ, 100 kΩ and 470 kΩ].

Note: theoretical shot, 1/f and PSRR noise sources are currently not included.

Results:

1. Time domain outputs of ECG (AFE)

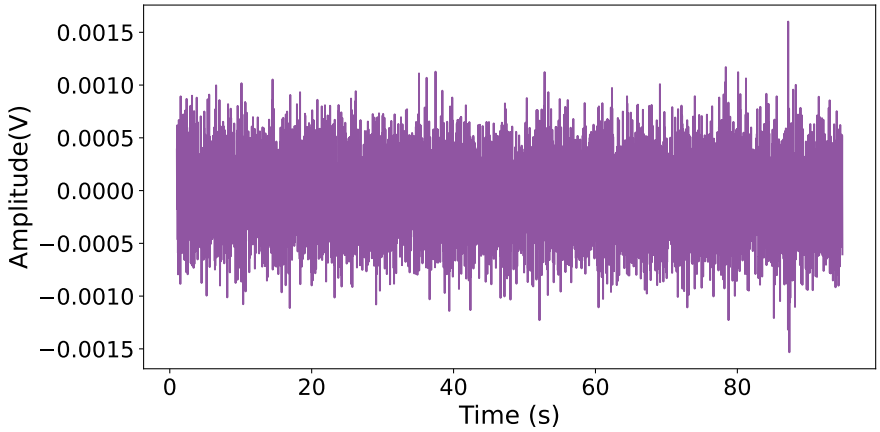

Figure A.4: *Output voltage from ECG in time domain connecting a load resistor of 1 kΩ at its input.* V_{rms} *= 3.281 mV*

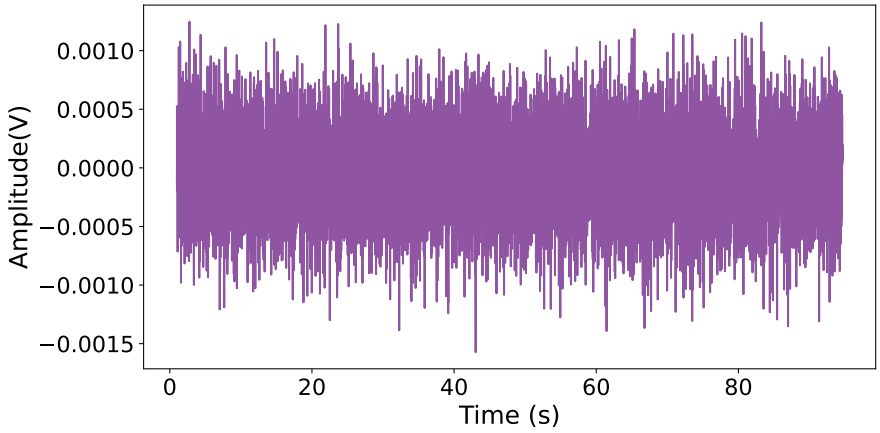

Figure A.5: *Output voltage from ECG in time domain connecting a load resistor of 4.7 kΩ at its input.* V_{rms} *= 3.628 mV*

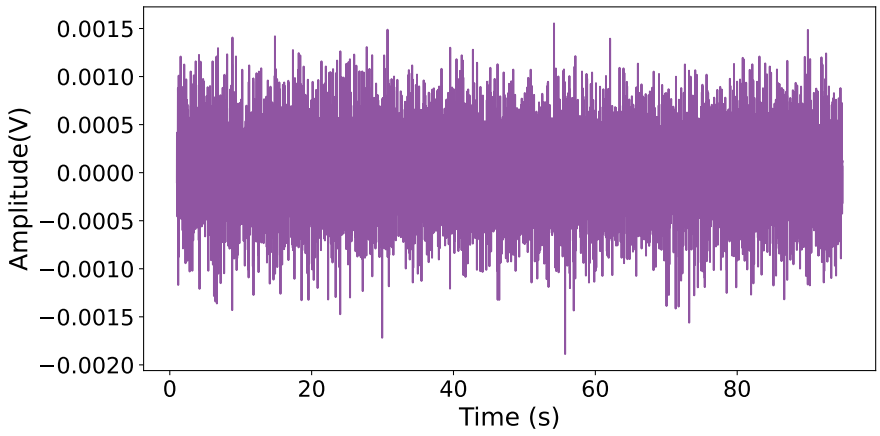

Figure A.6: *Output voltage from ECG in time domain connecting a load resistor of 10kΩ at its input.* $V_{rms} = 4.055\ mV$

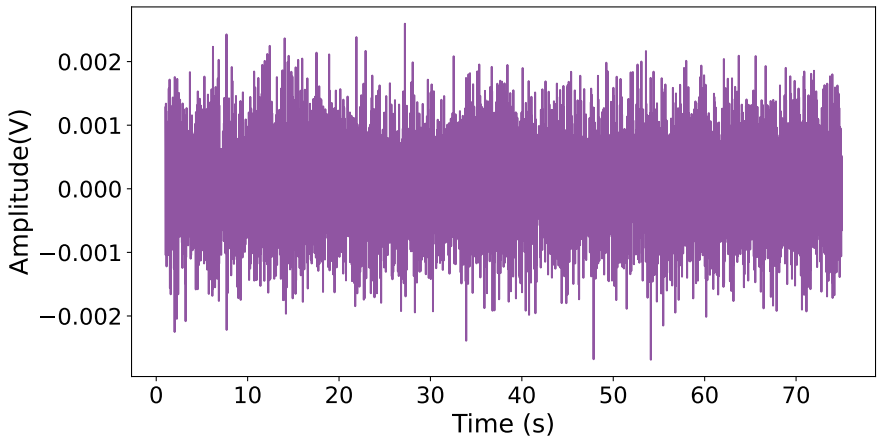

Figure A.7: *Output voltage from ECG in time domain connecting a load resistor of 47kΩ at its input.* $V_{rms} = 6.664\ mV$

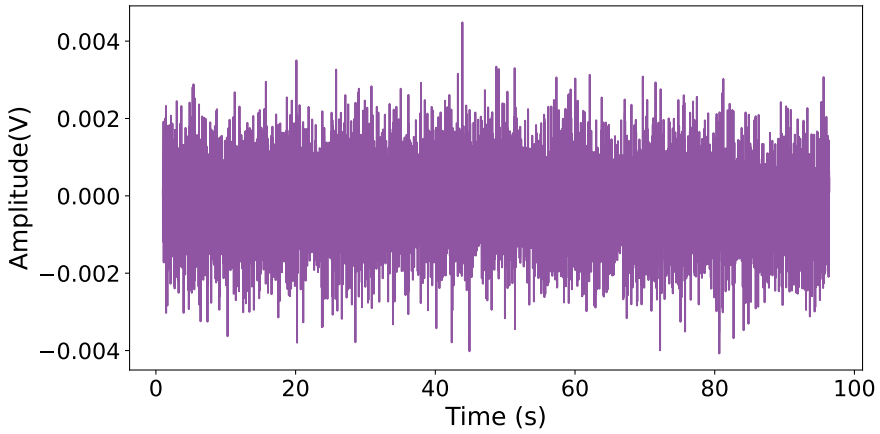

Figure A.8: *Output voltage from ECG in time domain connecting a load resistor of 100kΩ at its input.* $V_{rms} = 9.78\ mV$

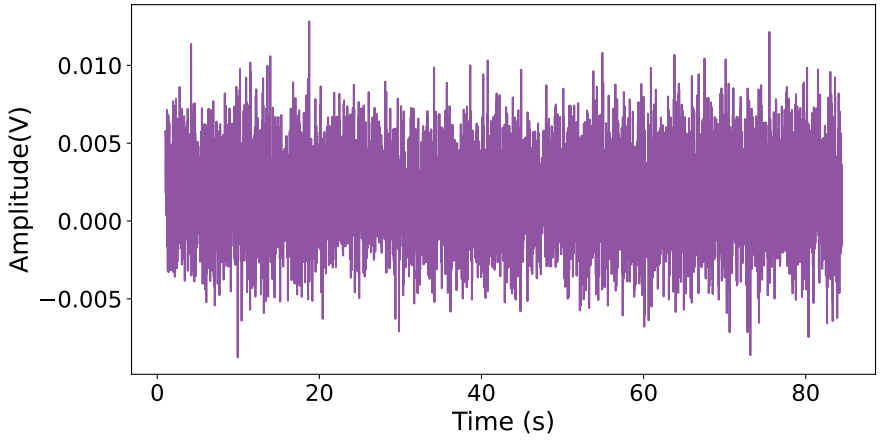

Figure A.9: *Output voltage from ECG in time domain connecting a load resistor of 470kΩ at its input.* V_{rms} *= 30.372 mV*

2. Output time domain, PSD and VSD plots for ECG

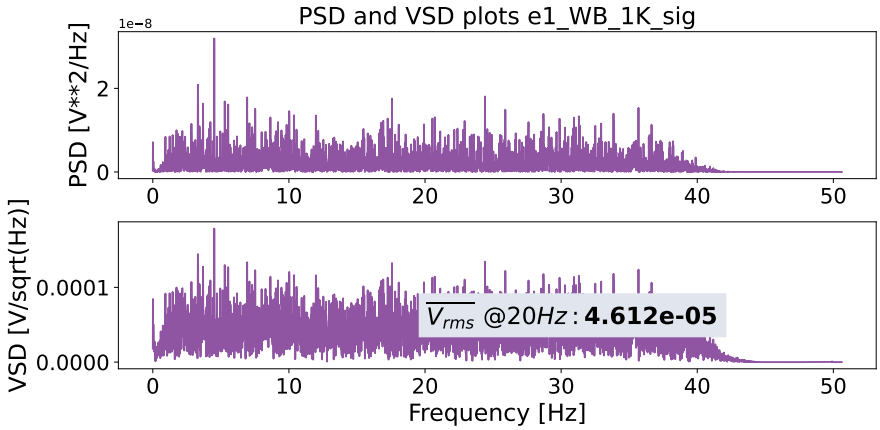

Figure A.10: *Power Spectral Density (PSD) and Voltage Spectral Density (VSD) plots for 1 kΩ for ECG. Note: average voltage per square root of Hertz at 20 Hz illustrated.*

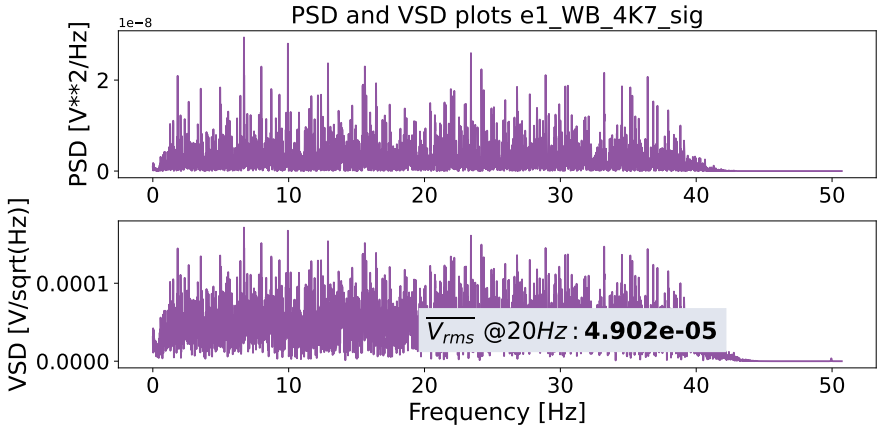

Figure A.11: *Power Spectral Density (PSD) and Voltage Spectral Density (VSD) plots for 4.7 kΩ for ECG. Note: average voltage per square root of Hertz at 20 Hz illustrated.*

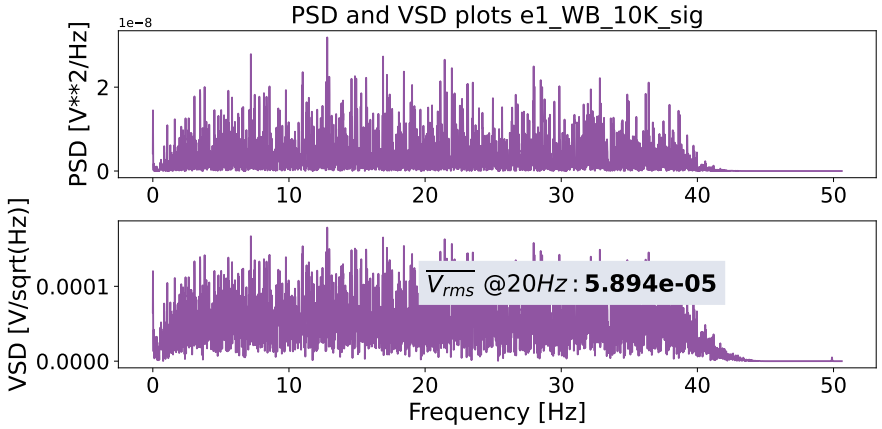

Figure A.12: *Power Spectral Density (PSD) and Voltage Spectral Density (VSD) plots for 10 kΩ for ECG. Note: average voltage per square root of Hertz at 20 Hz illustrated.*

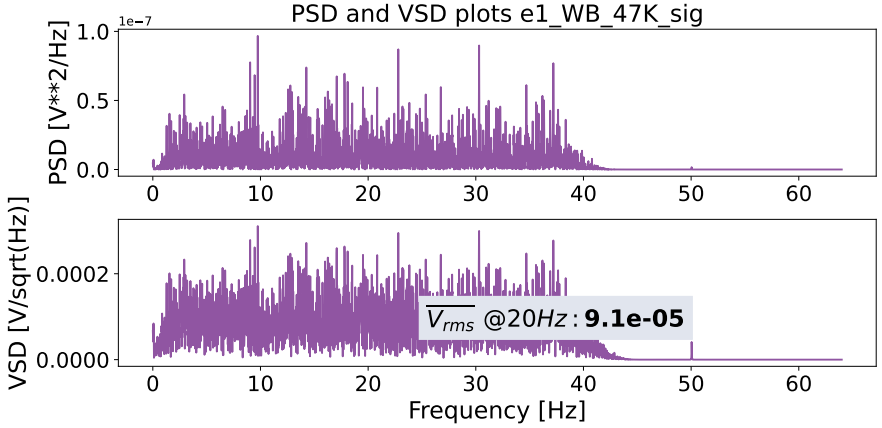

Figure A.13: *Power Spectral Density (PSD) and Voltage Spectral Density (VSD) plots for 47 kΩ for ECG. Note: average voltage per square root of Hertz at 20 Hz illustrated.*

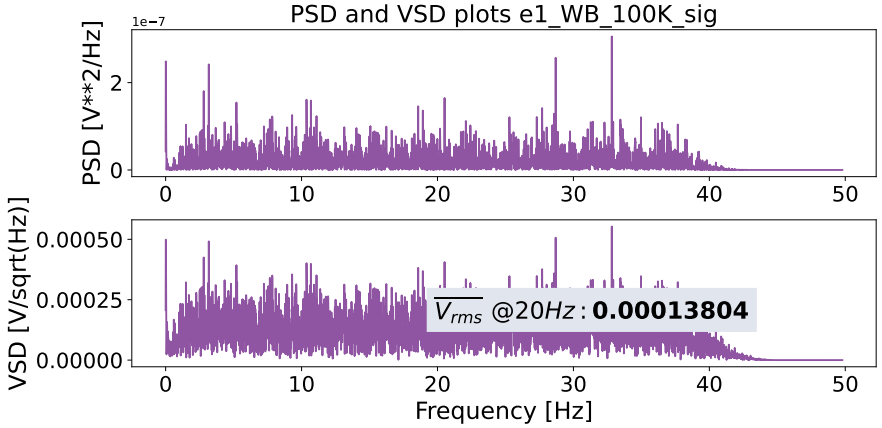

Figure A.14: *Power Spectral Density (PSD) and Voltage Spectral Density (VSD) plots for 100 kΩ for ECG. Note: average voltage per square root of Hertz at 20 Hz illustrated.*

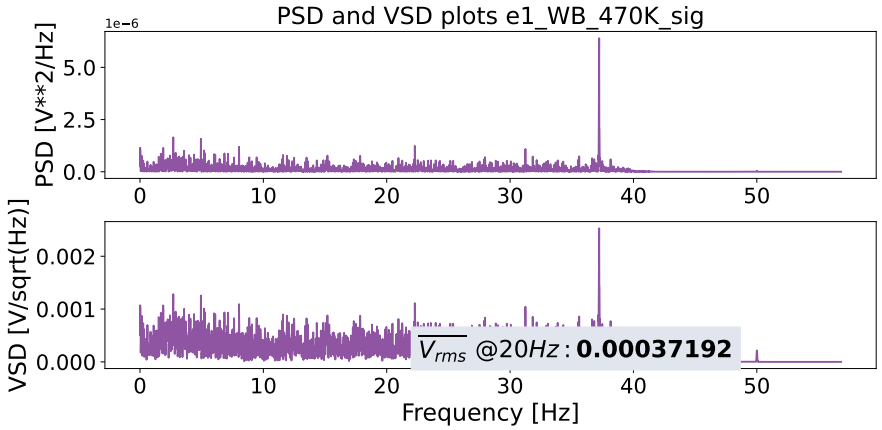

Figure A.15: *Power Spectral Density (PSD) and Voltage Spectral Density (VSD) plots for 470 kΩ for ECG. Note: average voltage per square root of Hertz at 20 Hz illustrated.*

3. Input referred voltage spectral density plots of ECG (AFE)

The input referred voltage spectral density plots are obtained by dividing each the voltage spectral density of the output amplified values of ECG (AFE) by the gain 3000.

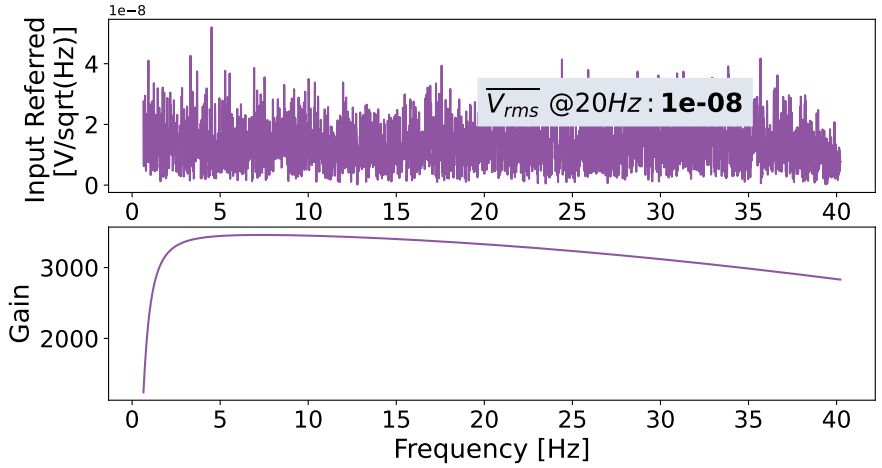

Figure A.16: *Input referred voltage spectral density plot for 1 kΩ of ECG (AFE).*

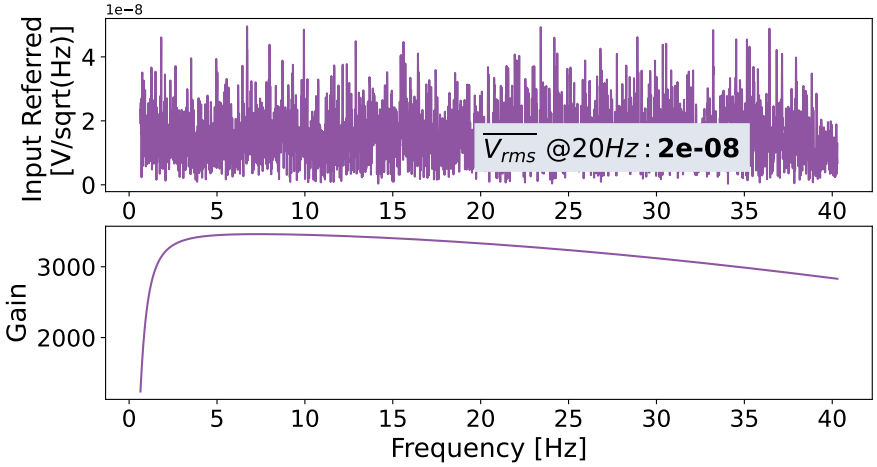

Figure A.17: *Input referred voltage spectral density plot for 4.7 kΩ of ECG (AFE).*

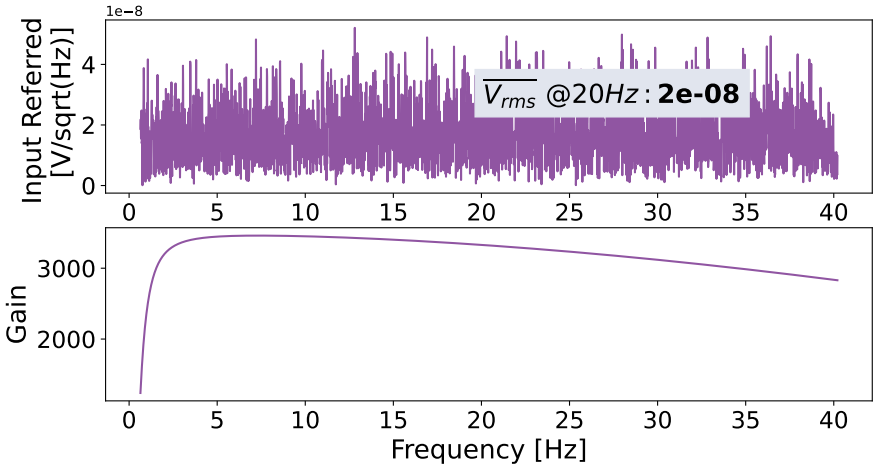

Figure A.18: *Input referred voltage spectral density plot for 10 kΩ of ECG (AFE).*

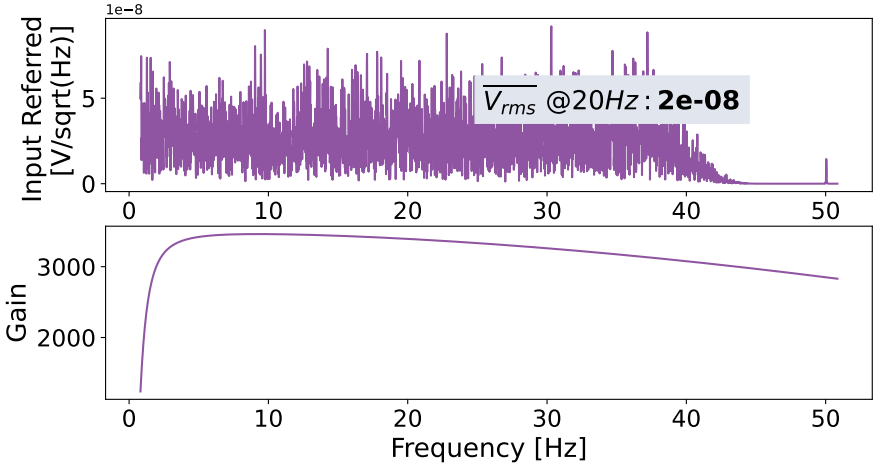

Figure A.19: *Input referred voltage spectral density plot for 47 kΩ of ECG (AFE).*

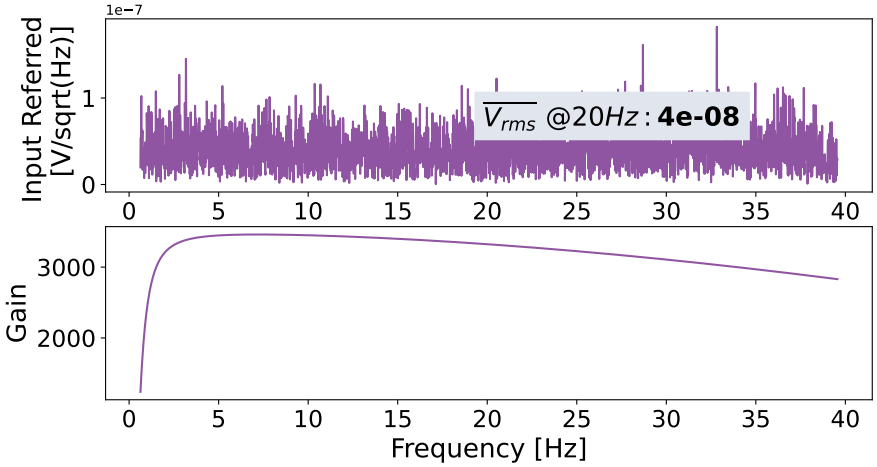

Figure A.20: *Input referred voltage spectral density plot for 100 kΩ of ECG (AFE).*

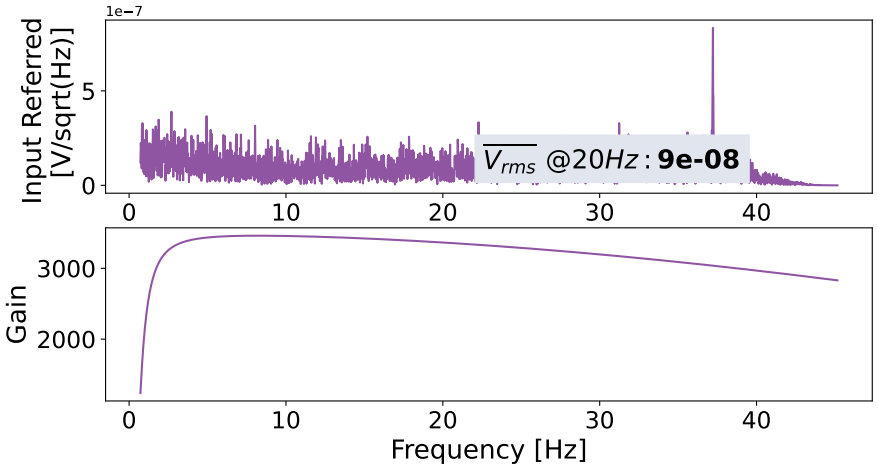

Figure A.21: *Input referred voltage spectral density plot for 470 kΩ of ECG (AFE).*

P-P value of ECG (AFE) vs Calculated thermal noise for different load resistors

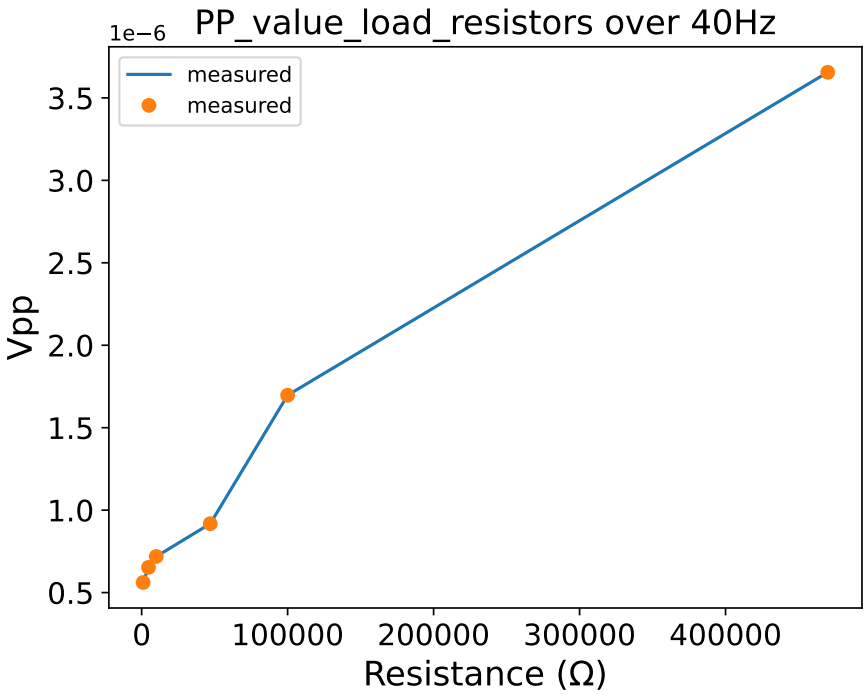

Figure A.22: *P-P value for different load resistors of ECG (AFE).*

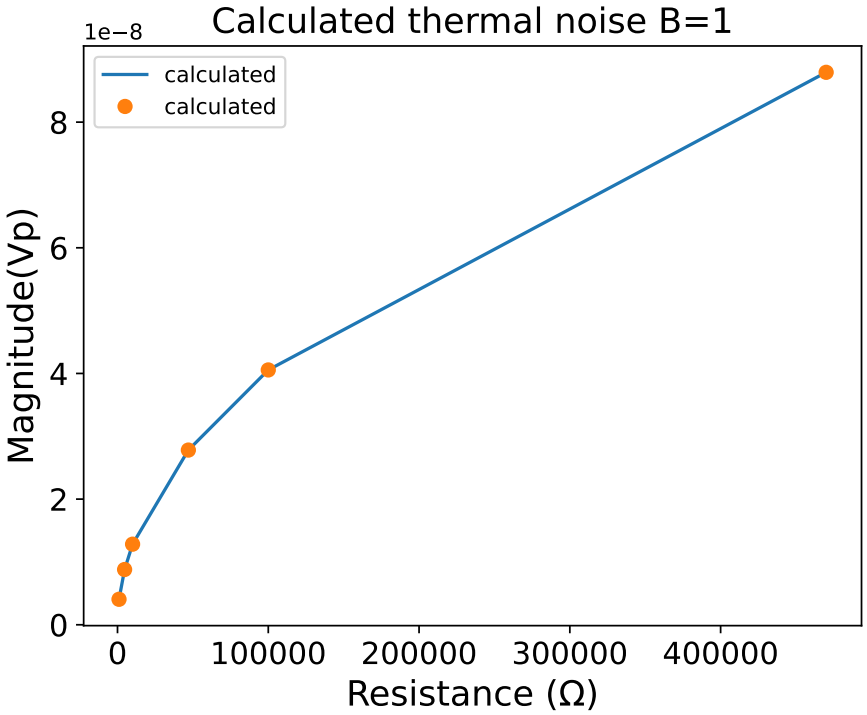

Figure A.23: *Calculated thermal noise for different load resistors.*

Preliminary Discussion from load resistor test

- The differences in the magnitude of the calculated thermal noise (Figure A.23) and the P-P value measured with different load resistors (Figure A.22) is because the shot, flicker, power supply and ambient noise were not considered.
- From Figure A.22 it is noticed that a load resistor of 4.7 kΩ has a peak to peak amplitude noise of 0.6 μV.

Sine test

Test the Signal to Noise ratio by placing at the input of the ECG amplifier, an attenuated sine wave.

Experimental setup:

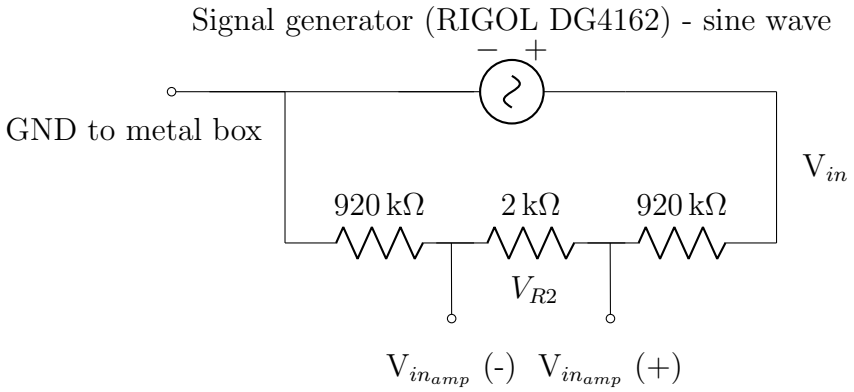

ECG Amplifier

$$V_{R2} = V_{in} \cdot (\frac{R_2}{R1 + R2 + R3}) = V_{in} \cdot (\frac{2\,\text{k}\Omega}{920\,\text{k}\Omega + 2\,\text{k}\Omega + 920\,\text{k}\Omega}) = V_{in} \cdot 0.001 \quad \text{(A.1)}$$

Procedure

1. Set V_{pp} to 5 mV and the frequency at 10Hz of the sine wave from the signal generator.
2. Measure the ECG amplifier output with an oscilloscope (In this case Tektronix TDS2024B oscilloscope at a sampling rate of 20 kHz was utilised).
3. Analyse the amplitude of the measured signal.
4. If the SNR is very small apply a LowPass filter with a cutoff frequency of 35 Hz.

A.1.3 Benchmarking of our ECG amplifier against BIOPAC ECG amplifier

Test the Signal to Noise ratio by placing at the input of the BIOPAC MP100 ECG amplifier, an attenuated sine wave.

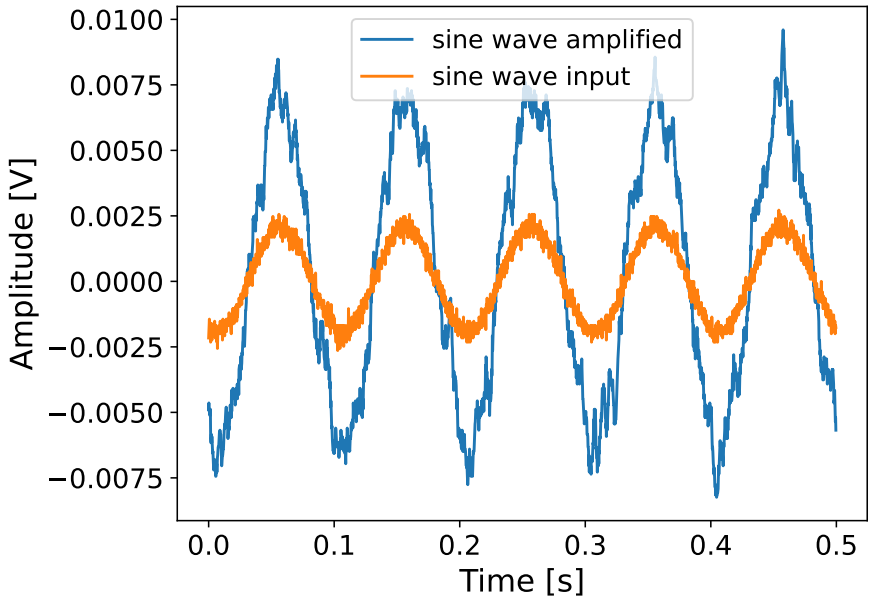

Figure A.24: *Sine wave at 10 Hz V_{in} =5 mV peak to peak coming from the signal generator (orange), which combined with the attenuator (1000x) generates a V_{R2} =5 µV peak to peak (not shown). Sine wave amplified by the ECG amplifier at output (blue)*

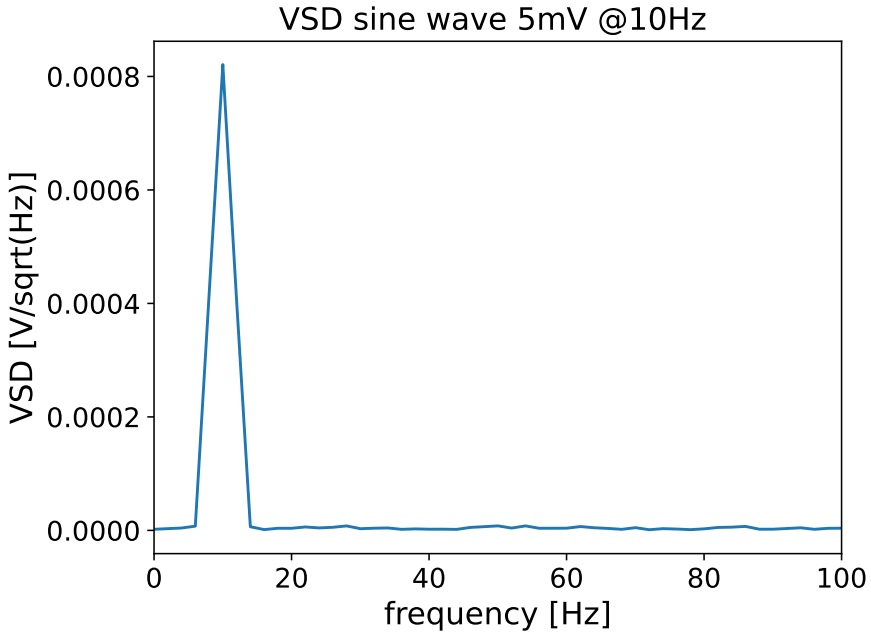

Figure A.25: *Voltage Spectral Density plot of the sine wave at the signal generator at 5 mV at 10 Hz.*

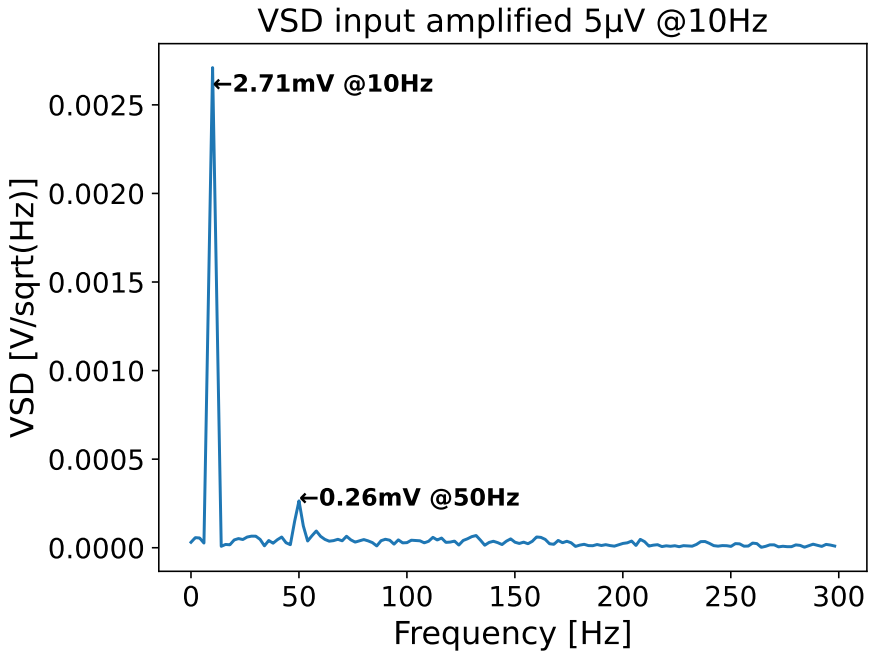

Figure A.26: *Voltage Spectral Density plot of the output amplified from the ECG device with an input sine wave of 5 µV at 10 Hz (G = 3000).*

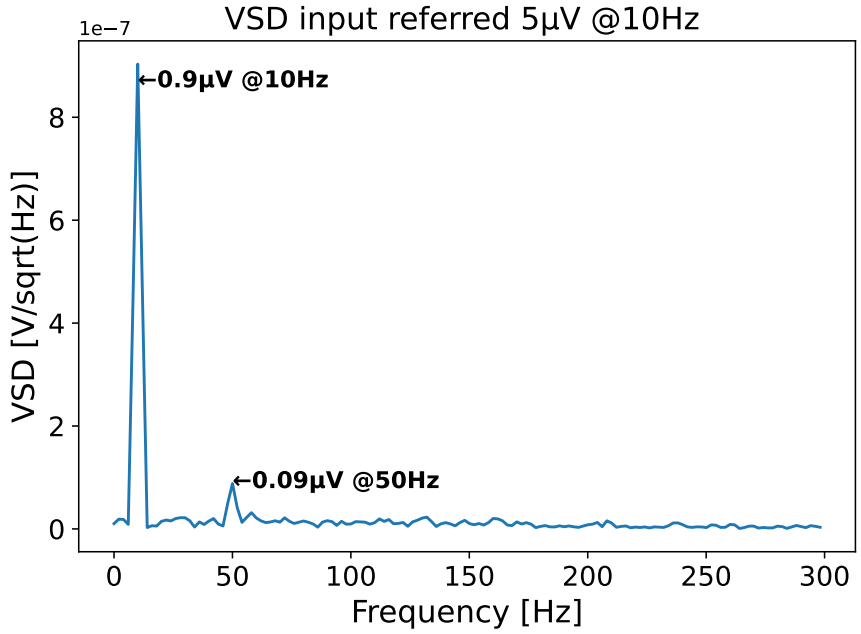

Figure A.27: *Voltage Spectral Density plot of the Input referred (accounting G = 3000) from the ECG device with an input sine wave of 5 µV at 10 Hz.*

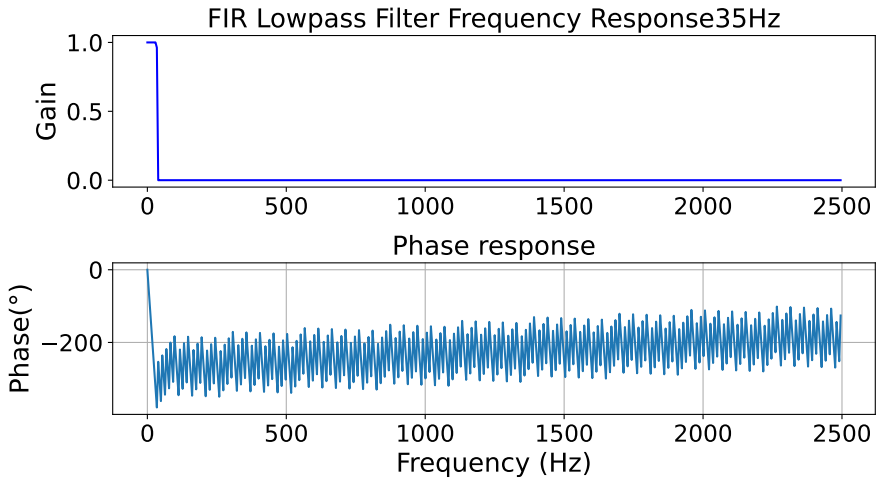

Figure A.28: *Finite Impulse Response Low pass Filter at 35 Hz, frequency and phase response. 35Hz cutoff frequency was chosen to match BIOPAC upper range of its in-built bandpass filter.*

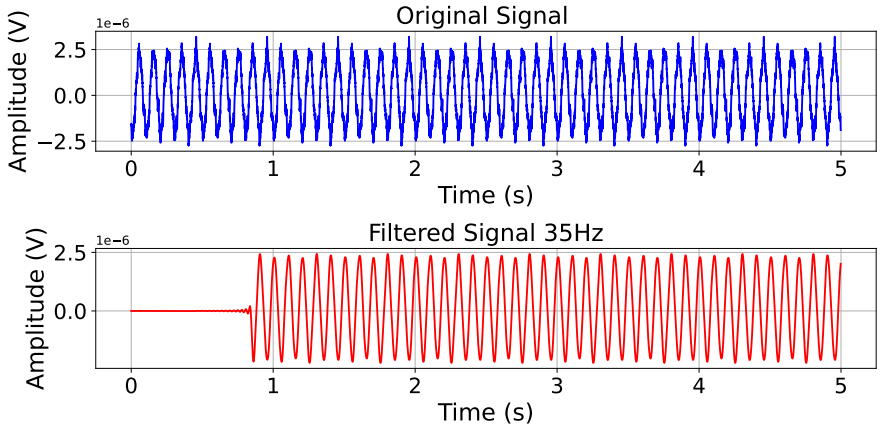

Figure A.29: *Raw (blue) and filtered (red) input referred signal of the ECG amplifier 5 μV at 10 Hz.*

Experimental setup:

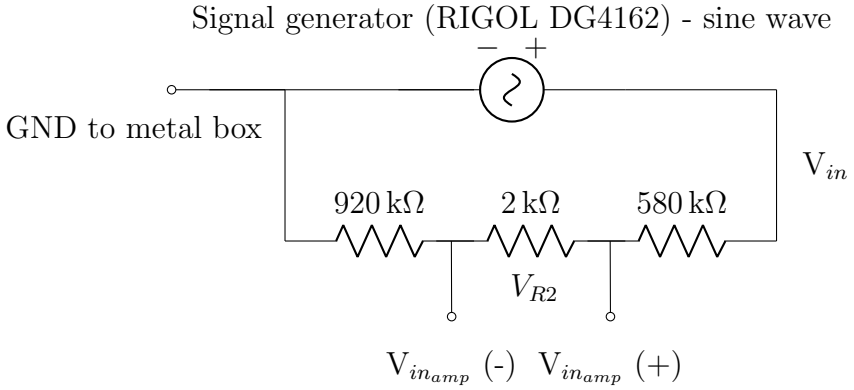

BIOPAC MP100 ECG Amplifier

$$V_{R2} = V_{in} \cdot (\frac{R_2}{R1 + R2 + R3}) = V_{in} \cdot (\frac{2\,\text{k}\Omega}{920\,\text{k}\Omega + 2\,\text{k}\Omega + 580\,\text{k}\Omega}) = V_{in} \cdot 0.001 \quad \text{(A.2)}$$

Procedure:

1. Set V_{pp} (5mV) and the frequency 10Hz of the sine wave from the signal generator.
2. Measure the BIOPAC MP100 ECG amplifier output with an oscilloscope (In this case Tektronix TDS2024B oscilloscope at a sampling rate of 20 kHz was utilised).
3. Analyse the amplitude of the measured signal.
4. Compare the output amplitudes of the ECG BIOPAC ECG amplifier against BIOPAC ECG amplifier with the same input signals.

Note: BIOPAC amplifier has an in-built bandpass filter from 0.05 - 35 Hz

Results:

Comparison against BIOPAC ECG amplifier

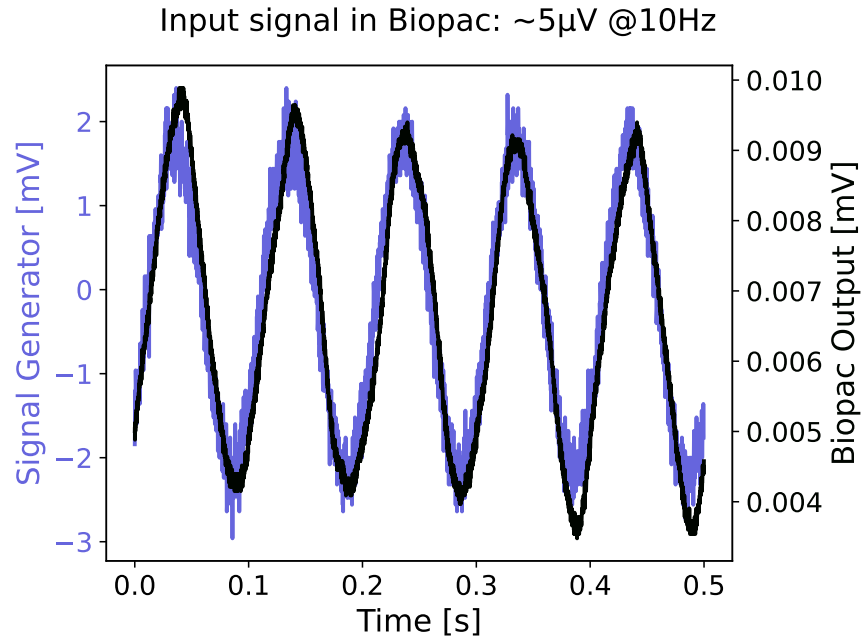

Figure A.30: *Sine wave input to the attenuator 1000x (purple) ≈ 5 mV at 10 Hz. Input referred signal from BIOPAC ECG amplifier (black) ≈ 5 µV at 10 Hz. It is noted that the noise recorded in the amplified signal in BIOPAC is less than 0.5 µV.*

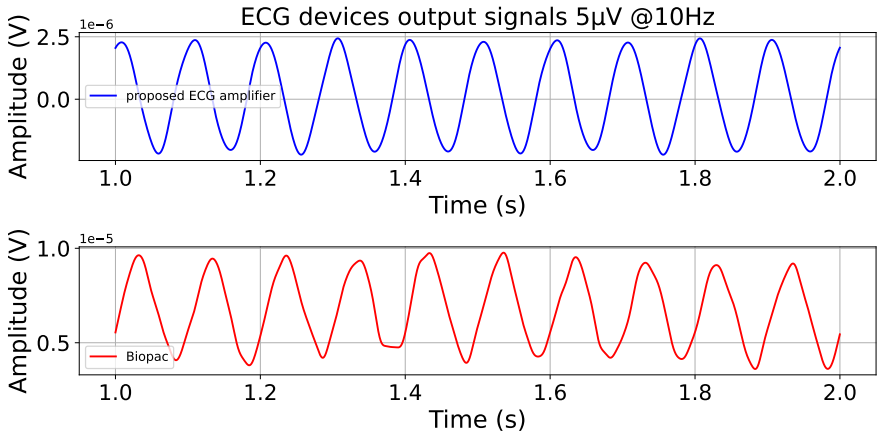

Figure A.31: *Comparison between our proposed ECG and BIOPAC ECG amplifier with an input signal of ≈ 5 µV at 10 Hz. Both Lowpass filtered at 35 Hz. Both amplifiers are showing similar performance detecting 5 µV signals at 10 Hz.*

ECG volunteers measurements

Figure A.32 illustrates the output amplified of an ECG measurement at the chest with the proposed ECG recorder. After considering the amplifier gain (G = 3000) the input referred ECG signals is obtained in Figure A.33.

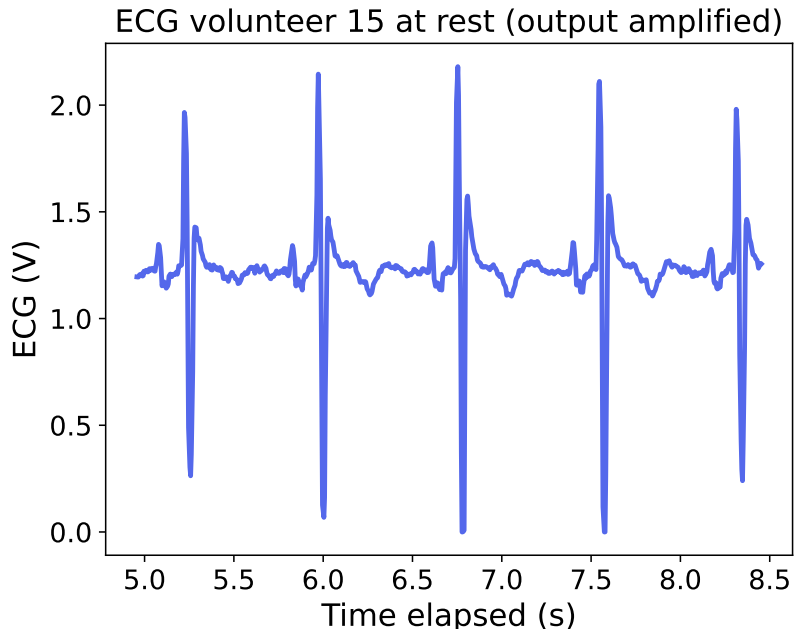

Figure A.32: *ECG measurement (output amplified) at the chest on volunteer 15 at rest position.*

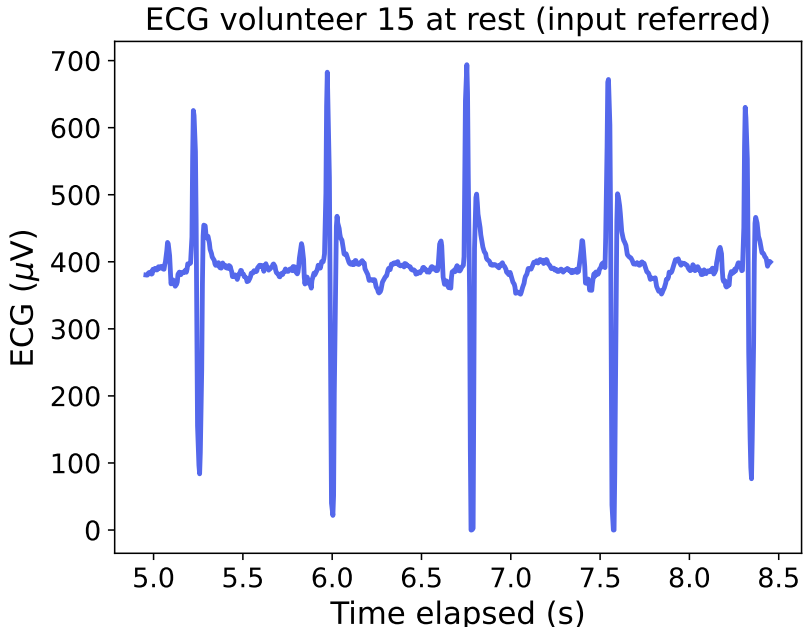

Figure A.33: *ECG measurement (input referred) at the chest on volunteer 15 at rest position.*

Summary

This appendix presented the design and testing of ECG device that in conjunction with the FBG-cantilever discussed in Chapter 3 allows the measurement of PAT between the electrical signals detected from the chest and the mechanical signals from the wrist.
The fabrication details of the ECG lead using shielded wires and Hirose connector were described. The thermal noise generated by the skin impedance was simulated by placing different resistor values at the input of the ECG amplifier, it was noticed that a load resistor of 4.7 kΩ (skin impedance order of magnitude), corresponds to a peak to peak amplitude noise 0.6 μV. The differences in the magnitude of the calculated thermal noise (Figure A.23) and the P-P value measured with different load resistors (Figure A.22) is because the shot, flicker, power supply and ambient noise were not considered. The signal-to-noise ratio of the output signal was assessed with an attenuated sine wave at 10 Hz of 5 µV. The device amplified the sine wave to 15 mV (peak-to-peak amplitude). At this signal amplitude, noise at 50Hz was visible with a peak to peak amplitude of 2.5 mV. This noise was filtered with a low-pass filtered at 35 Hz. The same sine wave input was tested in the BIOPAC Amplifier, and it was compared with our ECG amplifier Figure A.31. Finally, an ECG trace measured from the proposed ECG recorder is presented.

B. Appendix

B.1 PTT and PAT post-processing

Figure B.1 shows an example of incorrect PAT calculation due to false peaks detected in an FBG trace with noise artifacts. Figure B.2 shows the correct PAT calculation after the removal of the false peaks. In other cases some peaks need to be included, since the algorithm failed to detect them as the signal was corrupted by high frequency artifacts. Figure B.3 shows an example of an incorrect PTT calculation due to a missing peak because an artifact affected the automatic detection. Figure B.4 shows the correct PTT calculation after adding the missing FBG peak.

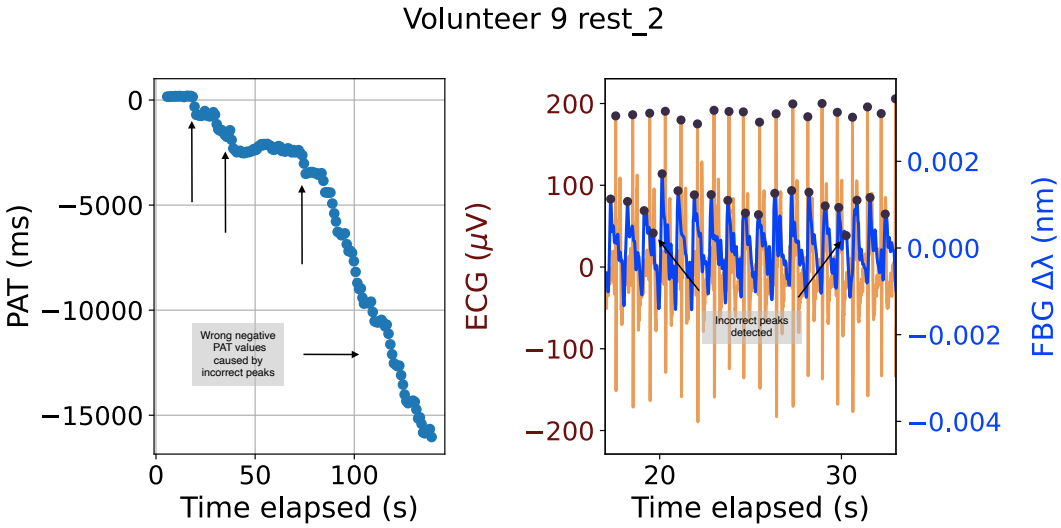

Figure B.1: *Example of incorrect PAT calculation due to false positives in the FBG traces (blue).*

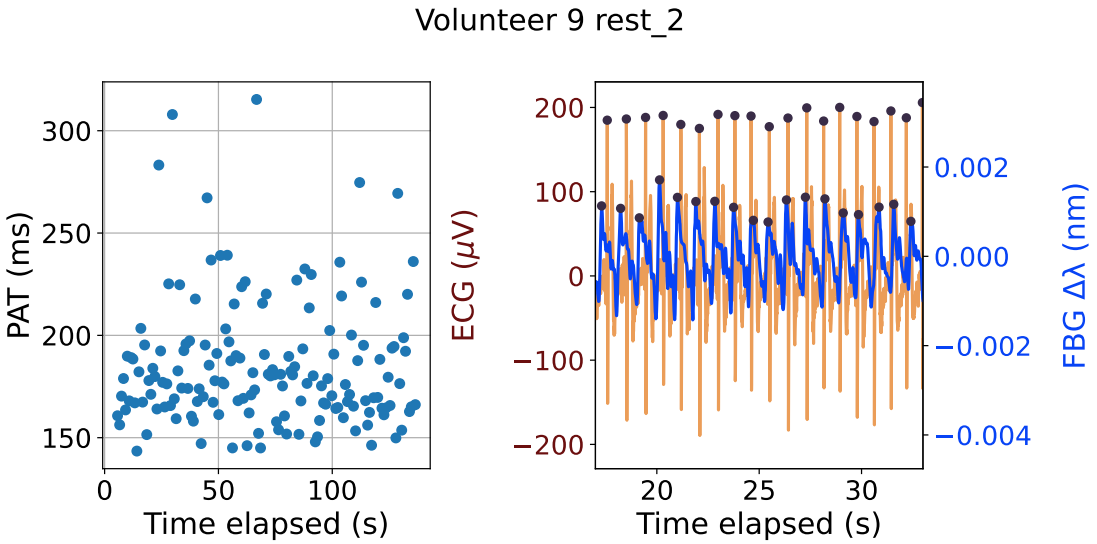

Figure B.2: *Example of correct PAT calculation after the manual removal of the false positive peaks.*

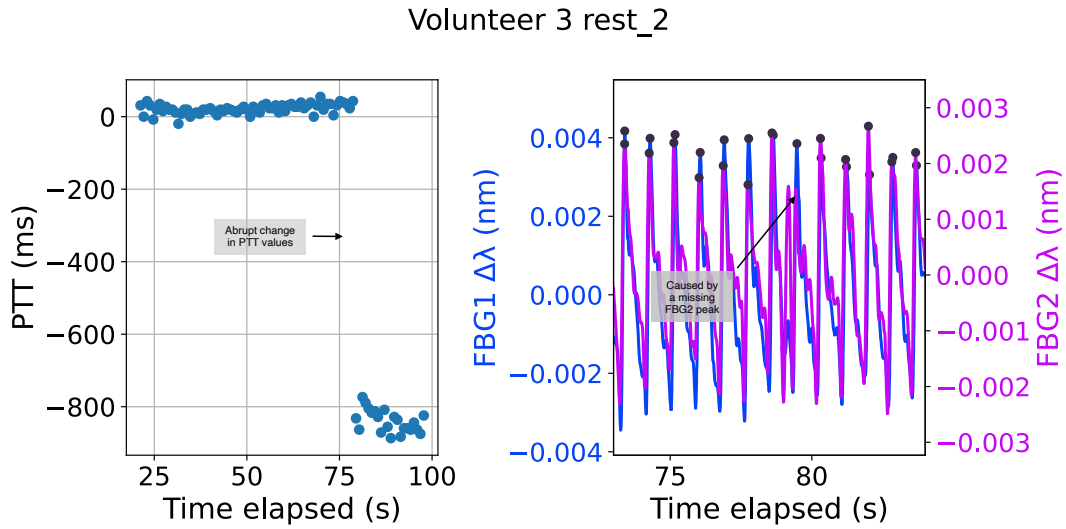

Figure B.3: *Example of incorrect PTT calculation due to a missing FBG peak.*

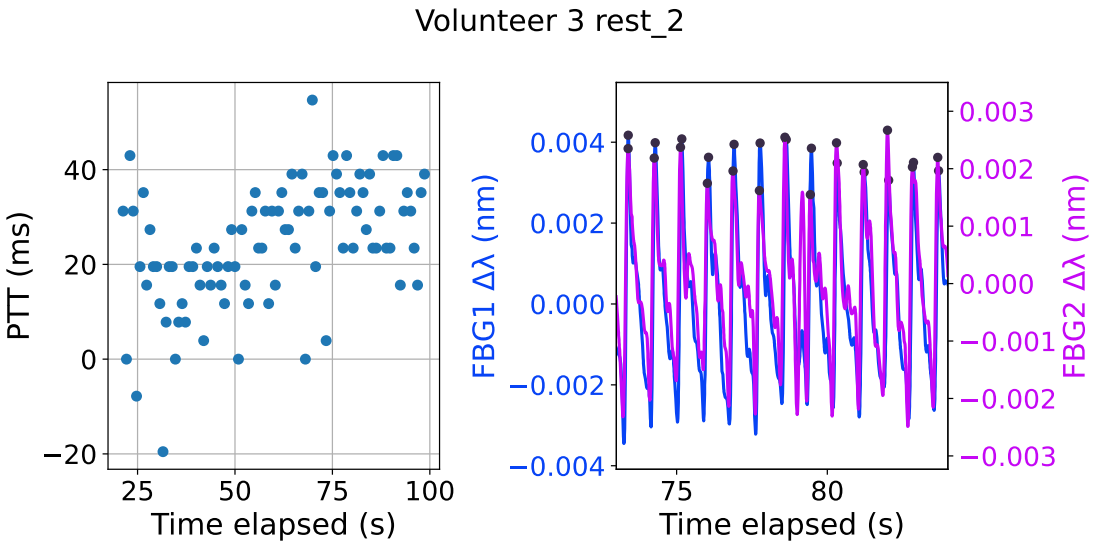

Figure B.4: *Example of the correct PTT calculation after the addition of the missed FBG peak.*

C. Appendix

C.1 Pulse Transit Time (PTT)

Figure C.1 presents the results for **volunteer 3**. The scatter plot in Figure C.1b shows the NIBP and HR trends. The SBP and HR show an increasing trend with exercise. The DBP shows only an increase from rest to cycle 30 s and a decrease from cycle 30 s to cycle 1 min. The DBP standard deviation is bigger in the last scenario. The average SBP increased by 18 mmHg, the average HR rose by 9 BPM, meanwhile the average DBP did not increase. As there is a clear increase in SBP and HR, the increase in the physical activity reflects the expected cardiovascular response. The violin plot in Figure C.1a displays the distribution of PTT values, the distribution of PTT values at rest is less spread compared to the other 2 scenarios, which can be attributed to the higher SNR of these pulses compared to the other scenarios, also explained by the less amount of negative PTT values. However, there is a reduction in the spread and maximum of PTT values from 170 to 120 ms, from cycling 30 s to cycling 1 min (both measurements taken at rest after the exercise). The decreasing trend that explains the increase in physical activity as well as the expected increase in BP and HR, is only demonstrated in the last two scenarios.

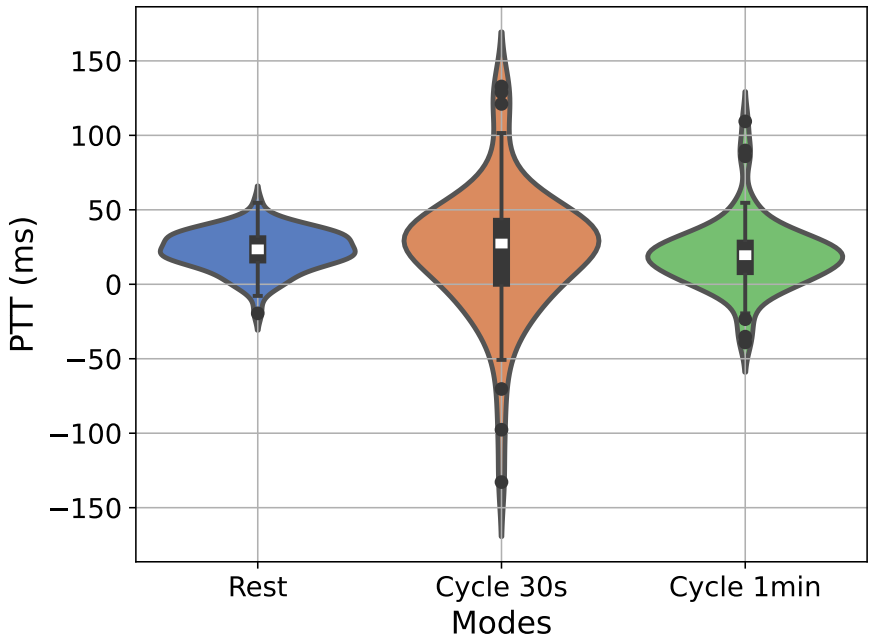

(a)

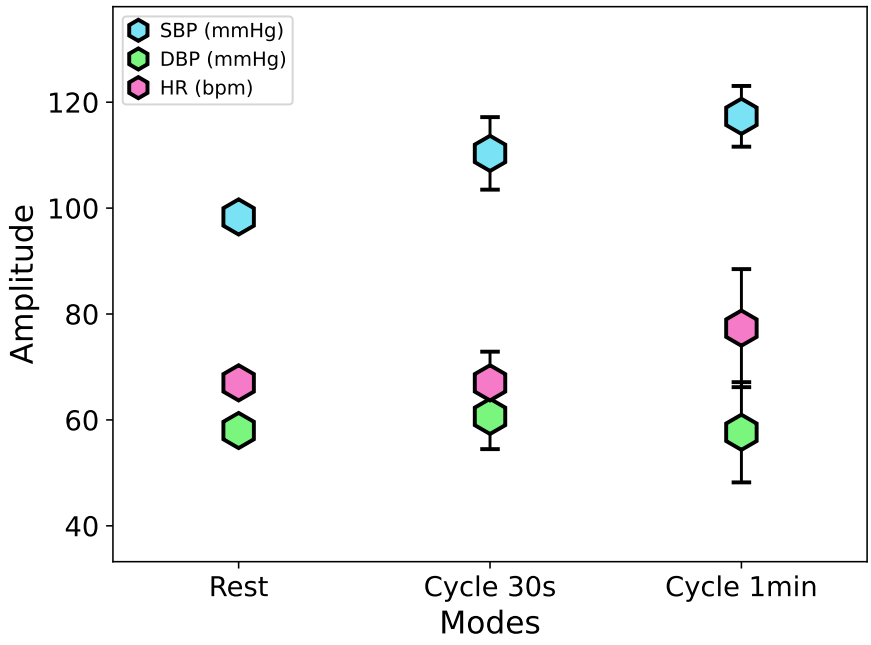

(b)

Figure C.1: *PTT values condensed in violin plots (a) vs NIBP (SBP and DBP) values and HR (b) of the different modalities (rest, cycle 30 s and cycle 1 min) of the experiment in* ***volunteer 3****. The PTT values did not show any trend, the decreasing trend is visible by increasing the exercise from 30 s to 1 min. The PTT values distribution has a wider distribution compared to the other modalities. The SBP and HR follows an increasing trend as the exercise increases.*

Figure C.2 presents the results for **volunteer 4**. The scatter plot in Figure C.2b shows the NIBP and HR trends. The SBP, DBP and HR show an increasing trend with exercise from rest to cycle 30 s. This trend becomes steady for SBP and HR from cycle 30 s to cycle 1 min, meanwhile DBP decreased from cycle 30 s to cycle 1 min. The average SBP increased by 10 mmHg, the average HR rose by 10 BPM, meanwhile the average DBP did not increase. As there is an increase in SBP and HR from rest to cycle 1 min, the increase in the physical activity reflects the expected cardiovascular response.
The violin plot in Figure C.2a displays the distribution of PTT values, the distribution of these values at rest is the widest with large spread, indicating a more variable PTT. The narrowest distribution is shown at the second modality, while the distribution at cycle 1 min shows a slight spread compared to cycle 30 s, but with outliers up to -250ms. Comparing the spread of the distribution of PTT values with SBP and DBP in each scenario an inverse relationship is observed. As the highest SBP and DBP was detected at Scenario 2 (cycle 30 s) correspond to the narrowest distribution of PTT values. Besides, the lowest BP values at rest correspond to the widest distribution of PTT values.

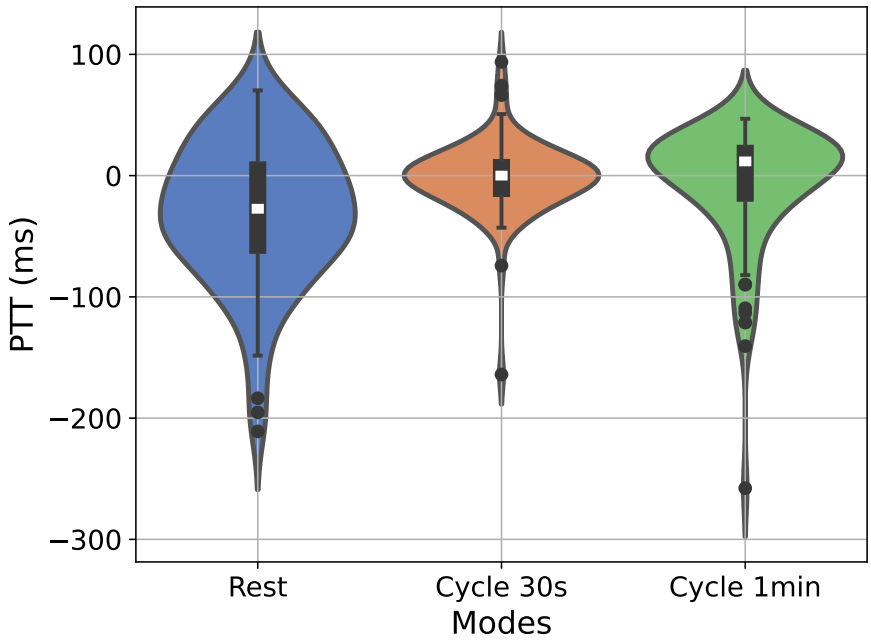

(a)

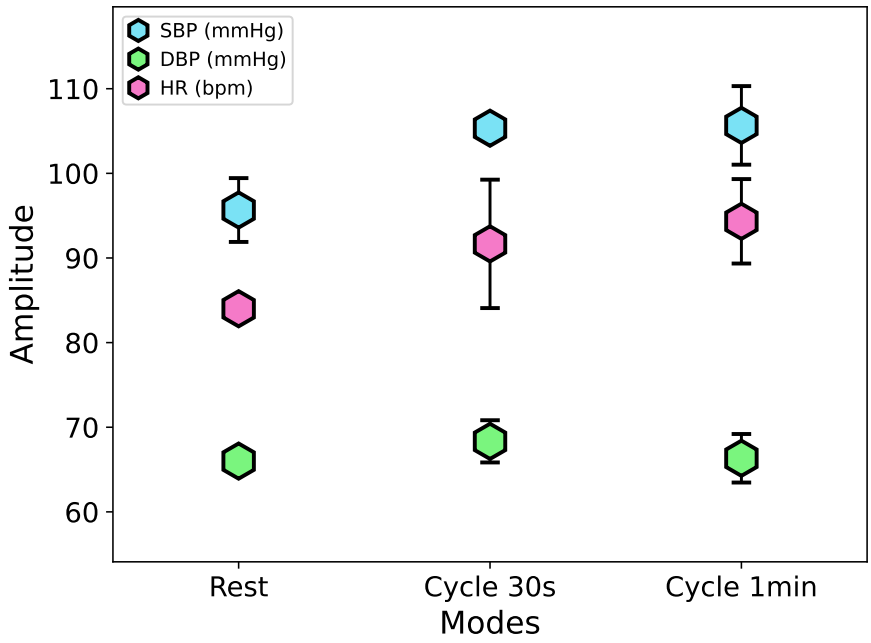

(b)

Figure C.2: *PTT values condensed in violin plots (a) vs NIBP (SBP and DBP) values and HR (right) of the different modalities (rest, cycle 30 s and cycle 1 min) of the experiment in* ***volunteer 4****. It can be observed that the data distribution shrank from rest to cycle 30 s.*

Figure C.3 presents the results for **volunteer 5**. The scatter plot in Figure C.3b shows the NIBP and HR trends. The SBP and HR show an increasing trend overall with exercise. Conversely, the DBP shows a decreasing trend. The average SBP increased by 5 mmHg, the average HR rose by 49 BPM, meanwhile the average DBP decreased by 7 mmHg. The increased HR and the small increase in SBP reflect the cardiovascular response to physical exertion. However, the lowest SBP was detected after cycling 30 s. The violin plot in Figure C.3a displays the distribution of PTT values, the overall distribution narrows with exercise. However, the widest distribution is observed in scenario 2 (cycle 30 s). This distribution at scenario 2 corresponds to the lowest SBP value across the 3 scenarios. The narrowest distribution was visualised in the third scenario (cycle 1 min), which corresponds to the highest SBP and HR.

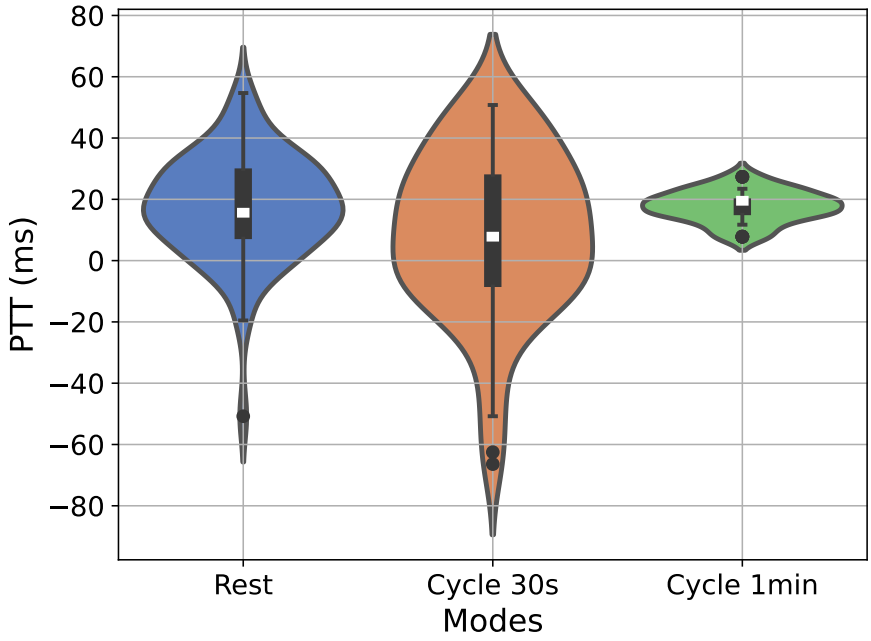

(a)

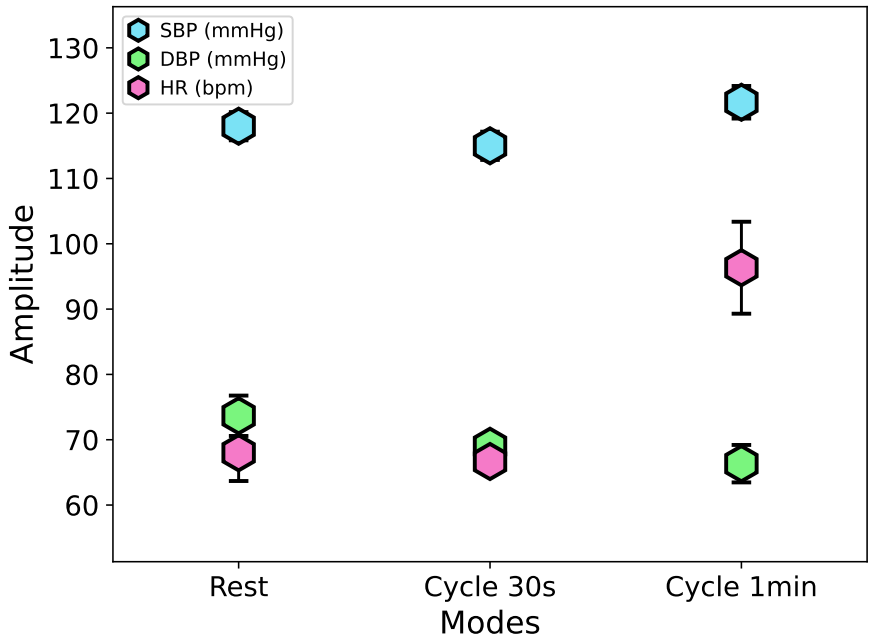

(b)

Figure C.3: *PTT values condensed in violin plots (a) vs NIBP (SBP and DBP) values and HR (b) of the different modalities (rest, cycle 30 s and cycle 1 min) of the experiment in* ***volunteer 5****. A decreasing trend was more visible from cycle 30 s to cycle 1 min aligned in with an increase of SBP and HR while the DBP decreases along modalities.*

Figure C.4 presents the results for **volunteer 9**. The scatter plot in Figure C.4b shows the NIBP and HR trends. The SBP, DBP and HR show an increasing trend with exercise. The average SBP increased by 27 mmHg, the average HR rose by 56 BPM, meanwhile the average DBP increased only 4 mmHg, reflecting the expected cardiovascular response to physical exertion. The left violin plot in Figure C.4a displays the distribution of PTT values, it shows that at rest, this distribution is the widest with large spread, indicating a more variable PTT, this distribution corresponds to the lowest SPB, DBP and HR values. As the exercise intensity increases (cycle 30 s and cycle 1 min), the maximum PTT values decrease, approximately from 170 to 50 ms, and their spread narrows. This decreasing trend suggests that PTT shortens with increased physical activity, aligning with the expected physiological response due to increased BP.

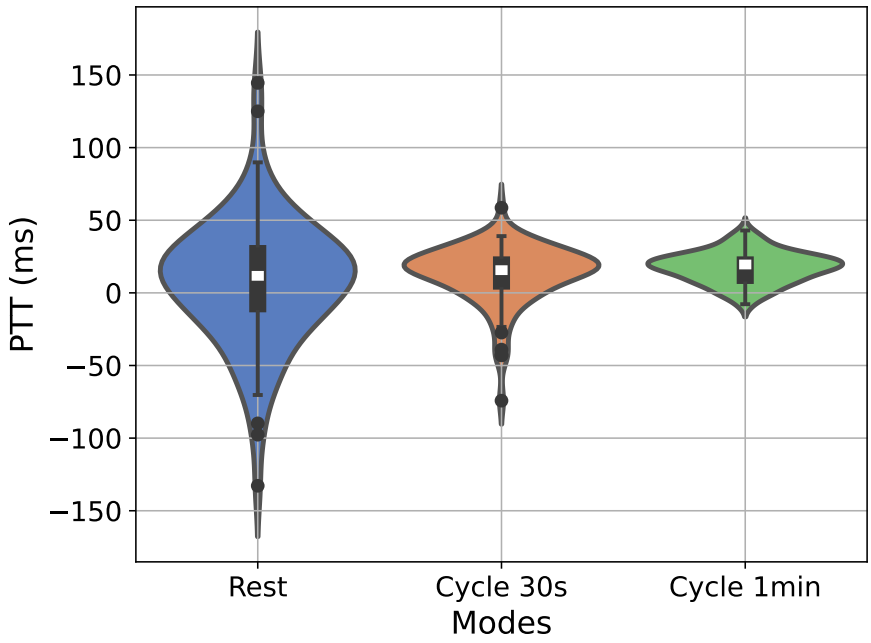

(a)

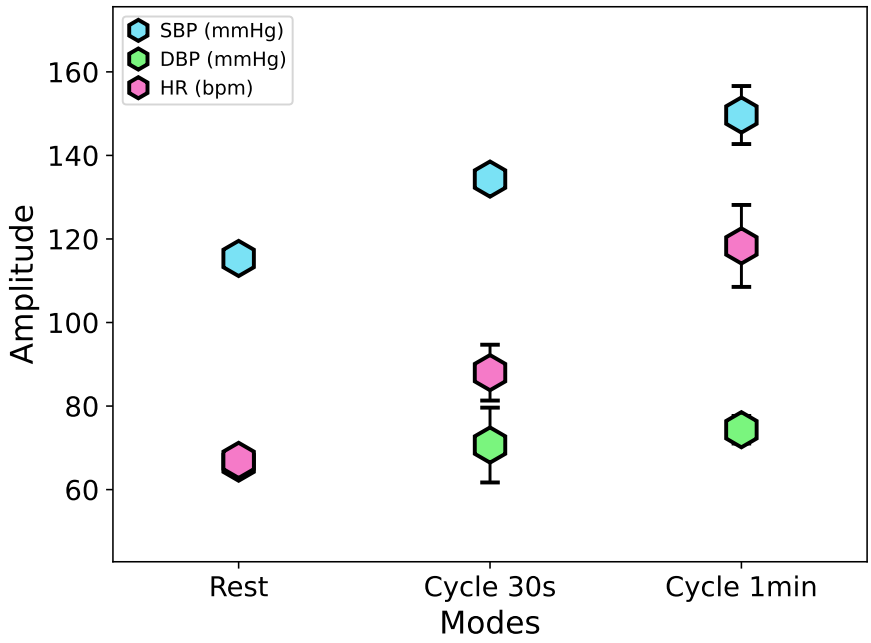

(b)

Figure C.4: *PTT values condensed in violin plots (a) vs NIBP (SBP and DBP) values and HR (b) of the different modalities (rest, cycle 30 s and cycle 1 min) of the experiment in* ***volunteer 9****. A decreasing trend of the maximum and minimum PTT values, as well as shrinking of the distribution aligned with an increasing trend of SBP and HR is observed in the data measured.*

Figure C.5 presents the results for **volunteer 10**. The scatter plot in Figure C.5b shows the NIBP and HR trends. The SBP, DBP and HR show an increasing trend with exercise. The average SBP increased by 36 mmHg, the average HR rose by 30 BPM, meanwhile the average DBP increased by 9 mmHg, reflecting the expected cardiovascular response to physical exertion. The violin plot in Figure C.5a displays the distribution of PTT values, at rest the distribution is the widest and corresponds to the lowest SBP, DBP and HR. A decrease in the PTT distribution is observed after cycling 30 s. However, this decreases was not palpable after cycling 1 min. The first two scenarios demonstrate an inverse relationship with SBP, DBP and HR values as expected. Nevertheless, this relationship is not explained in the third scenario.

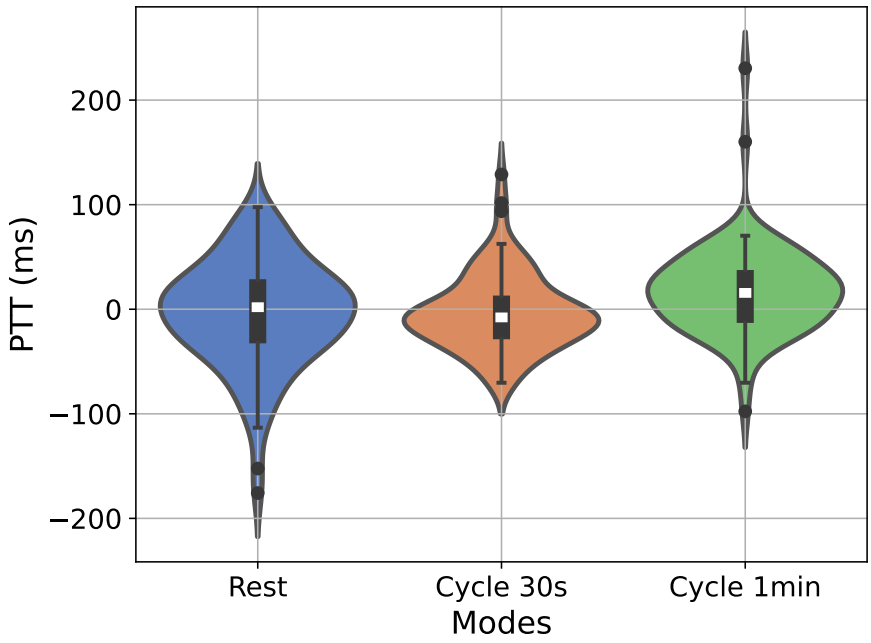

(a)

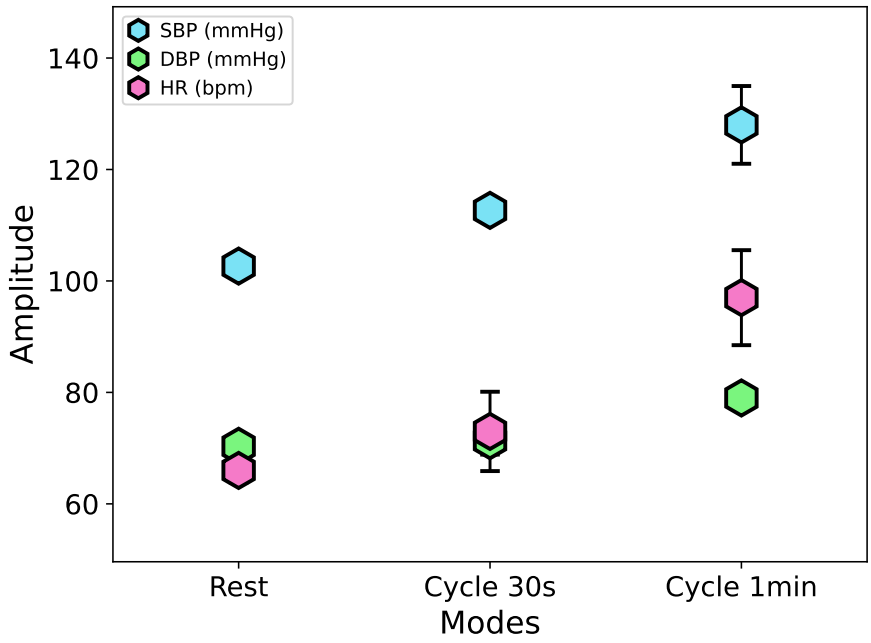

(b)

Figure C.5: *PTT values condensed in violin plots (a) vs NIBP (SBP and DBP) values and HR (b) of the different modalities (rest, cycle 30 s and cycle 1 min) of the experiment in* ***volunteer 10****. The mean of the distributions of* ***volunteer 10*** *decreased as well as shrinking of the data distribution from rest to cycle 30 s along with an increase of SBP, HR and DBP.*

Figure C.6 presents the results for **volunteer 12**. The scatter plot in Figure C.6a shows the NIBP and HR trends. The SBP, DBP and HR show an increasing trend with exercise. The average SBP increased by 27 mmHg, the average HR rose by 10 BPM, meanwhile the average DBP increased by 5 mmHg, reflecting the expected cardiovascular response to physical exertion. The violin plot in Figure C.6b displays the distribution of PTT values, at rest the PTT distribution is the widest and flattest but without any outliers. The maximum and median PTT values across the 3 scenarios show an increasing trend. The narrowest distribution is shown at scenario 2 after cycling 30 s. In this case only the wider and flatter distribution at rest follows an inverse relationship with the SBP, DBP and HR. Otherwise, there is no clear expected inverse relationship with BP as expected.

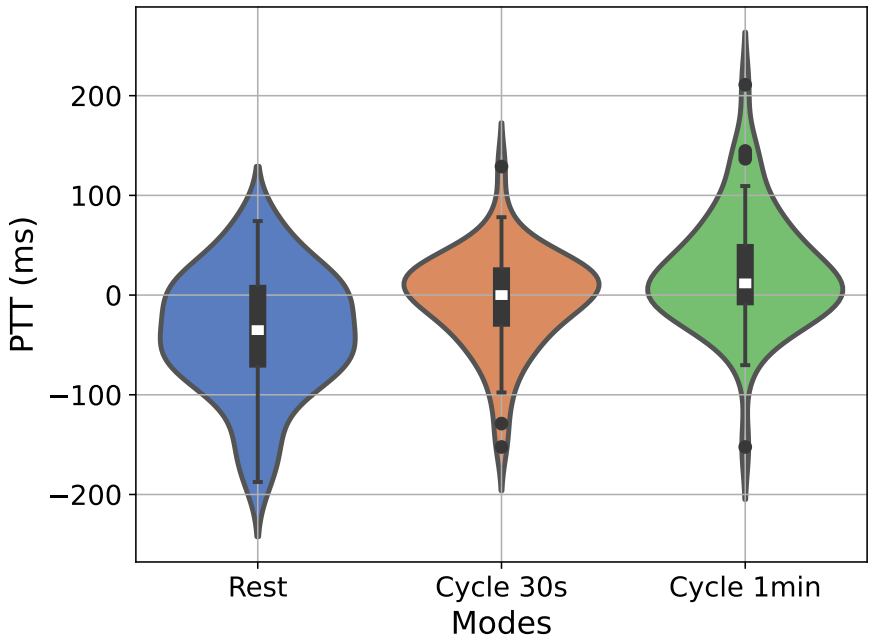

(a)

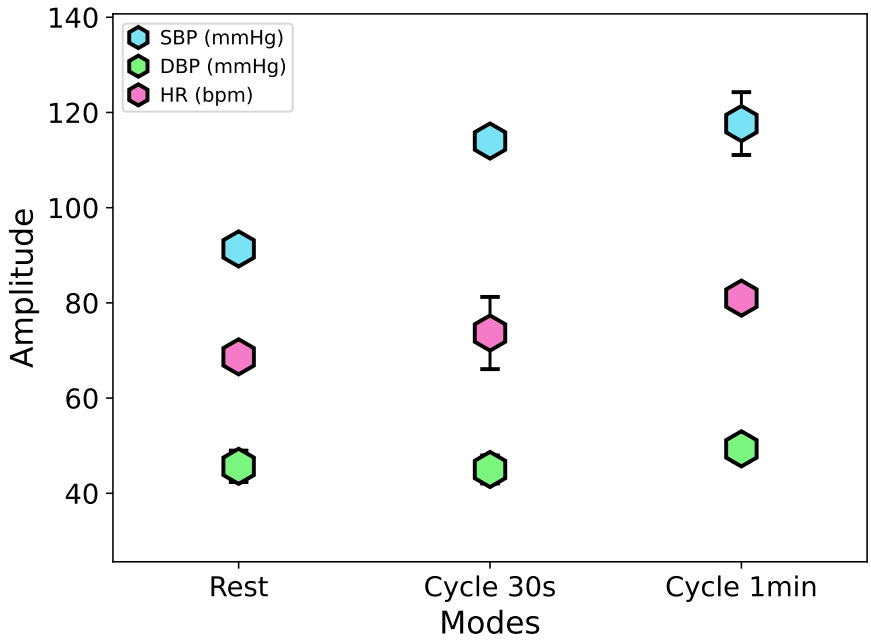

(b)

Figure C.6: *PTT values condensed in violin plots (a) vs NIBP (SBP and DBP) values and HR (b) of the different modalities (rest, cycle 30 s and cycle 1 min) of the experiment in* ***volunteer 12****. It shows a wider data distribution at rest compared to cycle 30 s and cycle 1 min modes.*

Figure C.7 presents the results for **volunteer 13**. The scatter plot in Figure C.7b shows the NIBP and HR trends. The SBP, HR show an increasing trend with exercise, however the SBP at scenario 2 is the highest and DBP shows an overall decrease of 1 mmHg. The average SBP increased by 23 mmHg and the average HR rose by 10 BPM reflect the expected cardiovascular response to physical exertion. The violin plot in Figure C.7a displays the distribution of PTT values, at scenario 3, the distribution is narrowest and at scenario 1 the distribution is the widest, however this distribution just slightly differs from scenario 2. These PTT distributions follow an inverse relationship with HR and DBP but not with SBP.

C.2 Pulse Arrival Time (PAT)

Figure C.8 presents the results for **volunteer 1**. The scatter plot in Figure C.8b shows the NIBP and HR trends. The SBP, DBP and HR show an increasing trend with exercise. The average SBP increased by 26 mmHg, the average HR rose by 17 BPM, meanwhile the average DBP increased only 5 mmHg, reflecting the expected cardiovascular response to physical exertion.
The violin plot in Figure C.8a displays the distribution of PAT values, the distribution of PAT values preserved the same shape among different exercise activities. There is a clear decrease in PTT values from rest to cycle 1 min, the maximum values dropped from 235 to 209 ms, the median values decreased from 209 to 189 ms and the minimum values decreased 180 to 165 ms. However, from rest to cycle 30 s there is a slight increase of around 5 ms. In general the lowest PAT values are observed by cycle 1 min. These PAT distributions follow a clear inverse relationship with the HR considering each scenario. Considering the decreased in general from rest to cycle 1 min the trend also follows an inverse relationship with SBP and DBP values.

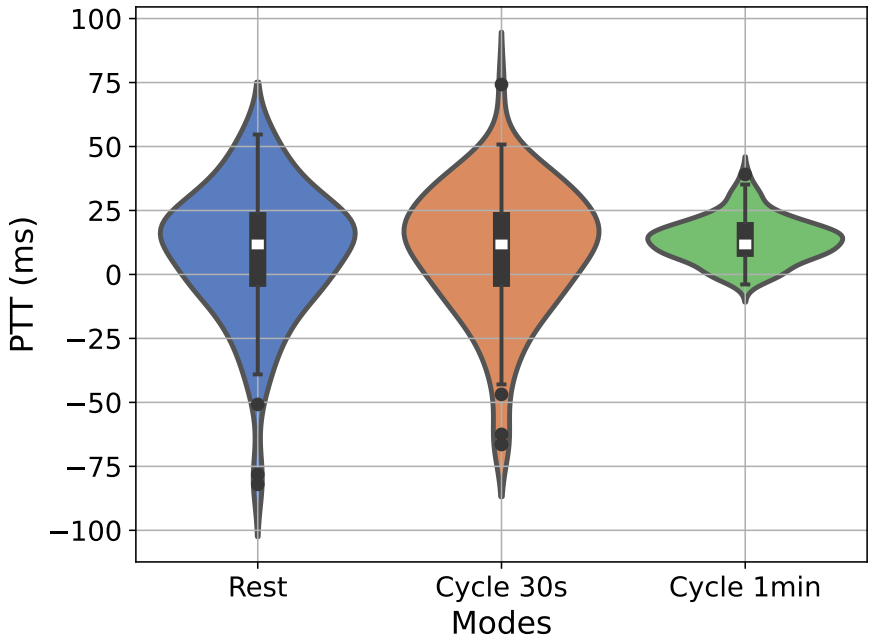

(a)

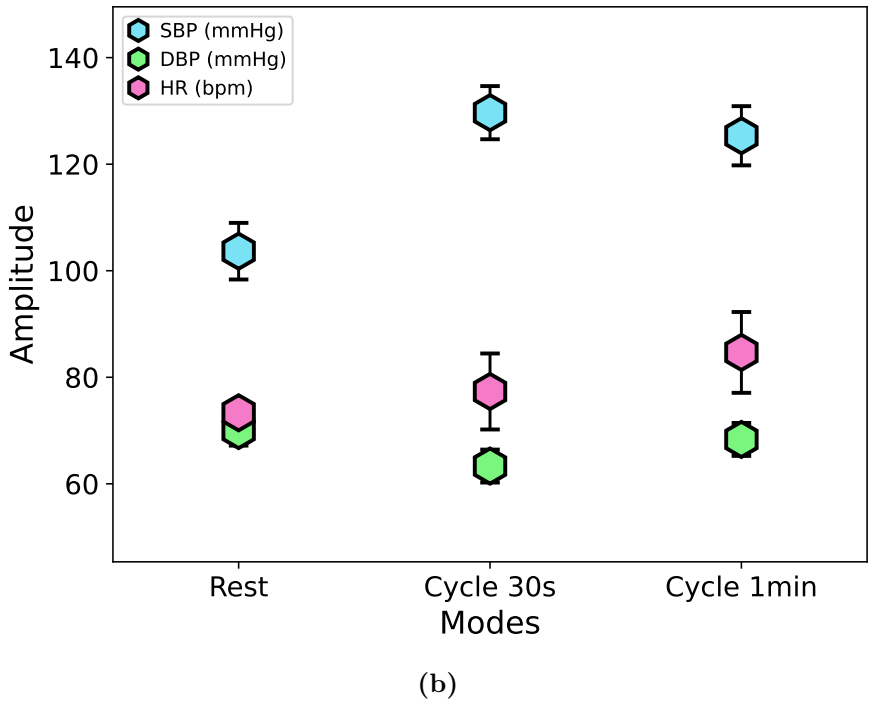

(b)

Figure C.7: *PTT values condensed in violin plots (a) vs NIBP (SBP and DBP) values and HR (b) of the different modalities (rest, cycle 30 s and cycle 1 min) of the experiment in* ***volunteer 13****. The data distribution of PTT values at cycle 1 min is narrower compared to the other modes.*

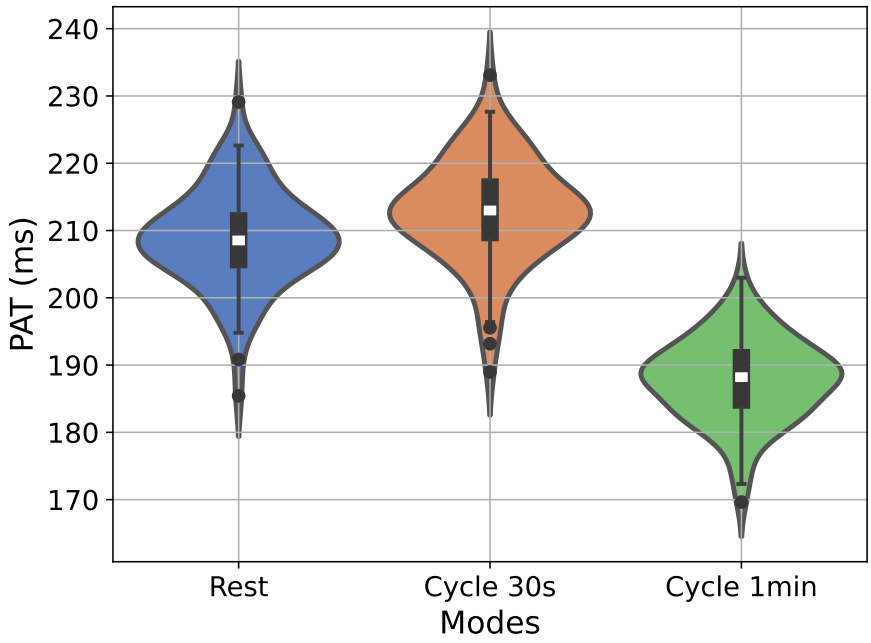

(a)

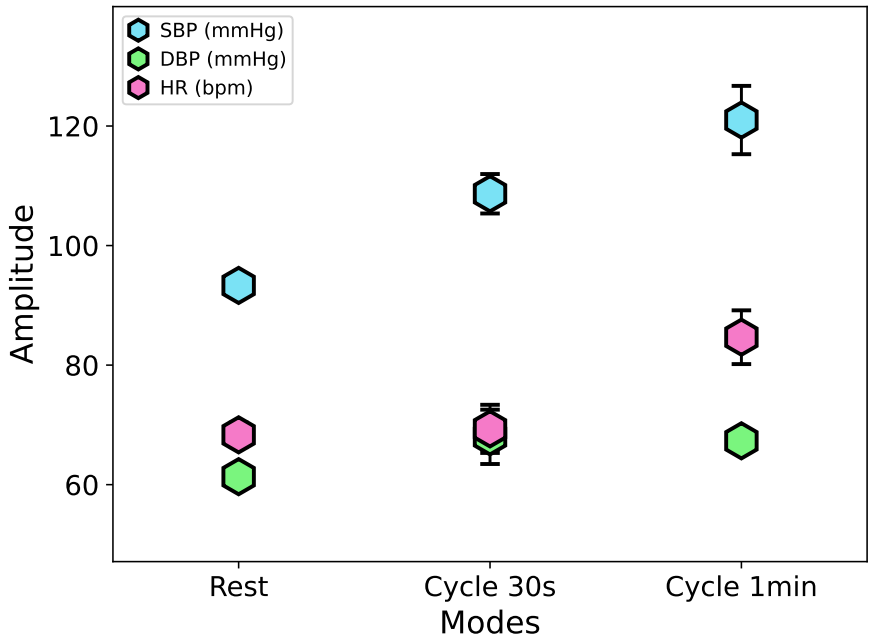

(b)

Figure C.8: *PAT values condensed in violin plots (a) vs NIBP (SBP and DBP) values and HR (b) of the different modalities (rest, cycle 30 s and cycle 1 min) of the experiment in* ***volunteer 1****. The data distribution of PAT values in the 3 different modes is very steady, a decrease in these values, comparing rest and cycle 1 min is clearly observed, however, this trend is not followed at cycle 30 s, the SBP and HR show on the other side an increasing trend. The PAT values vary among all modalities from 164 to 240 ms.*

Figure C.9 presents the results for **volunteer 3**. The scatter plot in Figure C.9b shows the NIBP and HR trends. The SBP and HR show an increasing trend with exercise. The DBP shows only an increase from rest to cycle 30 s and a decrease from cycle 30 s to cycle 1 min. The DBP standard deviation is bigger in the last scenario. The average SBP increased by 18 mmHg, the average HR rose by 9 BPM, meanwhile the average DBP did not increase. As there is a clear increase in SBP and HR, the increase in the physical activity reflects the expected cardiovascular response.
The violin plot in Figure C.9a displays the distribution of PAT values, at scenario 3, the PAT distribution is narrowest among the scenarios. There is a clear decrease in PAT values in the minimum and median PAT values of each scenario distribution as the exercise increased. The median values decreased from 255 to 220 ms and the minimum values decreased 230 to 130 ms. These PAT distributions follow a clear inverse relationship with the SBP considering each scenario. Considering the decrease in general from rest to cycle 1 min the trend also follows an inverse relationship with HR, but is not that clear with DBP.

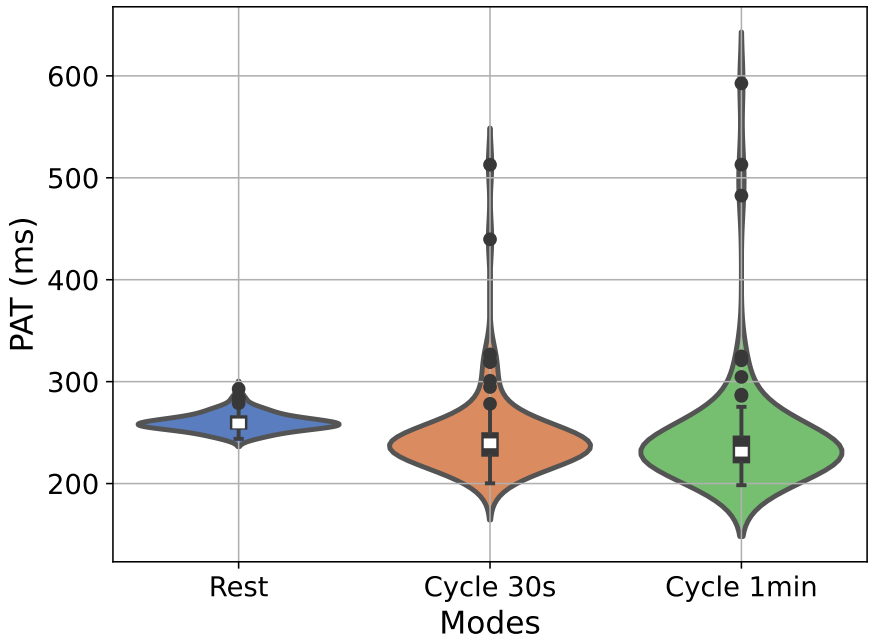

(a)

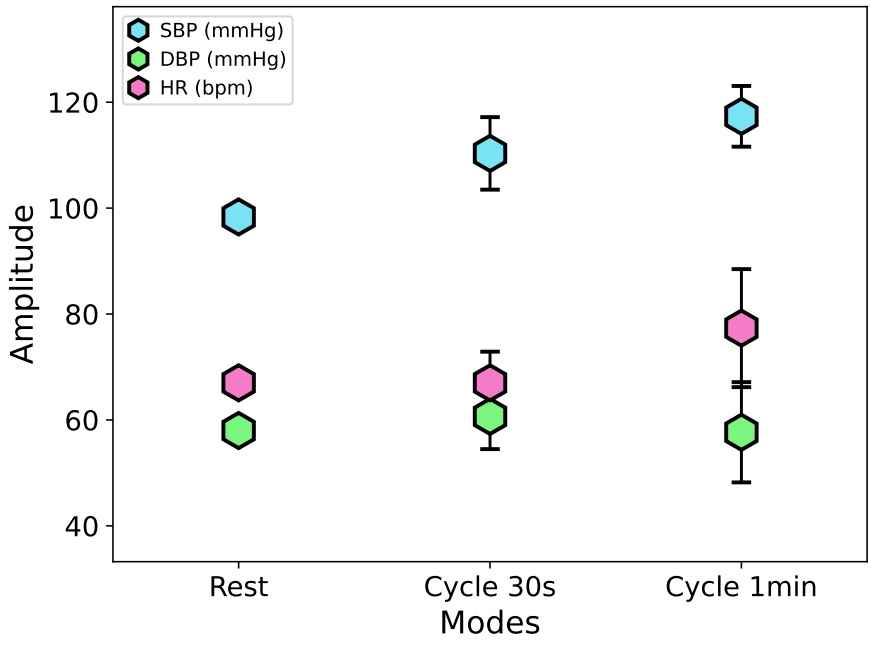

(b)

Figure C.9: *PAT values condensed in violin plots (a) vs NIBP (SBP and DBP) values and HR (b) of the different modalities (rest, cycle 30 s and cycle 1 min) of the experiment in* ***volunteer 3****. This figure shows a decreasing trend in the minimum PAT values detected and increasing spreading of the data distribution as the exercise increases, on the other side the SBP and HR increases with exercise, the PAT values vary from 150 to 650 ms.*

Figure C.10 presents the results for **volunteer 4**. The scatter plot in Figure C.10b shows the NIBP and HR trends. The SBP, DBP and HR show an increasing trend with exercise from rest to cycle 30 s. This trend becomes steady for SBP and HR from cycle 30 s to cycle 1 min, meanwhile DBP decreased from cycle 30 s to cycle 1 min. The average SBP increased by 10 mmHg, the average HR rose by 10 BPM, meanwhile the average DBP did not increase. As there is an increase in SBP and HR from rest to cycle 1 min, the increase in the physical activity reflects the expected cardiovascular response. The violin plot in Figure C.10a displays the distribution of PAT values, the distribution preserved similar shape among different exercise activities. There is a clear decrease in PTT values from rest to cycle 1 min, the maximum values dropped from 400 to 360 ms, the median values decreased from 310 to 260 ms and the minimum values decreased from 260 to 150 ms. however from cycle 30 s to cycle 1 min, a slight increase of around 10 ms is observed. In general the lowest PAT values are observed after cycle 30 min. These PAT distributions follow an inverse relationship with the SBP and DBP considering each scenario.

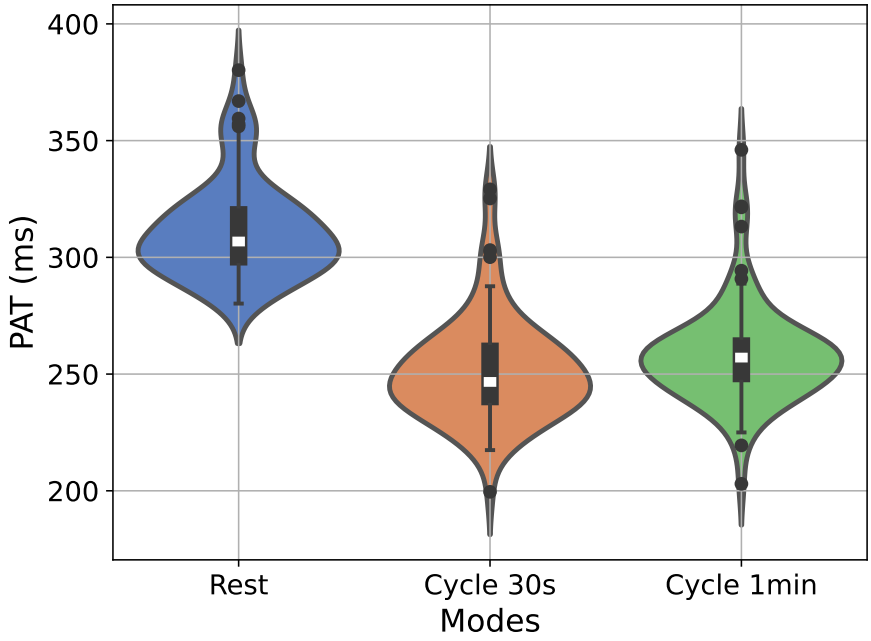

(a)

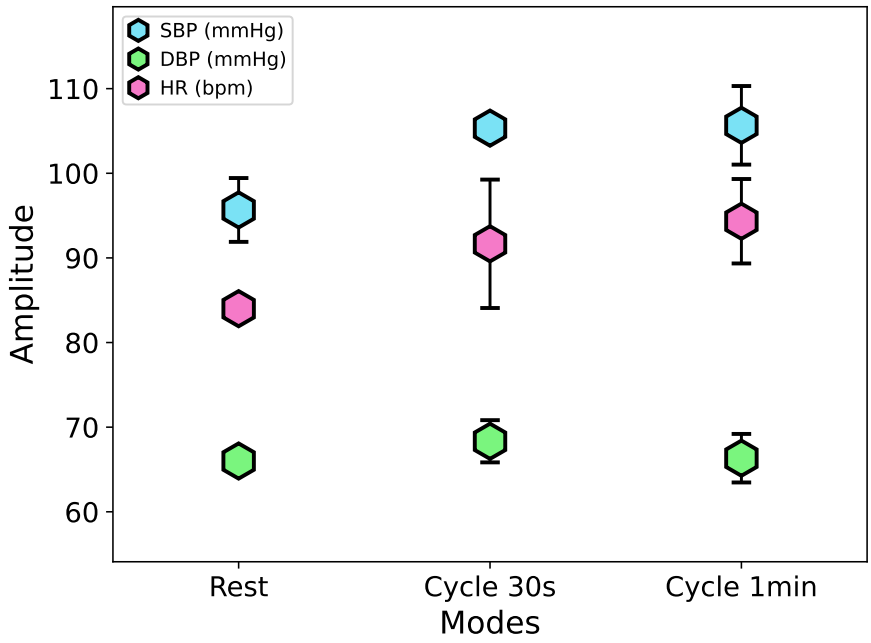

(b)

Figure C.10: *PAT values condensed in violin plots (a) vs NIBP (SBP and DBP) values and HR (b) of the different modalities (rest, cycle 30 s and cycle 1 min) of the experiment in* ***volunteer 4****. This figure shows a decrease in PAT values after exercise, however the difference is not clear from cycle 30 s to cycle 1 min which relates with the SBP and HR detected by the BP monitor.*

Figure C.11 presents the results for **volunteer 5**. The scatter plot in Figure C.11b shows the NIBP and HR trends. The SBP and HR show an increasing trend overall with exercise. On the other side the DBP shows a decreasing trend. The average SBP increased by 5 mmHg, the average HR rose by 49 BPM, meanwhile the average DBP decreased by 7 mmHg. The increased HR and the small increase in SBP reflect the cardiovascular response to physical exertion. However, the lowest SBP was detected after cycling 30 s. The left violin plot in Figure C.11a displays the distribution of PAT values, the distribution preserved similar shape among, same range variability between different exercise activities. The lowest PAT values are perceived at rest (median of 185 ms) and the biggest PAT values are at cycle 30 s (median of 265 ms). The PAT values decrease from cycle 30 s to cycle 1 min by 30 ms. These PAT distributions follow an inverse trend with the SBP values across the 3 scenarios.

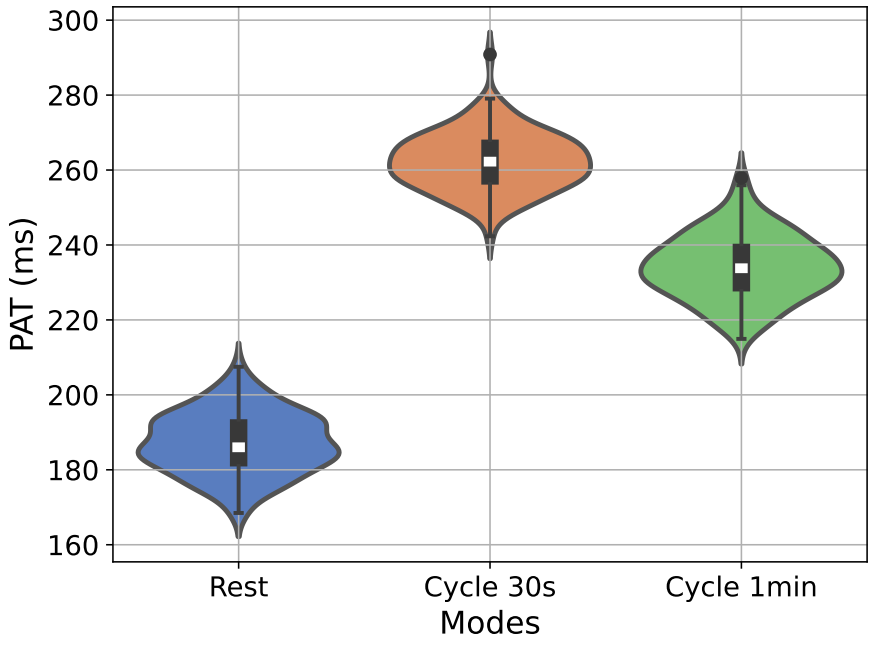

(a)

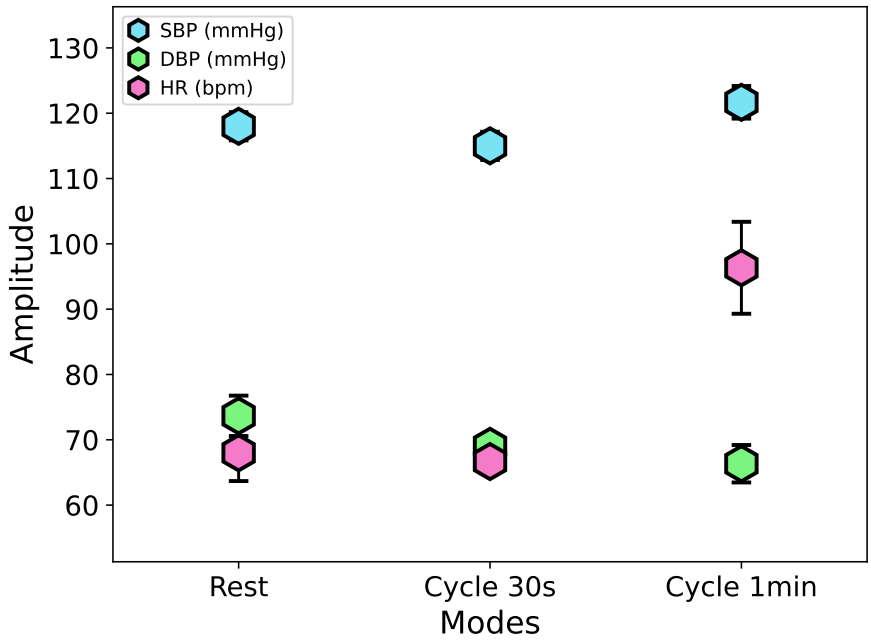

(b)

Figure C.11: *PAT values condensed in violin plots (a) vs NIBP (SBP and DBP) values and HR (b) of the different modalities (rest, cycle 30 s and cycle 1 min) of the experiment in* ***volunteer 5****. The PAT values show the opposite trend compared with the SBP values, the highest SBP values detected at rest and cycle 1 min follow smaller PAT values compared to cycle 30 s.*

Figure C.12 presents the results for **volunteer 10**. The scatter plot in Figure C.12b shows the NIBP and HR trends. The SBP, DBP and HR show an increasing trend with exercise. The average SBP increased by 36 mmHg, the average HR rose by 30 BPM, meanwhile the average DBP increased by 9 mmHg, reflecting the expected cardiovascular response to physical exertion. The violin plot in Figure C.12a displays the distribution of PAT values, the PAT distribution shape at scenario 3 (cycle 1 min) differs from the other scenarios. However, there is clear decreasing trend (median, maximum and minimum) as the exercise activity increased. At scenario 1 (rest) there is a median PAT around 190 ms, at scenario 2 (cycle 30 s) there is a median PAT around 165 ms and at scenario 3 (cycle 1 min) the median PAT is 110 ms. These PAT distributions follow a clear inverse trend with the SBP, HR and DBP values across the 3 scenarios, as the exercise increased.

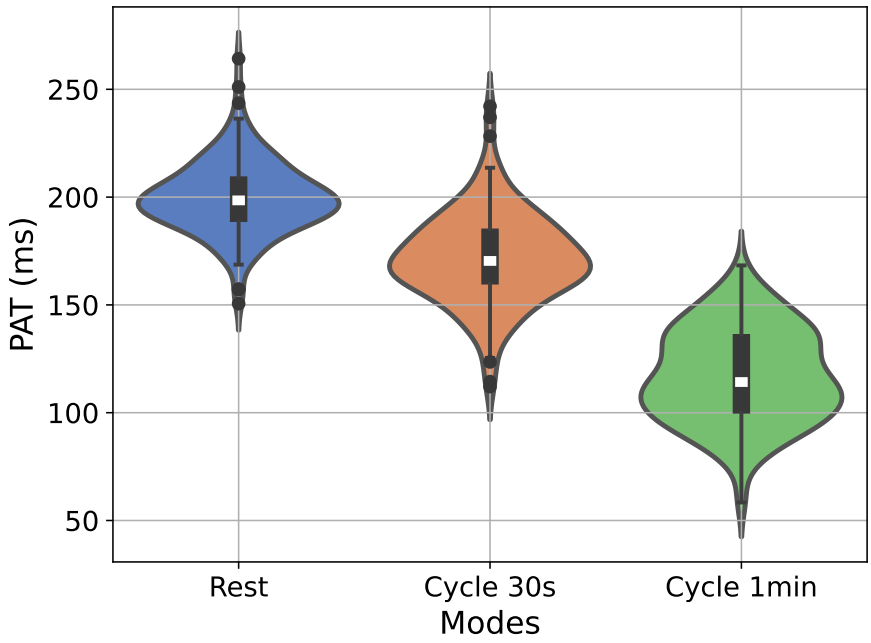

(a)

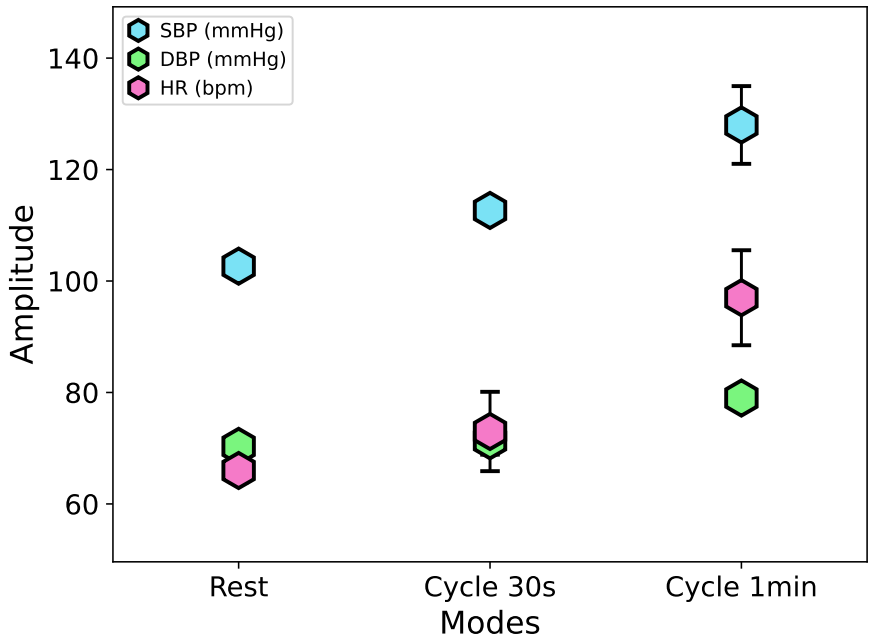

(b)

Figure C.12: *PAT values condensed in violin plots (a) vs NIBP (SBP and DBP) values and HR (b) of the different modalities (rest, cycle 30 s and cycle 1 min) of the experiment in* ***volunteer 10****. A decrease in PAT values and a spread of the data distribution after increasing the exercise, SBP, HR and DBP is visualised.*

Figure C.13 present the results for **volunteer 12**.
The scatter plot in Figure C.13b shows the NIBP and HR trends. The SBP, DBP and HR show an increasing trend with exercise. The average SBP increased by 27 mmHg, the average HR rose by 10 BPM, meanwhile the average DBP increased by 5 mmHg, reflecting the expected cardiovascular response to physical exertion. The violin plot in Figure C.13a displays the distribution of PAT values, the PAT distribution shape at scenario 3 (cycle 1 min) shows larger PAT variability. However, there is clear decreasing trend (median, maximum and minimum) as the exercise activity increased. At scenario 1 (rest) there is a median PAT around 250 ms, at scenario 2 (cycle 30 s) there is a median PAT around 150 ms and at scenario 3 (cycle 1 min) the median PAT is 110 ms. These PAT distributions follow a clear inverse trend with the SBP, HR and DBP values across the 3 scenarios, as the exercise increased.

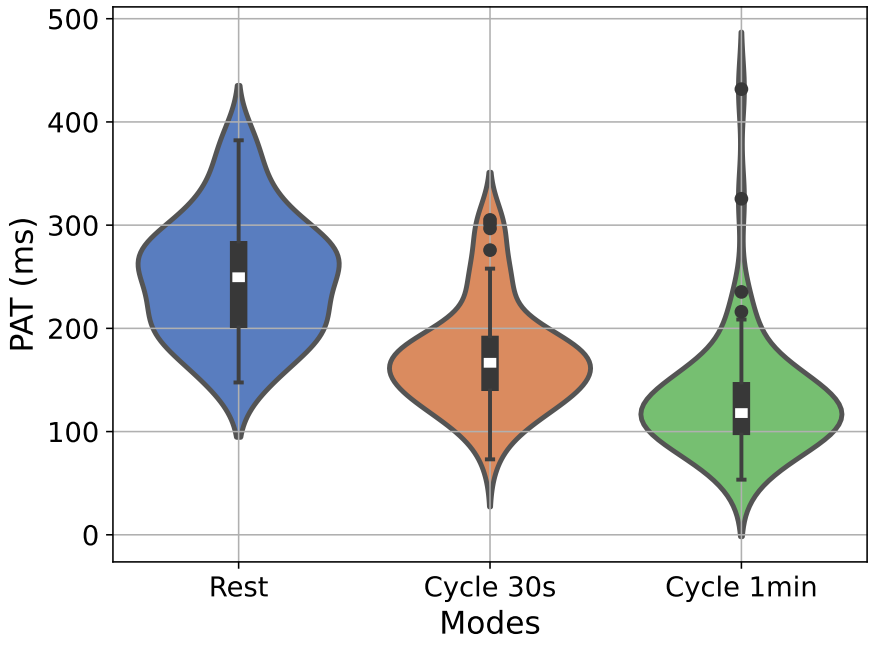

(a)

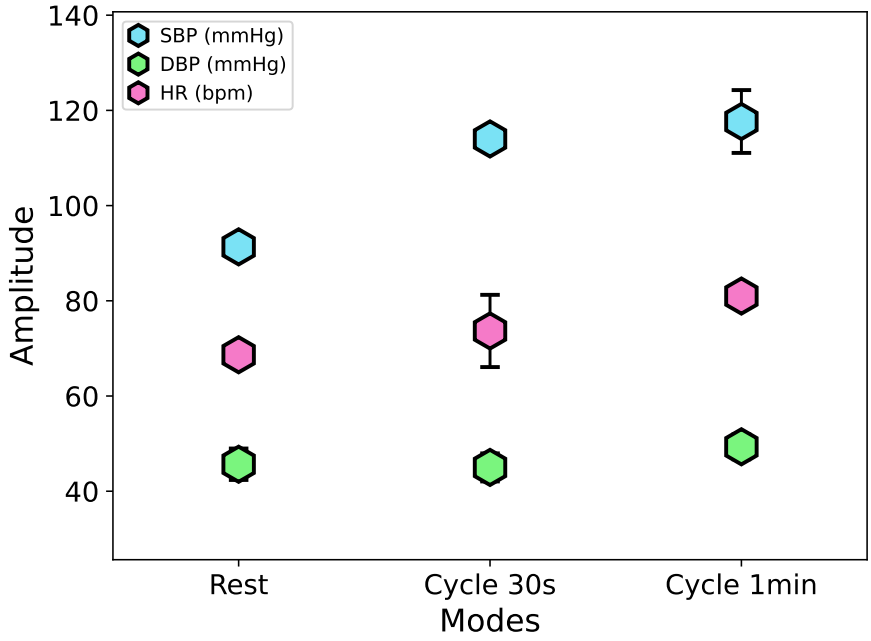

(b)

Figure C.13: *PAT values condensed in violin plots (a) vs NIBP (SBP and DBP) values and HR (b) of the different modalities (rest, cycle 30 s and cycle 1 min) of the experiment in* ***volunteer 12****. These plots show a decreasing trend of PAT as the exercise, SBP, DBP and HR increase, the PAT values at cycle 1 min show some outliers with PAT values of 500 ms.*

Figure C.14 presents the results for **volunteer 13**. The scatter plot in Figure C.7b shows the NIBP and HR trends. The SBP, HR show an increasing trend with exercise, however the SBP at scenario 2 is the highest and DBP shows an overall decrease of 1 mmHg. The average SBP increased by 23 mmHg and the average HR rose by 10 BPM reflecting the expected cardiovascular response to physical exertion. The violin plot in Figure C.14a displays the distribution of PAT values, the PAT distribution shape at scenario 3 (cycle 1 min) shows larger PAT variability while the distribution of PAT values at scenario 1 (rest) shows some outliers in the lower bound. However, there is a decreasing trend (median and maximum) as the exercise activity increased comparing these two scenarios. The highest distribution of PAT values is presented at scenario 2 (cycle 30 s). At scenario 1 (rest) there is a median PAT around 90 ms, at scenario 2 (cycle 30 s) there is a median PAT around 130 ms and at scenario 3 (cycle 1 min) the median PAT is around 60 ms. These PAT distributions follow an inverse trend with the DBP values, but not with SBP and HR values.

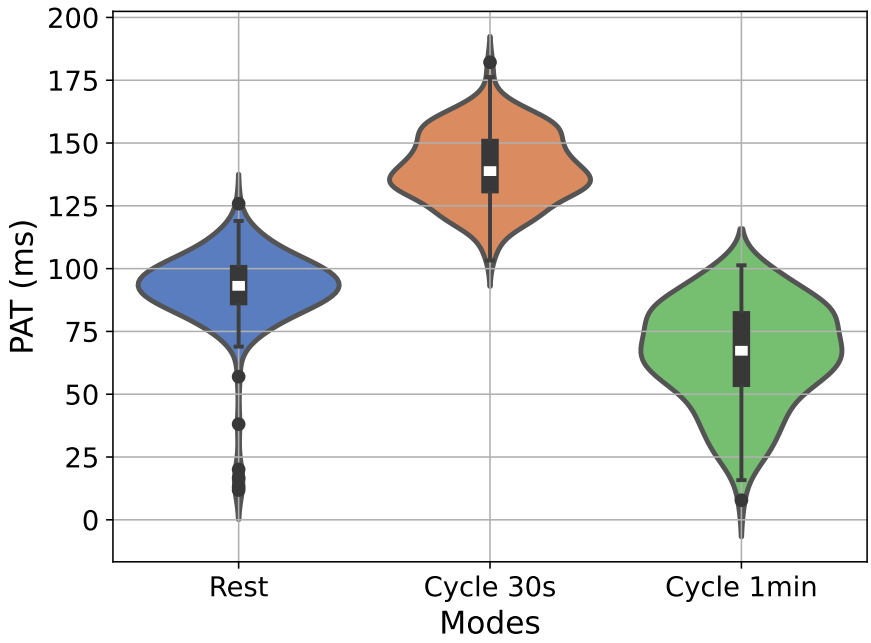

(a)

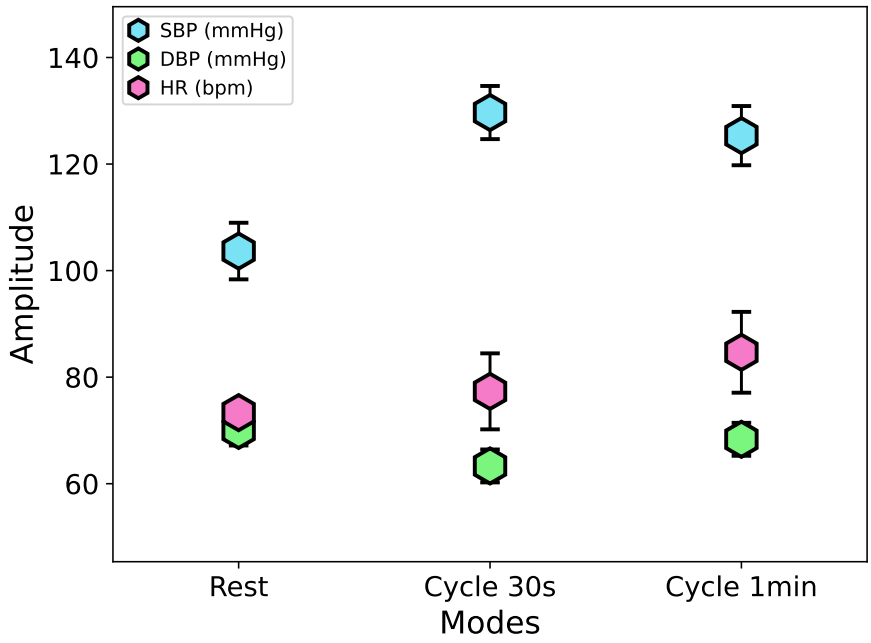

(b)

Figure C.14: *PAT values condensed in violin plots (a) vs NIBP (SBP and DBP) values and HR (b) of the different modalities (rest, cycle 30 s and cycle 1 min) of the experiment in* ***volunteer 13****. The PAT values show the same trend as the SBP and the opposite trend to DBP and HR after increasing exercise.*

Figure C.15 presents the results for **volunteer 14**. The scatter plot in Figure C.15b shows the NIBP and HR trends. The SBP, HR show an increasing trend with exercise, however, DBP remained steady across the scenarios. The average SBP increased by 25 mmHg and the average HR rose by 10 BPM reflecting the expected cardiovascular response to physical exertion. The violin plot in Figure C.15a displays the distribution of PAT values, the PAT distribution shape at scenario 2 (cycle 30 s) shows larger PAT variability. However, there is a decreasing trend with the median PAT values as the exercise activity increased. At scenario 1 (rest) there is a median PAT around 210 ms, at scenario 2 (cycle 30 s) there is a median PAT around 175 ms and at scenario 3 (cycle 1 min) the median PAT is around 155 ms. These PAT distributions follow an inverse trend with the SBP and HR values.

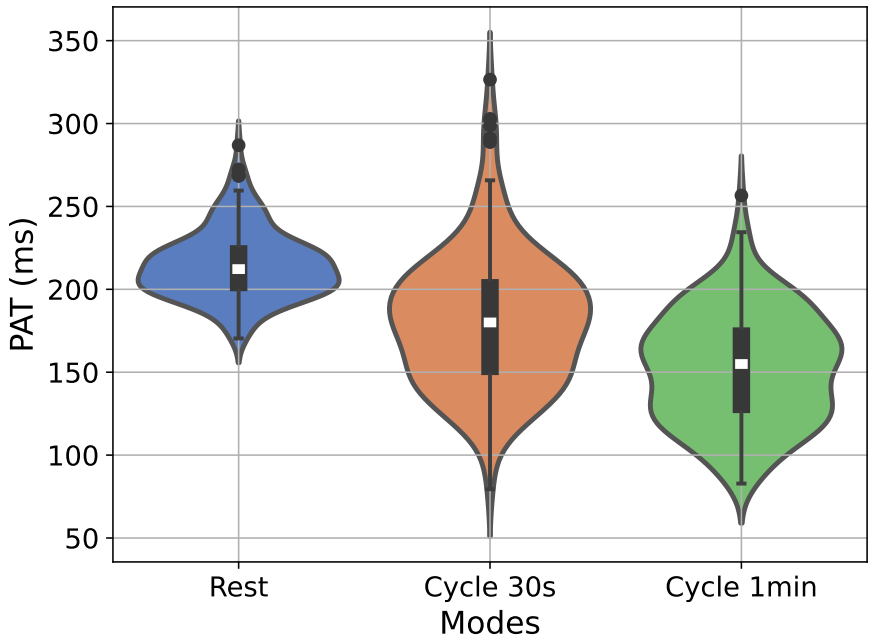

(a)

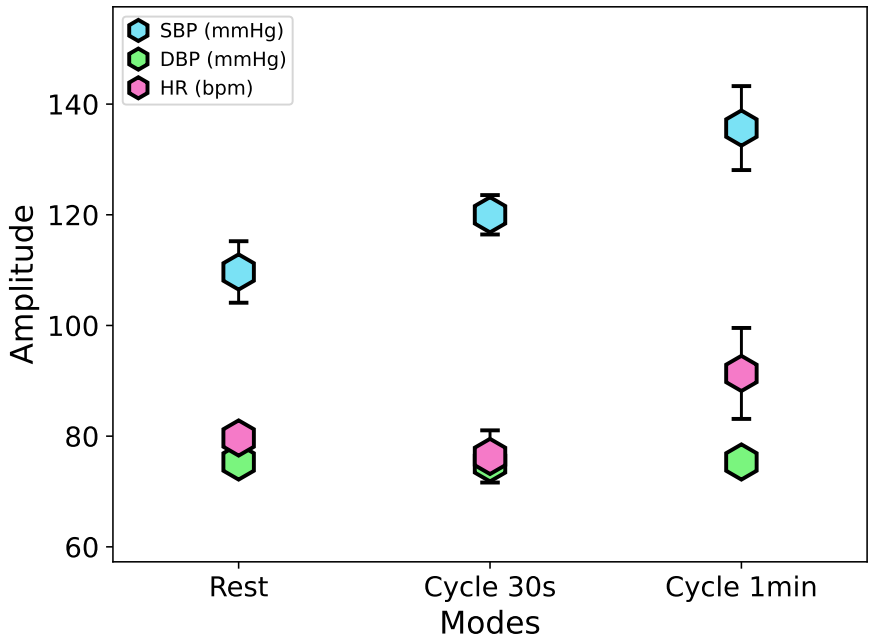

(b)

Figure C.15: *PAT values condensed in violin plots (a) vs NIBP (SBP and DBP) values and HR (b) of the different modalities (rest, cycle 30 s and cycle 1 min) of the experiment in* ***volunteer 14****. The center of the PAT data distribution follows a decreasing trend as the exercise, SBP and HR increase, however the DBP values remain steady.*

Figure C.16 presents the results for **volunteer 15**. The scatter plot in Figure C.16b shows the NIBP and HR trends. The SBP, HR show an increasing trend with exercise, however, DBP remained steady across the scenarios. The average SBP increased by 40 mmHg, the average DBP increased by 20 mmHg and the average HR rose by 40 BPM. These average values reflect the expected cardiovascular response to physical exertion. The violin plot in Figure C.16a displays the distribution of PAT values, the PAT distribution shape at scenario 1 (rest) shows larger PAT variability. However, there is an overall decreasing trend in the distribution PAT values as the exercise activity increased from rest cycle 30 s and from rest to cycle 1 min. At scenario 1 (rest) there is a median PAT around 160 ms, at scenario 2 (cycle 30 s) there is a median PAT around 75 ms and at scenario 3 (cycle 1 min) the median PAT is around 90 ms. These PAT distributions follow an inverse trend with the SBP and HR values.

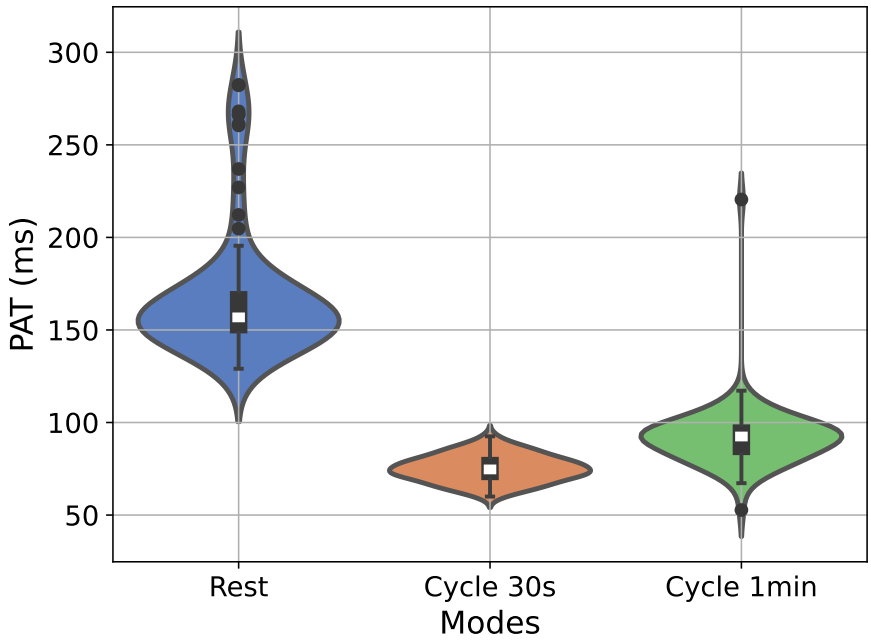

(a)

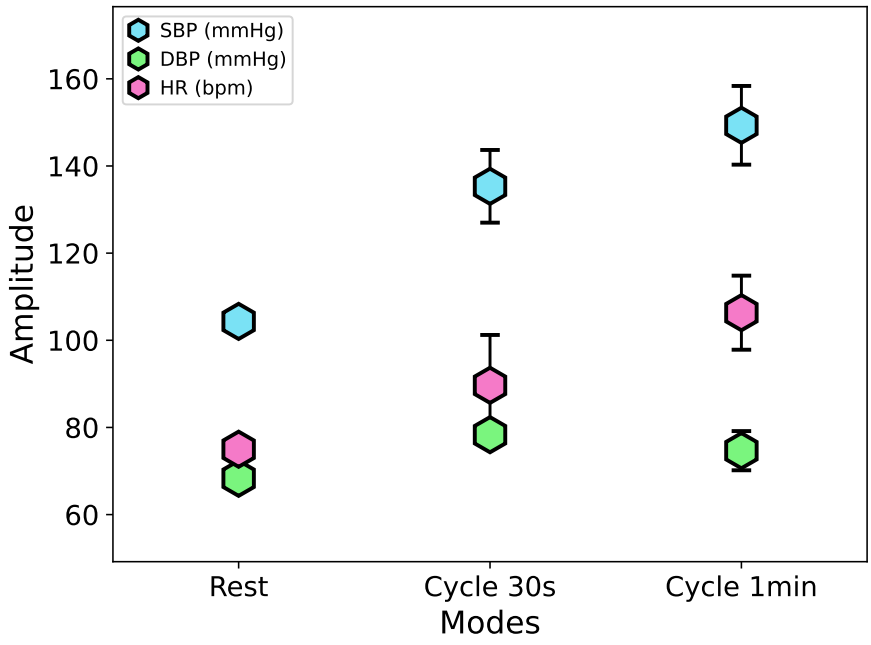

(b)

Figure C.16: *PAT values condensed in violin plots (a) vs NIBP (SBP and DBP) values and HR (b) of the different modalities (rest, cycle 30 s and cycle 1 min) of the experiment in* ***volunteer 15****. This figure shows an overall decreasing trend of PAT values as the exercise, SBP and HR increase, however at cycle 30 s the centre of the PAT values distribution is slightly smaller compared to the other modalities while the DBP values show the opposite behaviour.*

D. Appendix

D.1 Gaussian Process Regression model results

Volunteer 1 GPR model

Figure D.1 illustrates the results of the GPR model prediction with confidence intervals using the PAT values of **volunteer 1**. The SBP predictions (blue dotted line) tend to follow the trend of the actual SBP values (red dots), although deviations are observed for lower SBP values ($\leq$ 97 mmHg) and within the 113-116 mmHg range. About 29% of SBP values lie outside the CI. DBP predictions (green dotted line) align better with the actual values (orange dots), with only 10% outside the CI. The CI for SBP (light blue shaded region) shows more variability with widths up to 10 mmHg, while the DBP CI (light green shaded region) remains narrower and more consistent ($\approx$ 10 mmHg).

From the correlation analysis (Figures D.2a and D.2b), SBP predictions show moderate agreement with actual values (MAE = 6.66 mmHg, RMSE = 8.06 mmHg, R^2 = 0.5052, MBE = -1.00 mmHg), indicating a slight underestimation trend. DBP predictions show weaker correlation (MAE = 2.68 mmHg, RMSE = 3.41 mmHg, R^2 = 0.1596, MBE = -0.16 mmHg) but with smaller errors. From the Bland-Altman analysis (Figures D.3a and D.3b), SBP shows a negative mean bias with wider LoA, whereas DBP shows minimal bias with narrower spread. Overall, the model for volunteer 1 provides moderate performance in SBP and limited explanatory power for DBP.

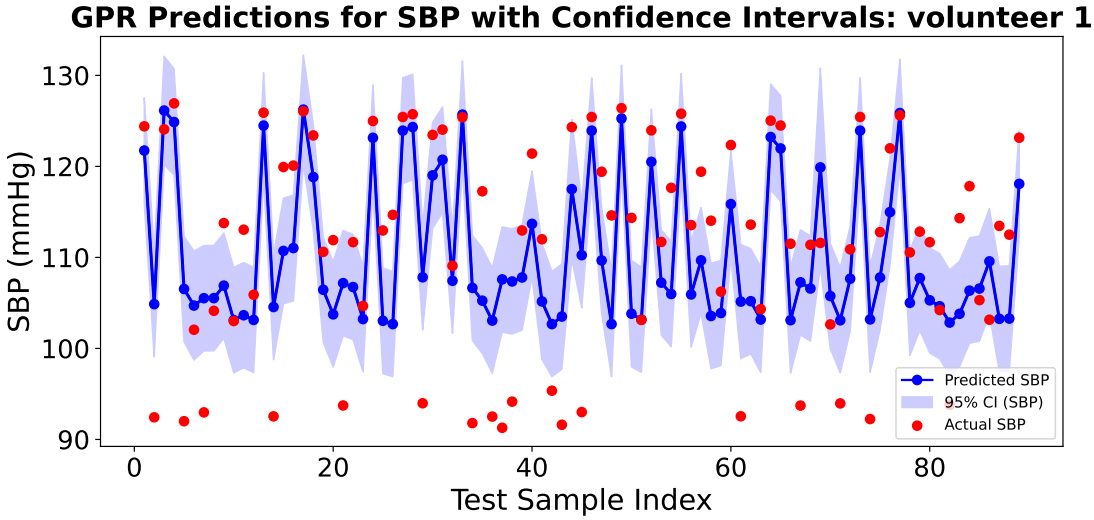

(a)

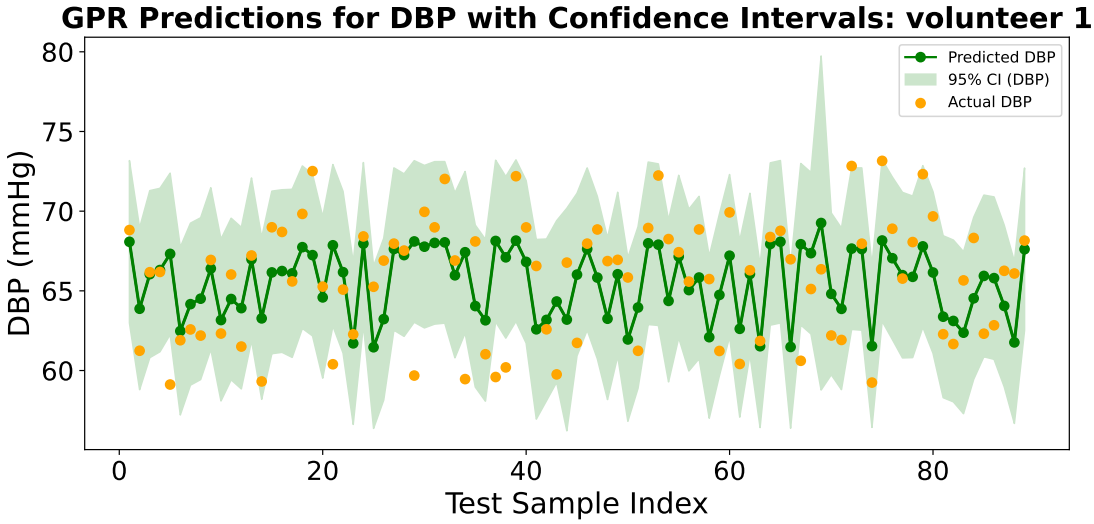

(b)

Figure D.1: *GPR model BP prediction plots for the* ***volunteer 1*** *test set. (a) SBP predictions with 95% CI (light blue shaded region). (b) DBP predictions with 95% CI (light green shaded region). 29% of SBP and 10% of DBP values lie outside their respective CI.*

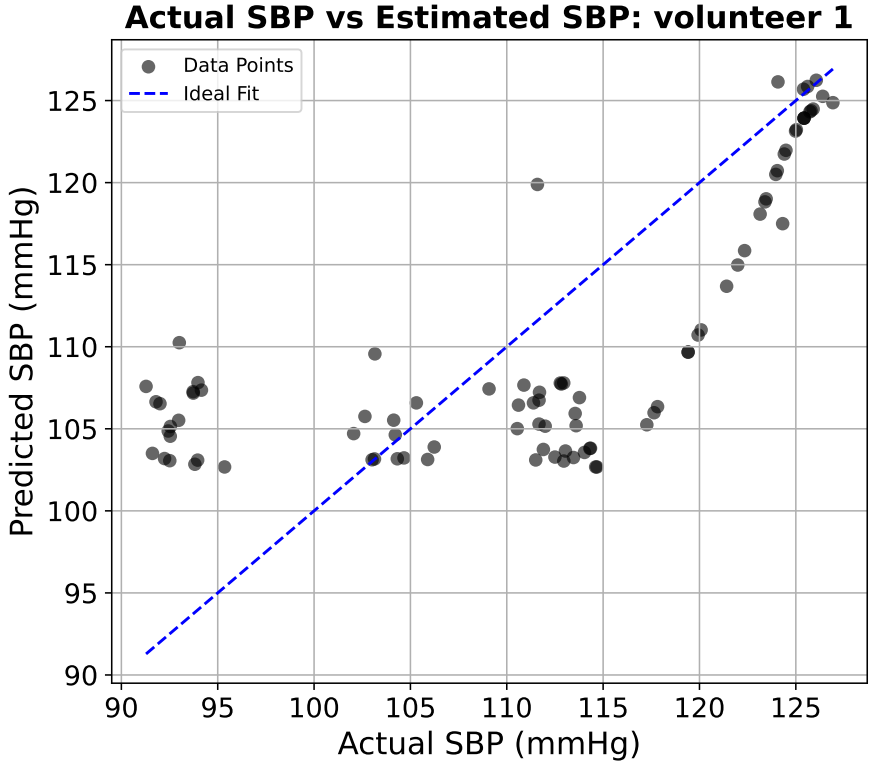

(a)

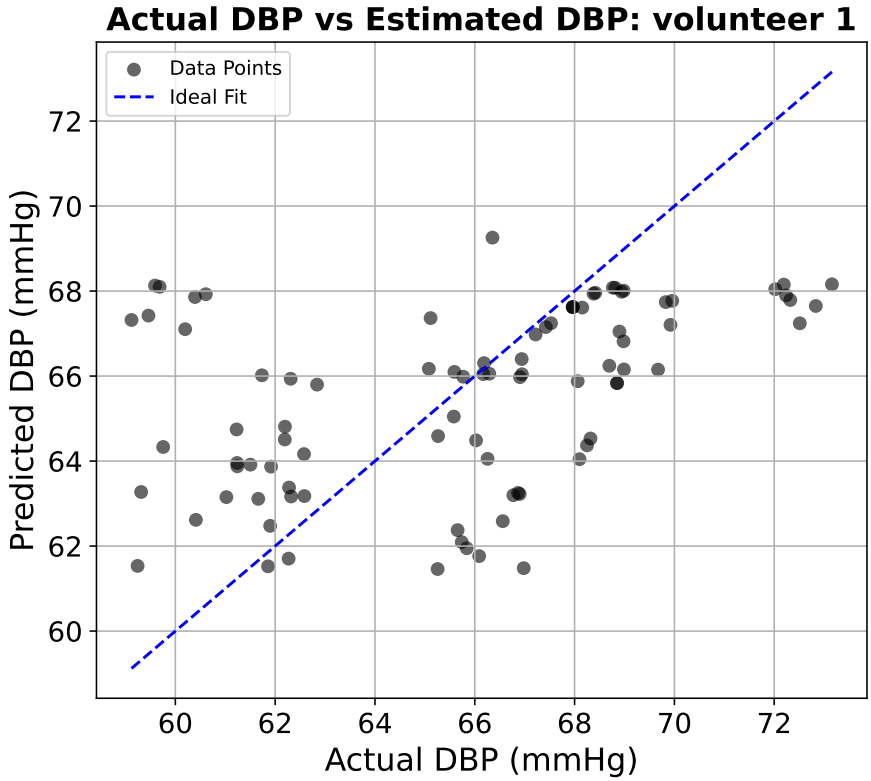

(b)

Figure D.2: *Correlation analysis for the **volunteer 1** test set. (a) Predicted vs actual SBP values. (b) Predicted vs actual DBP values. SBP shows moderate correlation, while DBP shows weaker agreement.*

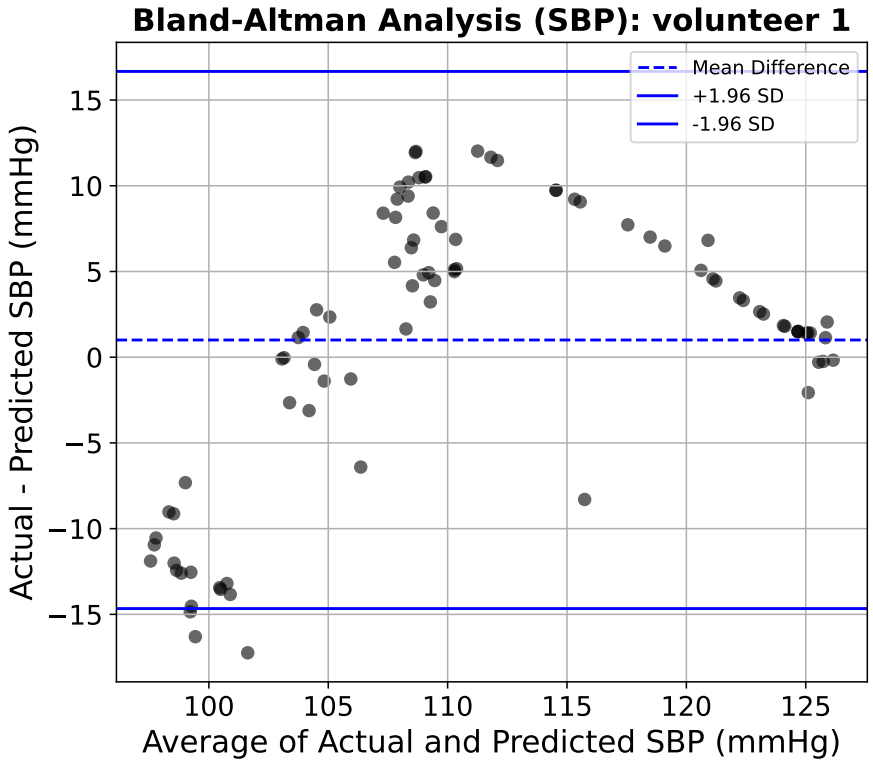

(a)

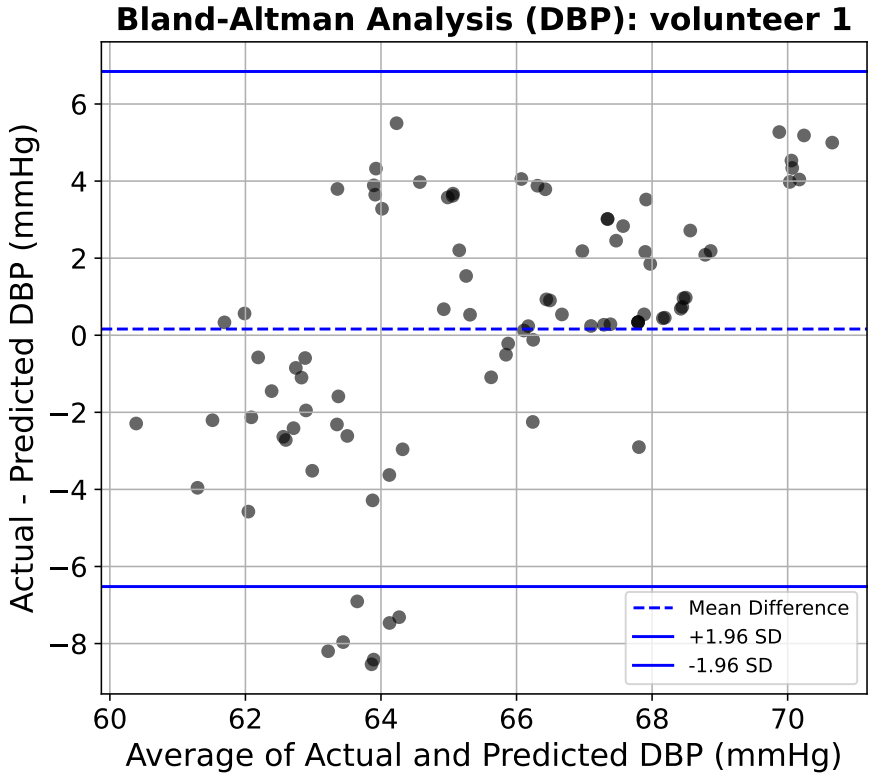

(b)

Figure D.3: *Bland-Altman analysis for the* ***volunteer 1*** *test set. (a) SBP predictions show negative bias and wider LoA. (b) DBP predictions show smaller bias with narrower LoA.*

Volunteer 3 GPR model

Figure D.4 shows the GPR model prediction with confidence intervals for **volunteer 3**. SBP predictions (blue dotted line) follow the actual SBP trend (red dots) but deviate for higher SBP values (115-125 mmHg). About 26% of SBP values are outside the CI. DBP predictions (green dotted line) show weaker alignment, with 40% outside the CI. The CI for SBP (light blue shaded region) varies in width up to 10 mmHg, while DBP CI (light green shaded region) is more consistent at ≈10 mmHg.

From the correlation analysis (Figures D.5a and D.5b), SBP predictions show moderate alignment (MAE = 5.45 mmHg, RMSE = 6.84 mmHg, R^2 = 0.4708, MBE = 1.25 mmHg), with a slight overestimation trend. DBP predictions show poorer correlation (MAE = 3.98 mmHg, RMSE = 5.38 mmHg, R^2 = -0.0623, MBE = 0.21 mmHg), with more variability. Bland-Altman plots (Figures D.6a and D.6b) indicate SBP overestimation with wider LoA, while DBP predictions show weaker bias but reduced explanatory power. Overall, the model demonstrates moderate SBP tracking but poor DBP reliability.

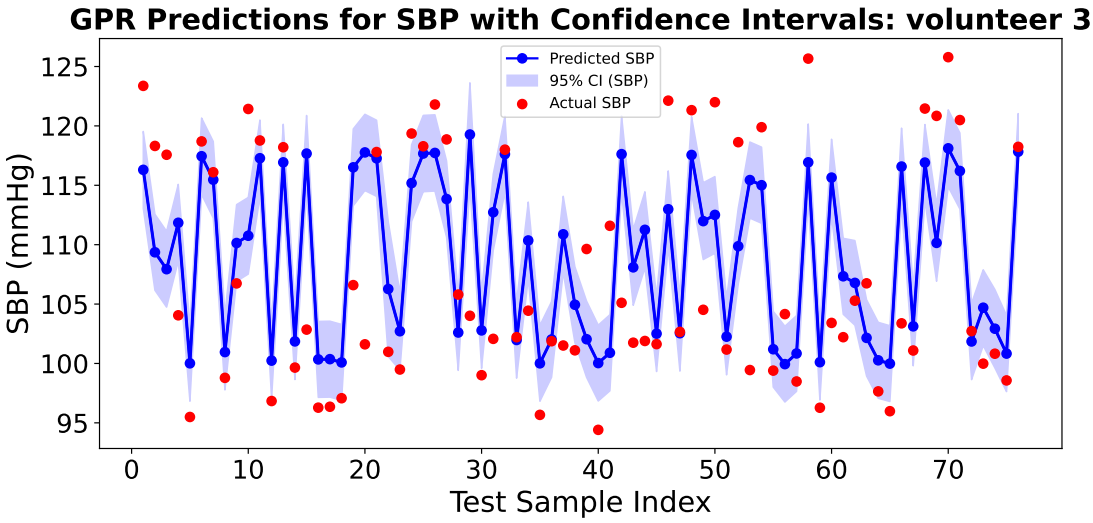

(a)

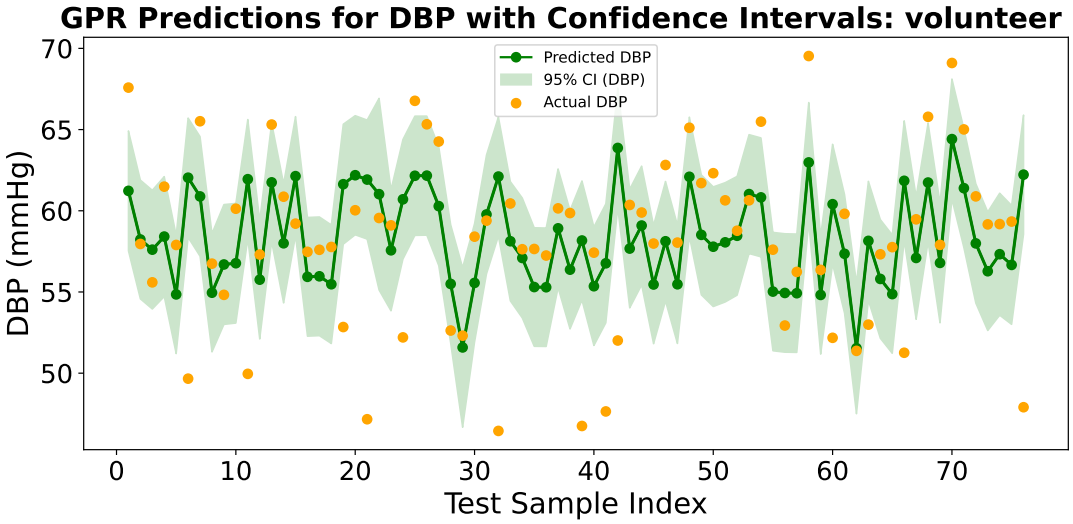

(b)

Figure D.4: *GPR model BP prediction plots for* ***volunteer 3****. (a) SBP predictions with 95% CI. (b) DBP predictions with 95% CI. 26% of SBP and 40% of DBP values are outside the CI.*

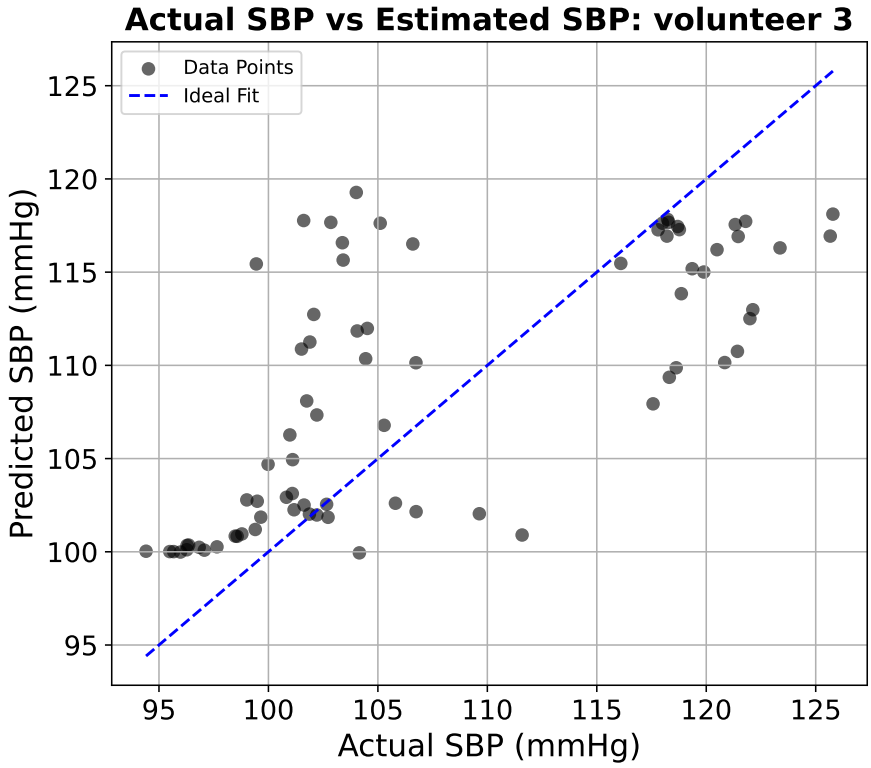

(a)

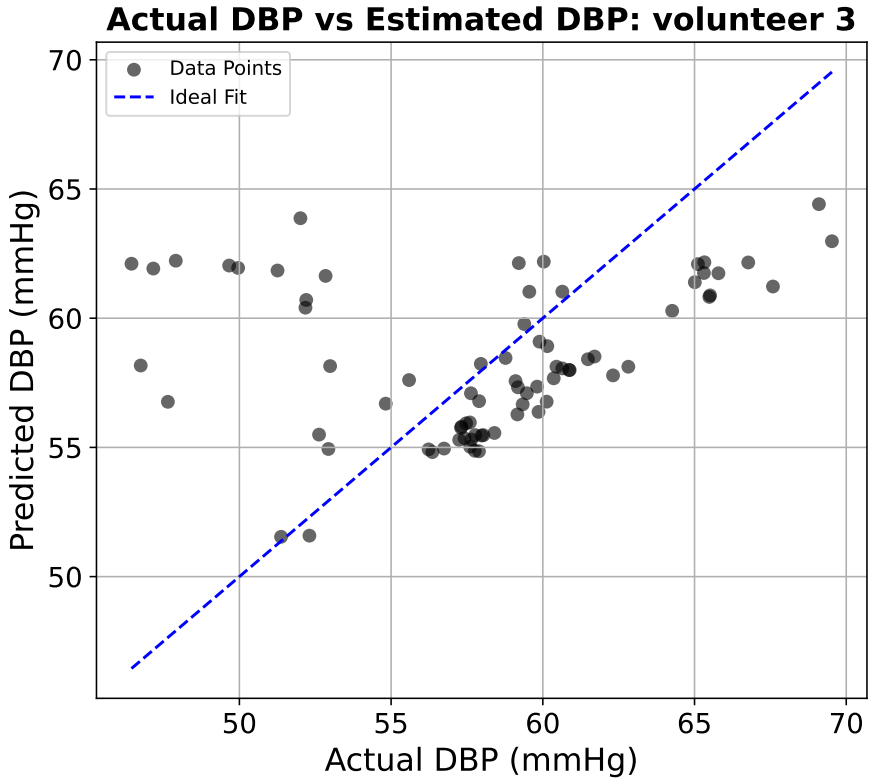

(b)

Figure D.5: *Correlation analysis for **volunteer 3**. (a) SBP predictions show moderate correlation. (b) DBP predictions show weak correlation.*

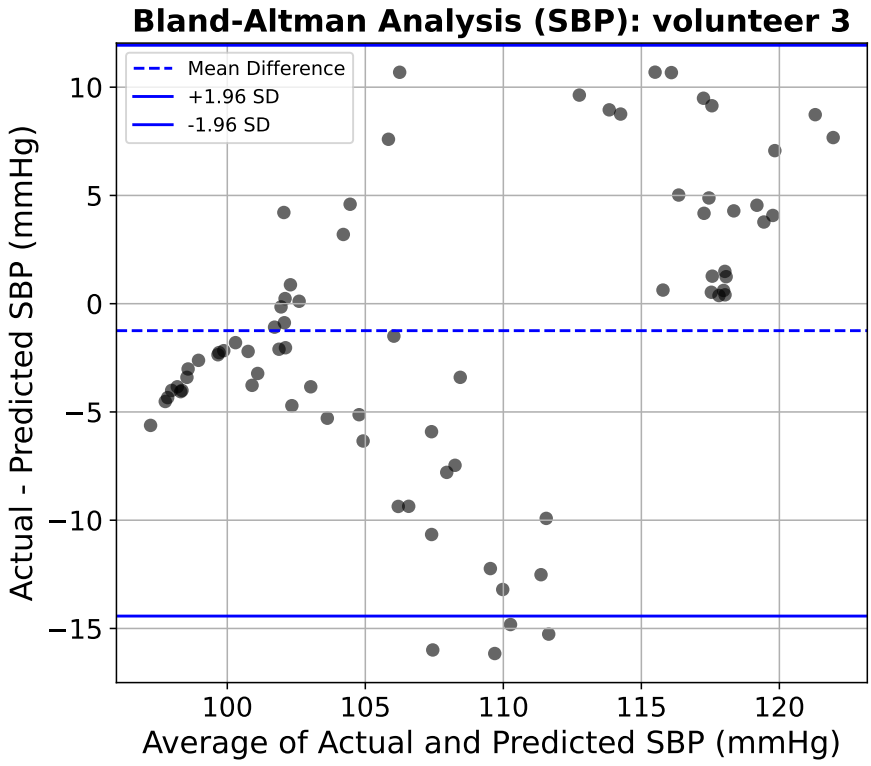

(a)

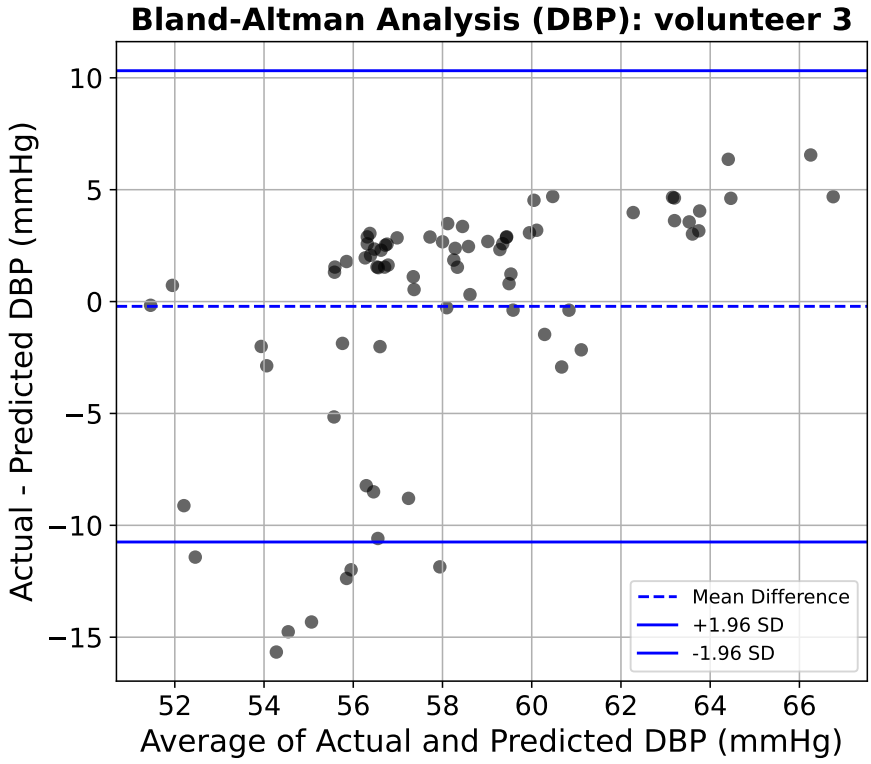

(b)

Figure D.6: *Bland-Altman analysis for* ***volunteer 3****. (a) SBP predictions show positive bias and wider LoA. (b) DBP predictions show minimal bias but high variability.*

Volunteer 4 GPR model

Figure D.7 illustrates the GPR predictions with confidence intervals for **volunteer 4**. SBP predictions (blue dotted line) closely follow the actual SBP values (red dots), with only 5% of points outside the CI. DBP predictions (green dotted line) also track the actual values (orange dots), with 3% outside the CI. The SBP CI (light blue region) varies across samples (max width $\approx$ 10 mmHg), whereas the DBP CI (light green region) is consistently narrower ($\approx$ 6 mmHg).

From the correlation analysis (Figures D.8a-D.8b), SBP shows strong agreement with low errors (MAE = 2.56 mmHg, RMSE = 3.26 mmHg, $R^2 = 0.6433$) and a slight positive bias (MBE = 0.35 mmHg). DBP shows solid alignment with modest explanatory power (MAE = 1.25 mmHg, RMSE = 1.85 mmHg, $R^2 = 0.4340$) and a small negative bias (MBE = -0.28 mmHg). Bland-Altman plots (Figures D.9a-D.9b) confirm a near-zero mean difference with relatively tight limits of agreement, slightly wider for SBP than DBP. *Overall: robust SBP performance and good DBP accuracy with small biases and narrow LoA.*

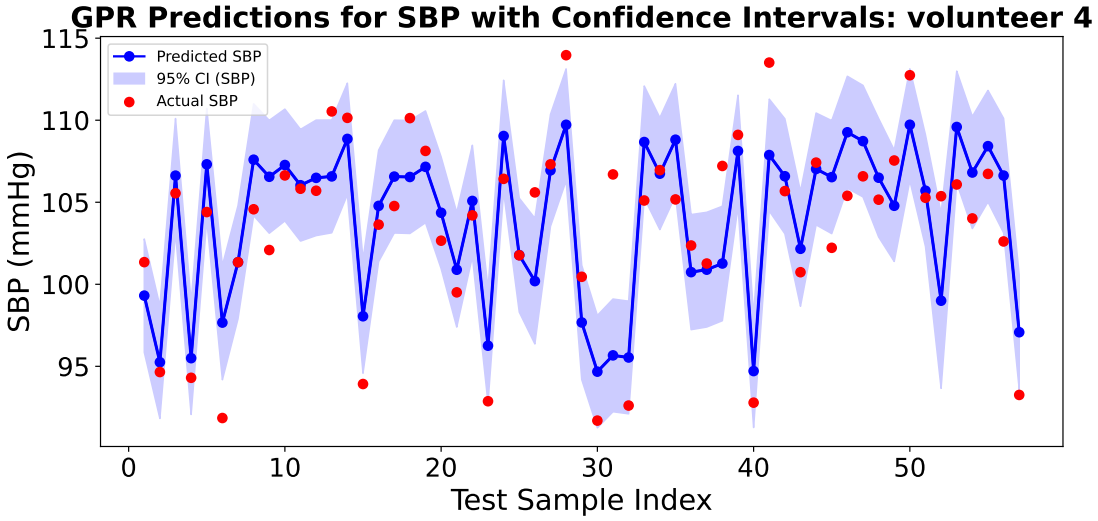

(a)

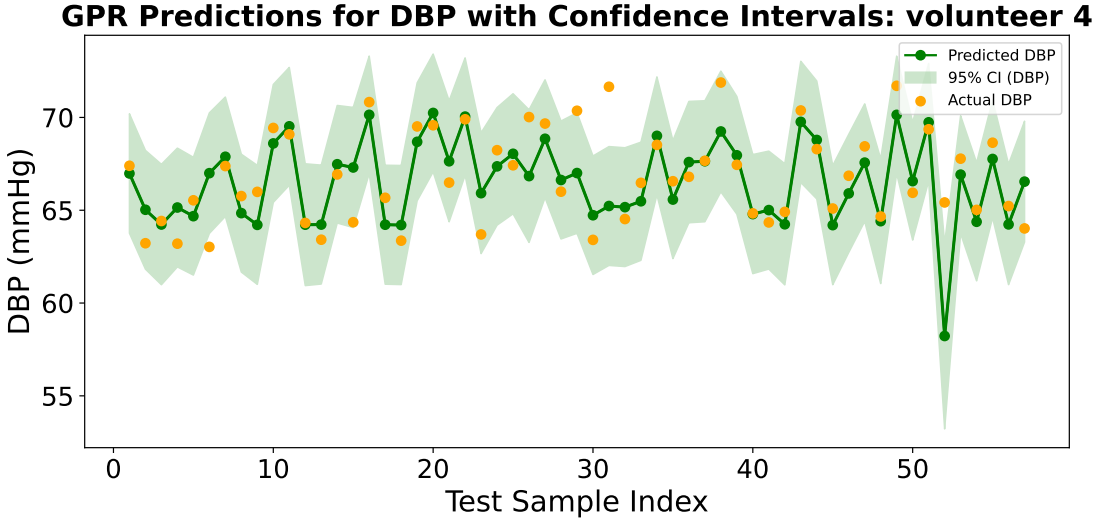

(b)

Figure D.7: *GPR model BP prediction plots for the* ***volunteer 4*** *test set. (a) SBP predictions with 95% CI (light blue). (b) DBP predictions with 95% CI (light green). 5% of SBP and 3% of DBP values lie outside their respective CI.*

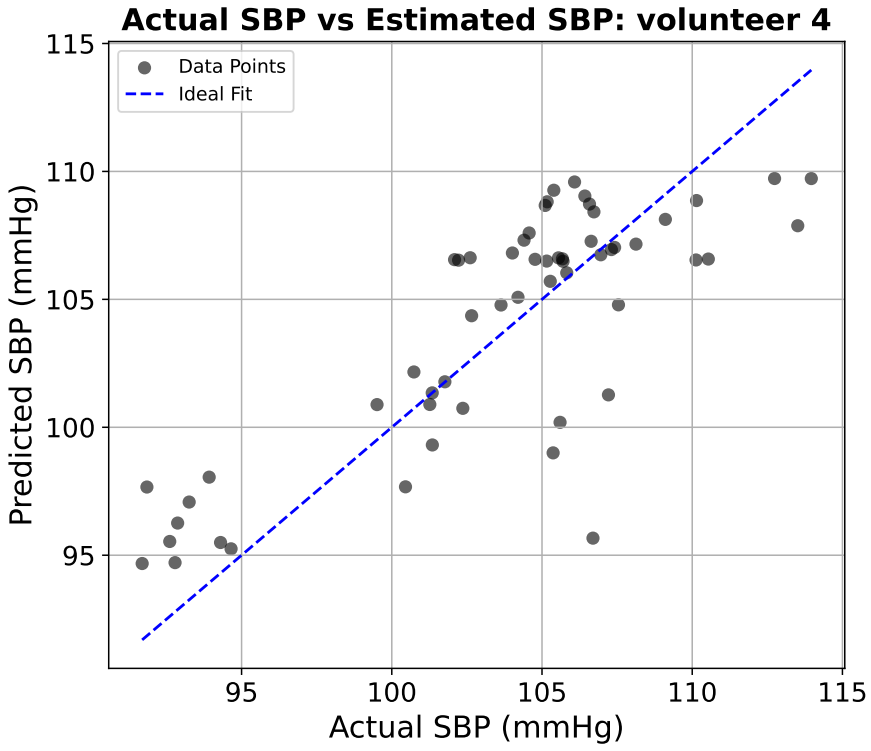

(a)

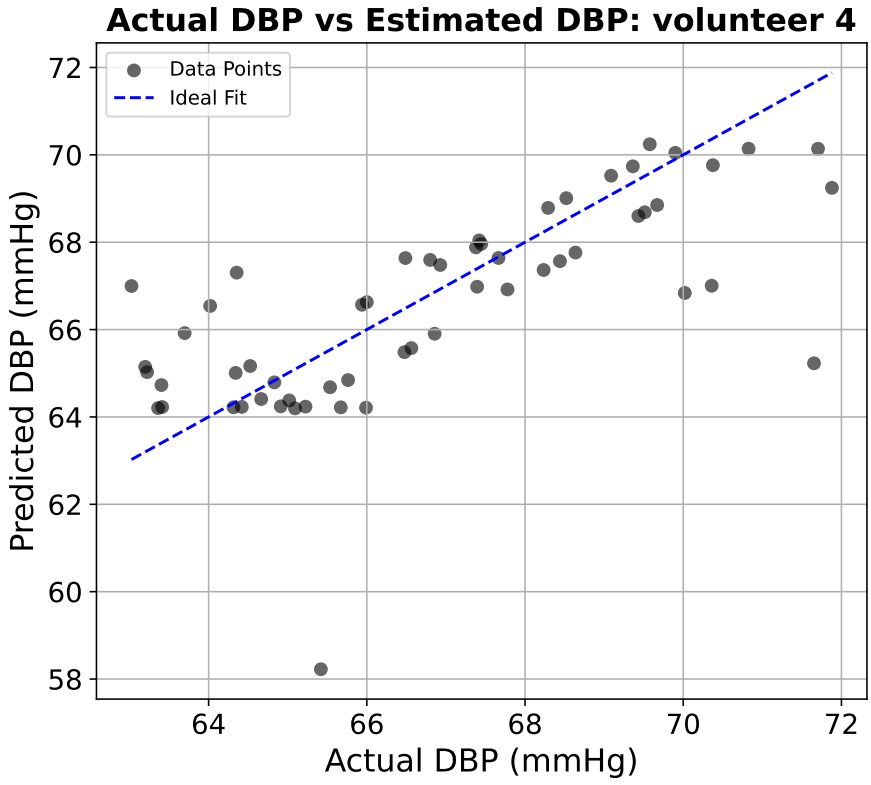

(b)

Figure D.8: *Correlation analysis for the **volunteer 4** test set. (a) SBP: strong agreement with slight positive bias (MAE = 2.56, RMSE = 3.26, R^2 = 0.6433, MBE = 0.35). (b) DBP: good agreement with slight negative bias (MAE = 1.25, RMSE = 1.85, R^2 = 0.4340, MBE = -0.28).*

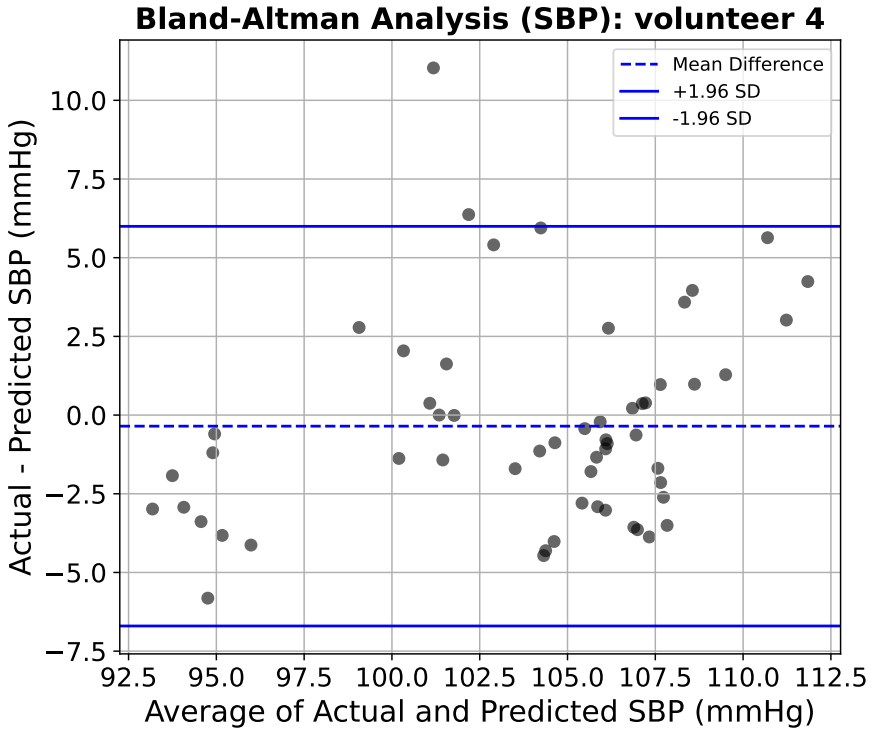

(a)

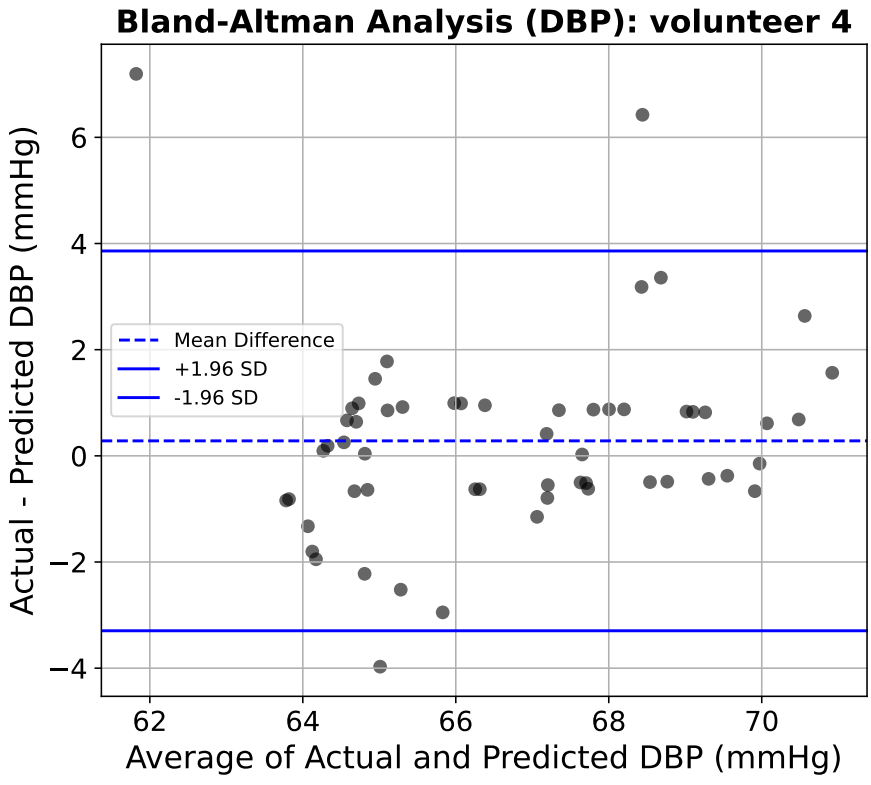

(b)

Figure D.9: *Bland-Altman analysis for the* ***volunteer 4*** *test set. (a) SBP: small positive mean difference with relatively tight LoA. (b) DBP: small negative mean difference with tighter LoA than SBP.*

Volunteer 9 GPR model

Figure D.10 illustrates the GPR predictions with confidence intervals for **volunteer 9**. SBP predictions (blue dotted line) follow the actual SBP trend (red dots) very closely, with only 5% outside the CI. DBP predictions (green dotted line) also align strongly with the actual DBP values (orange dots), with 4.5% outside the CI. Both SBP and DBP CIs are relatively narrow, with maximum widths $\leq$ 5 mmHg.

From the correlation analysis (Figures D.11a-D.11b), SBP shows excellent agreement with low errors (MAE = 1.27 mmHg, RMSE = 2.53 mmHg, R^2 = 0.9687, MBE = -0.09 mmHg), indicating negligible bias. DBP predictions are also very accurate (MAE = 0.42 mmHg, RMSE = 0.66 mmHg, R^2 = 0.9888, MBE = 0.00 mmHg). Bland-Altman plots (Figures D.12a-D.12b) confirm minimal systematic bias for both SBP and DBP, with narrow limits of agreement. *Overall: volunteer 9 demonstrates robust and highly reliable model performance for both SBP and DBP.*

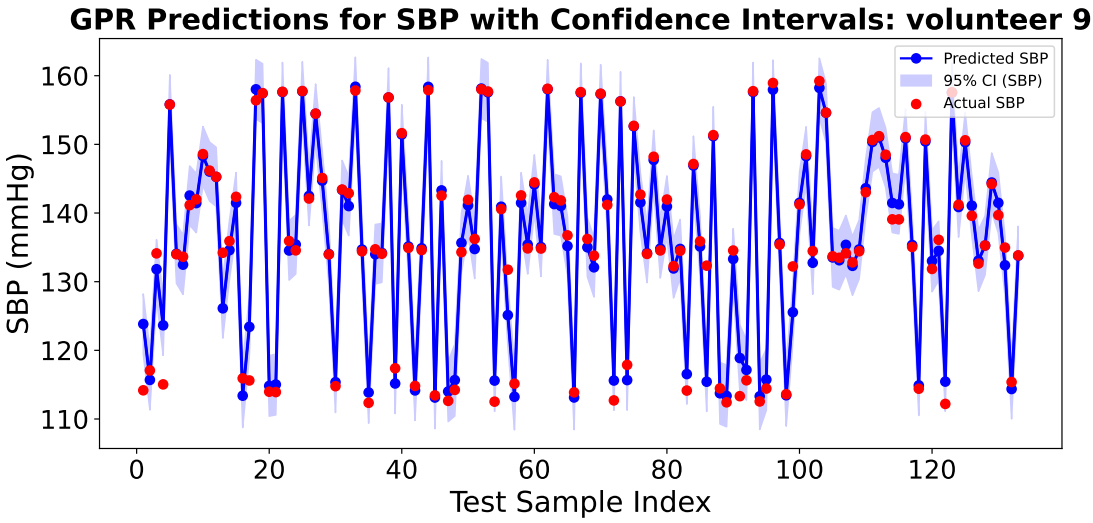

(a)

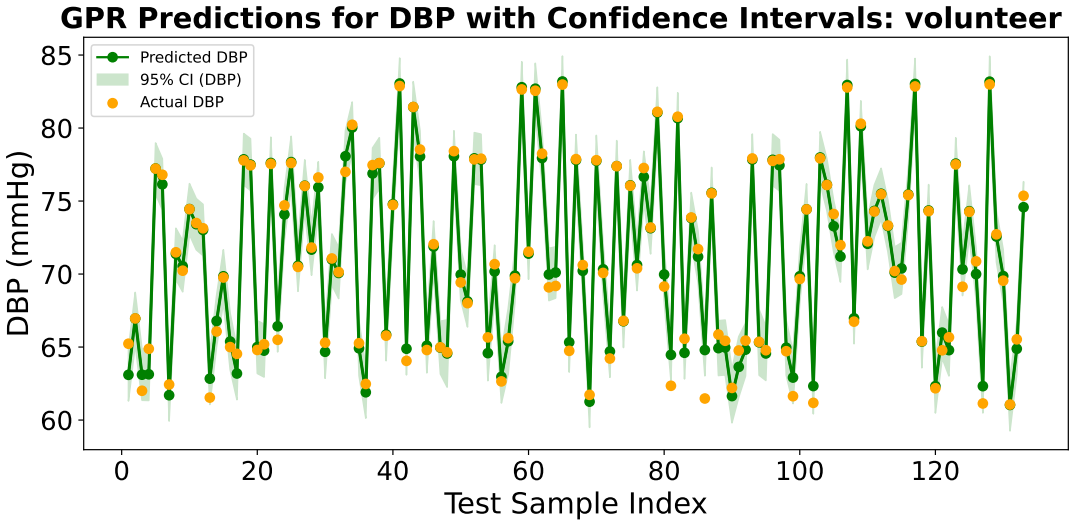

(b)

Figure D.10: *GPR model BP prediction plots for the* ***volunteer 9*** *test set. (a) SBP predictions with 95% CI (light blue). (b) DBP predictions with 95% CI (light green). Only 5% of SBP and 4.5% of DBP values lie outside their respective CI.*

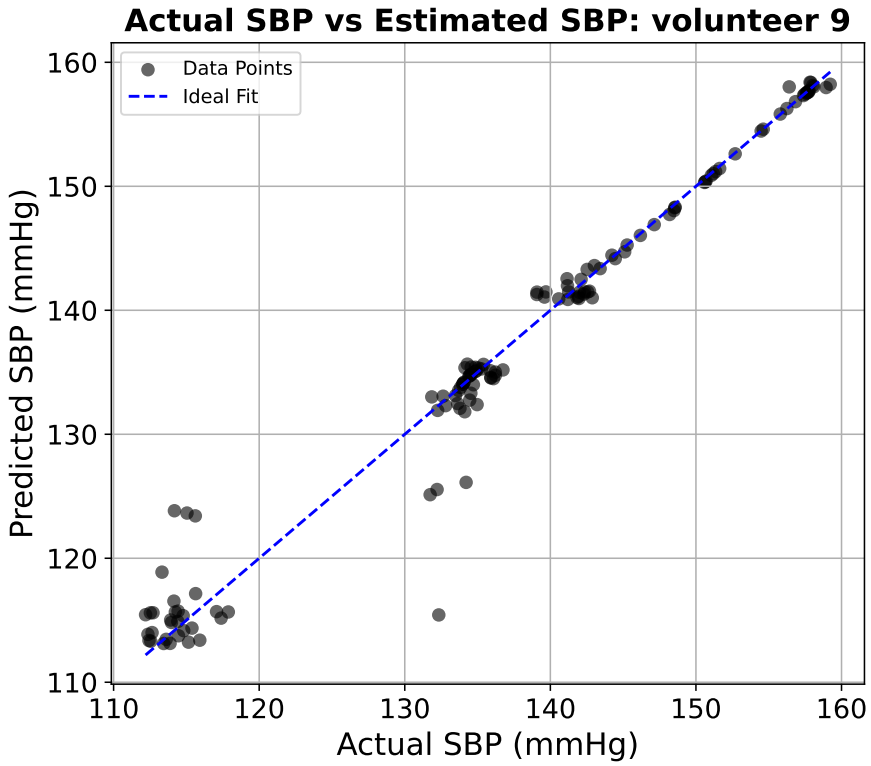

(a)

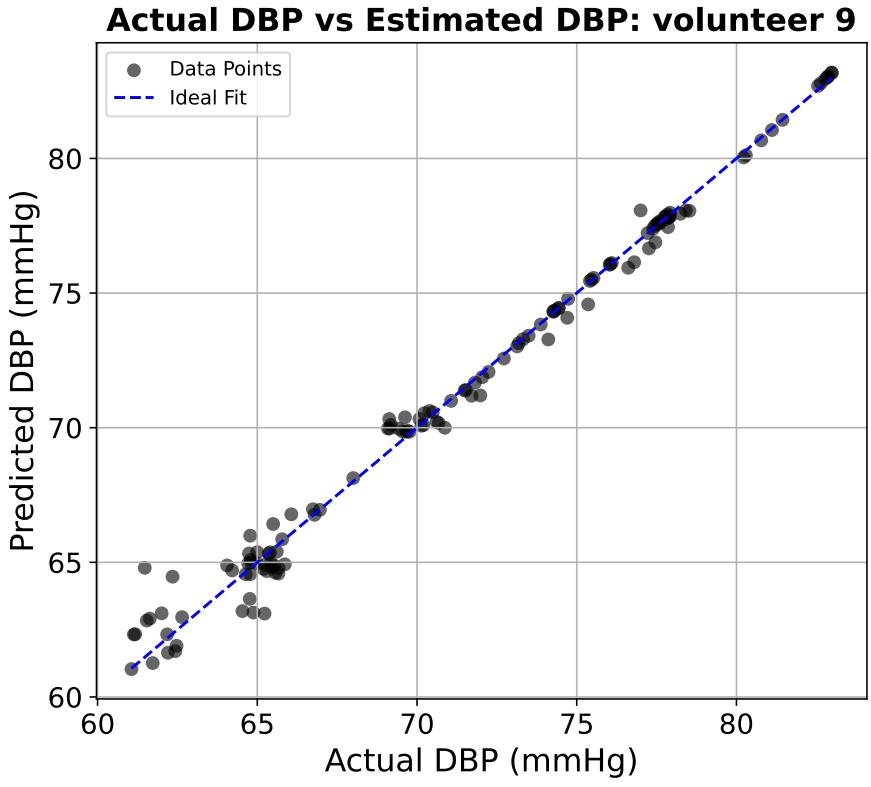

(b)

Figure D.11: *Correlation analysis for the **volunteer 9** test set. (a) SBP: strong correlation with negligible bias (MAE = 1.27, RMSE = 2.53, R^2 = 0.9687, MBE = -0.09). (b) DBP: very strong correlation with minimal error (MAE = 0.42, RMSE = 0.66, R^2 = 0.9888, MBE = 0.00).*

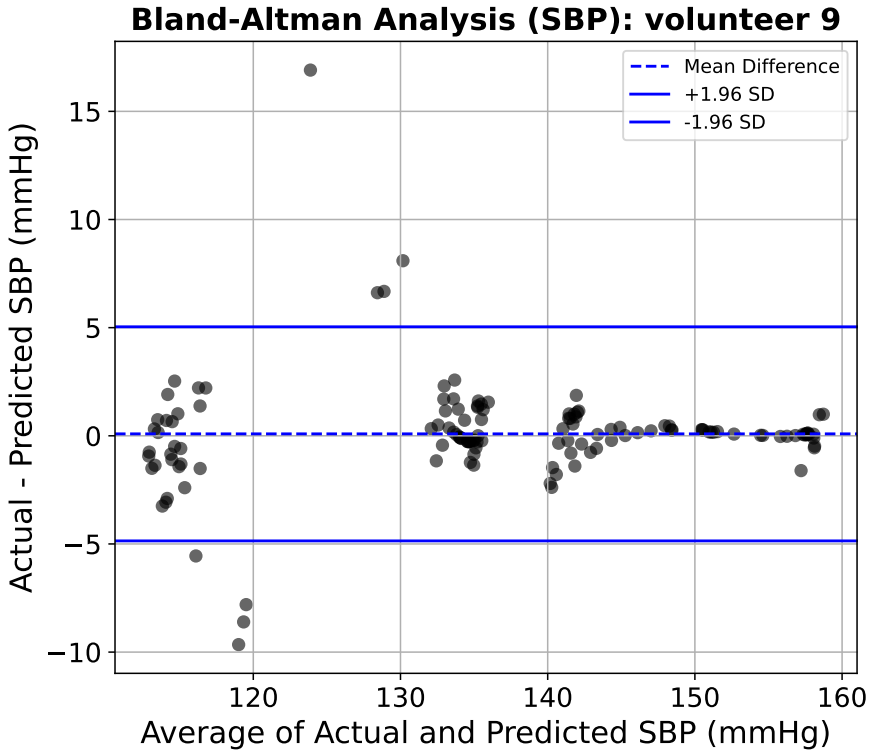

(a)

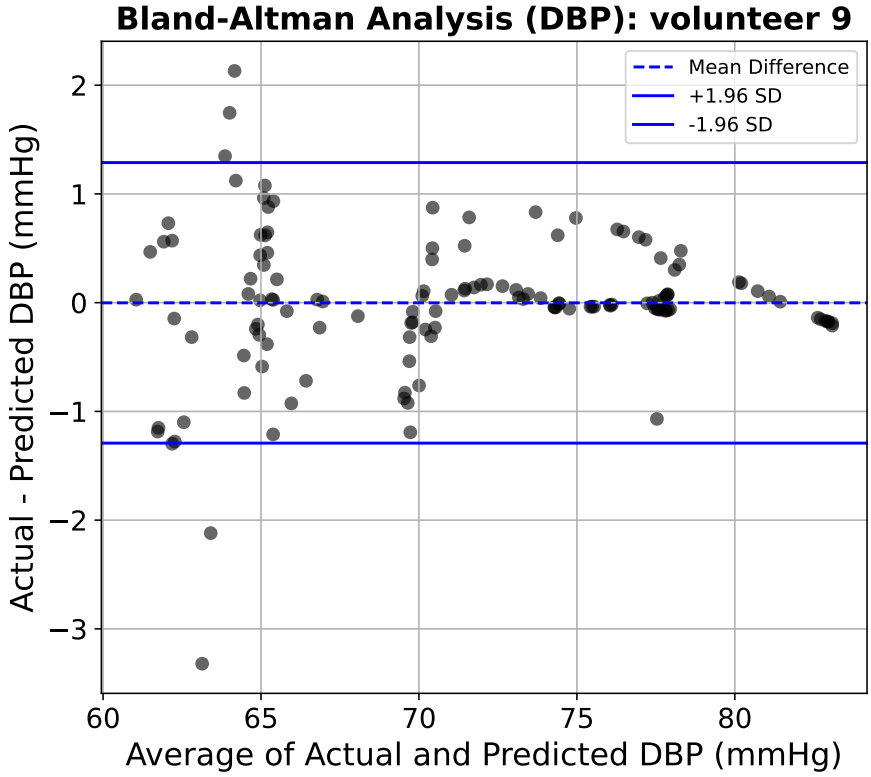

(b)

Figure D.12: *Bland-Altman analysis for the* ***volunteer 9*** *test set. (a) SBP predictions: near-zero mean difference with narrow LoA. (b) DBP predictions: negligible bias and very tight LoA.*

Volunteer 10 GPR model

Figure D.13 shows the GPR predictions with confidence intervals for **volunteer 10**. SBP predictions (blue dotted line) generally follow the actual SBP values (red dots), with 18% lying outside the CI. DBP predictions (green dotted line) also track the actual values (orange dots), with 9% outside the CI. The SBP CI (light blue region) varies more across the samples (width $\leq$ 10 mmHg), while the DBP CI (light green region) is narrower and more consistent (width $\leq$ 10 mmHg).

From the correlation analysis (Figures D.14a-D.14b), SBP predictions show acceptable alignment (MAE = 5.22 mmHg, RMSE = 7.55 mmHg, R^2 = 0.5654, MBE = -0.41 mmHg), with a slight underestimation trend. DBP predictions demonstrate moderate performance (MAE = 2.02 mmHg, RMSE = 3.23 mmHg, R^2 = 0.5398, MBE = -0.13 mmHg). Bland-Altman plots (Figures D.15a-D.15b) confirm near-zero mean differences, with wider LoA for SBP compared to narrower LoA for DBP. *Overall: the model provides moderate and balanced performance for both SBP and DBP in volunteer 10.*

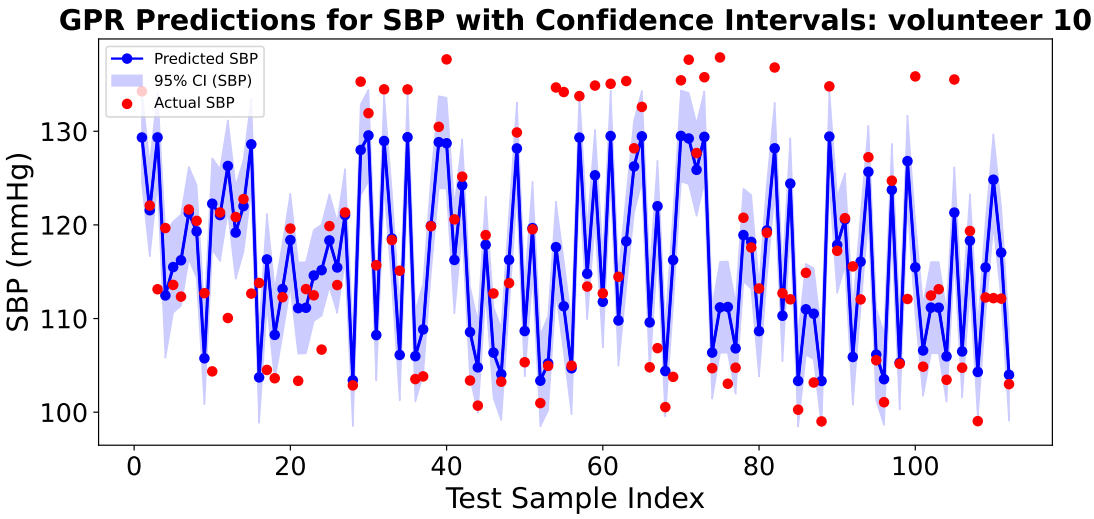

(a)

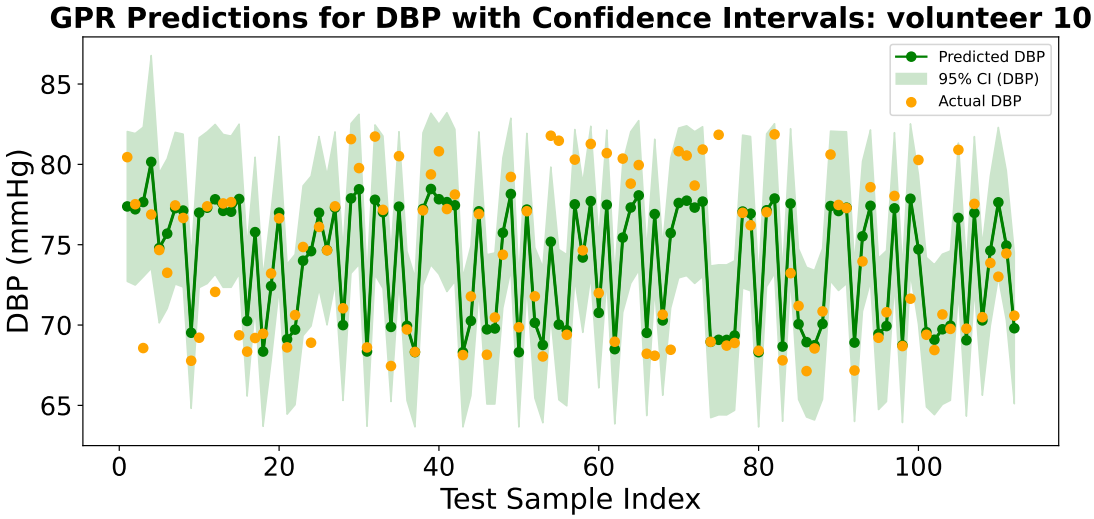

(b)

Figure D.13: *GPR model BP prediction plots for the* ***volunteer 10*** *test set. (a) SBP predictions with 95% CI (light blue). (b) DBP predictions with 95% CI (light green). 18% of SBP and 9% of DBP values are outside their respective CI.*

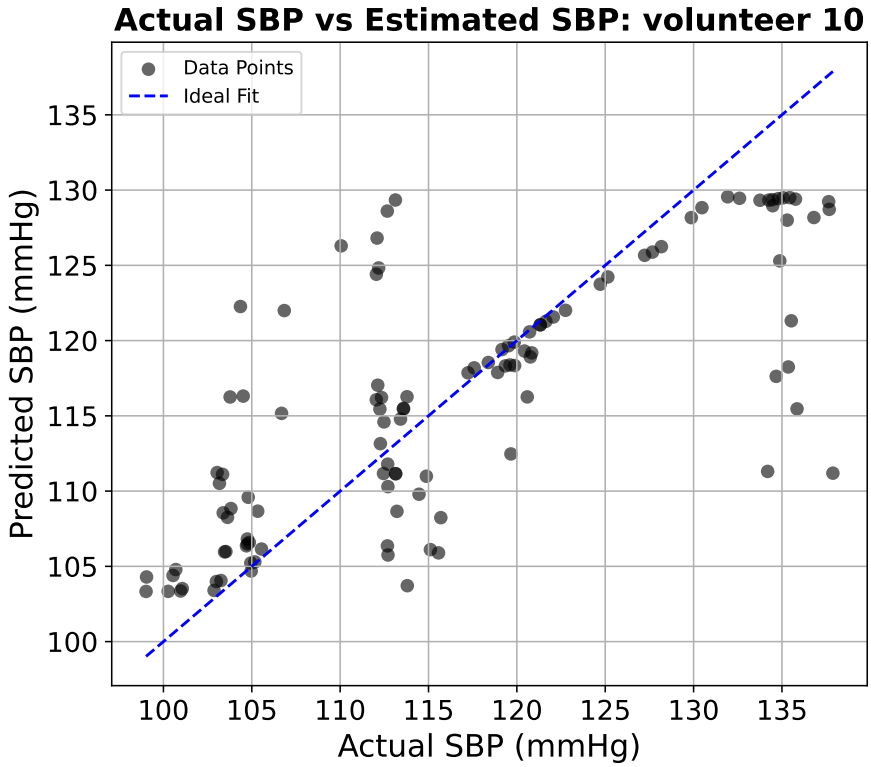

(a)

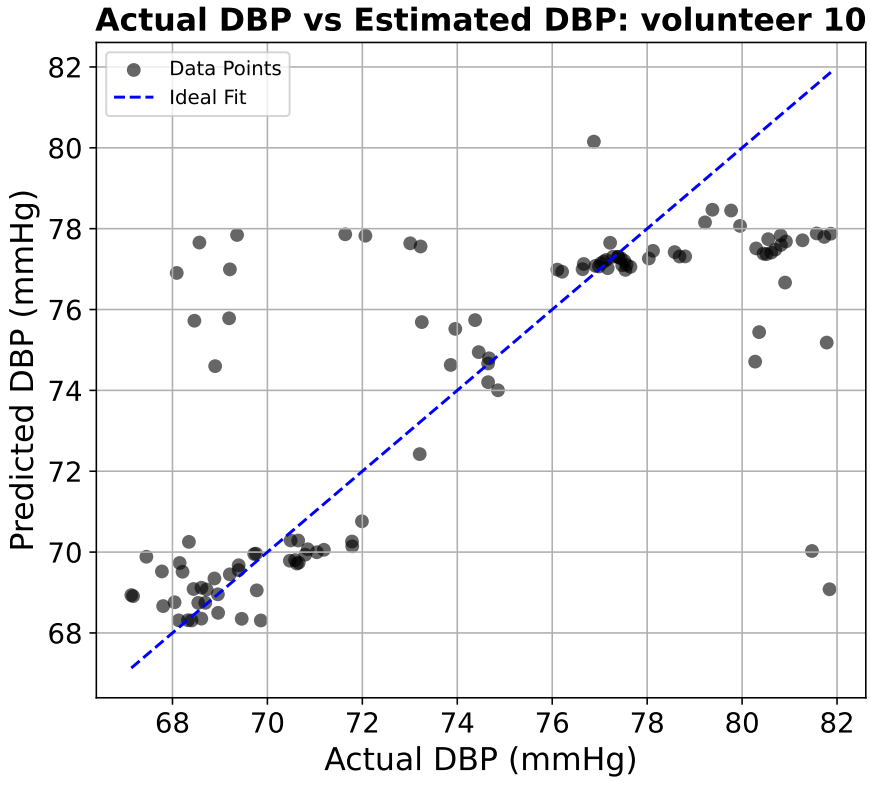

(b)

Figure D.14: *Correlation analysis for the **volunteer 10** test set. (a) SBP: acceptable correlation with slight underestimation (MAE = 5.22, RMSE = 7.55, R^2 = 0.5654, MBE = -0.41). (b) DBP: moderate agreement with smaller errors (MAE = 2.02, RMSE = 3.23, R^2 = 0.5398, MBE = -0.13).*

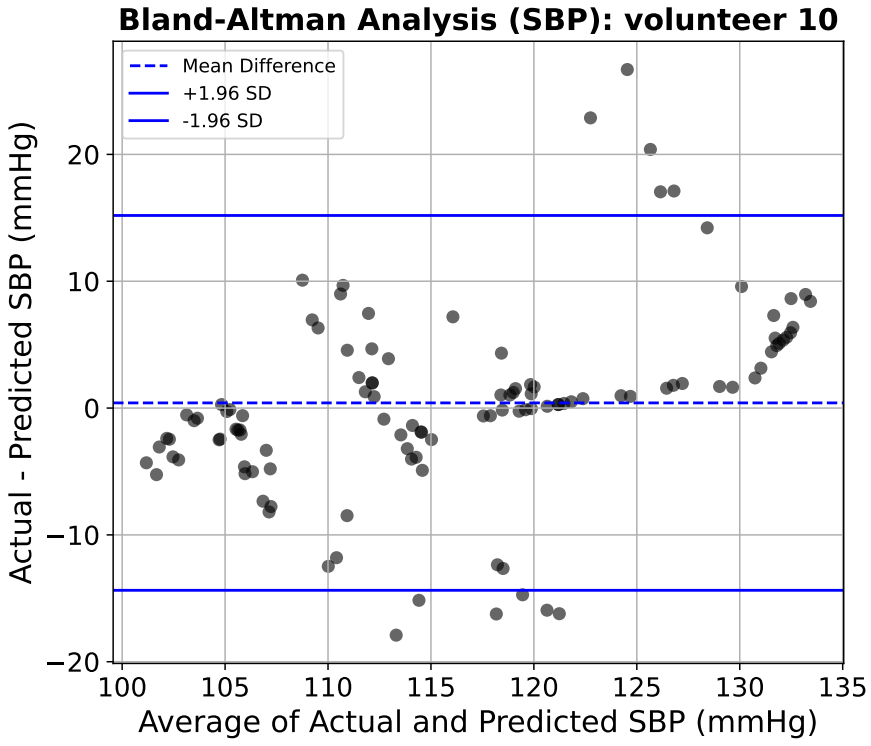

(a)

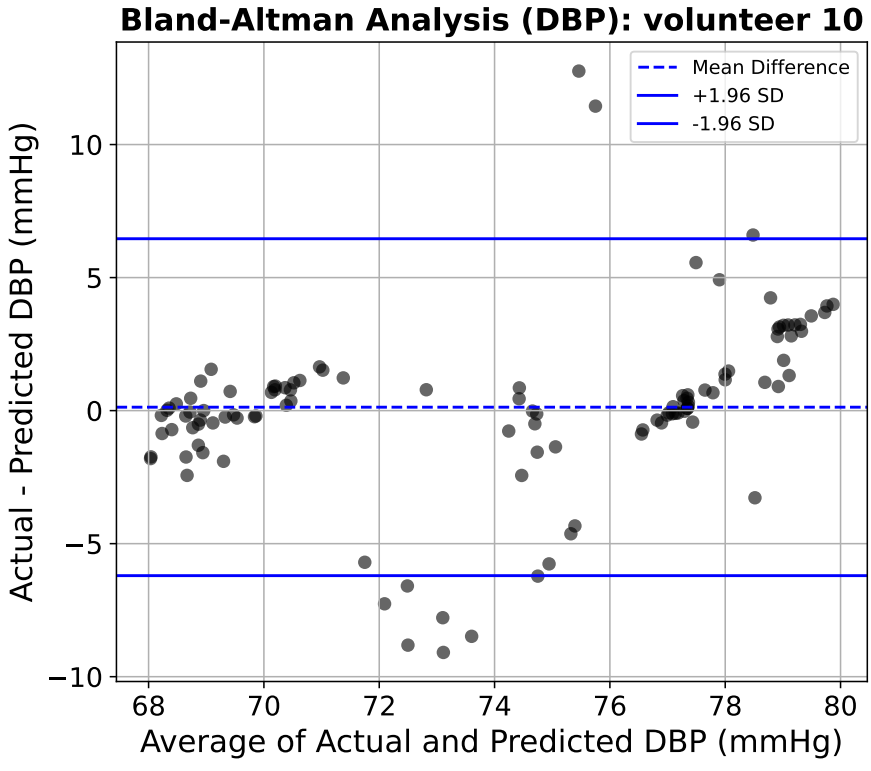

(b)

Figure D.15: *Bland-Altman analysis for the* ***volunteer 10*** *test set. (a) SBP: near-zero bias but wider LoA, indicating moderate variability. (b) DBP: minimal bias with narrower LoA, showing relatively stable predictions.*

Volunteer 12 GPR model

Figure D.16 shows the GPR predictions with confidence intervals for **volunteer 12**. SBP predictions (blue dotted line) attempt to follow the actual SBP trend (red dots), but performance decreases where SBP varies strongly. A high proportion of values (35%) lie outside the CI. DBP predictions (green dotted line) follow the trend more closely, with 10% of values outside the CI. The SBP CI (light blue region) is wider and more variable ($\leq$ 10 mmHg), while the DBP CI (light green region) is narrower and more consistent ($\leq$ 10 mmHg).

From the correlation analysis (Figures D.17a-D.17b), SBP predictions show weak agreement (MAE = 11.67 mmHg, RMSE = 16.56 mmHg, $R^2 = -1.2145$, MBE = -2.18 mmHg), reflecting systematic underestimation with large errors. DBP predictions also show poor performance (MAE = 3.53 mmHg, RMSE = 4.74 mmHg, $R^2 = -0.7032$, MBE = -0.98 mmHg). Bland-Altman plots (Figures D.18a-D.18b) confirm a strong negative bias for SBP and moderate negative bias for DBP, both with wide limits of agreement. *Overall: volunteer 12 demonstrates poor model performance, particularly for SBP, with systematic underestimation and high variability.*

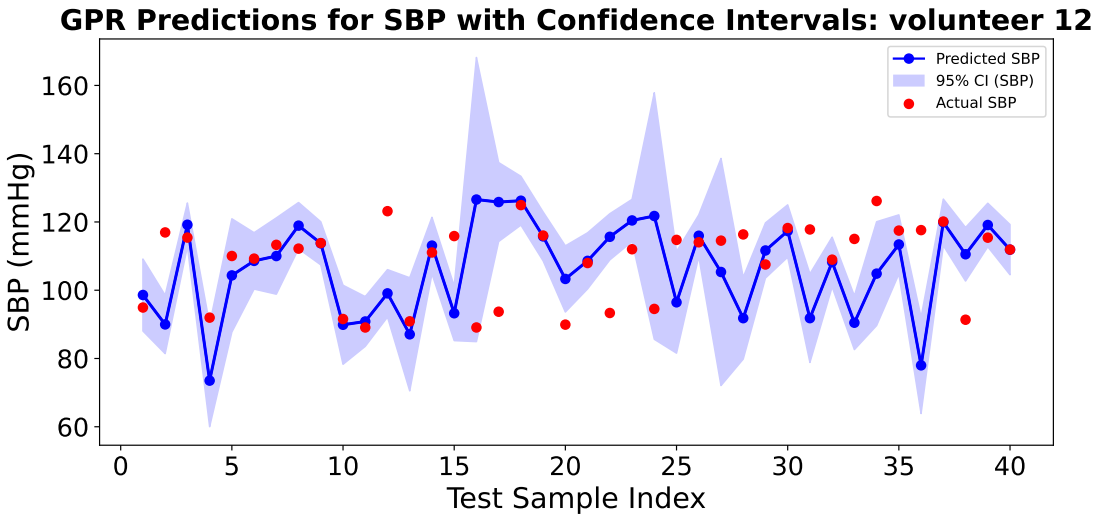

(a)

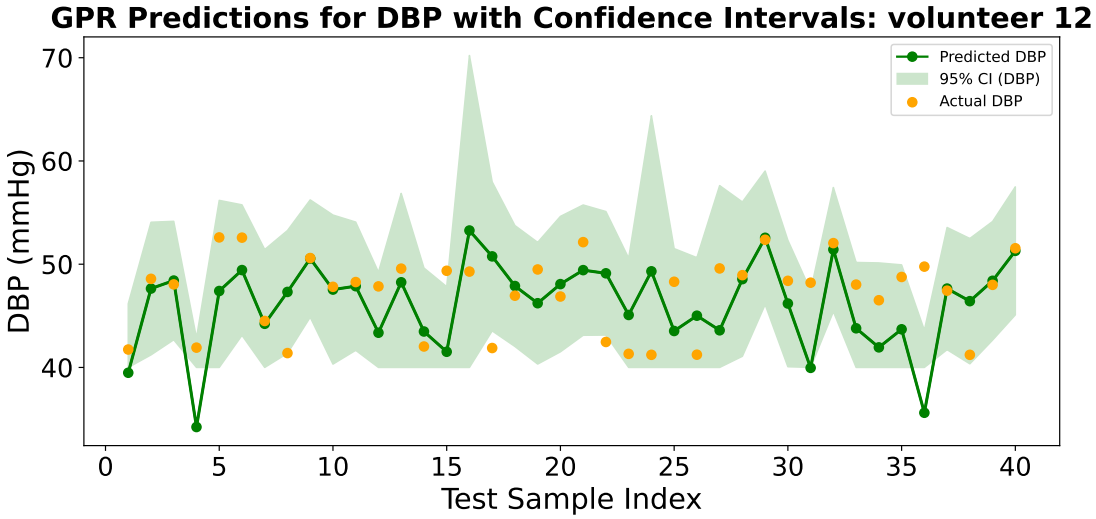

(b)

Figure D.16: *GPR model BP prediction plots for the* ***volunteer 12*** *test set. (a) SBP predictions with 95% CI (light blue). (b) DBP predictions with 95% CI (light green). 35% of SBP and 10% of DBP values lie outside their respective CI.*

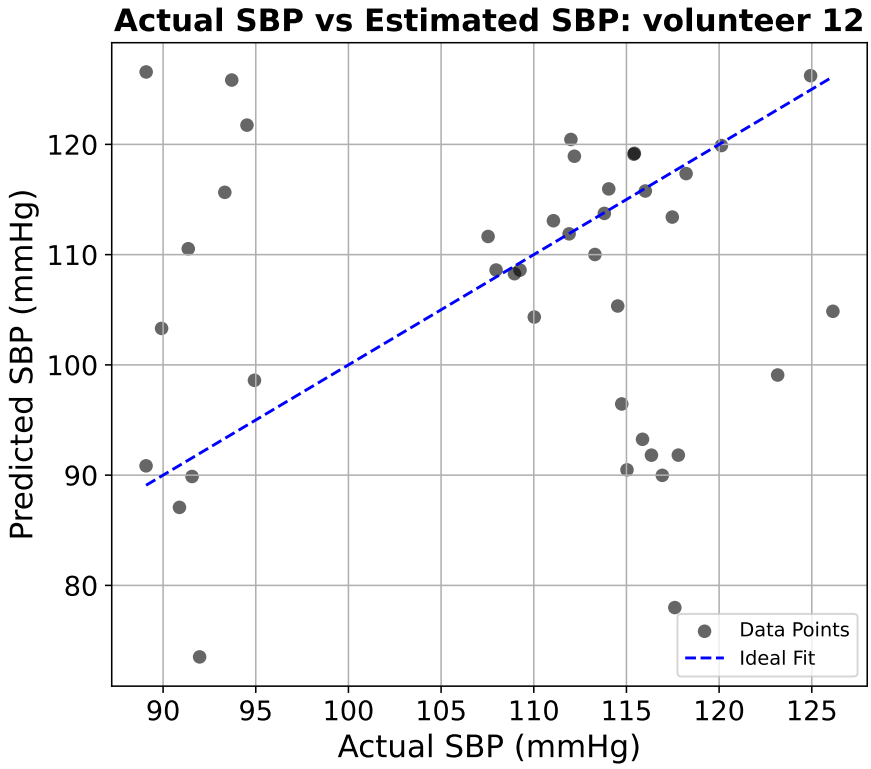

(a)

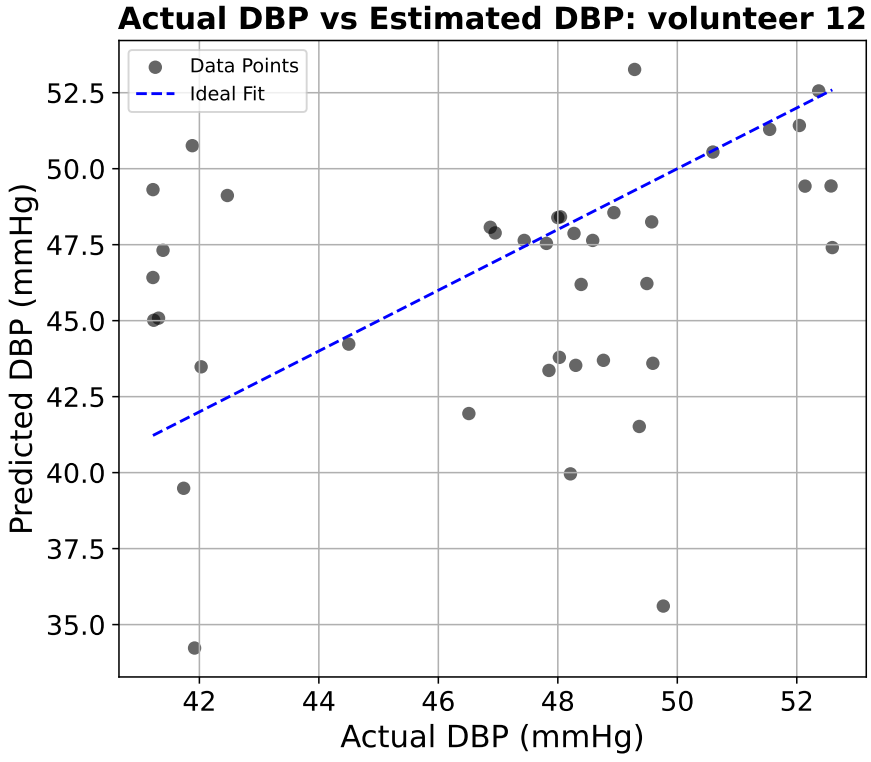

(b)

Figure D.17: *Correlation analysis for the **volunteer 12** test set. (a) SBP: weak correlation with large negative bias (MAE = 11.67, RMSE = 16.56, R^2 = −1.2145, MBE = -2.18). (b) DBP: poor agreement with negative bias (MAE = 3.53, RMSE = 4.74, R^2 = −0.7032, MBE = -0.98).*

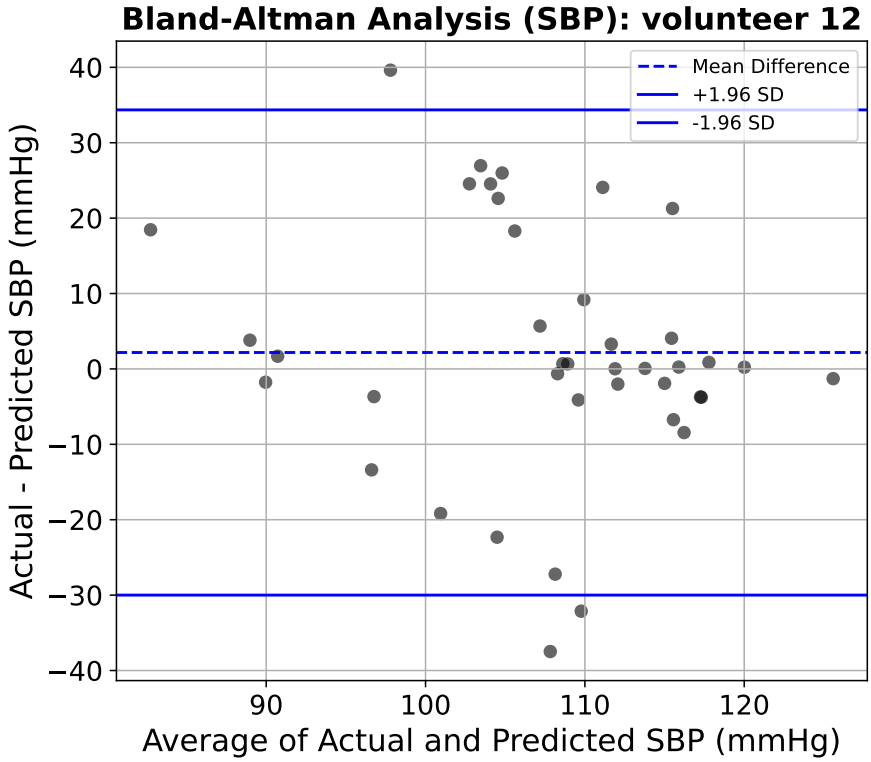

(a)

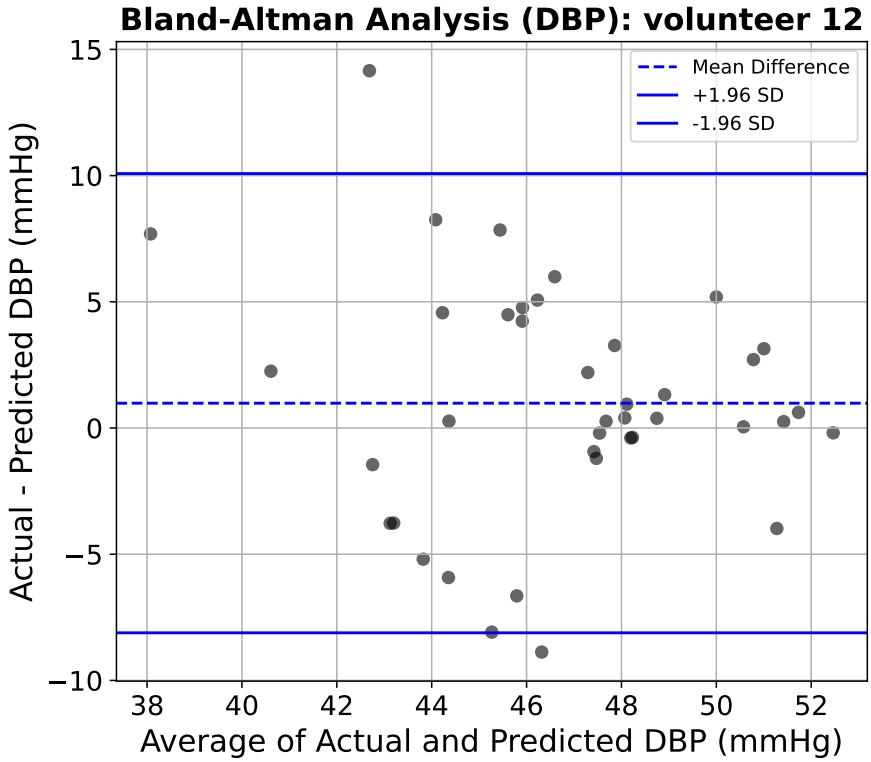

(b)

Figure D.18: *Bland-Altman analysis for the* ***volunteer 12*** *test set. (a) SBP: clear negative bias with very wide LoA. (b) DBP: moderate negative bias with wide LoA.*

Volunteer 13 GPR model

Figure D.19 shows the GPR predictions with confidence intervals for **volunteer 13**. SBP predictions (blue dotted line) partly follow the actual SBP trend (red dots) but deviate noticeably at higher values, with 34% of points outside the CI. DBP predictions (green dotted line) align more closely with the actual DBP values (orange dots), with only 2.7% outside the CI. The SBP CI (light blue region) reaches up to 10 mmHg, while the DBP CI (light green region) is narrower and more consistent ($\leq$ 10 mmHg).

From the correlation analysis (Figures D.20a-D.20b), SBP predictions show limited agreement (MAE = 6.74 mmHg, RMSE = 10.03 mmHg, R^2 = 0.2910, MBE = -1.05 mmHg), with underestimation at higher SBP values. DBP predictions show better performance (MAE = 1.17 mmHg, RMSE = 1.90 mmHg, R^2 = 0.6489, MBE = 0.17 mmHg), with stronger correlation and lower errors. Bland-Altman plots (Figures D.21a-D.21b) confirm a small negative bias for SBP with wide LoA, while DBP shows minimal bias and narrower LoA. *Overall: volunteer 13 demonstrates weak SBP prediction but good DBP accuracy.*

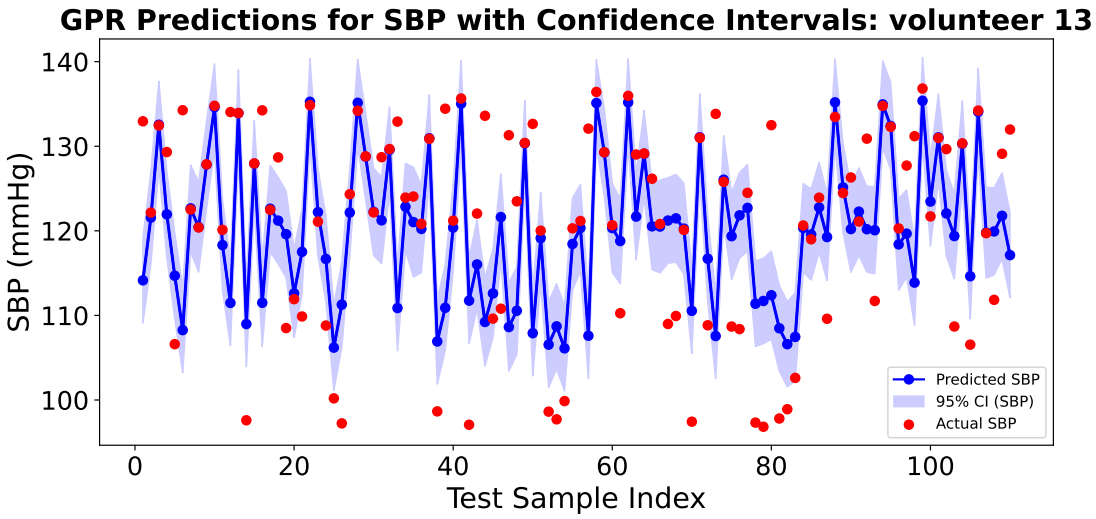

(a)

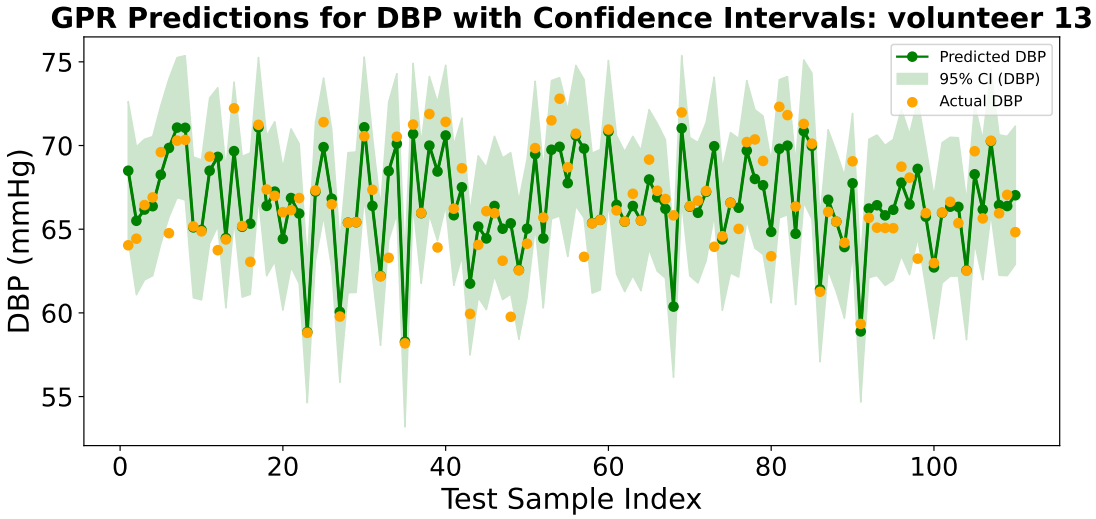

(b)

Figure D.19: *GPR model BP prediction plots for the* ***volunteer 13*** *test set. (a) SBP predictions with 95% CI (light blue). (b) DBP predictions with 95% CI (light green). 34% of SBP and 2.7% of DBP values lie outside their respective CI.*

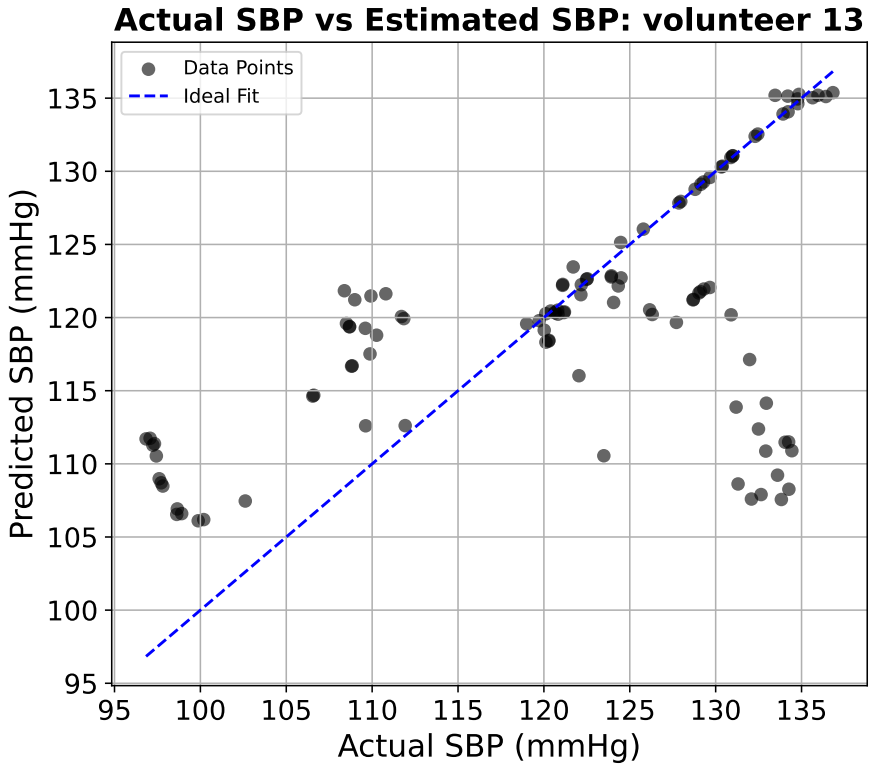

(a)

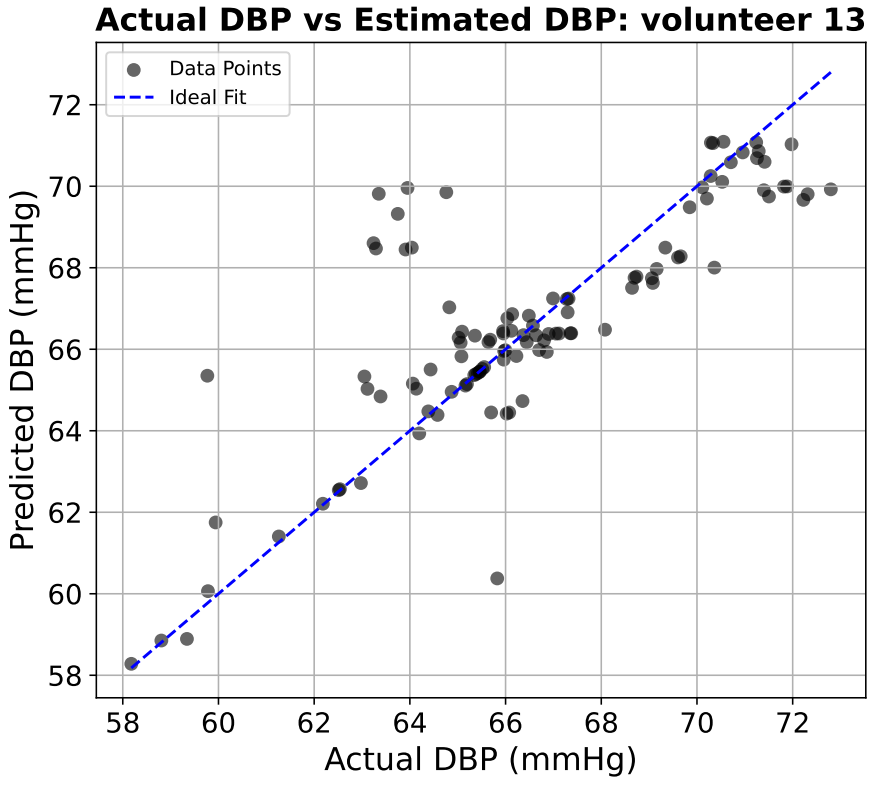

(b)

Figure D.20: *Correlation analysis for the* ***volunteer 13*** *test set. (a) SBP: weak correlation with negative bias (MAE = 6.74, RMSE = 10.03,* R^2 *= 0.2910, MBE = -1.05). (b) DBP: stronger correlation with minimal bias (MAE = 1.17, RMSE = 1.90,* R^2 *= 0.6489, MBE = 0.17).*

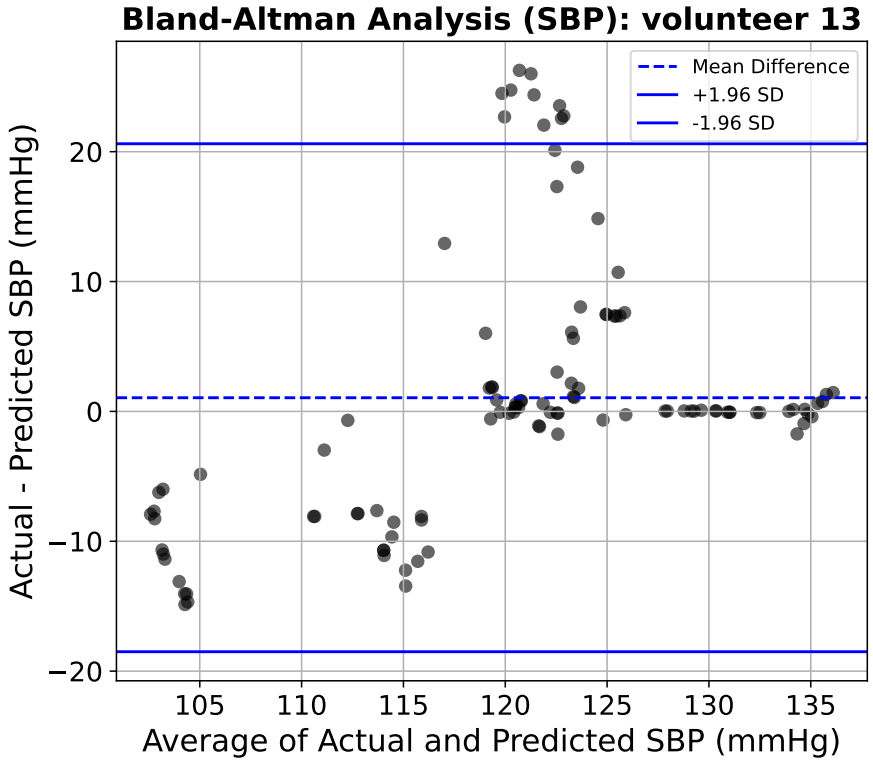

(a)

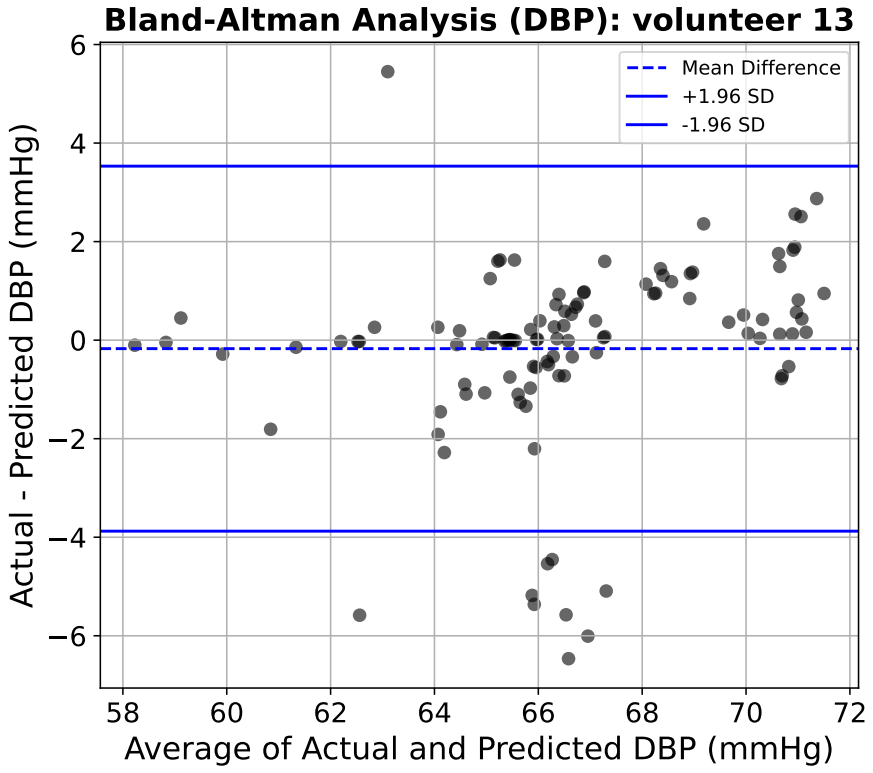

(b)

Figure D.21: *Bland-Altman analysis for the* ***volunteer 13*** *test set. (a) SBP: small negative bias with wide LoA. (b) DBP: minimal bias with tighter LoA.*

Volunteer 14 GPR model

Figure D.22 shows the GPR predictions with confidence intervals for **volunteer 14**. SBP predictions (blue dotted line) partly follow the actual SBP values (red dots), but deviations are frequent, especially at higher SBP values. A large proportion (43%) of SBP points lie outside the CI. DBP predictions (green dotted line) are more stable, with all values inside the CI. The SBP CI (light blue region) varies in width up to 10 mmHg, while the DBP CI (light green region) remains narrower ($\leq$ 10 mmHg).

From the correlation analysis (Figures D.23a-D.23b), SBP predictions show weak agreement (MAE = 10.26 mmHg, RMSE = 12.79 mmHg, R^2 = 0.2032, MBE = -0.75 mmHg), with consistent underestimation at higher values. DBP predictions perform better (MAE = 0.95 mmHg, RMSE = 1.25 mmHg, R^2 = 0.2946, MBE = 0.06 mmHg), showing small errors and near-zero bias. Bland-Altman plots (Figures D.24a-D.24b) confirm a negative mean difference with wide LoA for SBP, while DBP shows minimal bias and narrow LoA. *Overall: volunteer 14 shows poor SBP prediction but reliable DBP accuracy.*

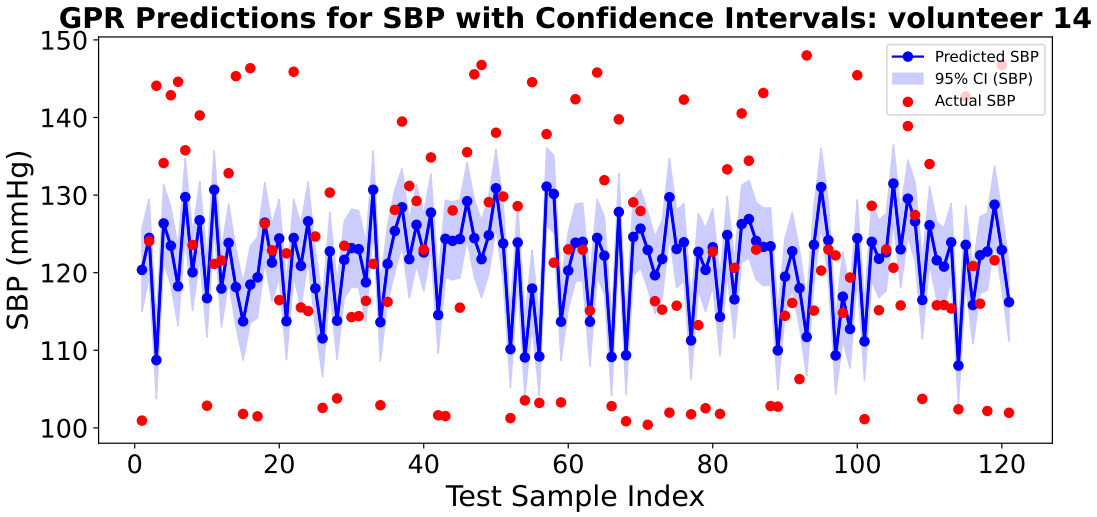

(a)

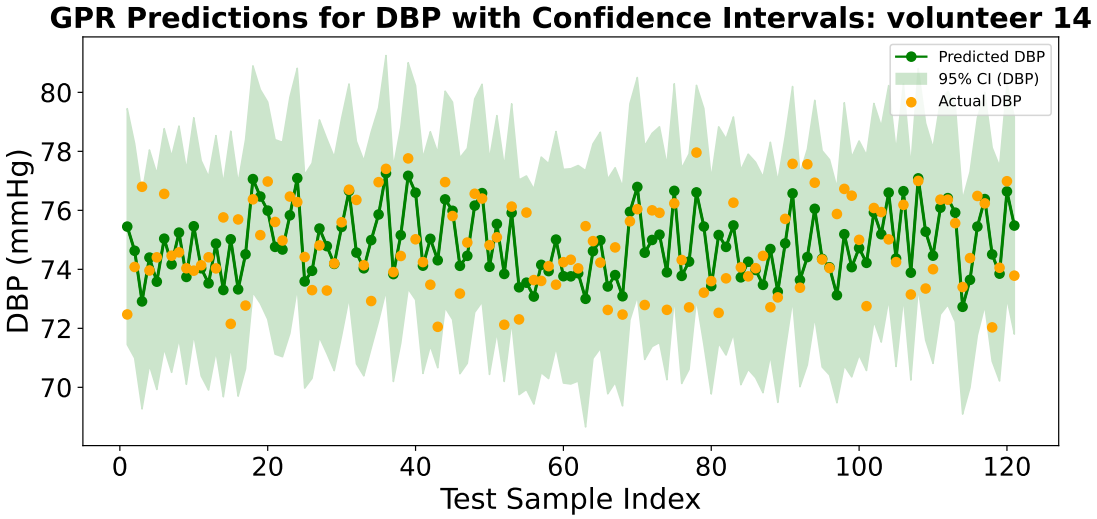

(b)

Figure D.22: *GPR model BP prediction plots for the* ***volunteer 14*** *test set. (a) SBP predictions with 95% CI (light blue). (b) DBP predictions with 95% CI (light green). 43% of SBP values lie outside the CI, while all DBP values are within the CI.*

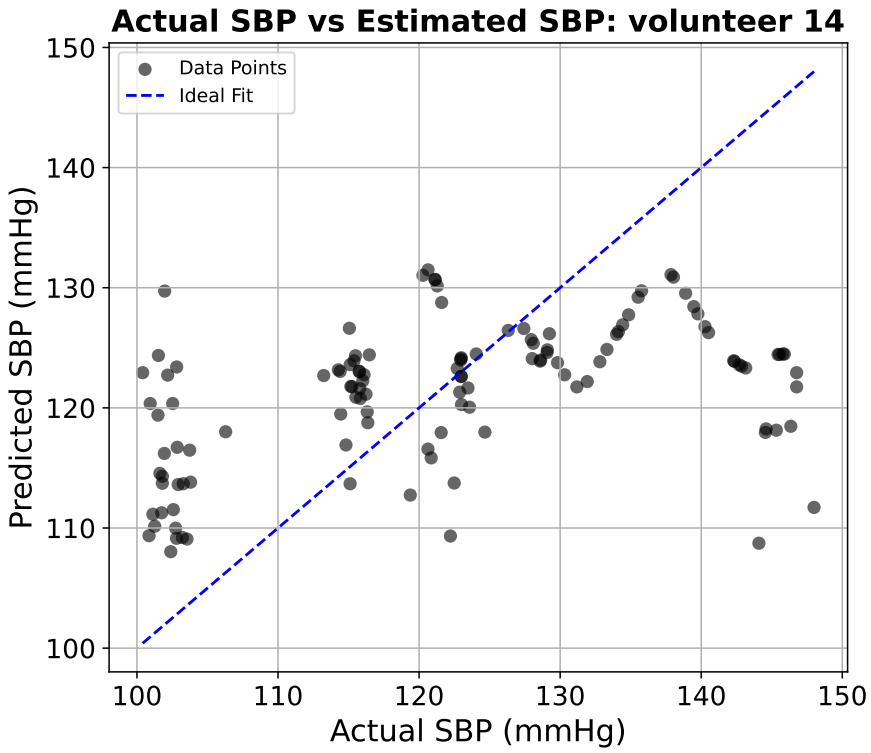

(a)

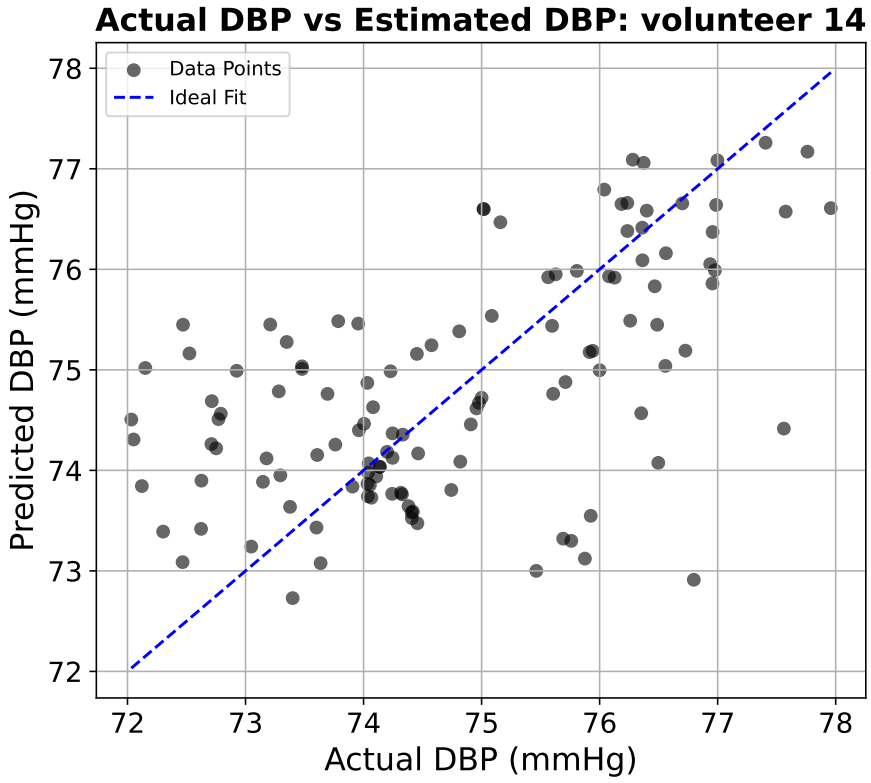

(b)

Figure D.23: *Correlation analysis for the **volunteer 14** test set. (a) SBP: weak correlation with negative bias (MAE = 10.26, RMSE = 12.79, R^2 = 0.2032, MBE = -0.75). (b) DBP: stronger correlation with small errors (MAE = 0.95, RMSE = 1.25, R^2 = 0.2946, MBE = 0.06).*

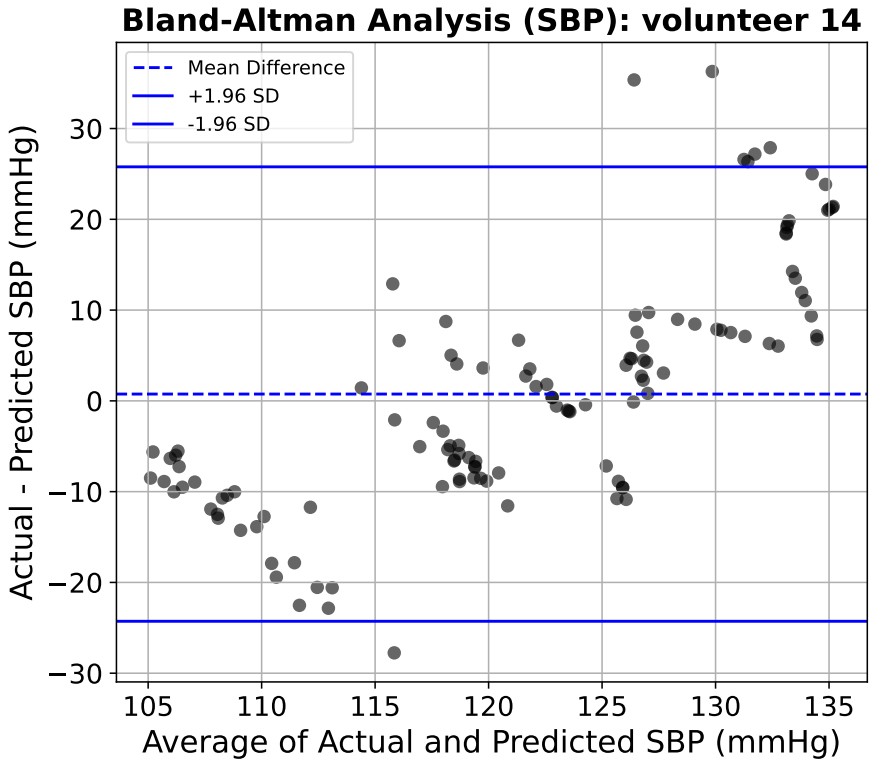

(a)

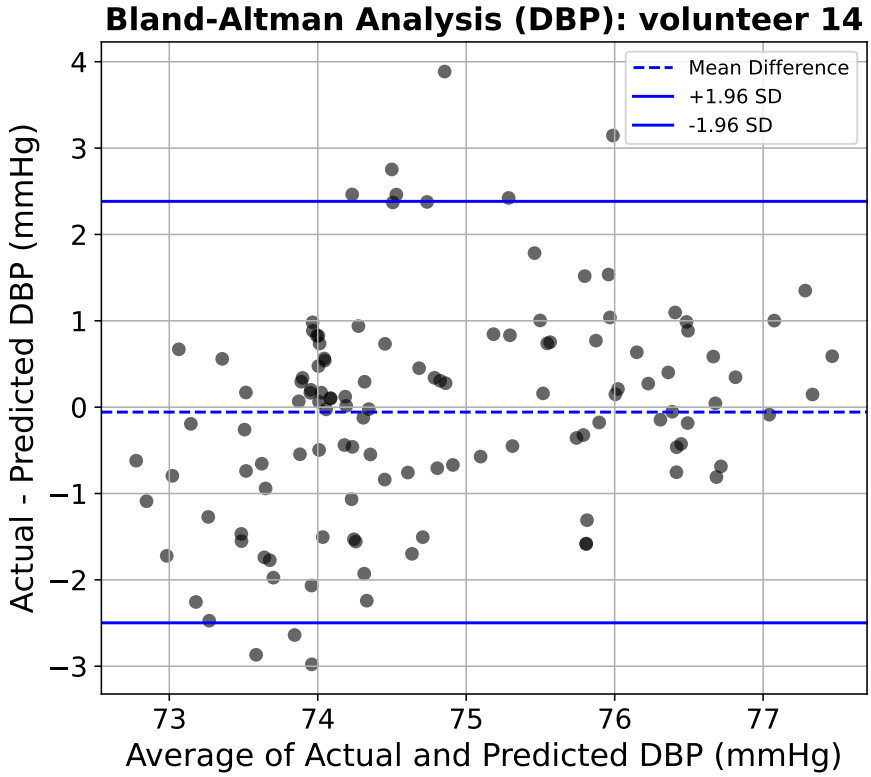

(b)

Figure D.24: *Bland-Altman analysis for the* ***volunteer 14*** *test set. (a) SBP: negative bias with wide LoA. (b) DBP: minimal bias with narrow LoA.*

Volunteer 15 GPR model

Figure D.25 shows the GPR predictions with confidence intervals for **volunteer 15**. SBP predictions (blue dotted line) broadly follow the actual SBP values (red dots), though 36% lie outside the CI. DBP predictions (green dotted line) are more accurate, with only 1.5% outside the CI. The SBP CI (light blue region) varies up to 10 mmHg, while the DBP CI (light green region) is narrower ($\leq$ 5 mmHg).

From the correlation analysis (Figures D.26a-D.26b), SBP predictions show good agreement overall (MAE = 6.67 mmHg, RMSE = 11.06 mmHg, R^2 = 0.7572), though with a systematic underestimation (MBE = -2.94 mmHg). DBP predictions perform strongly (MAE = 1.05 mmHg, RMSE = 2.37 mmHg, R^2 = 0.7970), with a very small negative bias (MBE = -0.23 mmHg). Bland-Altman plots (Figures D.27a-D.27b) confirm negative bias and wider LoA for SBP, while DBP shows minimal bias with tight LoA. *Overall: volunteer 15 demonstrates robust performance, with particularly strong DBP prediction and good SBP correlation despite some underestimation.*

Comparative summary of GPR model performance across volunteers

The GPR model performance varied considerably across volunteers, with notable differences between SBP and DBP predictions. Volunteer 5 exhibited the strongest overall performance, with very low errors (MAE $<$ 1 mmHg), high R^2 values, and negligible bias for both SBP and DBP, confirming the robustness of the model under this subject's conditions. Volunteers 9 and 15 also demonstrated highly reliable outcomes, with consistently low errors, strong correlation, and minimal bias, particularly for DBP, where both subjects showed tight agreement and narrow limits of agreement. Volunteer 4 performed well with balanced accuracy for both SBP and DBP, though with slightly higher errors compared to volunteers 5, 9, and 15.

In contrast, Volunteers 12 and 14 represented the weakest cases: volunteer 12 showed systematic underestimation with high SBP errors and negative R^2 values for both SBP and DBP, while volunteer 14 exhibited poor SBP tracking despite acceptable DBP accuracy. Volunteers 1, 3, 10, and 13 showed intermediate performance, achieving moderate SBP correlations but with larger deviations at specific pressure ranges and weaker explanatory power for DBP.

Overall, the results highlight that the model can achieve robust accuracy in favourable cases (e.g., volunteers 5, 9, 15, and 4), yet performance remains inconsistent across the population, particularly for SBP estimation where variability and bias are more pronounced. These findings emphasise both the feasibility of PAT-based GPR modelling for cuffless BP monitoring and the need for strategies to improve model generalisability across diverse subjects.

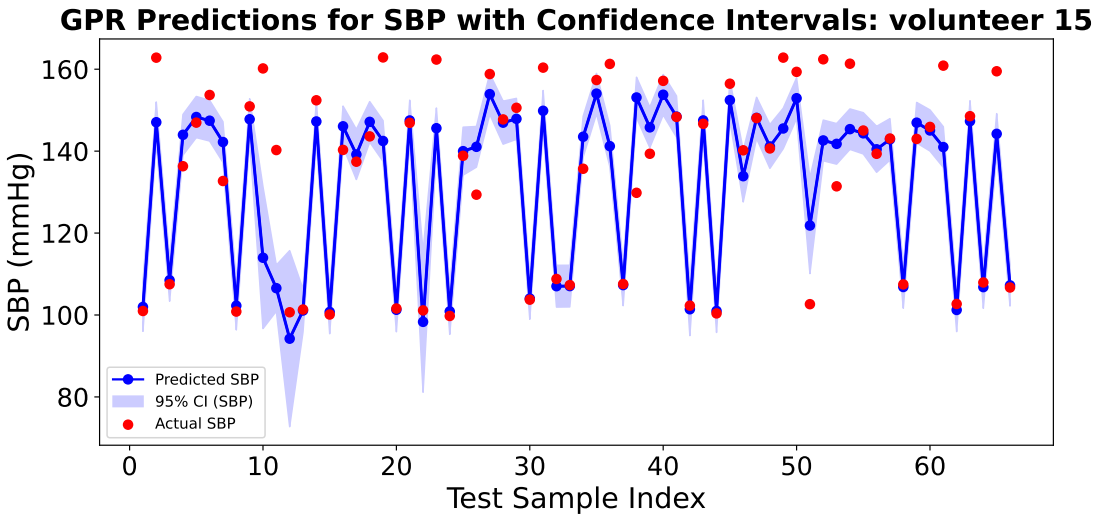

(a)

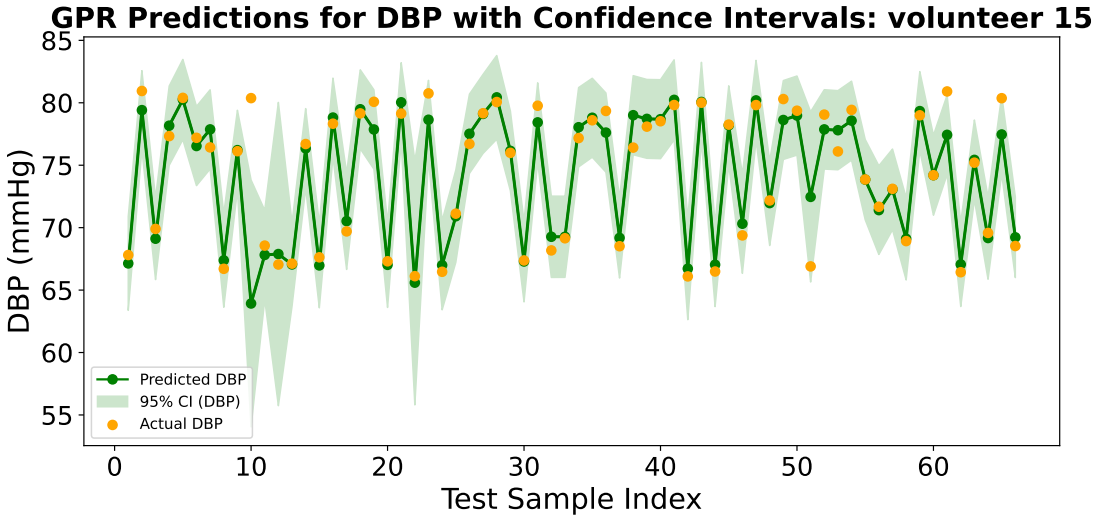

(b)

Figure D.25: *GPR model BP prediction plots for the* ***volunteer 15*** *test set. (a) SBP predictions with 95% CI (light blue). (b) DBP predictions with 95% CI (light green). 36% of SBP and only 1.5% of DBP values lie outside their respective CI.*

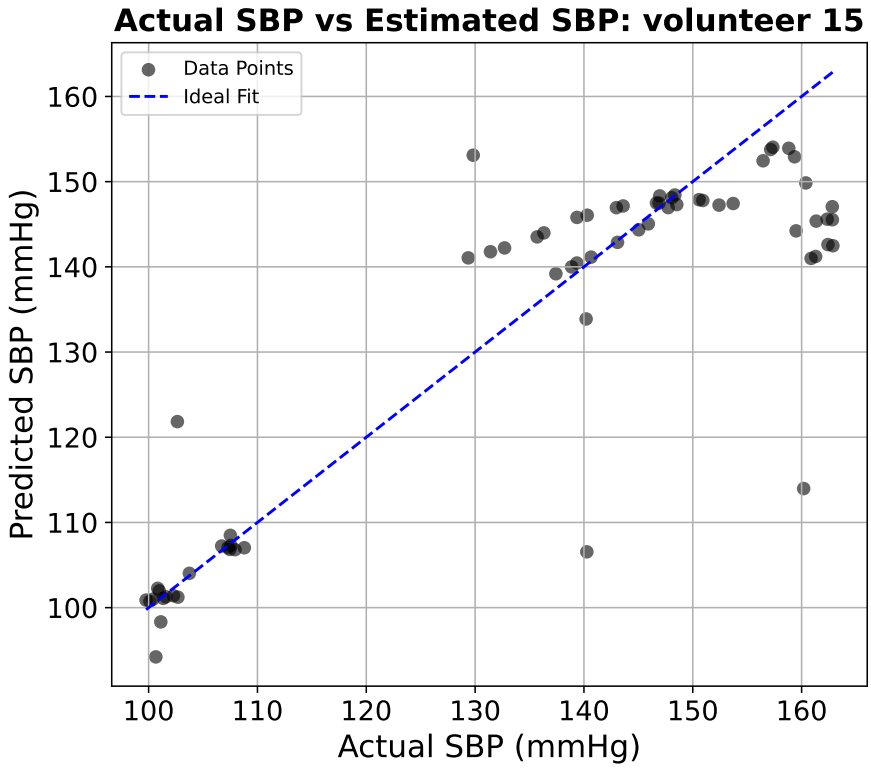

(a)

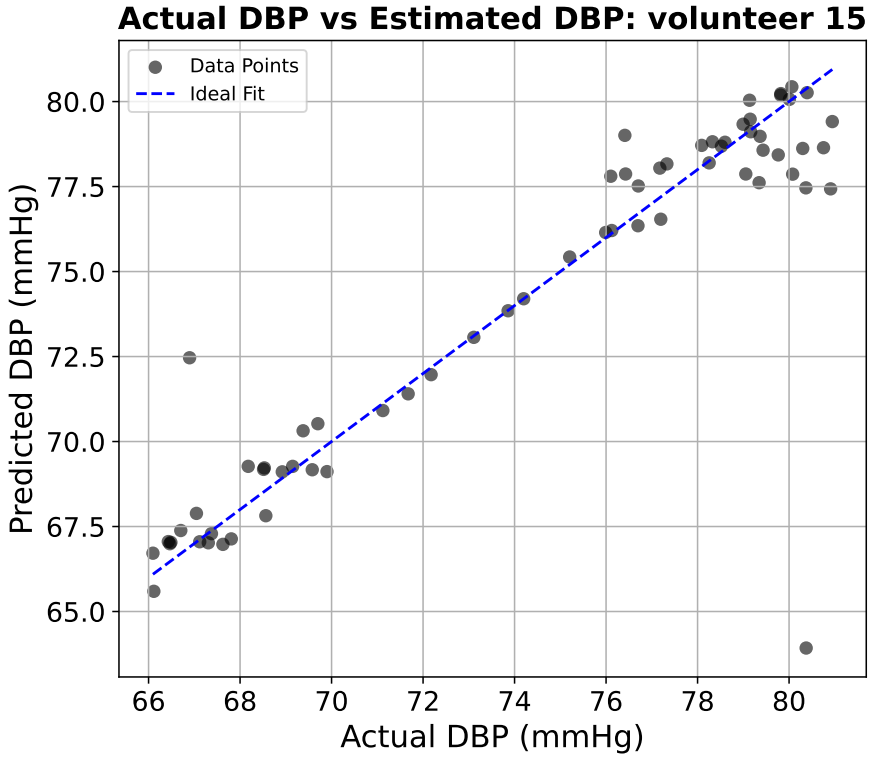

(b)

Figure D.26: *Correlation analysis for the* ***volunteer 15*** *test set. (a) SBP: strong correlation with negative bias (MAE = 6.67, RMSE = 11.06, R^2 = 0.7572, MBE = -2.94). (b) DBP: strong correlation with minimal bias (MAE = 1.05, RMSE = 2.37, R^2 = 0.7970, MBE = -0.23).*

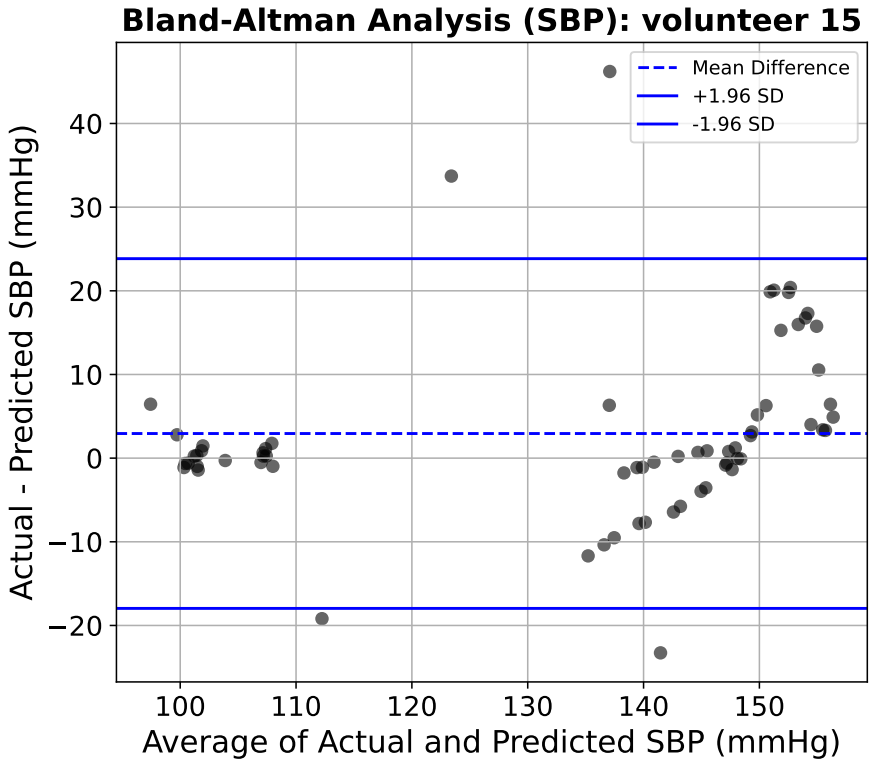

(a)

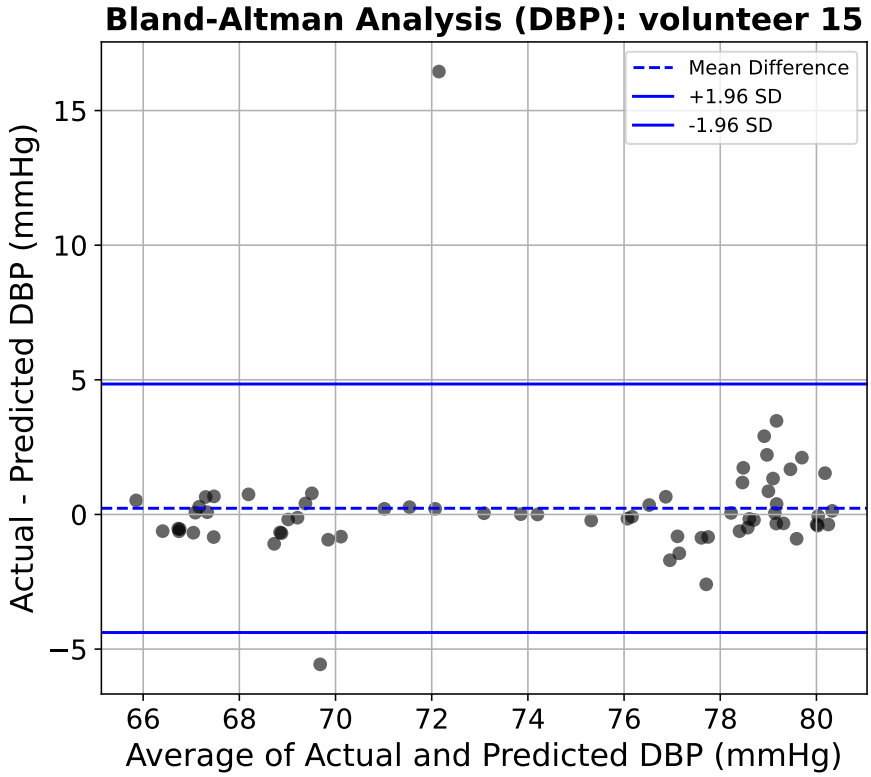

(b)

Figure D.27: *Bland-Altman analysis for the* ***volunteer 15*** *test set. (a) SBP: negative bias with wide LoA. (b) DBP: minimal bias with narrow LoA.*

E. Appendix

2020-21 academic year only

Faculty of Engineering
Process for approval of research study involving human participants

Introduction
This document describes the process to be followed when planning and obtaining approval for studies involving human participants within the Faculty of Engineering. The process is administered by the Faculty Research Ethics Committee, and managed by the Chair of the Ethics Committee and the Faculty Research Ethics Officer. All queries regarding the process should be initially sent to ez-eng-ethics@nottingham.ac.uk

What is Ethics Approval?

When conducting any study or observation or collecting data about individuals, it is essential that full consideration is given to ethical issues and that steps are taken to ensure participant well-being throughout the study.

Participants involved in research studies have a right to:
- Know the goals of the study and who is funding the work
- Make an informed decision about whether or not they wish to participate
- Leave the study at any time if they do not wish to continue
- Know what will happen to them during the study and how long it will take
- Know if they may experience any discomfort
- Know what will happen to the findings
- Privacy of personal information
- Be treated courteously

The University of Nottingham and Faculty of Engineering have an ethics procedure that requires all staff and students to submit an application for ethical approval before conducting any research study involving human participants. Members of the Ethics Committee read through study proposals to check that the researcher has demonstrated that they have given full consideration to ethical issues and that they have provided participants with appropriate and sufficient information.

Who needs Ethics Approval?

ANY member of staff or registered student of the University of Nottingham involved in conducting any study or observation or collecting data about individuals **MUST** adhere to the University Code of Research Conduct and Research Ethics. Those affiliated with the Faculty of Engineering **MUST ALSO** comply with the Faculty ethical approval process before commencing their study.

Ethics application procedure

The attached document outlines the ethics approval process within the Faculty of Engineering. For all applications required to undergo formal review, applications must be submitted to the **Ethics Administrator**, APM Hub, L4-B03, Faculty of Engineering. The application will then be reviewed by the ethics committee. We aim to return a decision to applicants within three weeks but the procedure may be delayed if the ethics committee require further information. It is the applicant's responsibility to make sure that applications are submitted in good time.

THE STUDY MAY **NOT** START UNTIL ETHICAL APPROVAL HAS BEEN AWARDED

2020-21 academic year only

Faculty of Engineering
Application for approval of research study involving human participants

ALL applicants must provide the following information
The applicant must be the person who will conduct the investigations; each application must be made by one applicant:

- usually the student in the case of taught or research courses,
- usually the researcher (the member of university research or academic staff) who will conduct the study in the case of funded research projects,
- usually the principal investigator in the case of applications for ethics approval in advance of submission of a research proposal

If the applicant is an Undergraduate or Postgraduate taught or research student please complete the information below. The application must be approved by a Supervisor.

Name of student:	Itzel Alexia Avila Castro	Student No:	4297904
Course of study:	PhD in Electrical and Electronic Engineering	Email address:	ezxiaav@nottingham.ac.uk
Supervisor:	Barrie Hayes-Gill	PGR ■	PGT ☐
		UG ☐	

If the applicant is a member of university research or academic staff, please complete the information below: For research staff, the application must be approved by the Principal Investigator

Name:		Principal Investigator (Budget Holder)	
Email address:		PI Signature: ……	

Title of investigation: **Blood pressure prediction using ECG and FBG signals**

Planned date for study to begin **19 August 2024** Duration of Study **3 Months**

Please state whether this application is:

☐ New ☐ Revised ■ A renewal ☐ For a continuation study

Selection of review process

Please indicate whether the application is required to go forward to the ethics committee for formal review, or, in the case of projects completed by ***taught undergraduate and postgraduate students only***, whether the application can be approved by the supervisor under the expedited review process*.

■ Formal review, application will be submitted to ethics committee

☐ Expedited review, application is approved by supervisor*
* This option can only be selected if the Supervisor is a member of the Faculty Ethics committee

Approval by supervisor: expedited review

I approve the application as supervisor of this project, under the expedited review procedure.

Name of supervisor…… Signature…… Date……..

Office use only

Date form received: **Date decision returned to applicant:**
Passed to reviewers: 1. Name…… Date……..
(formal review only) 2. Name…… Date……..

2020-21 academic year only

Ethical Issues Checklist

The purpose of this Checklist is to facilitate the review process and to identify any ethical issues that may concern the Committee. It is meant to be an aid to both the researcher and the Committee. Listed below are areas which require some justification and attention on your part in specifying your study protocol. Please answer each question honestly, giving full details where required. Answering "YES" to any of the questions will not necessarily lead to a negative response to your application but it will draw issues to your attention and give the reviewers the opportunity to ensure appropriate steps are being taken. In expedited review, supervisors should ensure that for any questions where the answer "YES" has been given, appropriate measures have been taken to maintain ethical compliance.

Applicant's full name: ..... **Itzel Alexia Avila Castro** .....

You must complete ALL of this section before submitting your application

1 Who is the population to be studied?

Healthy female/male volunteers (age: 30 ± 12 years), members of the research team (academic staff, researchers, PhD students)

.....

2 Please give details of how the participants will be identified, approached and recruited. (Include any relationship between the investigator and participants e.g. instructor-student).

The invitation to participate to the experiment will be posted among the member of the Optics and Photonics Research Group of University of Nottingham, either through email or teams group channel.

.....

3 Will the population studied include any vulnerable members of the public? **YES** ☐ **NO** ■
Note: for the purpose of ethics approval this includes participants who are under 18, people who are disabled or in poor health, and also those who are non-English speakers and may not be able to understand the consent forms. (If YES, please give further details)

.....

4 Will it be possible to associate specific information in your records with specific participants on the basis of name, position or other identifying information contained in your records? **YES** ☐ **NO** ■

.....

5 What steps have you taken to ensure confidentiality of personal information and anonymity of data both during the study and in the release of its findings?

All information which is collected about the subject during the course of the research will be kept strictly confidential and our procedures for handling, processing, storage and destruction of your data are compliant with the Data Protection Act 1998. The data, including ECG signal, FBG signals, and blood pressure measurements will be retained for 7 years following any publication, after this time it will be destroyed. All of the data will be stored on password protected computers in the research laboratory of the Optics and Photonics Group. Only members of the research group will have access to the data. It is not possible to identify any individuals because any data will be published anonymously.

.....

6 Describe what data will be stored, where, for what period of time, the measures that will be put in place to ensure security of the data, who will have access to the data, and the method and timing of disposal of the data.

ECG, FBG and Blood Pressure measurements and patient number will be stored, in one drive of Microsoft Office 365, and in the R drive with restricted access and all the paper records will be stored in a locked filing cabinet. All the data will be kept securely for a period of seven years following any publication. Access will be to members of the research team via an access link.

2020-21 academic year only

Paper records should be stored in a locked filing cabinet. Digital data should be stored only on a password-protected computer and/or on a secure server. In accordance with the Data Protection Act, the data needs to be kept securely for seven years following publication kept securely for seven years following publication of results. After this time, electronic files will be deleted and any hard copies will be destroyed.

At the end of a student project, students are responsible for ensuring that all data from the study is passed on to their academic supervisor/s. The supervisors/s will then have responsibility for the storage of that data.

The data that will be recorded are the Fiber Bragg Grating (FBG) signal, the Electrocardiogram (ECG) signal and Blood Pressure recorded by A&M ltd and GE B450 Monitor, respectively. All the paper records will be stored in a locked filing cabinet and the digital data will be stored on a password-protected computer and in one-drive with restricted access. All the data will be kept securely for a period of seven years following any publication. Access will be to members of the research team via password protected computer or access link.

		YES	NO
7	Will persons participating in the study be subjected to physical or psychological discomfort, pain or aversive stimuli which is more than expected from everyday life? (If YES, please give further details)	☐	■
8	Will participants engage in strenuous or unaccustomed physical activity? (If YES, please give further details)	☐	■
9	Will the investigation use procedures designed to induce participants to act contrary to their wishes? (If YES, please give further details)	☐	■
10	Will the investigation use procedures designed to induce embarrassment, humiliation, lowered self esteem, guilt, conflict, anger, discouragement or other emotional reactions? (If YES, please give further details)	☐	■
11	Will participants be induced to disclose information of an intimate or otherwise sensitive nature? (If YES, please give further details)	☐	■
12	Will participants be deceived or actively misled in any manner? (If YES, please give further details)	☐	■
13	Will information be withheld from participants that they might reasonably expect to receive? (If YES, please give further details)	☐	■
14	Will the research involve potentially sensitive topics? (If YES, please give further details)	☐	■
15	Will data be collected which requires potentially invasive procedures (eg attaching electrodes to the skin) and/or other health-related information to be identified (eg heart rate). If yes please give details	■	☐

2020-21 academic year only

- **Yes, for ECG measurements up to 3 electrodes will be attached to the chest's subject, for FBG measurements, the FBG sensors will be attached to the arms of the subject (A&M ltd electrical and optical physiological recorder), and for the blood pressure measurements, a health monitor (GE B450) will be placed on the right upper arm of the subject.**

……

If you require space for additional information, please add it here and identify the question to which it refers:

2020-21 academic year only

Checklist of information to include with your application:
Please tick the boxes below to confirm that you have included the following information with your submission. Failure to include the required information may result in your ethics application and approval for start of your research to be delayed.

- ■ A brief description of the study design:
  - number and type of participants
  - number and duration of activities participants will be involved in
  - equipment and procedures to be applied
  - information about how participants will be recruited
  - whether participants will be paid (state how this will be done)
  - plans to ensure participant confidentiality and anonymity
  - plans for storage and handling of data
  - information about what will happen to the data after the study
  - information about how any data and images may be used
  - state whether it will be possible to identify any individuals.

- ■ Copies of any information sheets to be given to participants (include recruitment information (e.g. adverts, posters, letters, etc)

- ■ A copy of the participant consent form

- ■ Copies of data collection sheets, questionnaires, etc

I confirm that all of the above is included in the application:

As the applicant I confirm that I have read and understand the Ethical requirements for my study and have read and complied with the University of Nottingham Code of Research Conduct and Research Ethics.

Itzel Alexia Aviles Castro

Signature of applicant ..... Date .....16/08/2024...

As supervisor, I confirm that I have checked the details of this application.

B K Hayes - 6.11

Signature of supervisor .... Date .....16/08/2024.....

NB The signature of the supervisor on this part of the application DOES NOT indicate supervisor approval for expedited review. If supervisor approval is granted then the front page of the application MUST be signed for approval to be confirmed.

Ethics Committee Reviewer Decision

This form must be completed by each reviewer. Each application will be reviewed by two members of the ethics committee. Reviews may be completed electronically and sent to the Faculty ethics administrator from a University of Nottingham email address, or may be completed in paper form and delivered to the Faculty of Engineering Research Office.

Applicant full name: Itzel Castro

Reviewed by: B18

Signature (paper based only) ……

05/09/24

- ☑ Approval awarded - no changes required
- ☐ Approval awarded - subject to required changes (see comments below)
- ☐ Approval pending - further information & resubmission required (see comments)
- ☐ Approval declined – reasons given below

Comments:

n/a

Please note:

1. The approval only covers the participants and trials specified on the form and further approval must be requested for any repetition or extension to the investigation.
2. The approval covers the ethical requirements for the techniques and procedures described in the protocol but does not replace a safety or risk assessment.
3. Approval is not intended to convey any judgement on the quality of the research, experimental design or techniques.
4. Normally, all queries raised by reviewers should be addressed. In the case of conflicting or incomplete views, the ethics committee chair will review the comments and relay these to the applicant via email. All email correspondence related to the application must be copied to the Faculty research ethics administrator.

Any problems which arise during the course of the investigation must be reported to the Faculty Research Ethics Committee

Ethics Committee Reviewer Decision

This form must be completed by each reviewer. Each application will be reviewed by two members of the ethics committee. Reviews may be completed electronically and sent to the Faculty ethics administrator from a University of Nottingham email address, or may be completed in paper form and delivered to the Faculty of Engineering Research Office.

Applicant full name: Itzel Castro

Reviewed by: D13

Signature (paper based only) ……

02/09/24

- ☑ Approval awarded - no changes required
- ☐ Approval awarded - subject to required changes (see comments below)
- ☐ Approval pending - further information & resubmission required (see comments)
- ☐ Approval declined – reasons given below

Comments:

n/a

Please note:

1. The approval only covers the participants and trials specified on the form and further approval must be requested for any repetition or extension to the investigation.
2. The approval covers the ethical requirements for the techniques and procedures described in the protocol but does not replace a safety or risk assessment.
3. Approval is not intended to convey any judgement on the quality of the research, experimental design or techniques.
4. Normally, all queries raised by reviewers should be addressed. In the case of conflicting or incomplete views, the ethics committee chair will review the comments and relay these to the applicant via email. All email correspondence related to the application must be copied to the Faculty research ethics administrator.

Any problems which arise during the course of the investigation must be reported to the Faculty Research Ethics Committee

Brief description of the study design
Title of the study: Experimental Study to create a predictive model of blood pressure based on FBG and ECG signals

- **Background**

Hypertension is considered a one of the silent health disorders [1,2], where its early detection with continuous blood pressure (BP) monitoring is crucial to undermine a potentially fatal outcome. Currently, there a two gold standards methods to monitor BP, one is the Invasive Arterial Catheter, which measures in real time the blood pressure in arteries in high risk surgical and critically ill patients, the other one is the sphygmomanometer which is most common used and a non-invasive method in the upper arm, it requires the user to inflate the cuff beyond a certain mercury level and auscultate to record the point correctly, however it is not ideal for self-use and continuous monitoring of BP. In order to combine the advantages of these gold standard methods, continuous measurements and non-invasiveness, there is a lot of research focusing on the development of cuff less blood pressure monitoring system [3-6], ensuring patient comfort and 24 hr continuous monitoring.

These methods for cuff-less blood pressure monitoring are classified into pure PPG signal based or in hybrid approaches comprising both ECG and PPG signal features [1]. In this study, we aim to extract features of both ECG and instead of PPG signals FBG signals with optical fibres to predict Blood Pressure Values. The accuracy of this model will be assessed with the correspondent BP values measured through the health monitor B450.

- **number and type of participants**

20 Healthy female/male volunteers (age: 30 ± 12 years)

To minimise risk of COVID-19 infection we have introduced guidelines for conducting healthy volunteer studies within our laboratories.

Following University of Nottingham guidelines

- If you have symptoms of COVID-19, cancel participation and do not come to the laboratory. Follow NHS guidance https://www.nhs.uk/conditions/coronavirus-covid-19/symptoms/
- Follow signage within the Tower building.
- Wear a mask in campus buildings.

Before Participation

- The researcher will collect participant information sheets, describe experiments beforehand via email or via Teams.
- Ensure that maintain maximum numbers associated with the laboratory environment.
- Participant does not enter laboratory until invited, communication via phone beforehand.
- Wipe down surfaces and sensors thoroughly using appropriate viricidal solutions/alcohol wipes. Minimise clutter on laboratory surfaces to make this easier.

The University of Nottingham
UNITED KINGDOM · CHINA · MALAYSIA

Experimental Study to create a predictive model of blood pressure based on FBG and ECG signals

Participant Information Sheet

You are invited to take part in a study which will investigate the features of electrocardiogram (ECG), Fiber Bragg Grating (FBG) signals to predict Blood Pressure (BP) values . Before you decide whether to take part it is important for you to understand why the research is being done and what it will involve. If you would like more information or have any questions, please contact Itzel Avila, itzel.castro@nottingham.ac.uk or Prof. Barrie Hayes-Gill, barrie.hayes-gill@nottingham.ac.uk

Background

Hypertension is considered a one of the silent health disorders, where its early detection with continuous blood pressure (BP) monitoring is crucial to undermine a potentially fatal outcome [1,2]. Currently, there a two gold standards methods to monitor BP, one is the Invasive Arterial Catheter, which measures in real time the blood pressure in arteries in high risk surgical and critically ill patients, the other one is the sphygmomanometer which is most common used and a non invasive method in the upper arm, it requires the user to inflate the cuff beyond a certain mercury level and auscultate to record the point correctly, however it is not ideal for self-use and continuous monitoring of BP. In order to combine the advantages of these gold standard methods, continuous measurements and non invasiveness, there is a lot of research focusing in the development of cuff less blood pressure monitoring system [3-6], ensuring patient comfort and 24 hr continuous monitoring.

These methods for cuff-less blood pressure monitoring are classified into pure PPG signal based or in hybrid approaches comprising both ECG and PPG signal features [1]. In this study, we aim to extract features of both ECG and instead PPG signals, FBG signals to predict Blood Pressure Values. The accuracy of this model will be assessed with the correspondent BP values measured through the health monitor GE B450.

You will be asked to carry out some physical procedures which will involve changing your blood pressure. It should be noted that the study organisers are not medically qualified and cannot offer advice about your health. If you have any concerns after participating in this study then you should contact your general practitioner.